Micro Strip Gas Chambers with Gas Electron Multipliers and their Application in the CMS Experiment

Von der Fakultät für Mathematik, Informatik und Naturwissenschaften der Rheinisch-Westfälischen Technischen Hochschule Aachen zur Erlangung des akademischen Grades eines Doktors der Naturwissenschaften genehmigte Dissertation

vorgelegt von

Diplom-Physiker Dirk Macke
aus Mönchengladbach

Berichter:

Universitätsprofessor Dr. rer. Nat. Günter Flügge
Privatdozent Dr. rer. Nat. Wolfgang Struczinski

Tag der mündlichen Prüfung: 16. Oktober 2000

Abstract

Micro Strip Gas Chambers (MSGCs) have become a very popular type of gaseous detector throughout the last decade. However, its good spatial resolution and high rate capability was overshadowed by instabilities when operated in environments with a high particle flux. Since a major part of the tracking system of the upcoming Compact Muon Solenoid (CMS) experiment at the Large Hadron Collider (LHC) was planned to be built based on this technology, considerable efforts have been taken to solve those difficulties.
This thesis looks at one possible approach to get rid of high rate instabilities: the application of a Gaseous Electron Multiplier (GEM) as a second amplification stage for an MSGC. The design goal was to build a robust detector with the capability of operating safely in the harsh LHC environment with expected particle fluxes up to 10^4Hz/mm^2 while maintaining the full MSGC performance in terms of spatial resolution and detection efficiency.
Such detectors have been successfully built. Stable operation with particle fluxes up to $3\text{x}10^4$Hz/mm^2 could be shown. Full detection efficiency of 99% has been reached at a signal to noise ratio of 18. A spatial resolution of better than 40µm has been achieved.
A full scale detector in the CMS baseline design for the forward tracker has been realised and successfully tested in LHC-like conditions.

Zusammenfassung

Mikrostreifengasdetektoren sind im letzten Jahrzehnt sehr populär geworden. Allerdings war ihre gute Ortsauflösung und hohe Ratenkapazität überschattet von Instabilitäten beim Betrieb mit hohen Teilchenflüssen. Da ein großer Teil der Spurkammer des neuen Compact Muon Solenoid (CMS) Detektors am Speicherring Large Hadron Collider (LHC) aus diesen Detektoren gebaut werden sollte, wurden verschiedene Ansätze zur Lösung dieses Problems untersucht.
Diese Arbeit untersucht einen dieser Lösungsansätze: den Einbau eines Gaseous Electron Multipliers (GEM) als zweite Verstärkungsstufe in eine MSGC. Das Ziel war der Bau eines Detektors, der zuverlässig bei den für LHC erwarteten Teilchenraten von bis zu 10^4Hz/mm^2 betrieben werden kann, ohne auf die Qualitäten einer MSGC – gute Ortsauflösung und hohe Nachweiseffizienz – einen negativen Einfluß zu haben.
Solche Detektoren sind erfolgreich gebaut und stabil mit Teilchenflüssen bis zu $3\text{x}10^4$Hz/mm^2 betrieben worden. Eine Nachweiseffizienz von 99% bei einem Signal-zu-Rausch-Abstand von 18 wurde erreicht. Ortsauflösungen unter 40µm konnten erzielt werden.
Ein kompletter Prototyp, basierend auf den Konstruktionsmerkmalen des CMS Vorwärts-Spurkammersystems, wurde gebaut und erfolgreich unter LHC-ähnlichen Bedingungen in Betrieb genommen.

Preface

This thesis presents results of measurements carried out with various Micro Strip Gas Chambers (MSGCs) combined with Gas Electron Multipliers (GEMs) as a second amplification stage. The realisation of a prototype of a detector module with trapezoidal strips is shown as an application within the framework of the forward tracker of the Compact Muon Solenoid (CMS) experiment at the Large Hadron Collider (LHC).

Following a brief discussion of the Standard Model of particle physics, the LHC and an overview of the CMS detector, the second chapter will present the fundamental concepts of gaseous detectors and introduce the MSGC and GEM.

In the third chapter the realisation of the various detector modules used in the laboratory and beam test experiments will be described. Some emphasis will be put on the considerations which led to the final layout of the GEMs. The design of the CMS forward tracker will be briefly presented and a solution for an MSGC with GEM compliant with those construction requirements is shown.

The fourth chapter introduces the different preamplifiers used throughout the measurements and introduces the data acquisition systems, gas supplies and analysis software used. A brief description of the experimental environment for the test beam experiments will be given.

The fifth chapter will present all analyses carried out. Comparisons between different ‘evolution’ steps of GEMs will be made. Crucial operational parameters such as gain, spatial resolution and detection efficiency will be checked against the CMS requirements. In the final section, the high rate behaviour will be closely looked at.

A conclusion will be given in the final chapter.

Contents

1 THE COMPACT MUON SOLENOID AT THE LARGE HADRON COLLIDER

The Standard Model of high energy physics describes the interactions of the fundamental constituents of matter, namely leptons and quarks, by the emission of gauge bosons in the framework of quantum field theories. Four types of interactions are known to date: The electromagnetic interaction is mediated by photons, and could be successfully united with the weak interaction, whose bosons are the $W^{\pm}$ and Z^0. The strong interaction is mediated by gluons. The unification of these interactions would lead to the demand of a local gauge symmetry under the combined symmetry group of *SU(3) x SU(2) x U(1)*. Little is known of the gravitational interactions, but it should be mediated by gravitons, which are spin-2 bosons. Although there is an impressive agreement between the predictions of the Standard Model and the experimental results, such as those obtained with the Large Electron Positron collider (LEP) at CERN[1], there are still questions to be understood. One of the most prominent is the mass of the $W^{\pm}$ and Z^0 bosons: The gauge invariance of the electroweak Lagrangian requires all gauge bosons to be massless. While this is true for the photon, the $W^{\pm}$ and Z^0 have been found to be quite massive (80GeV/c^2 and 91GeV/c^2 respectively). A scalar background field has been introduced, whose interactions with the gauge bosons give them their masses **[1]-[3]**. The characteristic property of the so-called *Higgs field* is the ground state attained at a non-zero expectation value. This preserves the renormalisation of the *SU(2)* during its spontaneous breakdown, which leads to the gauge bosons' masses. One consequence of this process is the prediction of the *Higgs boson* H. Although its mass can not be given by the Standard Model, a lower bound is yielded by the LEP experiments. The mass of the boson has to be $m_H > 107.7$GeV/c^2 **[4]**. By combining the results of radiative corrections of all LEP experiments, an upper limit of $m_H < 188$GeV/c^2 is expected **[4]**. One of the main goals of the next generation of collider experiments is to confirm the existence of the Higgs boson. This would prove the validity of the Standard Model. Future experiments are prepared to investigate alternative symmetry breaking mechanisms, such as supersymmetric extensions to the Standard Model, if no Higgs particle is found. This would lead to supersymmetric partners for the elementary particles. Not only the number of the constituents of matter would be doubled by a minimal supersymmetric extension, but also four additional Higgs bosons are predicted in this case.

Albeit the current Standard Model is highly successful in its predictions up to now, it is not satisfactory from a theoretical point of view: It contains 18 free parameters (at least) which can only be given by experimental results. It contains the so-called *mass hierarchy problem* between the masses of quarks and leptons and their arrangement in doublets, and it can not explain the existence of exactly three generations of leptons and quarks.

[1] European Laboratory for Particle Physics, Geneva

1.1 Physics at the Large Hadron Collider

The main goal of the Large Hadron Collider (LHC) is to prove the existence or non-existence of the Standard Model Higgs boson, along with the search for supersymmetric particles and the search for unexpected new physics.
LHC is the successor of the LEP collider, which was designed to work at the Z^0 mass of 91GeV/c^2. A recent upgrade allowed to reach collision energies up to 200GeV. For the given LEP tunnel, which has a circumference of 27km, this is the energy limit for a circular electron-positron collider due to synchrotron radiation loss.
LHC will be the next generation collider, located in the old LEP tunnel. It will accelerate protons, which have only a negligible radiation loss due to their large mass compared to electrons. The main disadvantage of hadron-hadron collisions is the distribution of the available centre-of-mass energy to the protons' constituents: All quarks and gluons will carry part of the available energy.
The collider will be able to accelerate bunches of protons up to 7TeV with an interaction rate of 40MHz. The already existing accelerators at CERN will serve the LHC as pre-accelerators, as can be seen in figure 1.

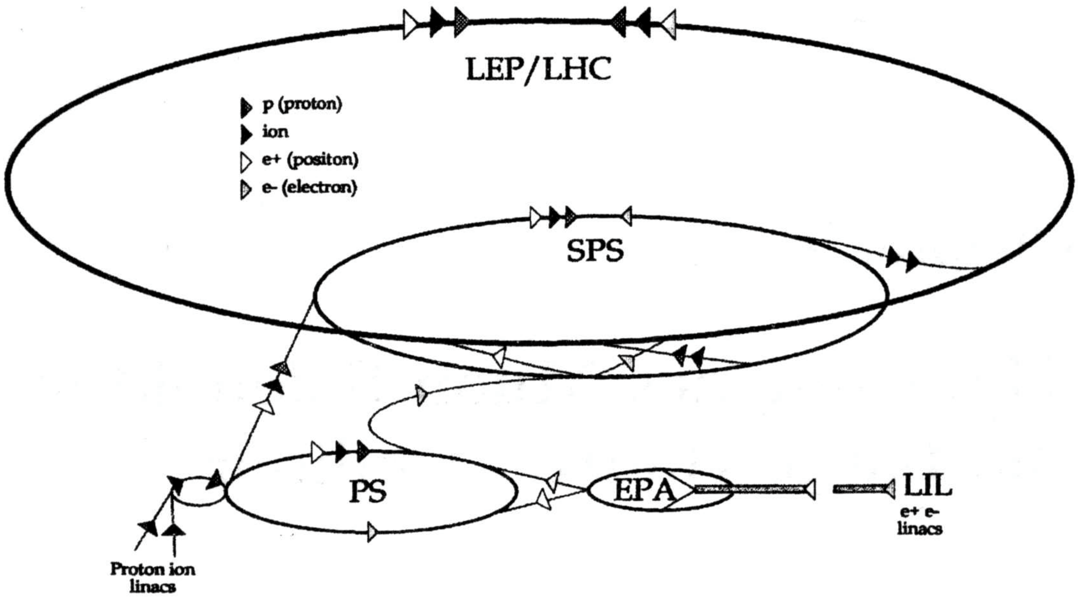

Figure 1 - Current and planned accelerators at CERN. A energy of 1.4GeV will be generated by a linear accelerator ('linac'). The Proton Synchrotron (PS) and Super Proton Synchrotron (SPS) will then accelerate the particles up to 450GeV – these protons are finally injected to LHC and accelerated to their target energy of 7TeV.

Superconducting coils forming 1232 dipole magnets with a length of ≈ 14m each will house two circular beam pipes in a magnetic field of 8T. A schematic of the beam line can be seen in figure 2. It is planned to re-install the LEP beam line in the future beneath LHC[2]. It is aimed for a luminosity of $10^{34}cm^{-2}s^{-1}$ **[5]**. 2835 bunches per injection will collide at four interaction points as shown in figure 3. There are three other experiments planned besides the Compact Muon Solenoid (CMS): A Toroidal LHC Apparatus (ATLAS), which directly

[2] Currently the LEP beam line is located at the position where LHC is sketched in figure 2.

competes with CMS in its physics goals, the LHC B-factory (LHC-B) and A Large Ion Collider Experiment (ALICE), which is foreseen for ion-ion collisions.

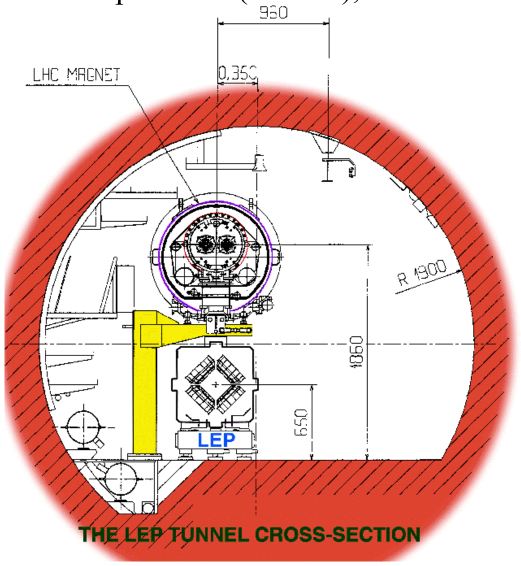

Figure 2 - Cross section of the LEP tunnel with the LHC beam line installed.

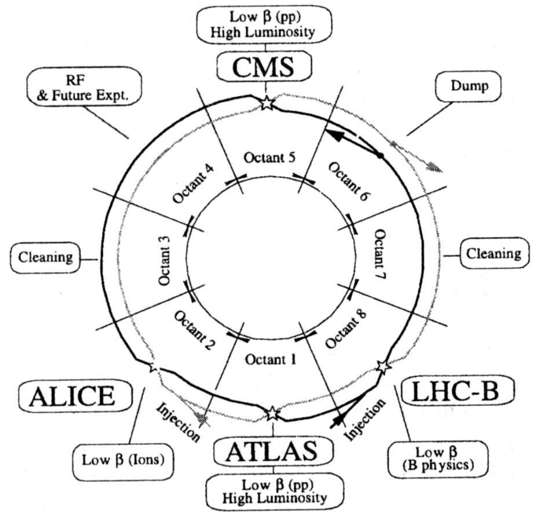

Figure 3 - LHC with its interaction points and the planned experiments

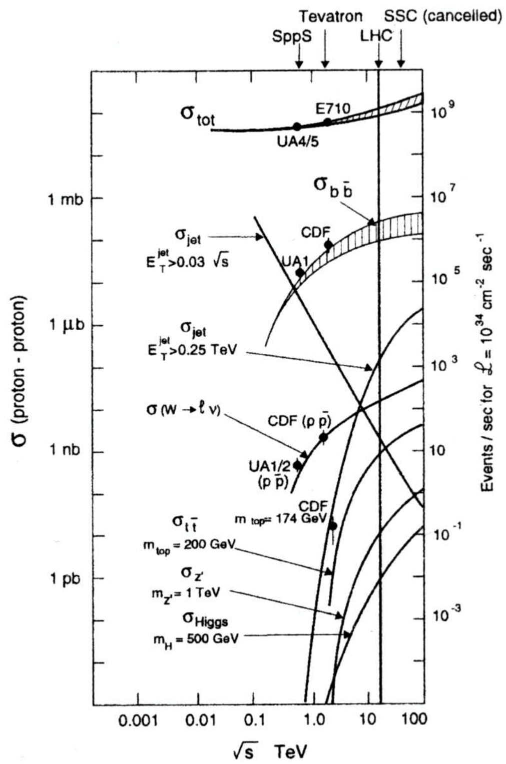

Figure 4 - Production cross sections and event rates for some selected processes in proton-proton collisions as a function of centre-of-mass energy

As can be seen in figure 4, LHC will produce a large number of b-pairs, 10^{12}-10^{13} per year, when operating at a luminosity of $10^{34}\text{cm}^{-2}\text{s}^{-1}$. This allows studies of B mesons with high statistics. Of particular interest are CP violations in the B sector for testing the validity of the Standard Model. Of paramount interest is the detection of the Higgs boson, either in the framework of the Standard Model or one of its supersymmetric extensions. It can be seen in figure 4 that the production cross section for Higgs bosons is very small. A high luminosity is required for that reason.

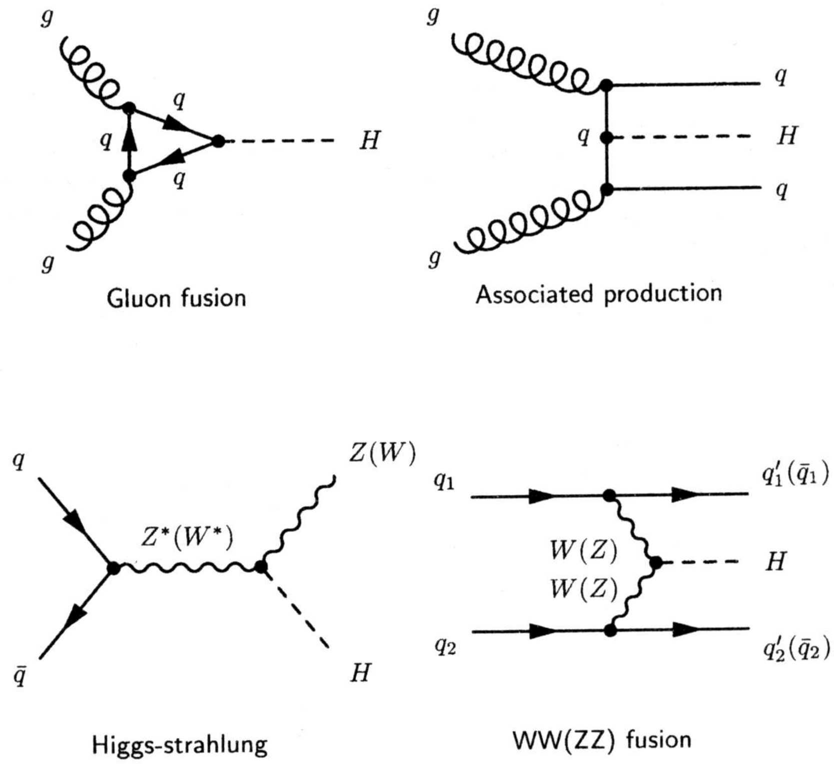

Figure 5 - Higgs production at the LHC

Figure 5 illustrates the production channels for the Standard Model Higgs boson. It will be detected at CMS by means of its decay products. The type of decay mode the Higgs boson will actually follow depends on its mass. Figure 6 gives a compilation of the decay channels for different Higgs masses m_H. The entire mass range from $m_H = 90\text{GeV/c}^2$ to the unitary limit of 1TeV/c^2 can be studied at LHC.

1.2 Design parameters of the Compact Muon Solenoid

The task of general purpose detectors like CMS is the registration of the reaction products of particle collisions. Trajectories, energies, charges and masses are measured. CMS consists of a multitude of different detector systems, which can be broken up into four major parts: The *tracker*, which is used to measure the trajectories of the reaction products by providing a high spatial resolution and yielding three dimensional space points, the *electromagnetic calorimeter* (ECAL), which measures the energy of all particles interacting electromagnetically, the *hadronic calorimeter* (HCAL), which measures the energy of strongly interacting particles, and finally the *muon system*, which plays a key role in detecting the Higgs boson by measuring its decay into four muons. All detector components, except the muon system, are located inside a superconducting coil providing a magnetic field of 4T, as can be seen in figure 7.

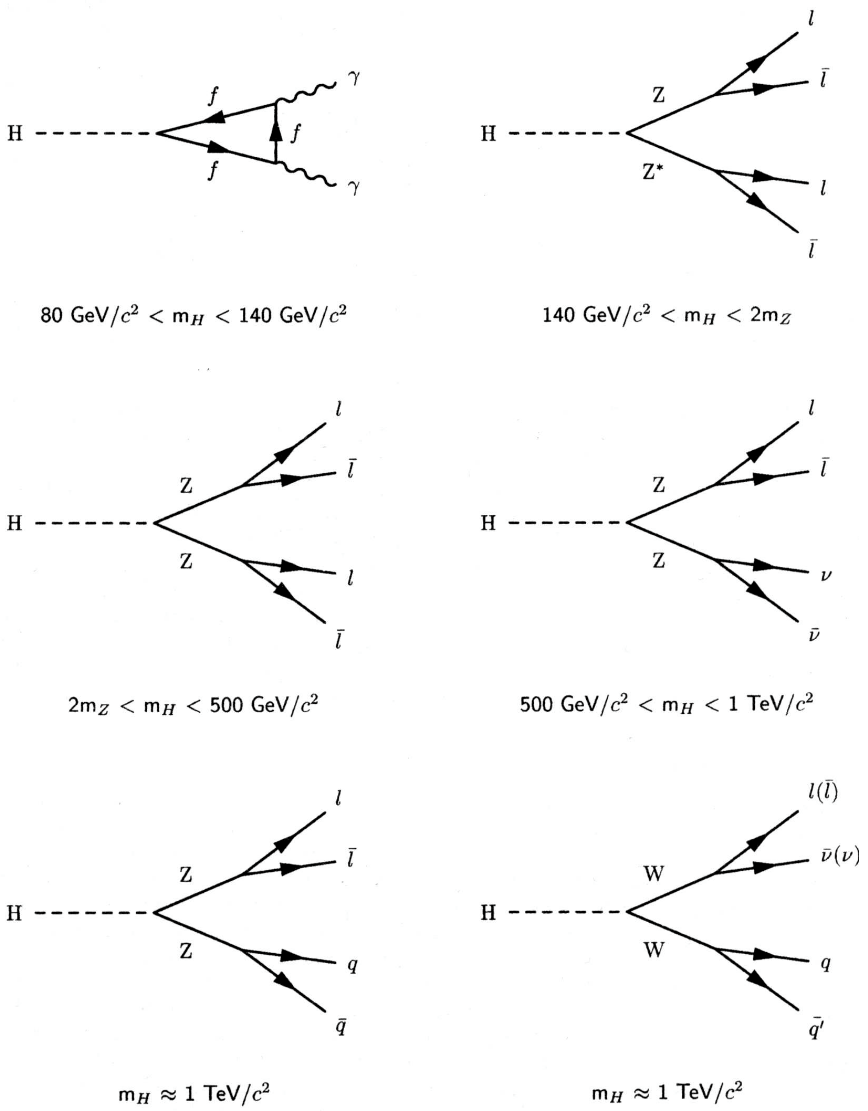

Figure 6 - Decay channels for the Standard Model Higgs boson in different mass ranges

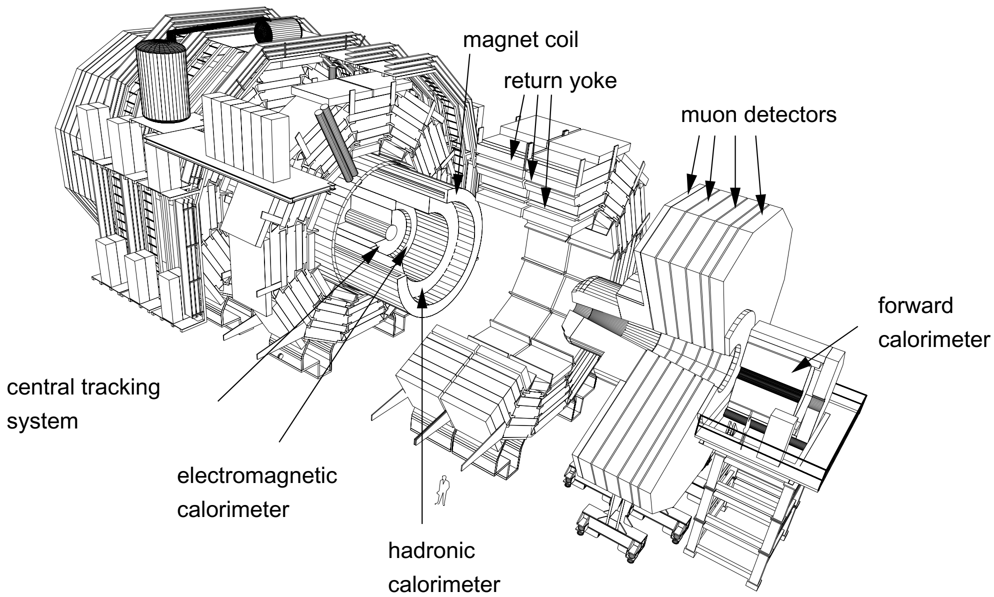

Figure 7 - Overview of the CMS detector

The magnetic field forces all charged particles on a curved track. The momentum can be calculated from its parameters. Since the particles have very large energies, a high magnetic field strength is required to be able to measure the curvature with a reasonable spatial resolution. The whole CMS detector will be about 21m long and 15m in diameter. It will have a total weight of 13000t.

1.2.1 Tracker

The tracker system of CMS was planned to consist of three different types of detector modules: Silicon pixel detectors closest to the interaction point, silicon strip detectors around that central part and Micro Strip Gas Chambers (MSGCs) in the outermost part of the detector **[6]**. Since the tracker is closest to the LHC beam pipe, it has to face the highest radiation levels and particle rates. All detector modules therefore have to be radiation hard and fast to cope with the LHC bunch crossing rate of 40MHz. Since the reaction products of the proton collisions are very close together in space, a high spatial resolution is required to be able to resolve the different trajectories. An additional requirement on the tracker is a large radiation length to leave the particles' properties as undisturbed as possible for the measurements in the calorimeter systems.

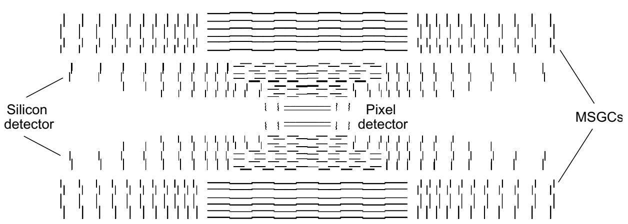

Figure 8 - Schematic cross section of the CMS tracker system. The different layers of detector modules can be seen.

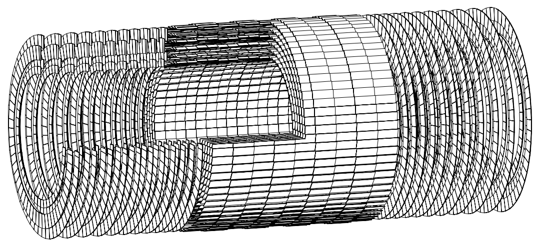

Figure 9 - The tracker part of CMS consisting of MSGCs. The forward and barrel part of the tracker can be seen.

Figure 8 illustrates the layout. The small silicon pixel detector system located directly around the interaction point can be seen. Those detectors provide two dimensional space information for each particle passing through a sensor plane. Like all other CMS detector subsystems, it is divided in a *barrel* and a *forward* [3] part: The barrel part is symmetric around the beam axis, as denoted with horizontal bars in figure 8. The forward detector modules are perpendicular to the beam axis, recognisable by vertical bars in the figure.
Several layers of silicon strip detector modules are located around the pixel detectors both in the barrel and forward region. These provide a lesser spatial resolution than the pixel detectors, but significantly reduce the number of required readout channels.
The outermost detection layers of the tracker were planned to be made of MSGCs. Figure 9 shows a drawing of the forward and barrel MSGC modules.
The main goal of the tracker is the reconstruction of high p_t muons and isolated electrons in the pseudorapidity range of $|\eta| < 2.5$, because this region is not covered by the forward muon system. Additionally, the tracker provides information on the trajectories to the ECAL and HCAL. It is used together with the muon system's track reconstruction for redundancy, too.

[3] Since pp-collisions are symmetric, no distinction between 'forward' and 'backward' is made.

1.2.2 Electromagnetic calorimeter

The ECAL is made of lead-tungsten ($PbWO_4$) crystals and designed to completely stop electrons and photons for a precise energy measurement **[7]**. As shown in figure 6, the most important decay channel for a Standard Model Higgs boson, or the lightest supersymmetric Higgs boson, is $H \to \gamma\gamma$. The detection therefore relies completely on the γ energy measurement. Since the width of the Higgs boson is small in this mass range, a high energy resolution is mandatory. An energy resolution of 0.7% for 120GeV electrons and photons is envisaged.
The reason for choosing $PbWO_4$ as material for the ECAL is its short scintillation decay time which matches the 25ns bunch crossing interval of LHC. Of additional interest is its short radiation length which allows building a compact calorimeter. The latter is important for putting the ECAL inside the coil.

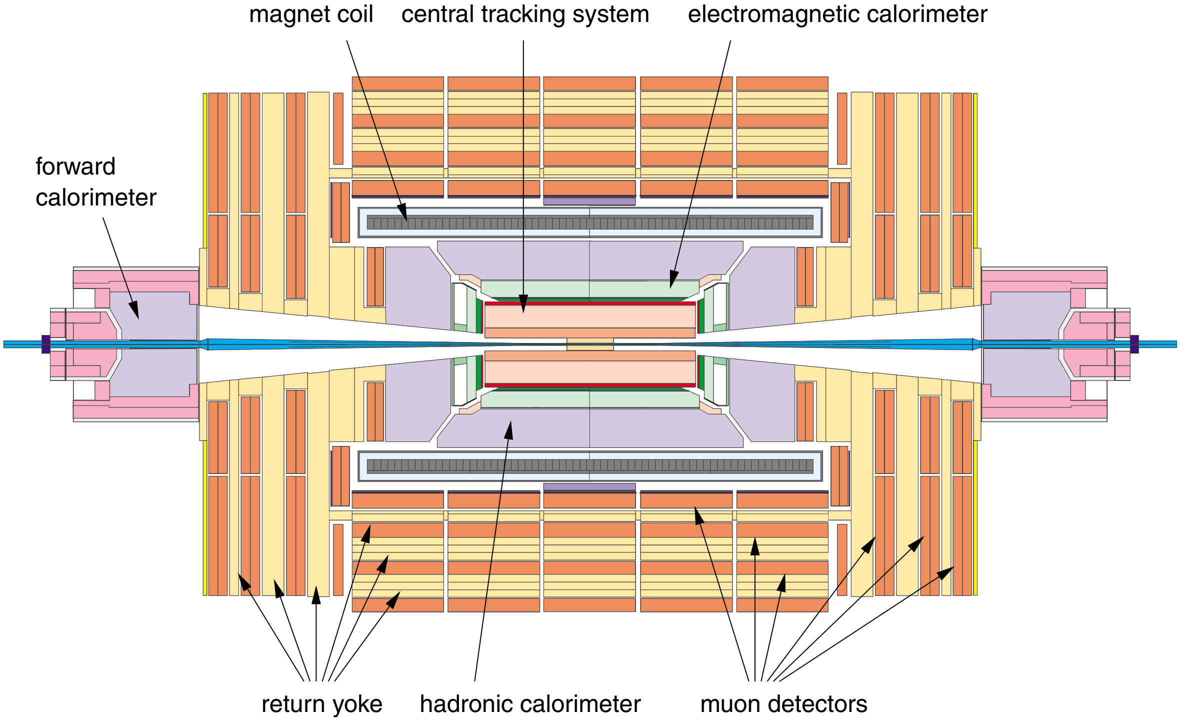

Figure 10 - Schematic layout of CMS

The ECAL is made up of a barrel and forward part like the tracker, as visible in figure 10. Contrary to the tracker's detector modules, the $PbWO_4$ crystals are 23cm long sticks which always point in the direction of the interaction point. Readout is done by avalanche photodiodes. The face side of the crystals is a quadratic area of $2 \cdot 2cm^2$, and spatial resolution is therefore limited. The tracker is used to provide information on the tracks for particles detected in the calorimeter.

1.2.3 Hadronic calorimeter

The setup of the HCAL is close to the ECAL's **[8]**. As can be seen in figure 10, it consists of additional forward calorimeters outside the muon system to measure jets produced along the beam axis. The calorimeter is finely segmented, which is necessary to be able to resolve nearby jets, and to measure their properties such as direction and energy.

It is made of alternating copper plates and layers of plastic scintillators, which are read out by wavelength shifting fibres. The expected hadronic energy resolution is about 70% $E^{-1/2}$.

1.2.4 Muon System

The muon system can be considered as a tracker for muons. Its task is to identify muons, reconstruct their trajectories, and measure their momentum **[9]**.
As muons are very important particles to detect the decay of the Higgs boson into four leptons, the muon system's signals will be included in the CMS trigger scheme. To select the desired events, the muon detectors have to be fast enough to allow the application of cuts on the particles' momentum at trigger level.
Three different technologies will be used to make up the muon system: Drift tubes, which are drift chambers filled with Ar/CO_2, cathode strip chambers, i.e. multiwire proportional chambers filled with $Ar/CO_2/CF_4$, and resistive plate chambers. Drift tubes will be used in the barrel region, while the forward sectors will be made of cathode strip chambers. Resistive plate chambers will be added to both parts of the muon system due to their excellent time resolution, which is required for the CMS trigger decisions.
It will be possible to use the muon system to trigger both on high and low p_t muons and to select the desired Higgs decay channel by this measure. An energy resolution of 8-15% for 10GeV muons and 20-40% for 1TeV muons is envisaged.

2 MICRO STRIP GAS CHAMBERS AND GAS ELECTRON MULTIPLIERS

Micro Strip Gas Chambers are miniaturised proportional counters, invented 1988 by *Anton Oed* to overcome some limitations of Multi Wire Proportional Counters **[10][11]**. Because of their small structures, they provide very good spatial resolution and a high rate capability[4] – demands imposed on tracking detectors by the next generation of high energy experiments. When operating in high particle fluxes, limitations of stability were encountered. One possible approach to overcome these instabilities is the addition of a Gas Electron Multiplier, invented by *Fabio Sauli* in 1997 **[12]**. After a brief discussion of the processes initiated by charged particles and photons in the gas, the Micro Strip Gas Detector and Gas Electron Multiplier will be introduced.

2.1 Gaseous Detectors

The working principle of the devices covered in this thesis, the Micro Strip Gas Chamber (MSGC) and the Gas Electron Multiplier (GEM), is the ionisation of a gas by charged particles and photons. By means of drift and diffusion processes, the charge is transported through the gas volume to the amplification region close to the electrodes, where the primary charge is amplified to provide an electronically measurable signal.

2.1.1 Ionisation processes

Both charged particles and photons interact mainly electromagnetically with the gas. Such interactions are orders of magnitude more probable than weak or strong interactions, especially in thin gas layers like those used in MSGCs and GEM-MSGCs. The processes leading to ionisation are different for charged particles and photons however: A charged particle mainly experiences Coulomb interactions between its electromagnetic field and that of the gas molecules, leading to both ionisation and excitation of the medium while traversing the detector volume. On the other hand, the electromagnetic interaction for the photon is a single localised event.

2.1.1.1 Charged particles

A charged particle in a gaseous medium can generate ion pairs along its track through the detector in two ways: Either by providing enough energy to liberate an electron of a gas atom, or by exciting one of the medium’s constituents, which then liberates an electron by

[4] Rate capability is the frequency with which two successive particles can be recognised by a detector.

deexciting when interacting with another atom[5]. The average differential energy loss per unit length due to Coulomb interactions is described by the *Bethe-Bloch* formula:

$$-\frac{dE}{dx}=\frac{4\pi z^2 e^4 N_A}{m_e c^2}\frac{Z}{A}\rho\frac{1}{\beta^2}\left\{\ln\left(\frac{2m_e c^2\beta^2\gamma^2}{I_0}\right)-\beta^2\right\} \tag{1}$$

A and Z denote the atomic mass and number of the medium, ρ is its density, ε_0 is the dielectric constant, m_e the mass of an electron, c the velocity of light, $\gamma = E/m$, $z \cdot e$ the charge of the ionising particle in units of the electron charge, and β is its velocity. I_0 is the effective ionisation potential of the medium, N_A Avogadro's constant, and x the thickness of the traversed medium. A good approximation for I_0 is $I_0 \approx Z^{0.9} \cdot 16\text{eV}$ **[13][14]**. The maximum kinetic energy which can be transferred to an electron from the incident particle is given by

$$E_{\max}=\frac{2m_e c^2\beta^2\gamma^2}{1+2\gamma\frac{m_e}{m}+\left(\frac{m_e}{m}\right)^2} \tag{2}$$

The mass of the incident particle is m. For 1GeV/c protons one calculates $E_{\max} = 1.2\text{MeV}$ while $E_{\max} = 100\text{MeV}$ is obtained for 1GeV/c muons. The dependence of the energy loss $-dE/dx$ on the energy of the incident particle is shown in figure 11.

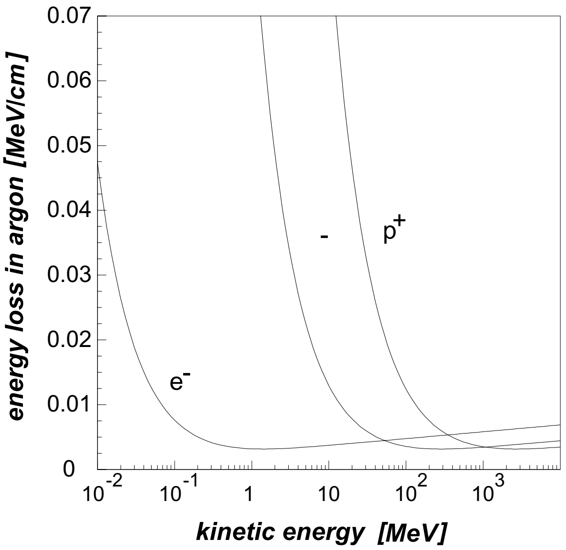

Figure 11 - Energy loss for electrons, muons and protons in argon.

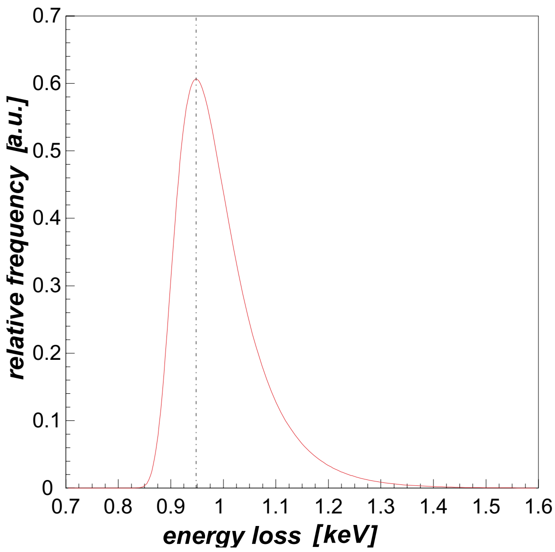

Figure 12 - Energy loss distribution of a muon in 3mm of argon.

The energy loss for charged particles is a function of β only, as can be seen in equation (1). After a decrease with $1/\beta^2$, the energy loss reaches an almost constant value around $\beta = 0.97$.[6] Above some 100MeV, all particles lose the same amount of energy per unit length[7]. This plateau is called the 'minimum ionising region' and particles having this kinetic energy are called 'minimum ionising particles' (MIPs). The curve continues with the 'logarithmic rise', dominated by the factor $\ln(\gamma^2)$. In addition, the dependence of $E_{\max}$ on γ^2 leads to more

[5] This requires that the excitation energy of the first atom is higher than the ionisation energy of the second.
[6] $\beta = 0.97$ corresponds to approximately three times the mass of the ionising particle.
[7] Around 2MeV g^{-1} cm^2 **[12]**.

ionisation processes in that region, increasing the energy loss per unit length. $\Delta E \approx dE/dx \cdot x$ is a good approximation for the total energy loss in a gas layer of thickness x for MIPs. For typical values of dE/dx see appendix A. In the special case of incident electrons, the Bethe-Bloch formula has to be modified to match Pauli's principle.

Equation (1) does not take into account statistical fluctuations arising from the ionisation processes. There are mainly two sorts of interactions: Distant ones, which usually result in the excitation of the interaction partner, and close ones, liberating an electron. Especially the latter processes result in the production of so-called δ- electrons with high kinetic energy, which lead to significant non-Gaussian deviations from the predictions of the Bethe-Bloch formula. Due to the small number of interactions in thin gas layers, this effect becomes even more important. The deviations can be calculated in the framework of the *Landau theory*. Here the energy loss distribution is written as

$$f(\lambda) = \frac{1}{\sqrt{2\pi}} \mathrm{e}^{-\frac{1}{2}\left(\lambda + \mathrm{e}^{-\lambda}\right)} \tag{3}$$

λ denotes the normalised deviation of the real energy loss ΔE_R from the most probable energy loss ΔE_{mp}:

$$\lambda = \frac{\Delta E_R - \Delta E_{mp}}{\xi}, \qquad \xi = \frac{2\pi N_A z^2 e^4}{m_e c^2} \frac{Z}{A} \rho \frac{1}{\beta^2} x$$

ξ is essentially the average energy loss given by the first term of the Bethe-Bloch formula. The energy loss of a minimum ionising muon in 3mm of argon can be seen in figure 12. The long tail for high energy losses is caused by events in which one or more δ- electrons have been produced. The energy resolution of such tracking devices is comparatively poor as a result. The strong demands on dynamic range of the electronics used to read out such detectors are a result of the large fluctuations in energy loss.

Two types of ion pairs have to be distinguished when calculating the average number produced by a charged particle in a gaseous detector. The number of primary ionisations n_p, generated by the incident, and secondary ionisations, caused by primaries having enough energy to ionise or excite constituents of the gas themselves, e.g. δ- electrons. The total number of ion pairs n_T can be expressed as

$$n_T = \frac{\Delta E_R}{W} \tag{4}$$

with W denoting the average energy necessary to produce an ion pair in a given gas. Some numbers are given in appendix A. While the total ionisation in a thin gas layer can be computed using equation (4), no expression exists to calculate the number of primary ionisations. As the production of ion pairs by the incident particle is a statistical process, and assuming a small number of independent interactions in a thin gaseous detector, the probability $P(k,n_p)$ to generate k ion pairs by n_p ionisations is given by the *Poisson distribution*:

$$P(k, n_p) = \frac{n_p^k}{k!} \mathrm{e}^{-n_p}$$

Distributions for different numbers of n_p can be found in **[15].** Assuming a perfect detector which is capable of detecting every ion pair produced, it is possible to calculate a theoretical limit for the inefficiency[8] $1 - \varepsilon$:

$$1-\varepsilon = P(0,n_p) = \mathrm{e}^{-n_p} \tag{5}$$

It is given by the requirement that at least one ionisation process has occurred. For a 3mm thick layer of argon, one computes[9] $1\text{-}\varepsilon = 4.5 \cdot 10^{-3}$ % and $1\text{-}\varepsilon = 1.7 \cdot 10^{-13}$ % for a 1cm thick layer. It is possible by use of adequate detectors to determine n_p experimentally by means of inefficiency measurements **[12]**. Some numbers obtained that way can be found in appendix A. An approximation is $n_p \approx 1.45 \cdot Z\,\mathrm{cm}^{-1}$ and $n_T \approx 4.45 \cdot Z\,\mathrm{cm}^{-1}$ **[16]**. A simple composition law can be used for gas mixtures:

$$n_T = \sum_{i=1}^{n} \frac{\Delta E_i}{W_i} p_i\,, \qquad n_p = \sum_{i=1}^{n} n_p^i p_i \tag{6)(7}$$

ΔE_i, W_i and n_p^i denote the energy loss, average energy necessary to produce an ion pair, and number of primary ion pairs released in the i-th component of the gas mixture. p_i is the fraction of the i-th gas in the mixture **[13]**. The number n_S of secondary ion pairs is finally $n_S = n_T - n_p$.

2.1.1.2 Photons

Unlike charged particles, the interaction of a photon with a gaseous medium by photoeffect is a single localised event. The photon is absorbed and its full energy is available for the electromagnetic interaction with the gas. This leads to a Gaussian distribution of the energy loss as shown in figure 13. The effects responsible for the Landau shape of figure 12 are not present. The probability of absorption in the gas is dependent on the cross section σ. The attenuation of a beam of photons traversing the thickness x with mass attenuation coefficient μ is given by

$$I = I_0\,\mathrm{e}^{-\mu x}\,, \quad \mu = \sigma N$$

I_0 denotes the initial intensity of the photon beam and I the intensity after traversing the distance x in the material. N is the molecular density of the material. The interaction can follow different mechanisms, each with its unique cross section, dependent on the energy of the incident photon. At energies up to ≈ 100keV the dominant process is the photoeffect, as can be seen from figure 15. Compton scattering takes over for higher energies until the production threshold for electron pair production at $2 \cdot m_e c^2 \approx 1$MeV is reached. This is the dominant process for energies beyond 10MeV. Since all photon measurements in this thesis have been carried out with a ^{55}Fe source[10], the only relevant process is the photoeffect[11].

[8] The efficiency is the probability that a particle traversing the detector is detected.

[9] In reality, the inefficiency is dominated by imperfections of the detector and therefore much higher.

[10] The dominant process for ^{55}Fe is K-capture with a branching ratio of 24%, emitting 5.89keV photons.

[11] This is also true for the other gases used, namely neon, carbon dioxide, propane and DME. For cross sections see **[18]**.

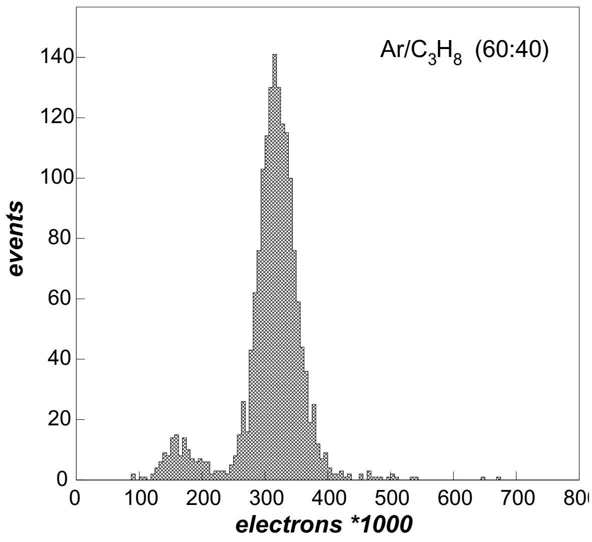

Figure 13 - Energy loss distribution of a photon in 3mm of argon/propane with a ^{55}Fe source. Signals for the ^{55}Fe and argon escape peak are shown.

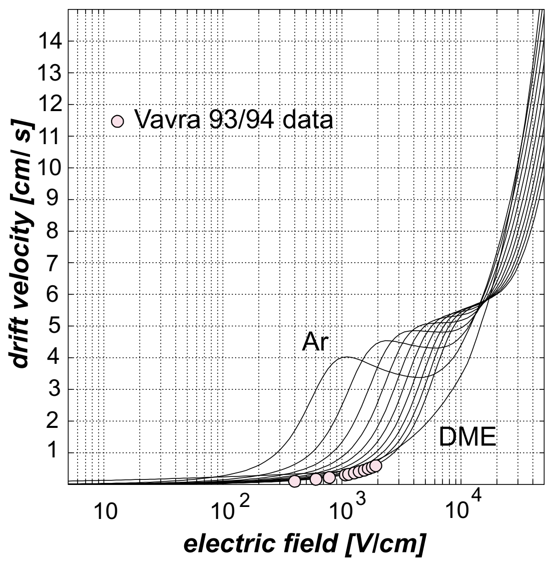

Figure 14 - Drift velocity as a function of the electric field in Ar/DME. Mixtures range from pure argon (upper curve) to pure DME (lower curve) Source: **[17]**.

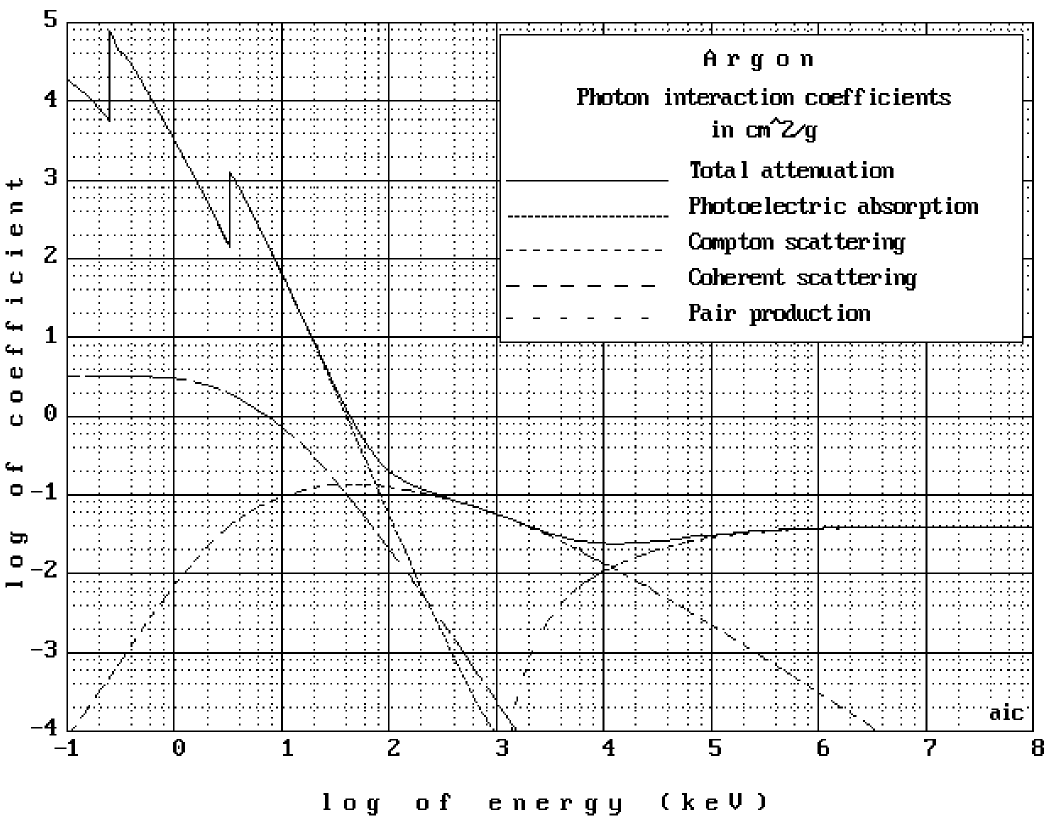

Figure 15 - Cross sections for the different interaction processes in argon. The figure has been taken from **[18]**, which is a compilation of **[19] - [21]**.

The photoeffect is a quantum process involving one or more transitions in the shell of an atom or molecule. Absorption can only take place if $E_\gamma \geq E_j$, with E_γ denoting the energy of the incident photon and E_j the energy of the j-th shell. The contributions for all $E_j < E_\gamma$ add up for a given energy E_γ. The absorption is at maximum for $E_\gamma = E_j$. It then decreases rapidly until the energy of the ($j + 1$)-th shell is reached. This can be seen in figure 15. For a gas mixture or complex molecules a simple composition rule analogous to equations (6) and (7) can be used:

$$\mu_T = \sum_{i=1}^{n} \mu_i p_i \qquad (8)$$

μ_T is the combined mass attenuation coefficient for n sorts of atoms, which each contribute a fraction p_i and a coefficient μ_i to the gas mixture or molecule **[13]**.
The excited atom or molecule can use two different mechanisms to reach its ground state again: Either by the transition of an electron from a shell with $E_i > E_j$, emitting a fluorescence photon with $E_\gamma = | E_j - E_i |$, or by a radiationless transition, or *Auger effect*, which involves an internal rearrangement of electrons from several shells. The latter results in the emission of a second electron with an energy $E_\gamma \cong E_j$. This effect is dominant for 5,89keV photons in argon with a branching ratio of 85%. In 15% of the events a fluorescence photon is emitted **[13]**. Since this photon has an energy just below E_j, it has a large mean free path, and a high probability of escaping the detection volume without further interaction. This yields the characteristic 'escape peak' in argon based gas mixtures. It can be seen in figure 13. The number of ion pairs n generated by a single photon of energy E_γ in a medium with average ionisation energy W is given by

$$n = \frac{E_\gamma}{W}$$

Using the composition rule for gas mixtures given by equation (6) and the numbers for W_i given in appendix A, one obtains the following numbers for ^{55}Fe and the gas mixtures used in this thesis: Ar/CO_2 (80:20) $n = 189$; Ar/Propane (60:40) $n = 239$ and Ne/DME (40:60) $n = 213$.

2.1.2 Drift and diffusion

The charge produced by ionisation events in the gas – regardless whether produced by an incident charged particle or photon – quickly lose their kinetic energy in multiple collisions. They acquire the average thermal distribution of the gas, described by the Maxwellian probability distribution:

$$F(E) = C\sqrt{E}\, \mathrm{e}^{-\frac{E}{kT}} \qquad (9)$$

E is the energy with an expectation value of $\langle E \rangle = 3/2 \cdot kT$, C a proportionality constant, k the *Boltzmann factor*, and T the temperature. The distribution in space is described by a Gaussian distribution with a time dependent width x:

$$\frac{dN}{N} = \frac{1}{\sqrt{4\pi Dt}} e^{-\frac{x^2}{4Dt}} dx \qquad (10)$$

dN/N denotes the fraction of charge in dx at the time t. D is a diffusion constant which is dependent on the gas. The standard deviation of equation (10) yields the linear diffusion width

σ_x of the charge distribution in the gas volume at the time t; under the assumption of an isotropic medium, the volume diffusion is σ_{vol}:

$$\sigma_x = \sqrt{2Dt}, \quad \sigma_{vol} = \sqrt{3}\sqrt{2Dt} = \sqrt{6Dt} \tag{11}$$

The diffusion process is superimposed by the drift of the ion pairs due to the electrostatic force in the presence of an electric field **E**. Electrons drift towards the positively charged anodes, while ions move to the negatively charged cathodes. The velocity of the electrons is different from the ions due to their small mass. The drift velocity **u** can be obtained by solving the differential equation for a frictional force **[14]**:

$$m\frac{d\mathbf{u}}{dt} = e\mathbf{E} - K\mathbf{u} \tag{12}$$

The solution of equation (12) is a constant for $t \gg \tau$. The ratio $\tau = m/K$ defines the time between two collisions. It is now possible to introduce the mobility μ as the proportionality between the drift velocity **u** and the field **E**:

$$\mathbf{u} = \frac{e}{m}\tau\,\mathbf{E} = \mu\,\mathbf{E}, \quad \mu = \frac{e}{m}\tau \tag{13}$$

The mobilities for ions and electrons are not the same because of the big difference in mass. While electrons experience constant acceleration and deceleration, ions reach a constant drift velocity only dependent on the electric field **E** and the gas.

2.1.2.1 Electrons

Electrons can significantly increase their energy between two collisions under the influence of an electric field. According to *Townsend*, their average drift velocity v^- is given by

$$v^- = \frac{e}{m_e}|\mathbf{E}|\tau$$

The mean time τ between two consecutive collisions, and therefore the drift velocity, is strongly dependent on the electric field **E**. A good example is the *Ramsauer* effect, where the velocity passes through maxima and minima every time the electron's wavelength approaches those of an shell of an atom or a gas constituent. To determine the drift velocity for different gases, and their dependence on the electric field, extensive measurements were carried out. A good compilation can be found in **[22]**. One example is given in figure 14. Simulated data for the gases used in this thesis can be found in appendix B.

Drifting electrons can get lost for the amplification process when recombining with ions. Electron capture in the gas or in the detector material is another source for charge losses. Mainly noble gases are used as gas filling for that reason. Especially gases with a high electron affinity, e.g. oxygen and water or steam, are usually avoided[12]. Even a small pollution by such elements adversely affects the detector performance.

[12] There are special circumstances when a controlled amount of water is added to a gas mixture to increase the stability of operation.

2.1.2.2 Ions

The ions experience a net movement under the influence of the electric field **E**, too. The velocity of this movement is dependent on the mobility defined in equation (13). It is unique for a given sort of ion in a gas mixture. The mobility remains constant up to very high fields., Ions can not increase their velocity significantly between consecutive collisions due to their large mass. An equilibrium between acceleration by the electrostatic field and deceleration by collisions is reached at some point. The relation between the diffusion coefficient for ions D^+ and their mobility μ^+ is given by the *Einstein formula* **[13][15]**:

$$\frac{D^+}{\mu^+} = \frac{kT}{e}$$

Some values for mobilities can be found in appendix A. For a mixture of gases, a composition rule analogous to equations (6) – (8) exists:

$$\frac{1}{\mu_i^+} = \sum_{j=1}^{n} \frac{p_j}{\mu_{ij}^+}$$

μ_{ij}^+ denotes the mobility of the i-th type of ion in gas j with the fraction p_j in the total gas mixture.

2.1.3 Gas amplification

The generation of ion pairs and their migration towards the electrodes by means of an electric field has been described. The drift of the charges induces a current on the electrodes. It could be read out with a high gain electronic amplifier. Practically, this is limited by the impossibility to distinguish between a particle signal and electronic noise[13] in such a device., An amplification is generated in the gas volume for that reason: One makes use of the high mobility of the electrons. Electrons gain enough energy between consecutive collisions to ionise the gas. Since this effect is repeated for all electrons produced in the gas volume, their number increases exponentially, forming a so-called avalanche. The fast electrons of the avalanche reach the anodes within 1ns, while the much slower ions still move towards the cathodes. To estimate the number of electrons produced in that process, it is assumed that the first secondary ionisations[14] take place at a distance $x_{\min}$ from the electrode, where the acceleration of the electric field has just provided enough energy to overcome the ionisation potential of the gas. The number of generations z in an avalanche is then given by

$$z = \frac{V_A - V(x_{\min})}{\Delta V}$$

$V(x_{\min})$ denotes the potential at the location where enough energy for ionisation is reached for the first time. ΔV is the average ionisation potential and V_A is the potential of the anode. Gaseous detectors often make use of a low homogeneous drift field as described in the

[13] Electronic noise in semiconductor devices is caused by the thermal movement of the electrons in the amplifying circuit. The higher the gain and therefore the power drain of the device, the higher is the electronic noise.
[14] "Secondary ionisation" is meant to distinguish this process from the generation of ion pairs by the incident particle, which is called "primary ionisation".

previous section to make the amplification of a detector independent of the localisation of the first ionisation. A high amplification field, confined as much as possible to the electrodes connected to the readout of the detector, is then used to generate the required gain. If n_0 electrons were present at the beginning of the amplification process, one obtains N electrons in the end:

$$N = n_0 2^Z = n_0 \ln 2\, e^{\frac{V(x)-V(x_{\min})}{\Delta V}} \tag{14}$$

The ratio $G = N/n_0$ is the gain of the amplification process. The dependence of the gain of a gaseous detector on the potentials applied is therefore exponential. A limiting factor to the achievable gain of a detector is the generation of photons in the UV range of the spectrum. These photons are able to initiate new avalanches in a wide area around the original track of the incident particle. The total charge in the detector, or the signal amplitude, is then no longer proportional to the energy of the incident particle. This effect is used intentionally for Geiger-Müller counters. Gases which absorb UV photons are added to the counting gas to avoid this effect for proportional counters. These are usually organic molecules – like light hydrocarbons (CH_4, C_3H_8), DME (C_2H_6O, dimethyl ether) or carbon dioxide – which provide many degrees of freedom and absorb UV photons in their rotation and oscillation bands.

2.1.4 Signal generation

The motion of the ion pairs leads to an induced current on the electrodes. A general description of that current is provided by *Ramo's theorem* **[23]**: Assume i electrodes connected to a power supply in such a way that the motion of charges between them does not modify their potentials. Ramo's theorem is then simplified to

$$\sum_i Q_i V_i^{'} = \sum_i Q_i^{'} V_i \tag{15}$$

Q_i and V_i are the start, and $Q_i^{'}$ and $V_i^{'}$ the end values for the charges and potentials sketched in figure 16. With only two electrodes, Q_i representing an electrode of the detector and q_t representing a charge as the other electrode, equation (15) is reduced to

$$Q_1 V_1^{'} + q_t V_t^{'} = Q_1^{'} V_1 + q_t^{'} V_t$$

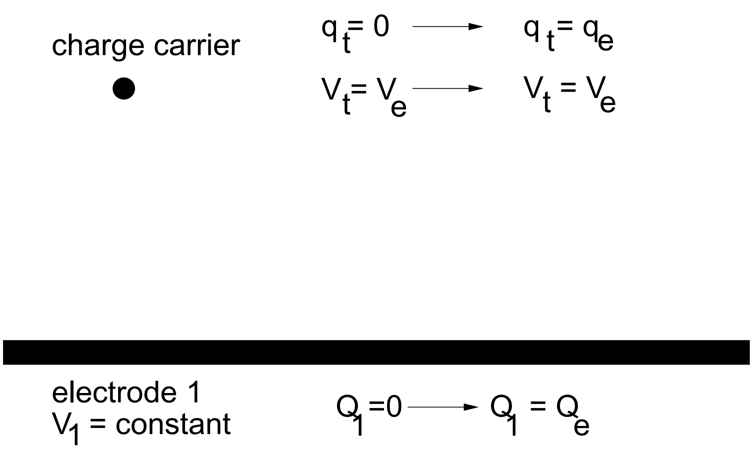

Figure 16 - Explanation of the start and end values for charges and potentials

Replacing the start and end values as described in figure 16, this yields

$$q_e V_e = -Q_e V_1$$

The current induced on electrode 1 by the motion of q_t along an infinitesimal track segment $d\mathbf{l} = \mathbf{v} \cdot dt$ is then given by

$$I_1 = \frac{dQ_e}{dt} = -q_e \frac{d}{d\mathbf{l}}\left(\frac{V_e}{V_1}\right)\frac{d\mathbf{l}}{dt} \Rightarrow I_1 = q_e \mathbf{v}\mathbf{E}_w \qquad (16)$$

The weighting field $\mathbf{E}_w = -\nabla (V_e/V_1)$ has been introduced in equation (16). $\mathbf{E}_w$ can be obtained by solving the Poisson equation for the given electrode geometry. Since the current induced on the electrodes depends on the velocity **v** of the charge, electrons contribute to the detector's signal only during the first nanosecond. The signal is generated by the drift of the ions only afterwards. Calculations show that only $\approx 10\%$ of the signal of an MSGC is generated by the electrons **[25]**. A confinement of the high amplification field close to the electrodes helps to shorten the length of the signals, and therefore increase the rate capability. This is an additional reason for dividing a gaseous detector into a drift region with a low field and an amplification region with a high field.

2.2 Micro Strip Gas Chambers

Micro Strip Gas Chambers (MSGCs) are the successors of the Multi Wire Proportional Chambers (MWPCs), invented 1968 by *Georges Charpak* **[27]**. Since they are produced using common photolithographic technology, better reproducibility and easier mass production is possible. Due to their small size, they offer better spatial resolution and higher rate capabilities than MWPCs.

2.2.1 Components

Figure 17 shows a schematic view of an MSGC. The most important part is the so-called 'substrate'. It carries the electrodes, which are produced in a photolithographic process. A sketch of the production process can be found in appendix C. The most widely used material for the substrate is glass, although different choices do exist[15]. The glass plates typically have a thickness of 300µm. in the detector. The use of a high, but nevertheless controlled surface resistance is mandatory due to the demands on the substrate imposed by the electrostatic fields. Typical glasses are D263[16] and S8900[17].
The electrodes are made of metal. The most common material is gold, since it offers superior conductivity while not being susceptible to oxidation. Other metals often used for the electrodes are aluminium and chromium, which are either limited in conductivity (chromium) or susceptibility to oxidation (aluminium). Both anodes and cathodes are called 'strips' due to the parallel pattern they usually form on a substrate, as can be seen in figure 18.

[15] The most important materials besides glass are silicon and polyimide.
[16] Desag, Deutsche Spezialglas AG, Germany
[17] Schott Glaswerke GmbH, Germany

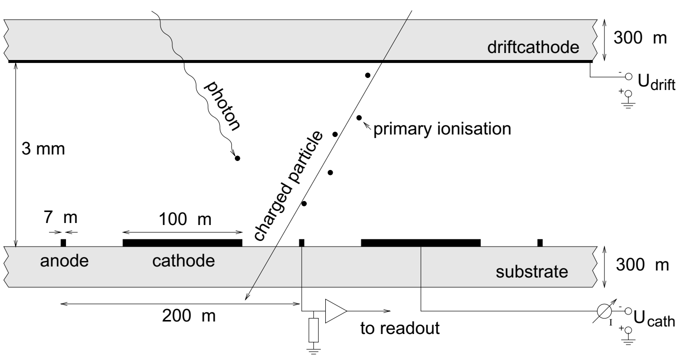

Figure 17 - Schematic cross section of an MSGC (not to scale). The substrate with the electrodes is glued to the drift cathode by means of a distance frame (not shown). Typical voltages are U_{cath} = -530V and U_{drift} = -2500V, yielding a drift field of ≈ 8kV/cm for a 3mm high distance frame.

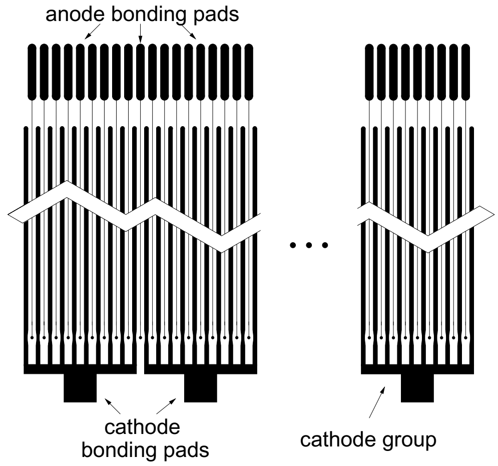

Figure 18 - Pattern of an MSGC substrate with parallel strips.

A frame is glued on top of the substrate. It defines the gas volume of the detector and is completed with the drift cathode on top. This electrode is a metallised plane which defines the drift field. There are several possible approaches to realise a drift plane. One of the most common is using the same glass as for the substrate with a metallisation on the whole surface. This has the advantage that such drift planes can be produced within the regular etching process without any additional production steps. Another convenient method is the use of metallised foils, which are readily available[18]. Another design for drift cathodes is the use of glass fibre enforced materials[19], which are metallised on one side. This type of drift cathode is most useful when large area detectors, such as the modules for the CMS experiment, are being built. For such detectors, glass drift cathodes are not obtainable because the machinery used to create the metallisation is limited in size[20]. The use of foils is not possible, because the deformation caused by the gas pressure inside the detector volume would result in a distortion of the drift field, creating an amplification dependent of the localisation of the ionisation in the detector (see section 2.1.3). The advantage of both glass fibres and foils is the robustness against pressure changes in the detector volume. Both are more flexible than glass and therefore do not only reduce the risk of breaking, but also relieve the substrate from stress caused by pressure variations. The drift cathode and the cathode strips on the substrate are powered by negative high voltage (HV).

From now on, all voltages will be given as absolute values, since only negative voltages are applied to the detectors. A voltage of U_{cath} = 500V is therefore to be read as U_{cath} = -500V.

A certain amount of cathode strips, usually between 10 and 16, are grouped together to form a so-called ‘HV group’. The HV groups are bonded[21] to a connection interface. The anodes are bonded to amplifiers and are grounded that way.

[18] Aluminised Mylar® foil and copper clad Kapton® foil by DuPont, Delaware, USA, are commercially available.
[19] One example is Ferrozell® by Ferrozell GmbH, Augsburg, Germany.
[20] Machinery used for this type of production process usually originates from the semiconductor industry and is therefore limited to standard sizes of 6” and 8”, set by the wafer diameter.
[21] A technique developed to connect the silicon core of microchips to its external connections. It makes use of ultrasonic welding.

2.2.2 Detector perfo rmance

The most important performance issue for every detector used for tracking purposes is its efficiency. The capability to detect a particle passing through the gas volume is crucial for reconstructing its trajectory in a detector like CMS. Since the efficiency only depends on the signal amplitude, the most important parameter is the gain of the detector.

Electric field

As already emphasised in section 2.1.2, the crucial parameter for understanding the operation of a gaseous detector is its electric field configuration. A computation of the potentials inside an MSGC has been carried out: The glass of the substrate has been considered to be a perfect insulator to simplify the calculation. The strips have been treated as metal layers with zero thickness; the metal is regarded as a perfect conductor for simplicity. The applied potentials are $U_{\mathrm{drift}} = 3000\mathrm{V}$ for the drift plane, $U_{\mathrm{cath}} = 530\mathrm{V}$ for the cathode strips and $U_{\mathrm{anode}} = 0\mathrm{V}$ for the grounded anodes. The geometry put in the computation is $g = 3\mathrm{mm}$ for the distance from substrate to drift plane, and $a = 7\mu\mathrm{m}/c = 100\mu\mathrm{m}$ for the width of the anode and cathode strips respectively. The 'pitch', which describes the distance from the middle of one anode strip to the next, is set to $p = 200\mu\mathrm{m}$.
If one makes use of the periodicity of an MSGC substrate, Maxwell's equation can be solved for an 'elementary cell' of the substrate, consisting of one half of an anode and cathode. An analytical solution for that problem is a Fourier series **[25]**:

$$V(x,y) = c_0 + \frac{U_{drift} - c_0}{g} y + \sum_{n=1}^{N} c_n \, \mathrm{e}^{\frac{-n\pi y}{p/2}} \cos\left(\frac{n\pi x}{p/2}\right) \tag{17}$$

The Fourier coefficients are:

$$c_0 = \frac{1}{p/2} \int_0^{p/2} f(x)\,dx, \qquad c_n = \frac{2}{p/2} \int_0^{p/2} f(x) \cos\left(\frac{n\pi x}{p/2}\right) dx$$

The use of only the cosine terms of the series is imposed by parity and periodicity constraints. $f(x)$ is a piecewise defined function, which describes the boundary conditions for solving the problem. For the situation depicted in figure 19b, one obtains

$$f(x) = \begin{cases} U_{anode} & x < \frac{a}{2} \\ 0 & \frac{a}{2} < x < \left(\frac{p}{2} - \frac{c}{2}\right) \\ U_{cath} & x > \left(\frac{p}{2} - \frac{c}{2}\right) \end{cases} \tag{18}$$

Equation (17) has been computed for the $f(x)$ defined in formula (18) for a detector region consisting of a half anode and cathode. The density of points in the (x,y) plane has been adapted to find a compromise between smooth curves and computation time. The order of the

Fourier series has been set to $N = 10$. The result is shown for 300µm of drift space in figure 19b and has been obtained by using Maple[22]. The lines connect points of the same potential.

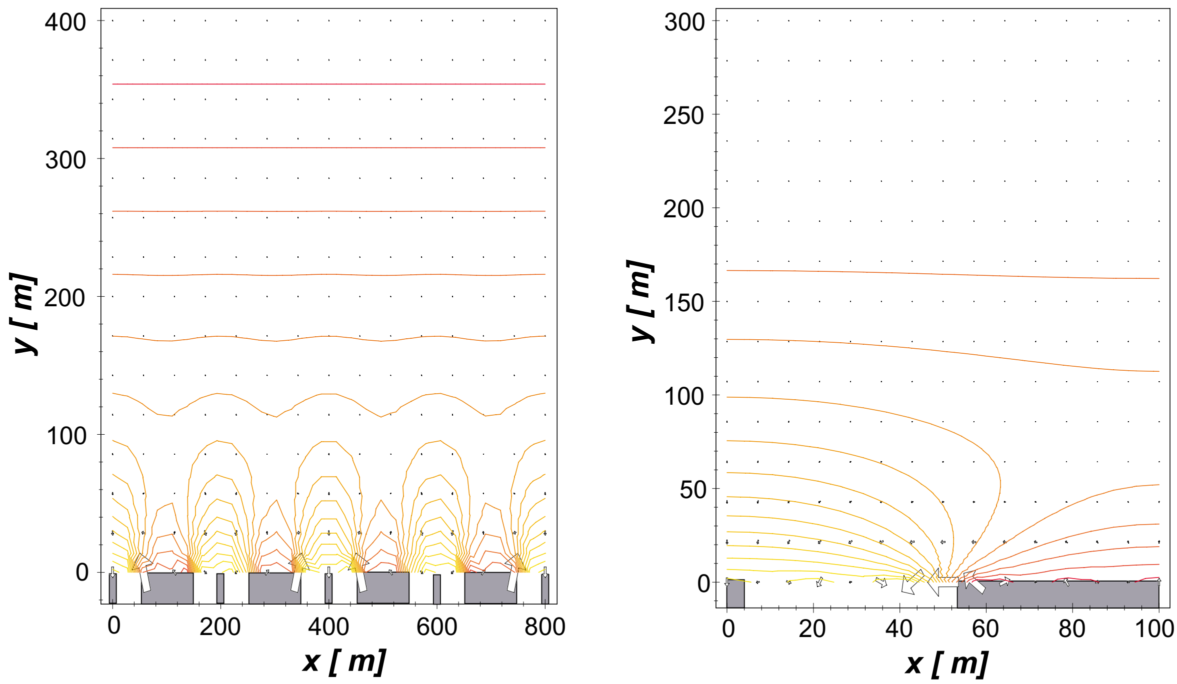

Figures 19a) and **b)** – The field in an MSGC consists of the inhomogeneous amplification field close to the strips (b), superimposed by the homogenous drift field (a). The plots show the potential lines; the arrows denote strength and direction of the electric field. It can be seen that the inhomogeneous part of the field extends up to ≈ 150µm in the drift space of the detector only.

For each point where the potential has been computed, the field vector can be calculated[23] by $\mathbf{E} = -\nabla V(x,y)$. The small arrows in figure 19 depict the electric field. The bars at the bottom of the figures symbolise the strips. It can be immediately recognised, that the field strength is at its maximum at the edges of the strips. The separation of the homogeneous drift field and inhomogeneous amplification field mentioned in section 2.1.2 can be seen in figure 19a. A larger segment of the MSGC has been simulated here. Since the simulated drift region has been enlarged in that plot, one can see that the amplification field distorts the drift field up to 150µm above the substrate – this is 0.5% of the drift region only. The field strength between neighbouring anode and cathode strips can be seen more easily in figure 20.[24] The corresponding potential can be seen in figure 21. The plots have been created using MSFIELD **[28].**

[22] Maple is a system for computational algebra developed by the University of Waterloo, CA, USA. Version V Release 4 has been used. The product is distributed by Waterloo Inc., USA

[23] Obviously, the field vector is not shown for every point calculated. For a better reading, only every 20^{th} value has been used.

[24] The keen reader will have noticed that this plot has been computed using a slightly different cathode width and pitch (80µm/160µm).

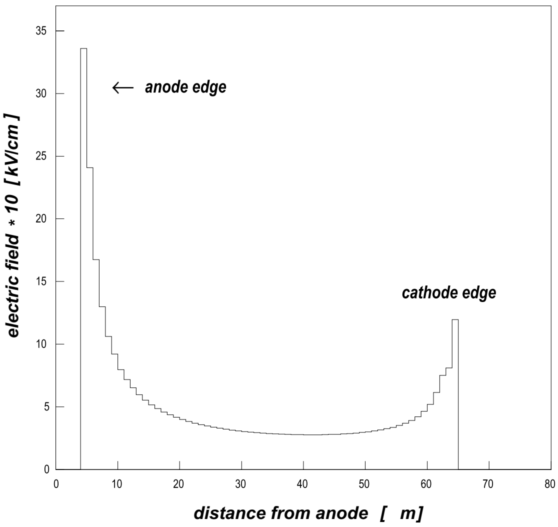

Figure 20 - Electric field between anode and cathode. The substrate is assumed to be a perfect insulator.

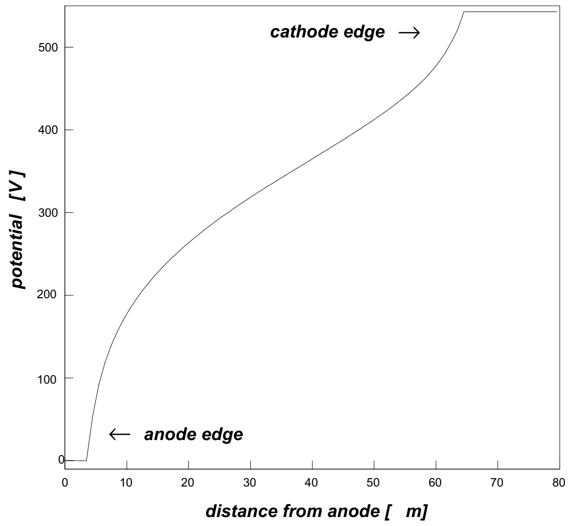

Figure 21 - Potential between anode and cathode strip.

Some arrows pointing towards the substrate between the strips can be seen in figure 19a + b. In reality this means that some drift lines will end on the substrate's surface. Particles following these trajectories will deposit their charge there. The substrate will start charging up, since the mobility is zero in case of a perfect insulator. This results in the building up of an electric field on the substrate with opposite sign to the amplification field. An equilibrium is reached at some point, and the deposition of charge is stopped. The amplification of the detector is reduced due to the field created by the charges on the substrate. This effect has been measured **[29] - [31]**. A coating of the substrate with a material providing a small conductivity has been introduced to cope with that effect. This allows the deposited charges on the substrate to migrate to the electrodes. It is even possible to make the bulk glass itself conductive **[32]**.

$$f(x) = \begin{cases} U_{anode} & x < \frac{a}{2} \\ \left(U_{cath} - U_{anode}\right)\dfrac{x - \frac{a}{2}}{\frac{1}{2}\left(p - c - a\right)} & \frac{a}{2} < x < \left(\frac{p}{2} - \frac{c}{2}\right) \\ U_{cath} & x > \left(\frac{p}{2} - \frac{c}{2}\right) \end{cases} \qquad (19)$$

Figure 22 shows the result of the computation of the potential for a coated substrate. It is notable that no field lines end up on the substrate anymore. The boundary conditions in equation (18) have to be changed as given in equation (19). This definition assumes a linear dependence of the surface resistivity along the conductive substrate between the strips. The charging up of the substrate can be avoided up to very high irradiation rates when using a conductive layer with a surface resistance in the order of $10^{-14} – 10^{-15}\Omega/\square$. This can be seen in figures 23 a+b.

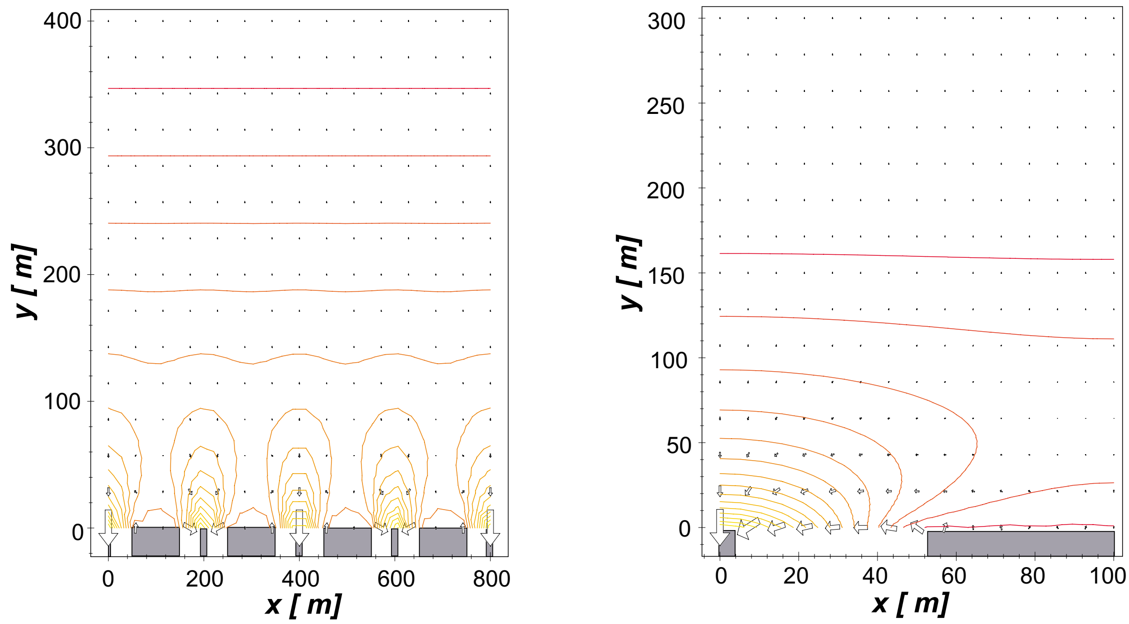

Figures 22a) and **b)** –The plots show the potential lines and the electric field for a coated substrate. No field lines end on the substrate surface anymore

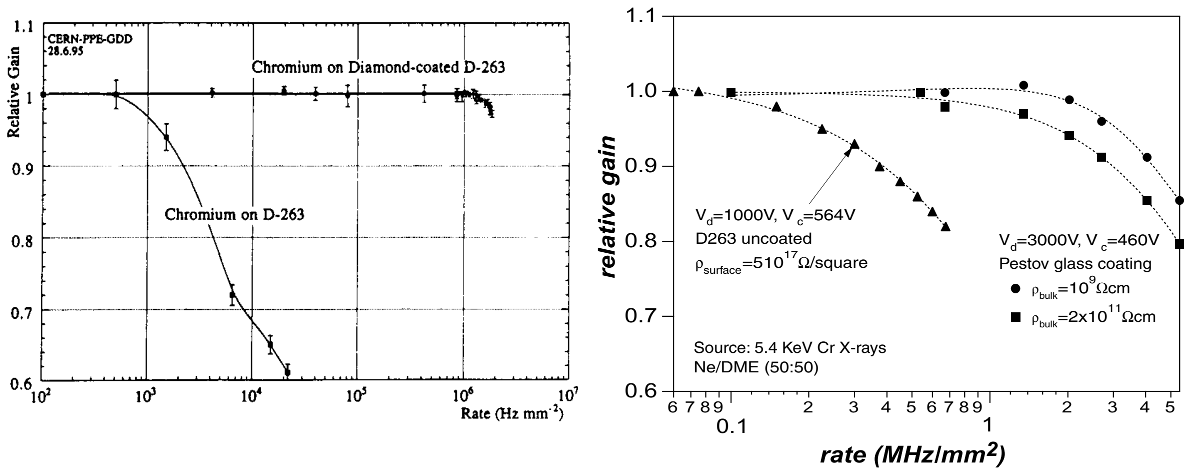

Figure 23a) and **b)** - Stability of detector gain with respect to the irradiation rate for different coatings. Figure a) taken from **[33]** and b) from **[6]**.

Amplification

The resulting amplification of the field configuration for an uncoated substrate can be seen in figure 24. The substrate had the same electrode dimensions as those used for the simulations in figures 19 and 22. Measurements in Ar/CO_2 (80:20), Ar/Propane (60:40) and Ne/DME (40:60) are shown. No effects from charging up of the substrate were present since the rate was well below 100Hz/mm^2 for all measurements,.
The dependence of the gain on the voltage of the electrodes U_{cath} is exponential as expected from equation (14). The different total gains for the gas mixtures are a result of the varying number n of ion pairs produced in the gases by the incident ^{55}Fe photon, as calculated at the end of section 2.1.1.2.

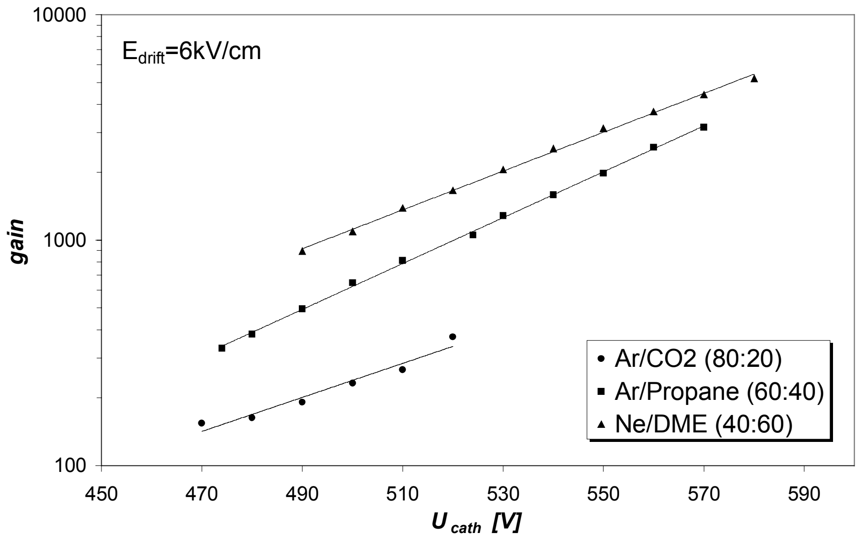

Figure 24 - Gain measurements with GEM4 and a ^{55}Fe γ- source. The detector and the corresponding analysis will be described in sections 3.2 and 4.1.3 respectively. The detector has been operated as an MSGC for these measurements, using the lower side of the GEM as drift cathode. The drift field of E_{drift} = 6kV/cm corresponds to a voltage of U_{drift} = 1080V for a 1.8mm drift space.

Efficiency

The most important parameter for operation as a tracking detector is the efficiency, which is dependent on the signal amplitude and therefore on the detector gain.

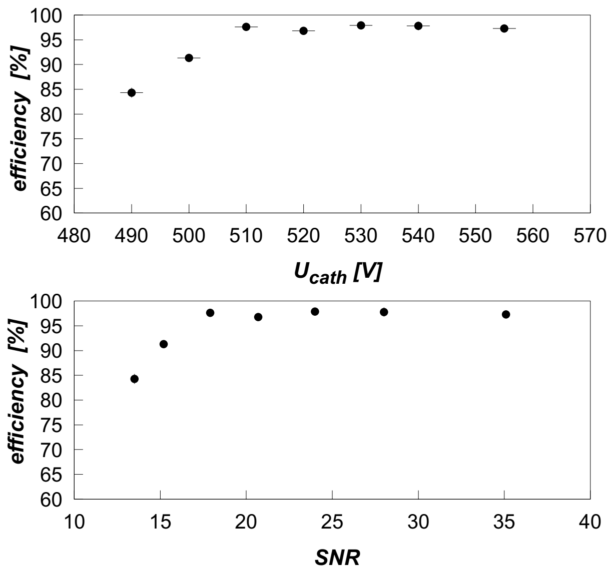

Figure 25 - Efficiency measurement of a prototype for the CMS forward tracker **[16]**. The upper plot shows the dependence on the cathode voltage U_{cath}. The lower diagram shows the same result for the signal-to-noise ratio (SNR), which is explained in section 4.2.3.

It can be seen in figure 25 that the efficiency reaches a plateau after an exponential rise. This is caused by the fact that the efficiency follows the shape of the gain measurements. At a certain voltage, it becomes fully efficient. A further increase of the gain therefore has no effect on particle detection anymore and a plateau is reached. Full efficiency is reached from a voltage of U_{cath} = 510V onwards for the detector presented in figure 25. Since the measurement has been carried out with MIPs, no direct measurement of the gain is possible. It is known from lab measurements that U_{cath} = 510V corresponds to a gain of ≈ 2000 **[16]**. The plateau is at 97% for that particular detector. The theoretical limit given by equation (5) is not reached, due to imperfections in the detector's construction and software algorithms.

Spatial resolution

The spatial resolution of a micro patterned detector like an MSGC depends on the granularity of the electrodes. It is given by the pitch p of the anode strips. If the charge generated by a particle detected in the MSGC is recognised by one strip only, the inaccuracy on the position measurement is $\pm p/2$. The intrinsic spatial resolution for such a detector is then given by the standard deviation of a uniform distribution between $\pm p/2$:

$$\sigma = \frac{p}{\sqrt{12}} \tag{20}$$

Equation (20) yields σ = 58µm for a pitch of p = 200µm. In reality, the charge is spread over more than one strip and the spatial resolution of an MSGC is increased by calculating the centre of gravity (COG) for the charge distribution. Spatial resolutions < 40µm have been achieved **[16][45][6]**.

Rate capability, occupancy and time resolution

Particle rates up to 10^4 Hz/mm^2 are expected in the LHC environment. It is mandatory to have a detector gain independent of the particle flux. This can be achieved by the use of conductive coatings, as shown in figures 23 a+b.
The percentage of multiple hits in a detector is meant by 'occupancy'. An occupancy < 1% is required for CMS – this means only one out of 100 events has more than one signal in a readout channel **[6]**. The pitch and strip length has to be chosen accordingly.
All readout electronics will be synchronised to the LHC bunch crossing rate of 40MHz in CMS. Every 25ns a particle collision will happen in the CMS detector. With a drift velocity of ≈ 50-60µm/ns, it takes an ion pair produced directly beneath the drift cathode approximately 60ns to reach the substrate in a 3mm drift space, which would be the worst case in terms of time resolution **[35]**. This causes inefficiencies, because the signal is read out when the charge has only partially arrived and therefore the signal is not at its full amplitude. This will be described in more detail in section 4.2.1. Dedicated electronics with on-chip signal processing capabilities and analogue memories are planned to cope with that problem **[6]**.

2.2.3 Known limitations

While problems due to charging up of the substrate in high particle fluxes can be efficiently handled by the use of conductive coatings, other effects when operating MSGCs in high rate environments can not that easily be coped with.
Destructive interactions of so-called 'highly ionising particles' (HIPs) with the strip pattern were encountered when carrying out high rate test experiments for the HERA-B experiment[25] at the PSI[26] pion test facility **[36]**. The beam had an intensity of 10^5 – 10^6 Hz/mm^2.

[25] HERA-B is a fixed target experiment currently running at the Deutsche Elektronen Synchrotron (DESY), Hamburg, Germany.
[26] Paul-Scherrer-Institut, Villigen, Switzerland

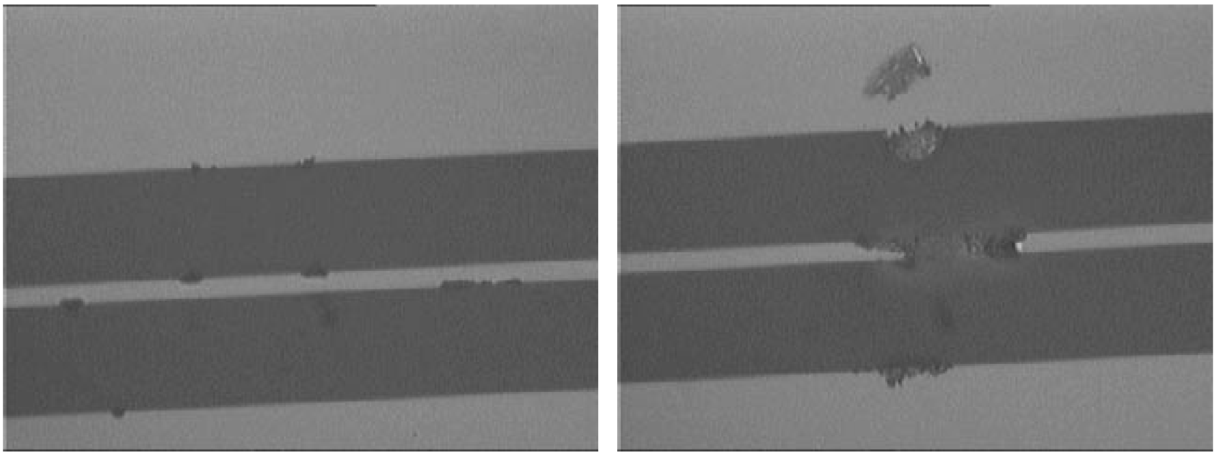

Figure 26 a) and **b)** - The photo (a) on the left shows a damaged, but still operational, anode strip between cathodes on the top and bottom of the picture. The photo (b) on the right shows a severely damaged anode: The strip is completely broken, and even the much more rigid cathode strips are damaged. This strip is no longer operational **[36]**.

A possible source for HIPs is the nuclear interaction of pions of the beam with atomic nuclei of the detector's materials. Low energy hadrons, which generate a high ionisation density along their track through the detector, can be produced in such reactions:, An average number of 1.7 interactions of that type occur in a substrate with 1μm thick gold strips and a 300μm thick glass substrate per 10^7 particles according to **[15]**.
All previous test beam experiments had been carried out with muons with considerably lesser rates. As an example, the rate at CERN's X5B facility, where some of the results discussed in chapter 5 have been obtained, is in the order of $10^2 – 10^3$ Hz/mm^2 only. The effect was not prominent in these experiments at this intensity, and occasional strip losses were not contributed to beam interactions.
This theory could be proven by injecting α-particles intentionally to MSGCs. The same damage as in the PSI test beam was observed **[36]**. It could be shown that the devastating effect was assisted by the conductive coatings used for the substrates to counter the charging up effects.

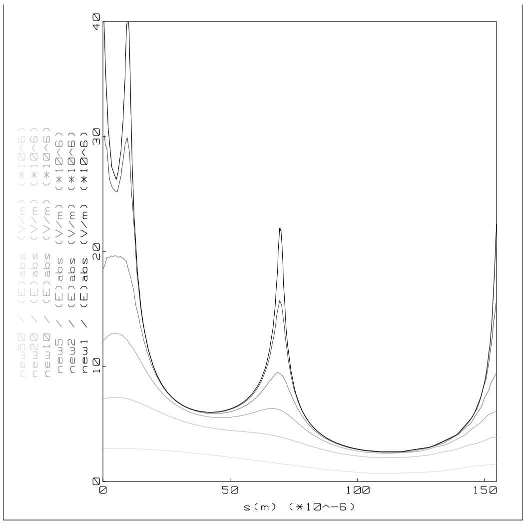

Figure 27 - Field strength above an uncoated substrate. The anode strip is on the left (0-10μm) and the cathode extends from 75-150μm to the right. The cathode edges can easily be seen (figure 27 and 28 taken from **[36]**).

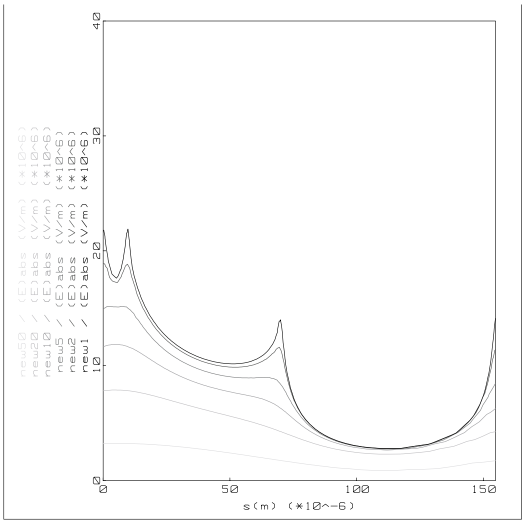

Figure 28 - Field strength for a coated substrate. The strip positions are the same as in figure 27. While the field strength is smaller at the strip edges, the field is significantly higher between the electrodes.

The reason can be seen in figure 28: The field between anode and cathode is significantly increased for a coated substrate compared to an uncoated one. If a nuclear interaction in the anode or cathode material takes place, a low energy hadron can be released directly on top of the electrodes in the region with the highest field, and therefore the largest gain. A huge charge is deposited between anode and cathode since the low energy hadron produces a high ionisation density. A short circuit between the two electrodes is the possible result. Dependent on the gain of the detector and location of the ionisation, the small anode strips can be damaged or broken by this discharge with the results depicted in figures 26 a+b.
The only possible solution to avoid this effect is to reduce the amplification field on the substrate. This means a reduction of amplification of course, therefore diminishing the detector performance. This is coped by the introduction of an additional amplification stage in the detector volume, namely the gaseous electron multiplier (GEM), which will be discussed throughout the remaining part of this thesis.
A different approach is the introduction of a thin insulating polyimide layer on the cathode edges, called 'advanced passivation'. It is depicted in figure 29. The peaks in the field strength visible in figures 27 and 28 are reduced by this protection. The electrode edges are protected in case of a discharge. This solution does not reduce the risk of a discharges, but helps to keep the anode strips operational. Similar to the addition of a GEM to an MSGC, the advanced passivation can be added to an already existing detector design with minor modifications in the production process. A second photolithographic process is necessary after the substrate production in the case of the advanced passivation. All other parts of the MSGC remain unchanged. This solution proved to be very successful by the end of 1999, when a large number of CMS prototypes manufactured that way were tested at the same PSI test beam, where the effect of strip destruction had been encountered for the first time. Nearly no strips were lost during a period of two months at a rate of $\approx 10^6$ Hz/mm^2 **[37]**.

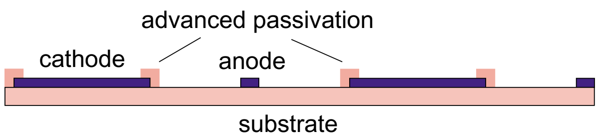

Figure 29 - Schematic cross section of a substrate with advanced passivation.

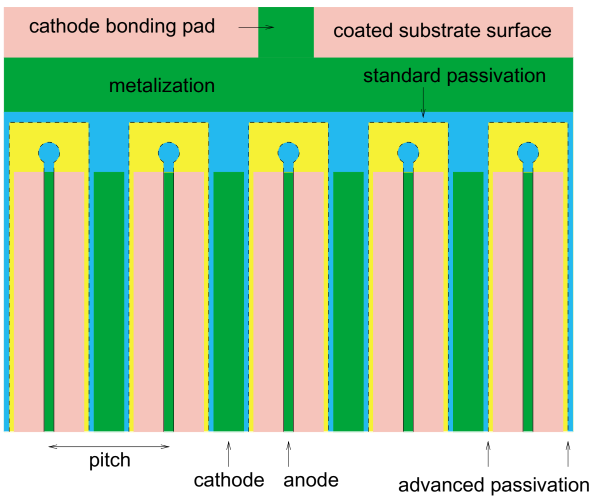

Figure 30 - Top view on a advanced passivated substrate.

2.3 Gas Electron Multipliers

Limitations of MSGC operation in high particle fluxes lead to the introduction of the Gas Electron Multiplier (GEM). The GEM is a foil with millions of microscopic holes. A high electric field in the same order of magnitude as the amplification field in an MSGC is generated in the holes. This leads to amplification processes such as those described in section 2.1.3. This results in an increased amount of charge for every incident particle with respect to the substrate. The gain on the MSGC substrate can be significantly lowered, reducing the risk of discharges, without decreasing the performance of the combined detector module.

2.3.1 Components

An MSGC with a GEM as additional amplification stage has two active detection elements: The substrate, as described in section 2.2.1, and the GEM itself. The role of the MSGC part of the detector remains unchanged, while the GEM provides additional gain to the combined detector module, significantly reducing the requirements on the substrate's amplification. The detector consisting of an MSGC and GEM will be called GEM+MSGC from now on.
Figure 31 shows a schematic cross section of an MSGC with the added GEM. It is basically the same detector as depicted in figure 17 with an additional foil. It is made of an insulating material which is metallised on both sides. Only foils made of Kapton[27] and Espanex[28] do exist up to the time of this writing. GEMs made of Espanex have been developed in an industrial production line together with Würth Elektronik. For the remaining part, reference is always to this type of foils unless otherwise noted. Espanex has the additional benefit that the copper coatings are attached to the polyimide by means of a sputter process. No adhesion layer or glue etc. is needed. The material is not susceptible to chemicals that way.

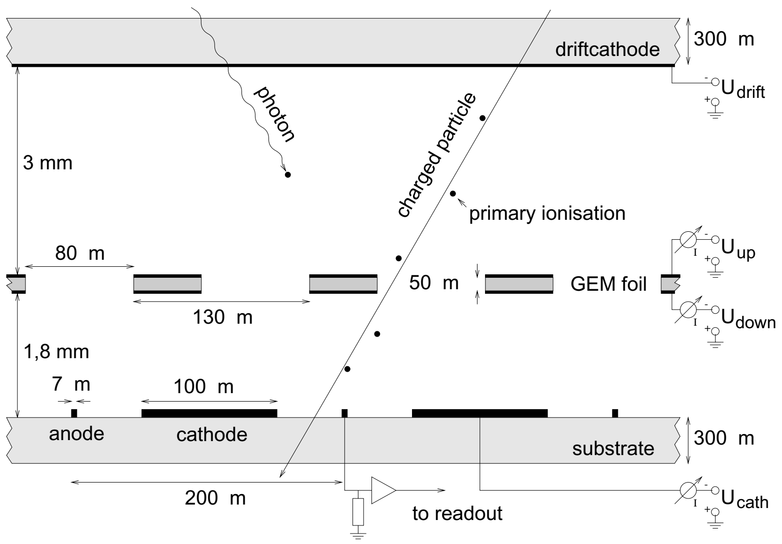

Figure 31 - Schematic cross section of a GEM+MSGC (not to scale). This drawing should be compared to figure 17 – one can see that the only additional component is the thin foil inserted between the drift cathode and substrate. Typical voltages are U_{cath} = 450V, U_{down} = 1080V, ΔU_{GEM} = 350V (U_{up} = 1430V) and U_{drift} = 2930V. This yields E_{drift} = 5kV/cm and E_{trans} = 6kV/cm for the drift spaces given in the figure. The space between drift cathode and upper side of the GEM is called 'drift space', while the region below the GEM is called 'transfer space'.

Although different choices of metallisation for the polyimide exist, only copper clad GEMs have been produced up to now. The reason for that is the limited availability of other materials from the industry. Copper clad polyimide foils are widely used as flexible printed

[27] CERN Surface Treatment Service, Geneva, Switzerland
[28] Espanex® by Nippon Steels, distributed by Holders Technology GmbH, Manndorf, Germany. GEMs produced by Würth Elektronik, Rot am See, Germany.

circuit boards, because they can be processed in standard etching devices. Other choices for the metallisation, e.g. aluminium, are available from the manufactures.

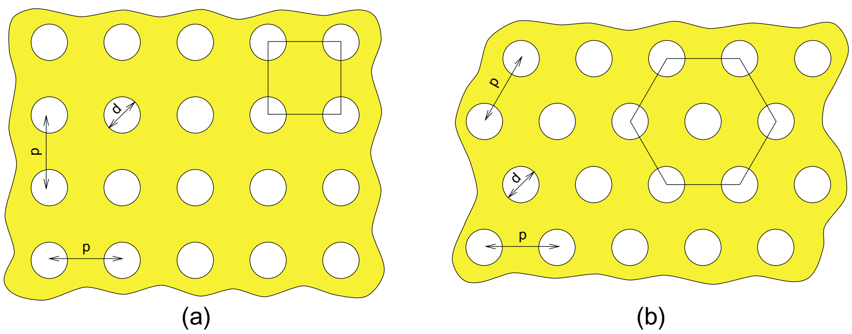

Figure 32 a) and **b)** - Top view on a GEM foil. The hole diameter *d* and pitch *p* can be seen. Two different layouts are shown: a) shows a symmetric pattern in both dimensions while b) has a triangular symmetry.

Small holes are etched into the metallised foil. The diameters range from 50µm to 200µm. Smaller holes are not realisable due to limitations of the etching process, and larger diameters are not useful, as will be shown in section 2.3.3. The principal layouts of GEM foils are shown in figure 32 a) + b). While a geometry according to 32a) is easier to produce, the design depicted in figure 32b) yields 16% more holes, as can be seen in figure 33:

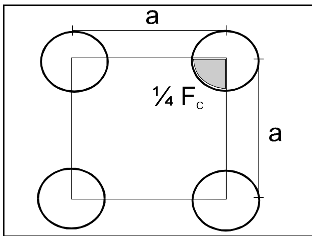	$F_C = \pi \frac{d^2}{4}$, $F_R = a^2$ $t_R = \frac{F_C}{F_R} = \frac{\pi d^2}{4a^2}$	F_C – area of a hole F_R – area of the rectangle t_R – ratio of area with holes to surface d – hole diameter a – length of one side
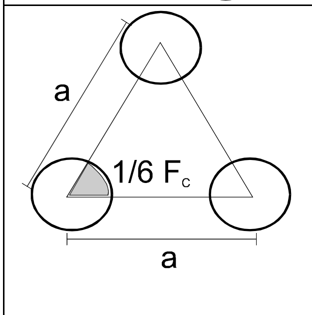	$F_C^{'} = 3 \cdot \frac{1}{6} \cdot F_C = \frac{\pi d^2}{8}$ $F_T = \frac{1}{2} a h = \frac{2\sqrt{3}}{8} a^2$ $t_T = \frac{F_C^{'}}{F_T} = \frac{\pi d^2}{2\sqrt{3} a^2}$	F_C – area of a hole $F_C^{'}$ – area of a hole inside triangle F_T – area of the triangle $h^2 + \frac{1}{4} a^2 = a^2 \Leftrightarrow h = \frac{\sqrt{3}}{2} a$ - height t_T – ratio of area with holes to copper d – hole diameter a – length of one side

Figure 33 - Ratio of opacity for the symmetric and triangular geometry.

The ratio t between the two geometries is given by

$$t = \frac{t_R}{t_T} = \frac{4a^2}{2\sqrt{3}a^2} = \frac{2}{\sqrt{3}} \approx 1.16$$

This results in a 16% greater opacity which has a positive effect on the amount of particles able to traverse the GEM. Figure 35 shows a magnified cross section of a GEM. All GEMs produced up to now have a thickness of either 25µm or 50µm. The reason for that is again the limited availability of other materials, although thicker foils exist. An additional reason is the increasing difficulty of etching those materials. This will be discussed in more detail in the next section.

An electric field develops inside the channels in the polyimide when a potential difference $\Delta U_{GEM} = U_{up} - U_{down}$ is applied to the two metal layers. Depending on ΔU_{GEM}, field strengths in the order of 40 – 100kV/cm are reached. This is in the same order as the amplification field just above the MSGC substrate. Amplification processes as described in section 2.1.3 take place in the foil's channels for that reason. The charge of every incident particle is multiplied by the gain of the GEM. Since the gain of the substrate and GEM are multiplied, a reduced gain on the substrate is required to reach the same total amplification as in an MSGC without GEM. The GEM foil is glued on top of the distance frame on the substrate. This frame is usually thinner than in an MSGC, because the drift spaces below and on top of the foil add up in a GEM+MSGC. This adversely affects the time resolution of the detector. The field below the GEM is called 'transfer field' E_{trans}, and the field between GEM and drift cathode is called 'drift field' E_{drift}. A transfer space of 1.8 - 2mm was used for the detectors covered in this thesis. The same structure as in an MSGC is on top of the foil: The frame defining the drift space is glued onto the GEM. The topmost part of the detector is the drift cathode. The drift space is 3mm for all detectors discussed in this thesis.
The connection of the substrate to the HV and readout electronics is identical to an MSGC. The foil itself requires two additional HV connections. There are basically two possibilities to provide the voltages to the GEM: Either by using two different HV lines as done throughout this thesis, or by use of a voltage divider. The latter has the advantage that only one HV line is required. A disadvantage of that solution is the inflexibility to changes of the voltage ΔU_{GEM}.

2.3.2 Foil processing

There are basically three methods of producing GEM foils: Laser drilling of the holes, wet etching and plasma etching. The first solution is more a technology study than a realistic production method. While it is easy to achieve the required position resolution for the laser, and it is an advantage of this method that strictly cylindrical holes are drilled, the production of foils is too time consuming and expensive for a large scale serial production, which would be required for an experiment like CMS.
The first GEMs ever produced were developed at the CERN Surface Treatment Service in a wet etching process. A detailed description can be found in **[38]**.
GEMs produced in the plasma etching process were realised together with an industrial partner, Würth Elektronik, in the course of the detector development for this thesis. The main advantage in contrast to wet etching is the increased speed of the process, making large scale production of GEMs possible and affordable. The copper clad material is coated with a light sensitive resin as a first step (figure 34b). The masks defining the holes are put on both sides of the foil afterwards. The resist is developed and cured after exposure to UV light (figure 34c). The next steps are wet etching with a copper solvent (d), and the removal of the photo resist (e). In a last processing step, the plasma etching is done. The etched copper surfaces of the foil act as mask for the plasma etching. The GEM is placed in a container with a low pressure[29] gaseous atmosphere, composed from CF_4, oxygen and nitrogen. A plasma is then generated by microwave induction. All molecules in the gas are ionised in this state. The reduced pressure is required to allow a large mean free path length for the ion pairs. Radicals are generated by this process. The reaction products interact with the polyimide, not affecting the copper. The 'etching' of the channels of the GEM is done as a result. Since the reaction of the plasma starts from the outsides of the foil, careful controlling of the plasma's temperature

[29] The container is first evacuated to remove the air, and then flooded with the etching gas. An absolute pressure around 0.2mbar is required for the process.

and the time of the process is necessary to reduce the ‘under-etching’. This denotes the effect that polyimide is etched away beneath the copper.

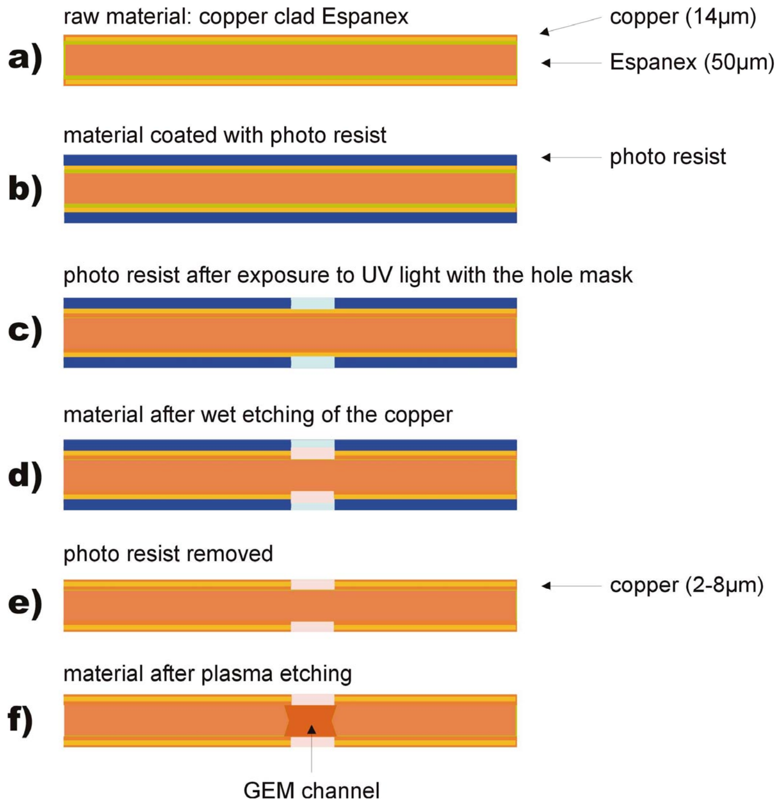

Figure 34 - Plasma etching process **[39]**.

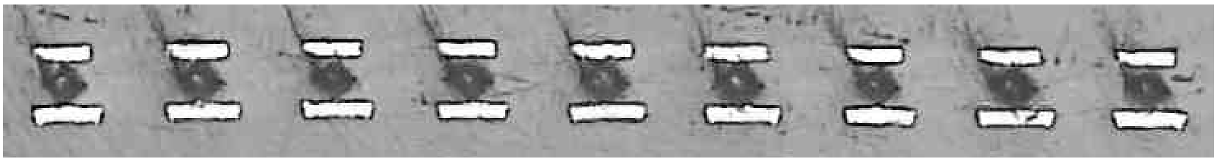

Figure 35 - Cross section of a plasma etched GEM. Photographs by Würth Elektronik **[40]**.

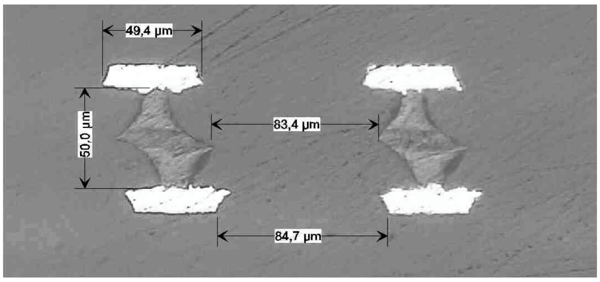

Figure 36 - Magnification of a single GEM hole of the first plasma etched foils.

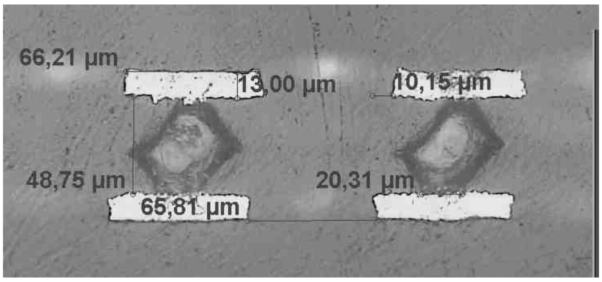

Figure 37 - Magnification of a GEM hole of one of the foils produced in the optimised plasma etching process.

Figure 35 shows a magnified cross section of a plasma etched GEM foils. The design parameters were $d = 80\mu m$ and $p = 130\mu m$. It can be seen in the magnification in figure 36 that these dimensions are closely matched. However, a displacement between the top and bottom copper layer can be seen. This results in a channel running diagonally through the polyimide. Some field lines end on the insulating material between the copper planes due to the distorted geometry when voltages are applied to the two sides of the GEM. The alignment of the masks for the etching of the copper layers was done by precision pins for this 'first generation' of foils. The method proved to be not precise enough, because a positioning accuracy of only ±25µm could be reached. The alignment of the masks was changed to optical positioning by means of fiducial marks for a second production run. In addition, the material used for the masks was changed to a more rigid one to avoid deformations of the hole shape due to bending of the masks. The greatly improved result can be seen in figure 37. A complication of this 'second generation' foils can be seen in this photograph as well: Since the plasma etching does not affect the copper, but the polyimide, under-etching happens to a high degree. In some regions the copper layers face each other with no insulating material extending between them. The field lines directly go from the top to the bottom copper layer in these areas. Charge following those trajectories is lost on the lower copper side, and the gain of the GEM is degraded. The under-etching effect is the limiting factor for the pitch. To avoid the complete removal of polyimide between neighbouring holes, a minimum thickness of 50µm of the material has to be maintained **[39]**. In reality, the thickness of the etched polyimide is reduced by the under-etching. Given that number, the minimum pitch p depending on the diameter d can be calculated by $50\mu m = p - d$. The GEM foils of the 'third generation' have been etched in an additional wet etching step after the plasma etching to remove the copper extending into the channels. This has the additional benefit of smoothing the holes' rims. They have small spikes and imperfections after the plasma etching, as can be seen in figure 37. This is caused by the heating of the copper during the process. The spikes distort the field and make the operation of such GEMs more unstable. Foils of the second generation did not reach the same high voltages ΔU_{GEM} as those of the first and third generation. With the last generation of GEMs, stable operation with an increased amplification could be achieved.

2.3.3 Performance

The most important parameter determining the performance of a GEM is its field. This has the additional complication of interacting with the drift and transfer field on the upper and lower side of the GEM respectively. Those interactions will be discussed in section 5.5.

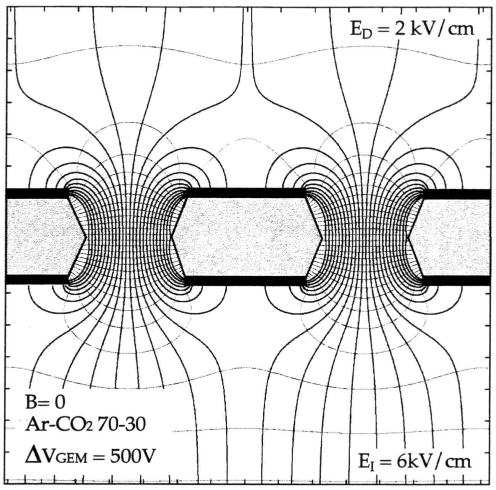

Figure 38 - The grey lines connect points of equal potential, calculated by MAXWELL[30] and the black lines are drift lines, calculated by GARFIELD[31]. Plot taken from **[41]**.

[30] MAXWELL, by Ansoft Corporation, USA
[31] GARFIELD is programmed and maintained by R. Veenhof, CERN

The electric field inside the GEM is created by the potential difference between the upper and lower copper layer.
Figure 38 shows the field inside a channel. The plot has been obtained using MAXWELL and GARFIELD. The drift and transfer fields used for the calculation are given in the figure. The transfer field is denoted as E_I. A closer look reveals that all field lines from the drift region go towards the transfer region. All charge produced in the drift space is transported towards the MSGC substrate. This is the optimal mode of operation for a GEM. The ratio of charge which passes to the transfer region to the charge produced in the drift space is called 'transparency'. Ideally a GEM has a transparency of 1 (or 100%) as depicted in figure 38. Deviations from this behaviour will be discussed in section 5.3.
The field strength inside the GEM channel along its central axis can be seen in figure 39. Curves for different hole diameters are shown. The maximum field strength is reached in the middle of the foil. This corresponds to $y = 0\mu m$ in the figure. The copper planes are reached for $y = \pm 25\mu m$. It can be seen that the field strength increases with decreasing hole diameters.
The field strength across the diameter of the channel is shown in figure 40. The maximum field strength is reached at the hole's rim in this dimension. The curve for $y = 0\mu m$ belongs to the middle of the foil. $y = 25\mu m$ is the surface of the foil. The spikes in the field strength when reaching the hole's rim at $x = \pm 32\mu m$ can be seen. This is the same effect as depicted for an MSGC in figure 20.

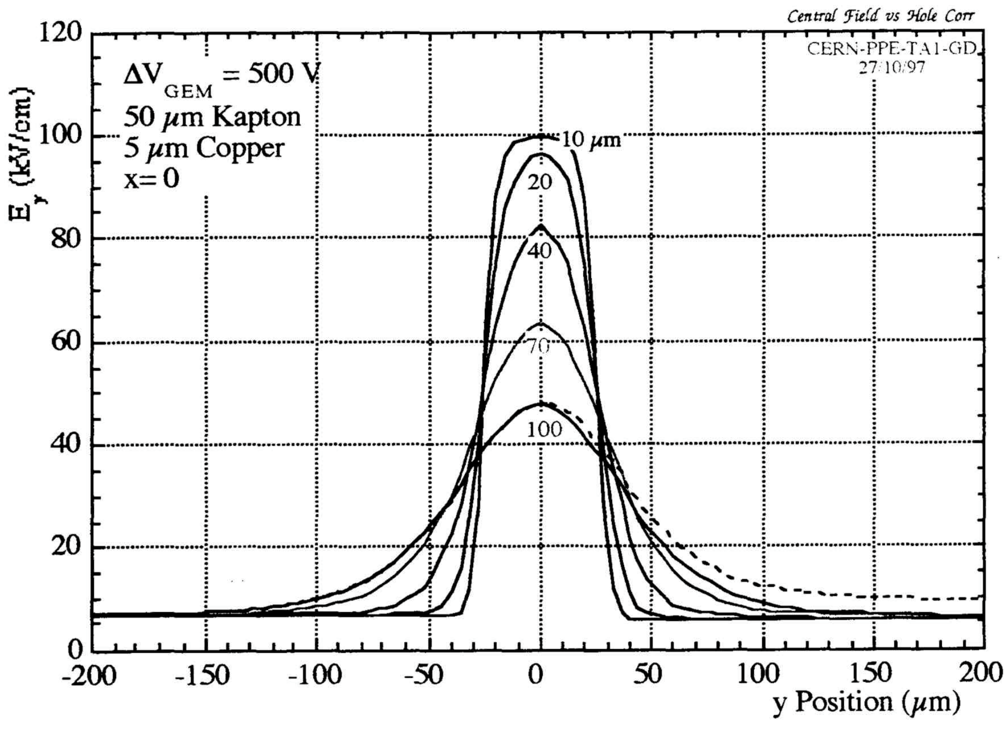

Figure 39 - Field strength along the GEM channel for different hole diameters in a foil of 50µm thickness. The calculations were done with MAXWELL. Picture taken from **[41].**

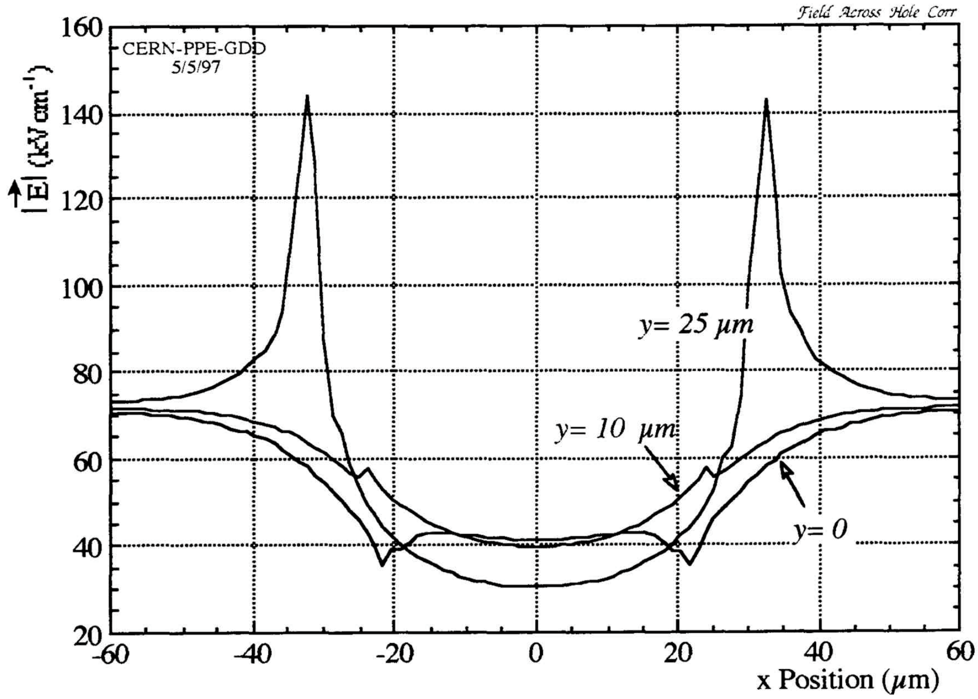

Figure 40 - Field strength along the top side of a GEM. This plot shows the field strength perpendicular to figure 39 for a hole diameter of 70µm. $y = 0$ is the middle of the foils which has 50µm thickness. $y = 25$µm is the top side of the GEM. The very high field strength at the hole's rim can be seen. Computations done with MAXWELL; picture taken from **[41]**.

Impact of the GEM geometry on the gain

Since the geometry of the GEM affects the electric field inside the channels, the diameter has an impact on the GEM's gain.

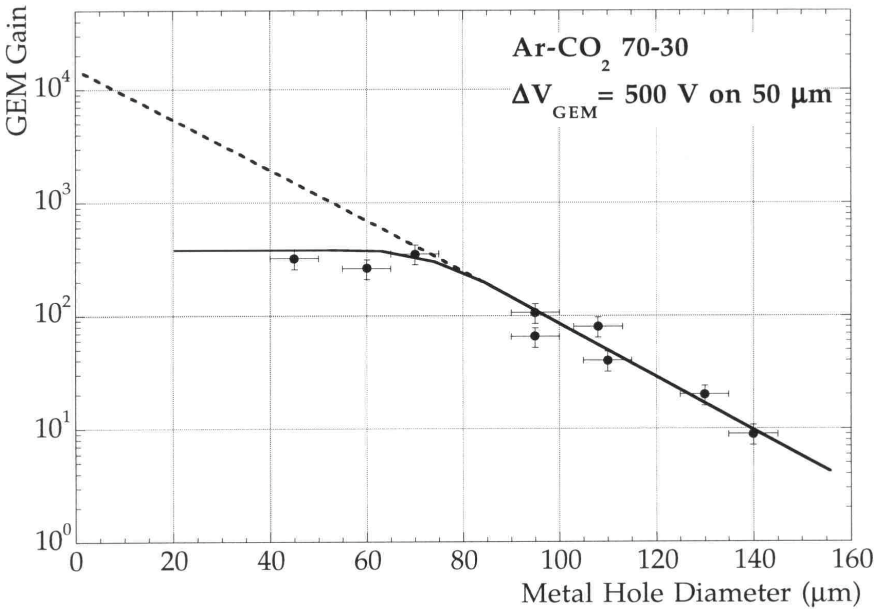

Figure 41 - Impact of the holes' diameter on the detector's gain **[43]**.

Increased gain in the GEM can be achieved either by reducing the hole diameter, or increasing the potential difference ΔU_{GEM}. The field density inside the channel is increased in

both cases. While the effect of varying ΔU_{GEM} will be discussed in section 5.1, the impact of a variation of the holes' diameter can be seen in figure 41.
The beginning of a plateau for diameters < 70µm is notable. This is caused by a saturation effect: The reason is an increased loss of electrons in avalanche to the lower GEM side due to diffusion **[43]**. It therefore makes no sense to reduce the diameter d of the holes below 70µm.
The pitch of the GEM has no direct effect on the behaviour of the GEM. There is no effect on the amplification, since the electric field is independent from the distance between the holes. There is an effect on the transparency however, as will be discussed in section 5.5.

3 CONSTRUCTION OF THE DETECTORS

A number of prototype detectors have been built to study the behaviour of GEM+MSGCs. Two sorts of detector modules were constructed: The so-called ‘MS-9 type’, named after the layout of the MSGC substrate[32], and a prototype module for the CMS forward tracker. The latter detector has trapezoidal shaped substrates with cathode strips of variable thickness and pitch, while the MS-9 type detectors have parallel strips and symmetric cathodes. Both types were equipped with plasma etched GEM foils produced by Würth Elektronik.

3.1 Choice of materials

The requirements on the detectors’ materials are well defined: Since a GEM+MSGC is an MSGC with an added amplification foil, all requirements imposed on the MSGC detectors by the LHC environment are valid for the combined detector modules as well. Regarding the mechanical realisation, the principal dimensions of the MS-9 type detectors were defined by the existing layout of the substrate. The remaining constructional design was centred on easy production and assembly. The CMS forward prototype module had to be developed within the framework of the CMS baseline as defined in **[6][16]**. The emphasis was put on using as much as possible of the already existing parts and machinery, and to modify the baseline as little as possible.

The choice of materials is mainly dictated by the requirement to be compatible with DME, which is a solvent, and to be able to withstand LHC’s enormous particle flux and radiation levels. Extensive research has been carried out throughout the last 10 years for MSGCs. A compilation of the results of those studies can be found in **[44]**. Only materials which already proved their readiness for the operation in CMS were used: The mechanical parts used for carrying the substrates and drift cathodes were made of Stesalit (Stesalit AG, Zuwill, Switzerland), an enforced glass fibre material. The frames defining the drift and transfer spaces were made of PEEK (Bohlender AG, Lauda, Germany), which has the advantage of a very smooth surface. This is important, because small chips extending from the frame into the active detector volume have to be avoided, because they distort the electric field. Stesalit always has these chips extending for some microns from the frame due to the fibre nature of the material. All substrates, both the MS-9 type and the ones for the CMS prototype module, were produced by IMT Masken und Teilungen AG, Greifensee, Switzerland. The drift cathodes were made of metallised foils and gold coated glass for the MS-9 type detectors. Only glass drift cathodes could be used for the forward module, because metallised enforced glass fibre cathodes, as described in section 2.2.1, were not available at that time. All parts in contact with the counting gas were glued with EPO93L (AXSON GmbH, Dietzenbach, Germany).

[32] The MS-9 layout has been developed by F. Sauli, CERN GDD group. He generously allowed the use of his production mask.

3.2 Construction of GEM+MSGC detector modules

The first GEM+MSGC modules constructed were based on the MS-9 layout. Due to their small size of only ≈ 10x10cm^2, it is easy to keep the GEM flat and stretched during assembly. Emphasis was put on easy assembly of the detector. A total of six detectors were built up to the time of this writing. Three of these detectors, which are equipped each with one of the three generations of GEMs described in section 2.3.2, will be treated.

3.2.1 Components

All MS-9 type GEM+MSGC detectors were built on substrates made of 300µm thick D263 glass. The first two detector modules, christened GEM4 and GEM5, have chromium strips. GEM5 has an additional coating. This so-called ‘diamond like coating’ (DLC) decreases the surface resistance to ≈ $10^{-14}\Omega/\square$. The third detector module, GEM6, is made of gold strips on uncoated D263 glass. The thickness of the strips is 500nm for all substrates. The anodes are 7µm wide and the cathodes have a width of 100µm. The pitch is 200µm. The layout can be found in appendix F, figure 139.

Detector	***Coating***	***Strip metal***
GEM4	none	chromium
GEM5	DLC	chromium
GEM6	none	gold

Table 1 - Compilation of the different substrates used for the measurements.

The detector is built on a base plate (appendix G, figure 143) which holds the substrate and the gas connector (appendix G, figure 146). These parts are made of Stesalit. The transfer region is 1.8mm high and the so-called ‘bottom spacer frame’ defining that dimension is made of PEEK. The drift region has a height of 3mm and is defined by the ‘top spacer frame’, made of Stesalit. Drawings of the two frames can be found in appendix G, figures 144 and 145 respectively. The top frame could be made of Stesalit, because the GEM has a border of ≈ 2mm around the area with the channels, caused by the production process. This border can be seen in figure 157. Chips sticking into the detection volume for some microns therefore do not distort the drift field. This would not be possible in the transfer region, because the electrodes go close to the frame there.
A glass drift cathode was used for GEM4. It is made of 300µm thick D263 glass and coated with a 5nm thick gold layer. A 1nm thick chromium adhesion layer is used between the glass and the gold. A drift cathode made of chromium clad Mylar foil has been used for GEM5 and GEM6. This material is easier to handle and due to the small size of the active detection area the deformation by the gas pressure is negligible. The detector module is finally connected to the high voltage by a HV connection circuit (appendix D, figure 138) and the readout electronics. A PreShape32 analogue shaping amplifier is used for GEM4 **[49]**. GEM5 and GEM6 are read out by a PreMux128 multiplexing amplifier **[50]**. The readout electronics are described in more detail in sections 4.1.1 and 4.2.1 respectively.

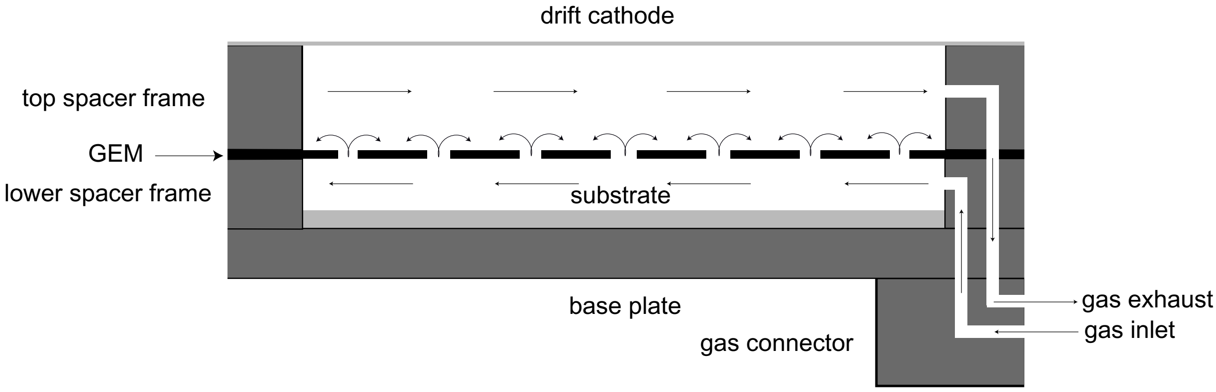

Figure 42 - Schematic cross section of the assembled detector.

The gas in- and outlets are glued to the gas connector below the base plate. The gas flowing into the detector module is distributed below the GEM, as shown in figure 42. It then flushes through the foil and ensures the gas exchange in the chamber. The exhaust is in the top spacer frame: There is a 'pocket' in one of the frame's sidebars, through which the gas is guided back to the gas connector. This is done by means of a channel going through the two spacer frames and the base plate. The holes for this channel can be seen in figures 43 and 44 on the top and right side of the photographs respectively.

3.2.2 Detector assembly

All parts are cleaned according to the procedures described in appendix E. The first step in the assembly of a new detector module is the cutting of the substrate. The outer dimensions of the glass plates are larger than the artwork, and the unnecessary borders have to be cut away. This is done with a diamond scriber. A cutting precision of ± 5µm is achieved. The cut substrate is then glued to the base plate. No special alignment is needed, because the base plate has a depression exactly matching the substrate's dimensions. The glass plate is self-centred that way. A gas tight connection of the substrate to the base plate is achieved by the high viscosity of the EPO93L glue. The bottom spacer frame is glued onto the base plate with the substrate. Grooves on each side of the frame fit to corresponding places on the base plate. Since PEEK is a flexible material, while Stesalit is rather rigid, the frame snaps on the base plate and is self-centred that way. The spacer frame has a width of only 1mm on the readout side, and 1.5mm on the HV side of the substrate. Special care has to be taken when applying the glue. If too much glue is put on the part, the resin is spread over the bonding pads of the substrate, making bonding extremely difficult. Figure 43 shows the module assembled so far.

The next step is the gluing of the GEM. A special device has been constructed for that purpose: The GEM is first stretched to a metal frame by adhesive tape. The inner dimensions of the metal frame exactly match the outer dimensions of the top spacer frame. The latter is put into an aluminium jig which matches its outer dimensions. The top spacer frame is fixed in a well defined position that way, and the glue can be applied. The metal frame with the stretched GEM is lowered onto the top spacer frame by means of precision pins. A metal plate which matches the outer dimensions of the spacer frame is then put on top of the construction. The GEM foil is now stretched by the weight of this metal plate around all four sides of the spacer frame.

Figure 43 - The lower part of the detector already assembled.

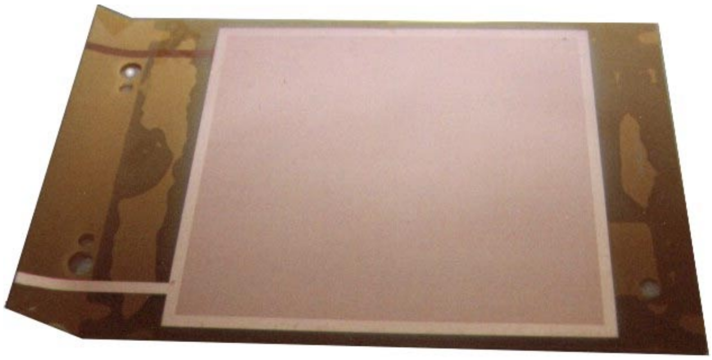

Figure 44 - The upper part of the MS-9 type detector. The piece is laying upside down, so that the GEM can be seen. The top spacer frame is below the foil. The HV connection lines to the two sides of the GEM can be seen to the left.

The metal plate and jig are removed after curing of the glue and the GEM is cut out of the aluminium frame. The result can be seen in figure 44. Now this part of the detector module is glued to the lower part already assembled.

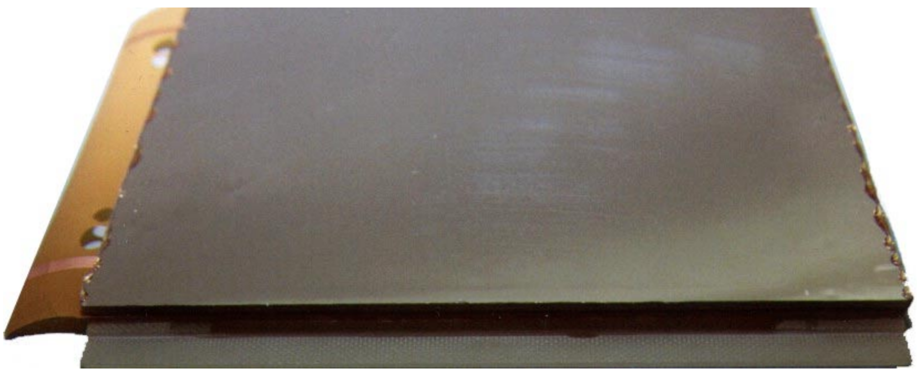

Figure 45 - The complete MS-9 type detector module without gas and electronics supports. This is a photograph of GEM6 with a Mylar drift cathode.

The last assembly step is the mounting of the drift cathode. The procedure varies with the type of drift cathode: For GEM5 and GEM6, the Mylar drift cathodes are glued to the top spacer frame exactly the same way as the GEM is mounted. The glass drift cathode used for GEM4 is first cut to size and then simply put onto the top of the detector module. Due to the high viscosity of the EPO93L glue, even the light weight of the thin glass plate is sufficient to guarantee a gas tight sealing of the detection volume. No special care is necessary for aligning the drift cathode.

After the curing of the glue, all grooves between the different frames are sealed with an additional layer of the glue. The last step is the gluing of the printed circuit boards for the HV and readout electronic connections to the base plate. Those boards are then connected to the substrate by bonding[33].

The complete detector is finally mounted to a plate, carrying all the supports for gas, cabling and cooling of the electronics. A picture can be seen in figure 46.

[33] The bondings for all detectors covered in this thesis have been done by O. Runolffsson, CERN (ret.).

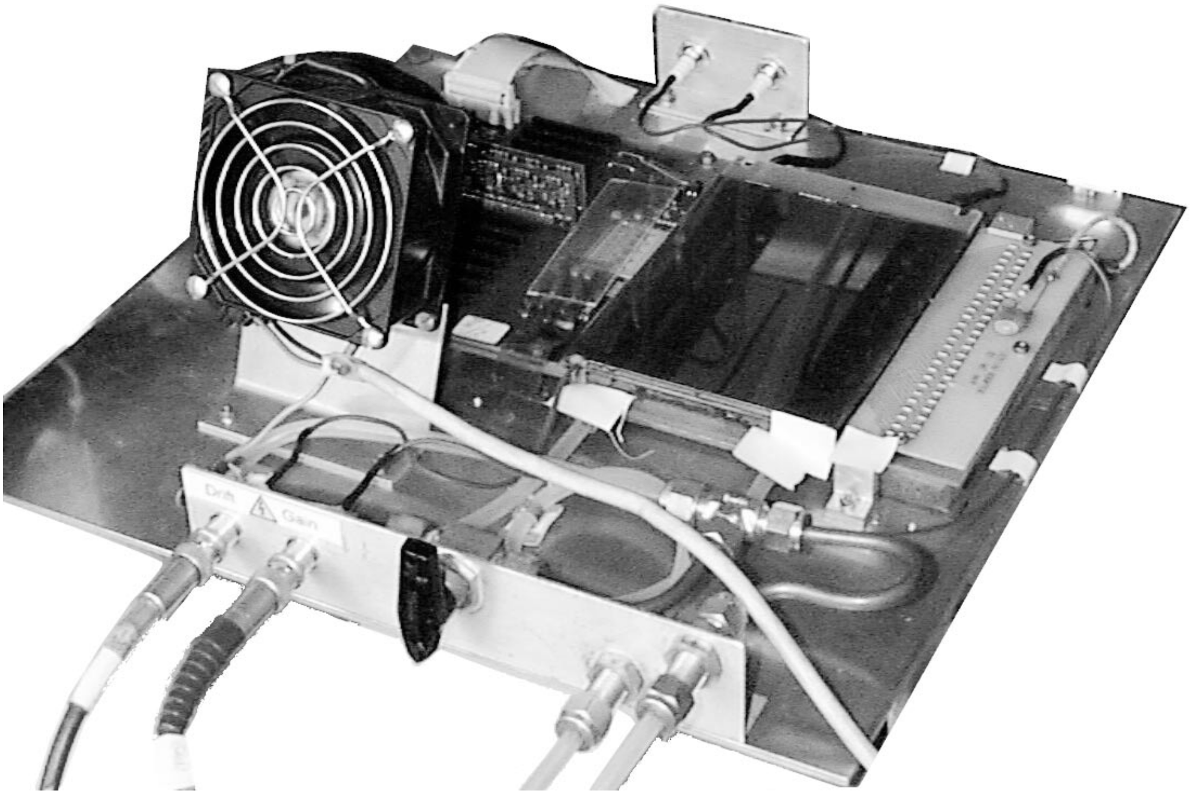

Figure 46 - The complete detector module with all services. This is a picture of GEM4, but the other MS-9 type detectors look the same, except the readout electronics (to the left). On the lower side of the photo, the gas in- and outlets and HV supports for the cathode and drift cathode voltages can be seen. The voltage lines for the GEM can be seen on top of the picture. The fan is necessary for cooling of the PreShape32 buffer cards on the left.

3.3 Construction of a CMS forward tracker prototype module

After successful operation of the small MS-9 type GEM+MSGCs, the construction of a full scale CMS forward tracker detector module was realised. The requirements for that prototype were:

- Compliance with the requirements of the CMS tracker as defined in **[6]**.
- Keeping in mind the possibility of serial production.
- Make maximal use of the parts and machinery already developed **[16]**.

While the first requirement – compliance with the CMS tracker baseline – was achieved on the mechanical side by using the frames developed for the MSGC modules, the compliance with the required performance of the detector modules will be shown in chapter 5. The issue of serial production readiness has already been covered in section 2.3.2 – all GEMs were produced in the industry. The assembly of the modules is done by using the same tools as specified for the MSGC modules.

3.3.1 Requirements of the CMS forward tracker

The CMS forward tracker[34] consists of 11 disks perpendicular to the LHC beam axis in both directions of the beam line. All disks on one side of the barrel tracker make up a so-called ‘supermodule’. The CMS tracker will therefore consist of two supermodules, such as the one depicted in figure 47.

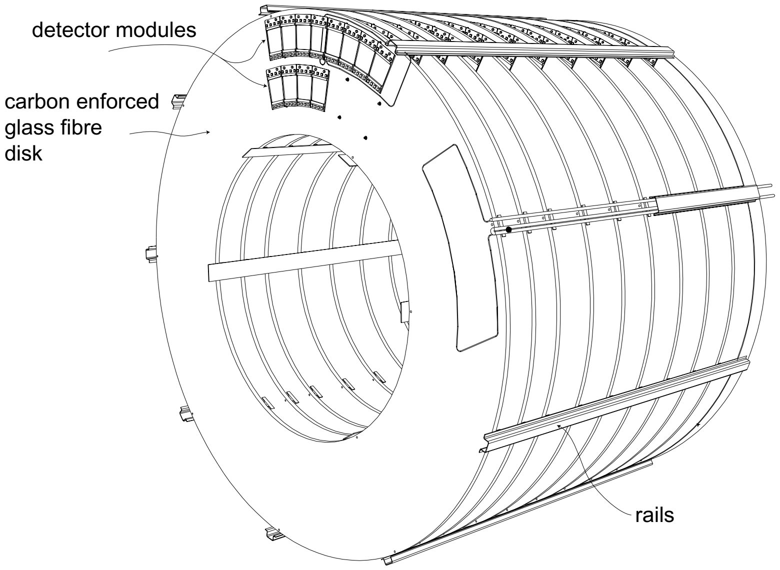

Figure 47 - A CMS forward tracker supermodule. The semi-circular detector modules form rings when attached to each other. Rings of different diameters cover the surface. The disks are in fact rings, because the silicon forward tracker will be inserted into the central part of the supermodule.

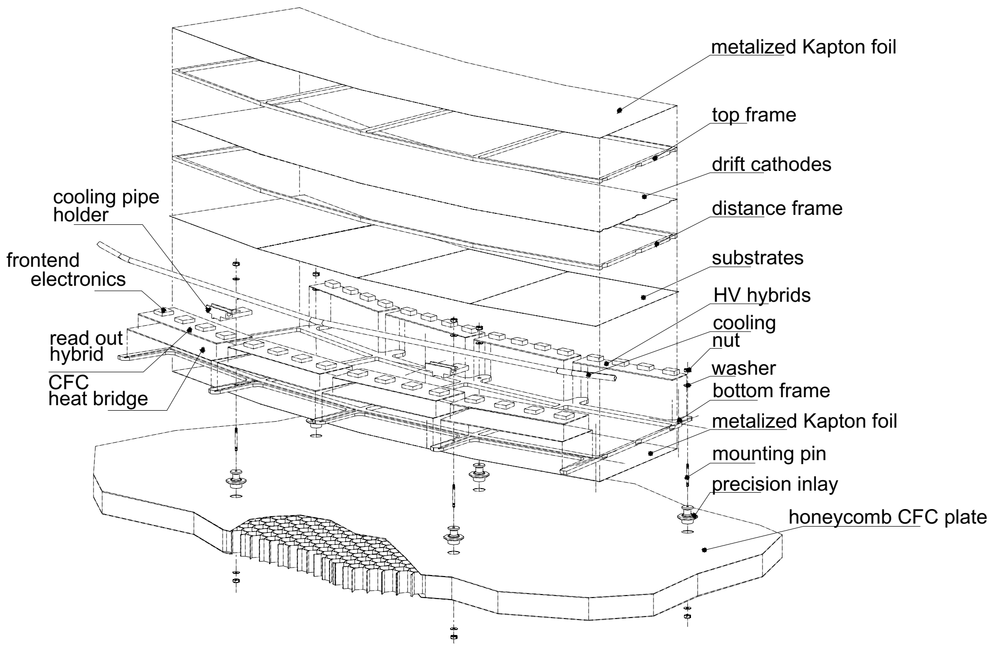

Figure 48 - A complete forward MSGC module, including all details and supports. The GEM+MSGC module makes use of exactly the same design, only adding the GEM and a second distance frame.

[34] Also referred to as ‘CMS forward-backward tracker’ – but since LHC is a p-p-collider, the tracker is symmetric.

The detector modules will be mounted on both sides of those disks. They therefore have to be of a semi-circular shape, as can be seen in figure 48. They form rings when attached to each other. Since detector modules with different radii will be constructed, the rings cover the entire surface of the disks. Two rings of modules will be attached to each side of the disk. The positioning will be done in a way that modules of consecutive radii are placed on alternating sides of the disk, partially overlapping. A total of approximately 4800 detector modules will be needed for the complete forward-backward tracker **[6]**. Four substrates are placed side by side in each detector module. A special cutting and alignment procedure ensures that no dead spaces exist between neighbouring substrates. All four MSGC plates form the active detection volume of $\approx 25x50cm^2$ (see appendix G, figure 147). This detector design already takes care of the logistic problems arising from the operation of such a large number of detectors. The frames for the detector modules are injection moulded to allow serial production, and are equipped with precision holes to allow alignment of the modules with respect to each other on the disks **[16]**.
The trapezoidal shape of the substrates has implications on the layout: For easier track reconstruction in the experiment, one wants to have a cylindrical symmetry in the r - ϕ - plane, which is parallel to the disks' surface. All strips then originate in a common point. The strips are no longer parallel as a result. The layout of the substrates used in the CMS forward detector modules is shown in appendix F, figure 141. The pitch is varying from 248.5μm on the readout side to 211.6μm on the HV side due to the geometric shape of the strips. To achieve a constant gas amplification along the strips, the cathode width has to be varied, too. This is done according to the so-called *NIKHEF-Formula* **[6]**:

$$g = \frac{p}{8} + 20\mu m \qquad (21)$$

Equation (21) has been obtained by simulations, but could be proven experimentally. A result has been already shown in section 2.2.2, figure 25. Since this type of detector module had already been tested successfully in the so-called 'milestone forward one' (MF1) experiment **[45]**, it was used as a basis for the development of a GEM+MSGC detector. Whenever possible, the original design was left untouched.

3.3.2 Components

The construction of the detector module follows the principal design ideas developed for the MF1 modules as depicted in figure 48. Figure 49 gives a schematic view of the GEM+MSGC forward module: The detector is built on top of a bottom frame made of Stesalit, which has extensions to carry the readout electronics and HV printed circuit boards. The four substrates are glued on top of it. The substrates are made of 300μm thick D263 glass with 500nm thick gold strips. The distance frame from figure 48 is replaced by the bottom spacer frame, which is only 2mm high instead of 3mm. The frame is made of PEEK. The GEM foil is glued on top of it. Since it was not possible to produce a GEM of this size in one piece in the plasma etching process, the foil had to be split in two. The layout of the 'half-GEM' can be found in appendix F, figure 142. To accommodate the assembly issues arising from the division, the top spacer frame had to be split, too. This is explained in detail in appendix H. The frame defines the drift space of the detector module and is 3mm high. It is also made of PEEK. The GEM foil with the top spacer frame is the only addition to the original CMS forward tracker MSGC detector module design.

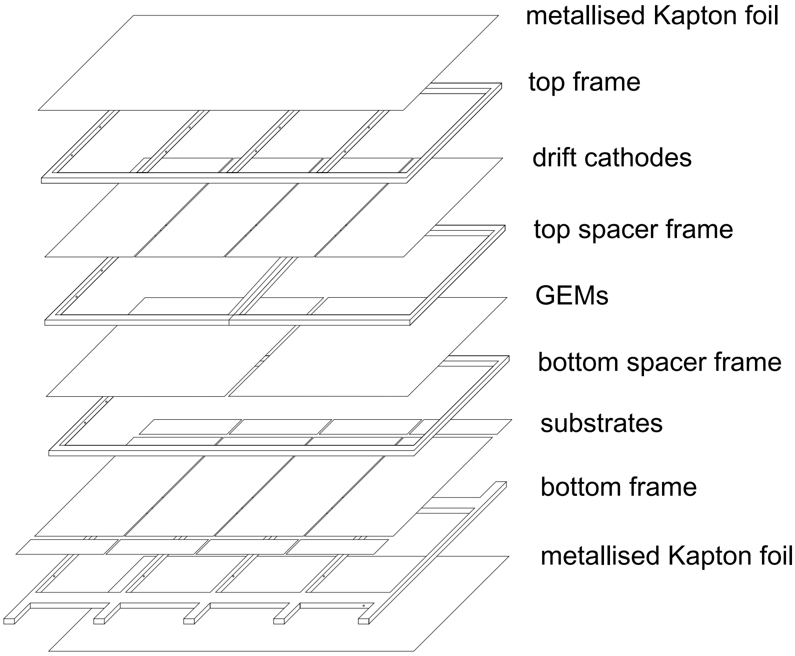

Figure 49 - Construction principle of the CMS forward GEM+MSGC module.

The drift cathodes, which are made of the same material as for GEM4, are glued on top of the structure. They are enforced by the top frame, made of Stesalit.

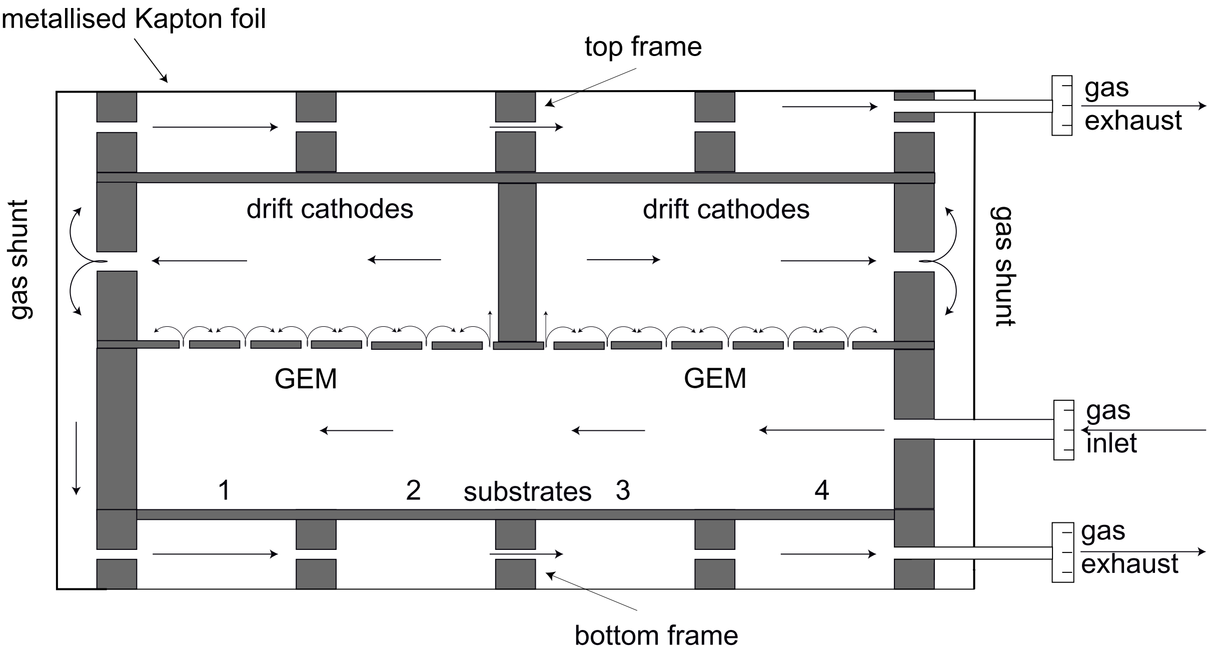

Figure 50 - Gas flow and distribution in the GEM+MSGC forward module.

Finally, the detector is wrapped in copper-clad Kapton foil, as depicted in figure 48 and 49. The reason can be seen in figure 50: The gas inlet is just below the GEM in the transfer region. The gas has to pass through the GEM to reach the exhaust. This supports the gas exchange. The gas is distributed to the top and bottom frames. To reach the exhaust, the gas has to pass between the drift cathodes and Kapton foil on the upper part of the module, or between the substrates and Kapton foil on the lower part of the chamber. No pressure differences can stress the fragile substrates or drift cathodes. The pressure on both sides of the glass plates is always the same. The remaining components of the detector are the printed circuit boards for the PreMux128 readout electronics **[50]** and the HV connection board.

3.3.3 Detector assembly

A detailed description of the assembly process can be found in appendix H. Only a short summary is given here: At first, the substrates are cut. This is a delicate process, since the cut has to be done with a position accuracy of 5µm. The reason for this requirement is the layout of the detector module: Since four substrates are placed side by side in a forward module, the cuts on the substrates have to be done in a way not modifying the pitch between consecutive MSGC plates. The substrates have to be aligned on the bottom frame after cutting. Special care has to be taken to ensure that the outermost strips on neighbouring substrates are parallel. This is done by a fibre optic alignment system, developed for this purpose **[47]**. Since only a region of ≈ 10cm diameter can be irradiated in the test beam facilities, only half of the module is equipped with substrates. The other half is made of glass plates to reduce the costs.
After the substrates are glued to the bottom frame, they are sealed gas tight from the back with EPO93L. The bottom spacer frame is then glued on top of the substrates. The alignment with respect to the bottom frame is done by precision pins. Figure 51 shows the pre-assembled 'lower' part of the module.

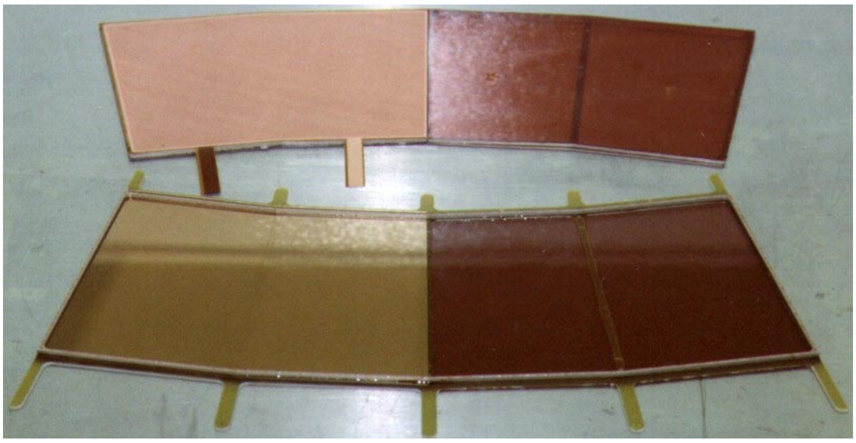

Figure 51 - The pre-assembled module halves. The upper part of the module consisting of the drift cathodes, drift region, top frame and GEM can be seen on top of the picture. The lower half of the module, made of the substrates, bottom spacer frame and bottom frame, can be seen on the bottom.

The next step is the assembly of the upper part of the detector module. Since only half of the detector module is equipped with substrates, only one half of the GEM+MSGC is equipped with a real GEM foil. A mock-up, made of bare Kapton, has been used for the other half. The foils are positioned on the jig by means of two precision pins for each half. The two parts are then flatly stretched and fixed by adhesive tape. Now the drift cathodes are glued on top of the structure. They are enforced by the top frame, which is glued onto them. Like the GEM and the substrates, only half of the detector module is equipped with 'real' drift cathodes. Bare D263 glass plates are used for the other half. All parts can now be removed from the gluing jig and the GEM is cut to size.
The upper and lower module halves are glued together finally. The last assembly step is the application of the Kapton foil on the top and bottom frames.

Figure 52 - The completed CMS forward GEM+MSGC module.

The upper Kapton foil is cut in a way that two flaps remain on each of the small sides of the module. They are folded around the frames and are glued onto the lower foil. This provides the gas flow as depicted in figure 50. Figure 52 shows the complete forward GEM+MSGC module. The readout electronics and HV connection boards are already mounted. Two copper HV connection pads for the GEM can be seen on top of the photograph. The only parts still missing are the gas connection lines, which are glued into appropriate holes in the frames.

4 EXPERIMENTAL SETUPS

This chapter describes the various setups used for measuring photons (^{55}Fe-source), electrons (^{90}Sr-source), minimum ionising muons and pions. The two different frontend electronics used, PreShape32 and PreMux128, with the accompanying data acquisition infrastructures will be introduced. The algorithms and software packages used for the data analysis are described.

4.1 Measurements with single-channel readout

The first GEM+MSGC built, GEM4, was read out with *PreShape32* amplifiers **[49]**. Each anode strip on the substrate is bonded to a dedicated shaper and amplifier channel on the PreShape32 chip, and digitised by a fast analogue-to-digital converter (FADC) for further processing. This has the advantage that the response of the detector module to variations of its operating voltages, the gas mixture etc., can immediately be seen 'on-line', that means without any additional analysis steps. In the beginning of the experiments, when no experience or knowledge about the correct voltage settings were available, this was a great advantage. It was possible to carefully approach the operating conditions, where the detector module became operational, without risking the then unique GEM+MSGC.
The goal of these measurements was to compare the gain of a GEM+MSGC with an MSGC., All experiments were carried out with an ^{55}Fe-source for that reason, since this allows a direct measurement of the GEM's amplification.

4.1.1 Signal amplification and shaping

Each PreShape32 consists of 32 shapers and amplifiers. Each anode strip of the substrate is connected to one channel of a PreShape32 chip. For a readout of a full MS-9 type substrate, 512/32 = 16 chips would be needed. This would require the enormous amount of 512 FADCs for a complete module, since each channel of the PreShape32 needs a FADC to digitise the analogue. It was chosen to use only four chips with a total number of 128 read out strips for that reason. This results in a 128x200µm = 2,56cm wide area in the middle of the substrate, which is accessible by the data acquisition system. Figure 53 shows a schematic circuit drawing of a single channel. The amplifier is coupled to the strip by a capacitor. The collected charge (IN) is then amplified by the pre-amplifying structure on the PreShape32 (PRE). The gain of the amplification can be adjusted (VFPRE, IPRE). As discussed in section 2.2.2, the electron signal is present within the first nanoseconds after the passage of the incident particle. The main part of the charge is on the other hand generated by the ions, which drift only slowly. A compromise between fast detection of the signal and a sufficient integration time for charge collection has to be found. This is taken care of by the shaping circuit on the

PreShape32 (SHP). It generates an output whose shape is defined by the so-called *CR-RC shaping*; t is the time, $\tau = RC$ is the time constant of the shaping circuit and B a norming constant defined by the area of the resulting signal, $B \cdot \tau$:

$$f(t) = \begin{cases} 0 & t < 0 \\ B\,\dfrac{t}{\tau}\,e^{-\frac{t}{\tau}} & t > 0 \end{cases}$$

The resulting signal (OUT) can be seen in figure 54. The time constant of the shaper can be adjusted (VFSHAPE, ISHAPE). It has been left on its default setting of ≈ 45ns for all measurements.

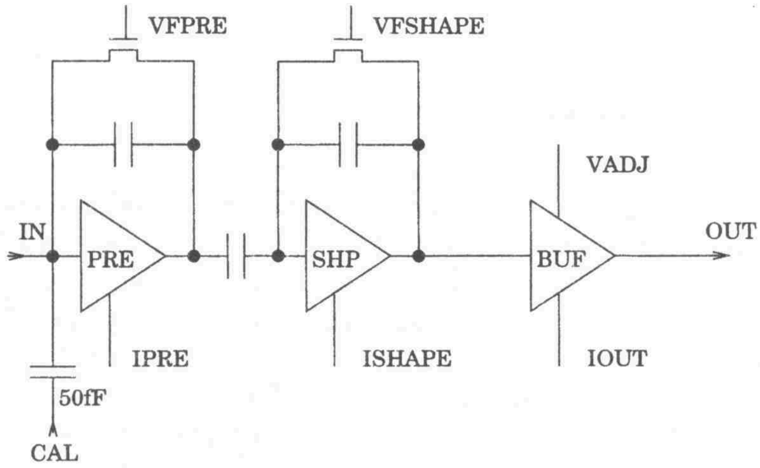

Figure 53 - Schematic circuit drawing of a single PreShape32 channel **[49]**.

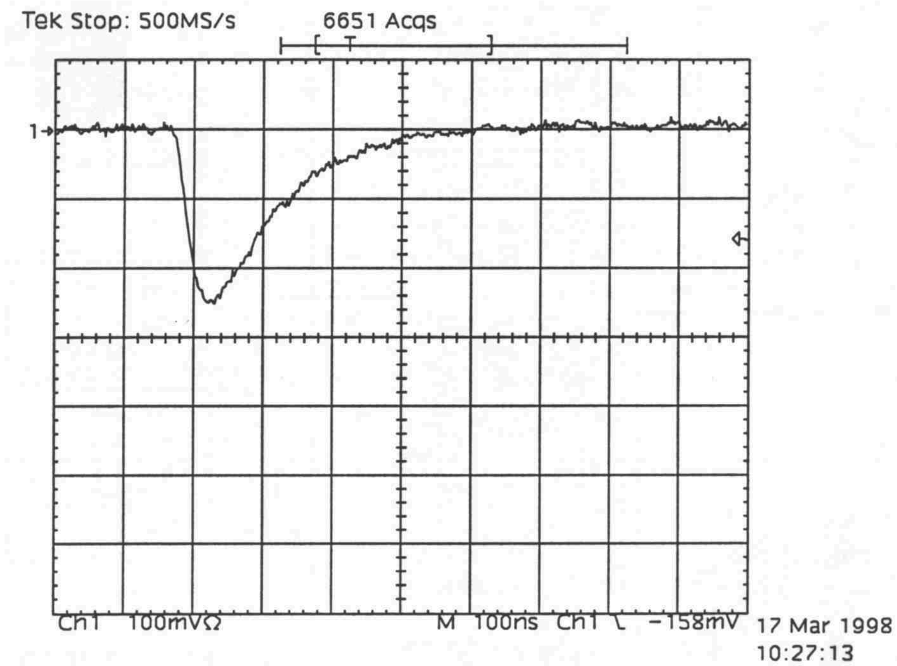

Figure 54 - Signal of a γ-particle emitted by a ^{55}Fe-source. The abscissa has a unit of 100ns/division and the ordinate has a unit of 100mV/division. The plot has been recorded using a digitising oscilloscope connected directly to the PreShape32 output.

The PreShape32 chips are mounted to a so-called 'motherboard', which carries all the connectors for signal and power lines, as well as the auxiliary components for generating VFPRE, VFSHAPE, IPRE and ISHAPE. It also has slots for connecting the so-called 'buffer cards' (BUF). Those are small printed circuit boards, which contain line drivers to adapt the motherboard's impedance to those of the cables used for connection to the data acquisition system. Each PreShape32 has additional calibration inputs (CAL) to allow an absolute charge measurement. A pulse generator with a precision capacitor is used to inject a well-defined charge into the calibration inputs. An absolute calibration in terms of electrons per FADC count is obtained by this procedure. An FADC count corresponds to the module's dynamic range dived by its resolution. For the 6bit FADCs with a dynamic range of 1V used for all measurements with ^{55}Fe, one FADC count represents 1V/64 = 15mV. With the calibration carried out, this corresponds to ≈ 700 electrons/count. This value differs for the different channels, of course. The detailed numbers for the calibration process and its result can be found in **[51]**. A picture of GEM4 connected to the PreShape32 amplifiers and the motherboard can be seen in figure 46.

4.1.2 Data acquisitio n

Each channel of the PreShape32 chips can be connected to a data acquisition system (DAQ). Since a limited number of FADCs were accessible, only eight neighbouring channels could be selected for readout.

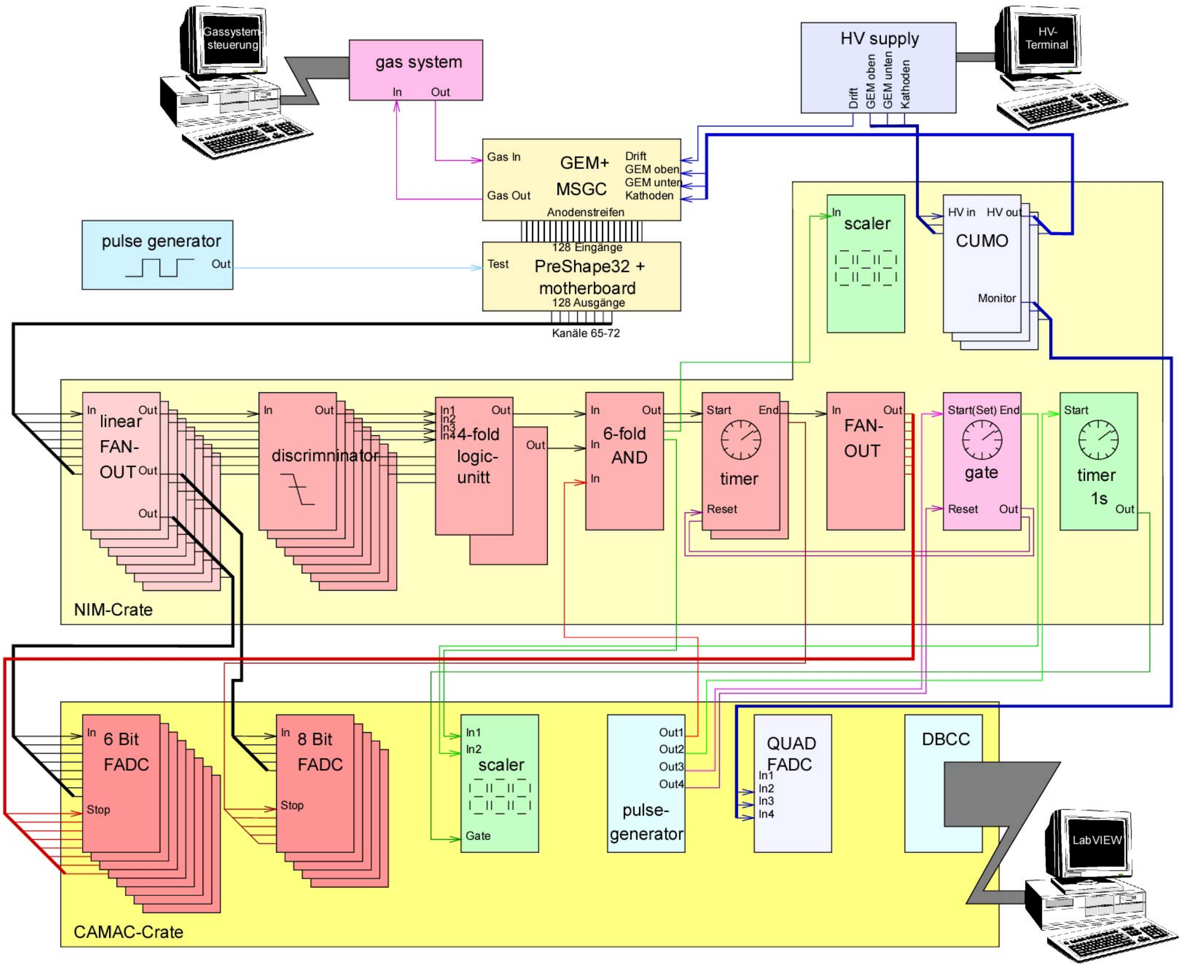

Figure 55 - Data acquisition system for PreShape32 readout. Picture taken from **[51]**.

Figure 55 shows the complete DAQ setup. A comprehensive description, along with a list of all modules used for the setup, can be found in **[51]**. A short description will be given here: Since eight strips were accessible for read out, a region of only 8 x 200µm = 1.6mm width of the substrate could be used for particle detection. It was not possible to collimate the ^{55}Fe-source that accurate. A trigger scheme was established, which starts the DAQ only for particles passing through the median four strips for that reason. Since the PreShape32 gives an immediate feedback of the signal created by the particle, triggering on the particle's signal is possible. The left- and rightmost strips were left out of the trigger for reasons which will be discussed in the next section. The detector module is only read out when a particle passes through the centre of the active strips. All events recorded by the DAQ contain at least one strip with a signal larger than the discriminators' threshold. The threshold was set to –40mV. This ensured a negligible false trigger rate: Nearly no event is recorded when the source is removed. The residual trigger rate is in good agreement with the expected cosmic particle rate of ≈ 1Hz/100cm^2. The trigger setup is depicted in figure 55 in the 'NIM-crate' section.
The signals are digitised by FADCs and stored by a DAQ software called *GEMon*, specially developed for that purpose **[51][52]**.

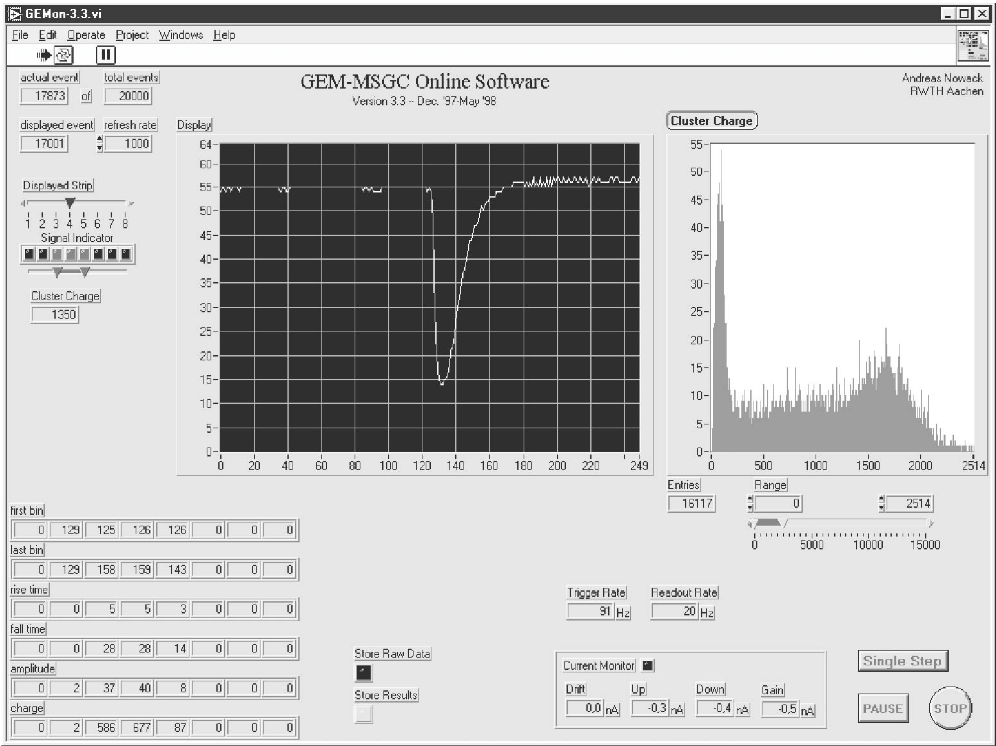

Figure 56 - Screenshot of the DAQ software *GEMon*.

The software acts as a multi-channel 100MHz digital sampling oscilloscope. Each time a particle passes through one of the selected strips, the signals for all eight strips in the readout are written on disk. Figure 56 shows a screenshot of the program. The oscilloscope-like display of the signal can be seen in the middle and shows the same information as figure 54. Only one channel is visible at a time due to space constraints. The analysis of the event's charge, described in the next section, is also available in this program. The resulting charge distribution is visible on the right. This allows on-line tuning of the GEM amplification. The lower right section of the display contains status information about the currents on the cathode-, drift cathode- and GEM-HV-lines. This information is sampled by using current monitors (CUMOs) connected to FADCs **[53]**. This information is not recorded for all events. The FADCs connected to the PC running the DAQ software are depicted in figure 55 in the

'CAMAC-crate' section. An additional scaler module can be found there, which is used to store information about the readout rate and number of events recorded.

4.1.3 Analysis software

A software package developed for the analysis of laboratory and test beam data has been used for the measurements acquired with GEMon **[54]**. This program, *Interactive Runfile Inspection System (IRIS)*, contains all the functions needed to access the data on disk, process the events and store the results in any format convenient for further treatment **[47]**. It provides a framework of C functions, within which the analysis algorithms can be executed.
The algorithms developed for the PreShape32 data analysis can be divided into three major parts: Calibration, peak finding and cluster finding. The calibration has been already discussed in section 4.1.1.
The important parameter of the signals as depicted in figure 54 is their charge. To calculate the charge, which is proportional to the area and amplitude of the pulse, one needs to know the beginning and the end of the pulse. This is called *peak finding*.

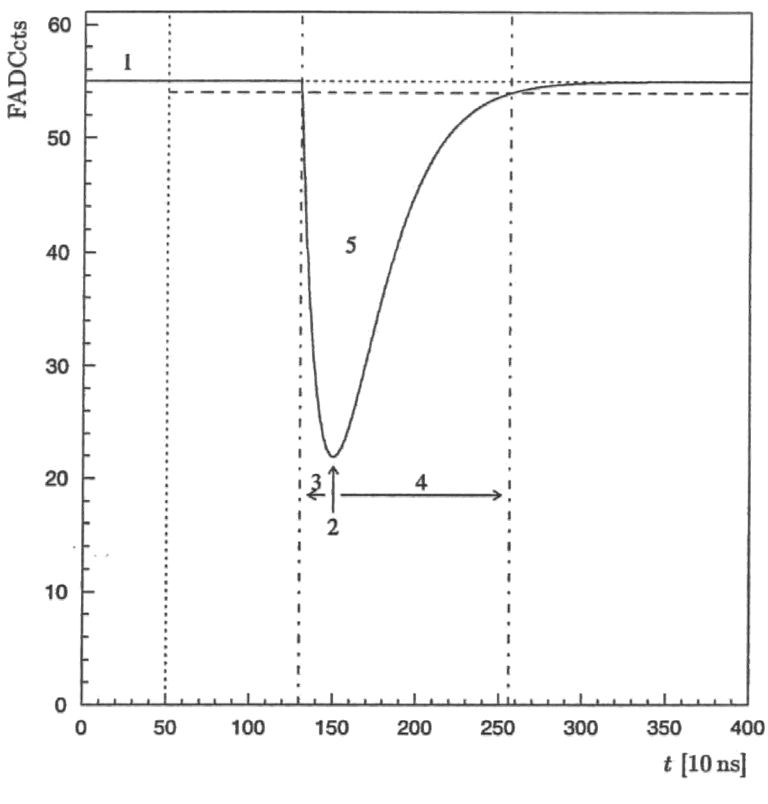

Figure 57 - The pulse shape as it is recognised by the software[35]: 1) baseline, 2) amplitude, 3) beginning of the peak, 4) length of the pulse and 5) area of the signal. The ordinate unit is FADC counts and the abscissa is a time scale. The divisions originate from the bandwidth and memory depth of the FADC used: 100MHz and 1kB memory make up for a sampling every 10ns for 10,24µs. To save disk space, only the part of the memory which contains the signal is stored (≈ 4µs).

To start the peak finding process, the software first has to know the FADC reading without any signal – the so-called baseline b_{ij}. This information is computed by averaging the first 50 samples for each of the i channels and j events. It is numbered as '1' in figure 57. The delay between the beginning of the signal shape in the FADCs' memory after a digitalisation was

[35] The time base has been stretched by a factor of five for better readability.

started is adjusted by a timing unit (figure 55). No signals therefore occur during that period. Since the mean is computed for all channels and for each event, event-to-event variations of the baseline are automatically dealt with. No special considerations have to be taken for the electronic noise: This is already taken care of by the trigger threshold. However, an uncertainty of $\pm$ 1counts remains due to rounding errors of the averaging process. All further peak finding steps require a signal to exceed the baseline at least for this. The threshold of -1 count is marked by the dashed line in figure 57. Since all signals from the detector module have a negative polarity, it is only searched for those pulse shapes. Positive signals exist as so-called *cross talk*. These are generated by very large signals, which influence charge of the opposite sign on neighbouring strips. The software does not take care of such events.
The position of the peak can now be determined. The algorithm first searches for the absolute minimum below the baseline in each channel for every event. Only the first in time is taken if more than one minimum is found,. This yields the amplitude of signal, which is denoted as ‘2’ in the figure. Starting at the position of the minimum, the software now searches to the left for the first value being greater than the baseline. This value is stored as the beginning of the pulse (‘3’). The procedure is repeated to the right and yields the length *l* of the signal (‘4’). The charge q_{ij} of the peak can now be calculated:

$$q_{ij} = \sum_{l} (r_l^{ij} - b_{ij}) \qquad (22)$$

r_l^{ij} is the measured value for the *l*-th memory position of FADC *i* in event *j*. This yields a positive value of the signal’s area, which is proportional to the deposited charge.
The charge is usually spread over more than one strip due to diffusion, as discussed in section 2.1. It is therefore necessary to locate neighbouring strips which have recorded a signal, too, and sum up their charge. This is done by the *cluster finding* algorithm. The software searches along the eight strips read out by the DAQ, and locates the strip with the largest charge. It then searches to the left and right for the first strip which has not shown a signal. The difference between the two strips’ positions yields the cluster width *w*. From the charges of the signals contributing to the cluster, its charge Q_j is calculated:

$$Q_j = \sum_{w} q_{ij}$$

It can now be explained why only the middle four strips were taken into account for the trigger: Since the analysis showed an average cluster width of $\approx$ 2 strips (see section 5.2), a possible loss of cluster charge would have been occurred if the triggered signal had been on one of the outer strips. Figure 58 shows this effect: The charge spectrum for all possible clusters on the eight strips is shown on the left plot. The trigger has been set to be active for all events for that measurement. The clusters which were centred on the border strips and therefore subject to potential loss in the reconstructed charge were selected by software. They are shown in dark grey on the plot. These clusters were removed for the right spectrum in figure 58. As expected, many of the clusters yielding a small charge in the far left of the histogram are removed.
The ^{55}Fe spectrum in figure 58 shows a significant deviation from the one shown in figure 13 for an MSGC: An additional peak can be seen. This is due to the fact that each photon interacts at exactly one location with the counting gas, depositing its fully energy there. In contrast to MIPs, it can therefore be distinguished between an interaction in the drift region, and one in the transfer region. Since the charge produced in the transfer region does not pass through the GEM, it does not benefit from the GEM amplification. One therefore obtains two energy distributions.

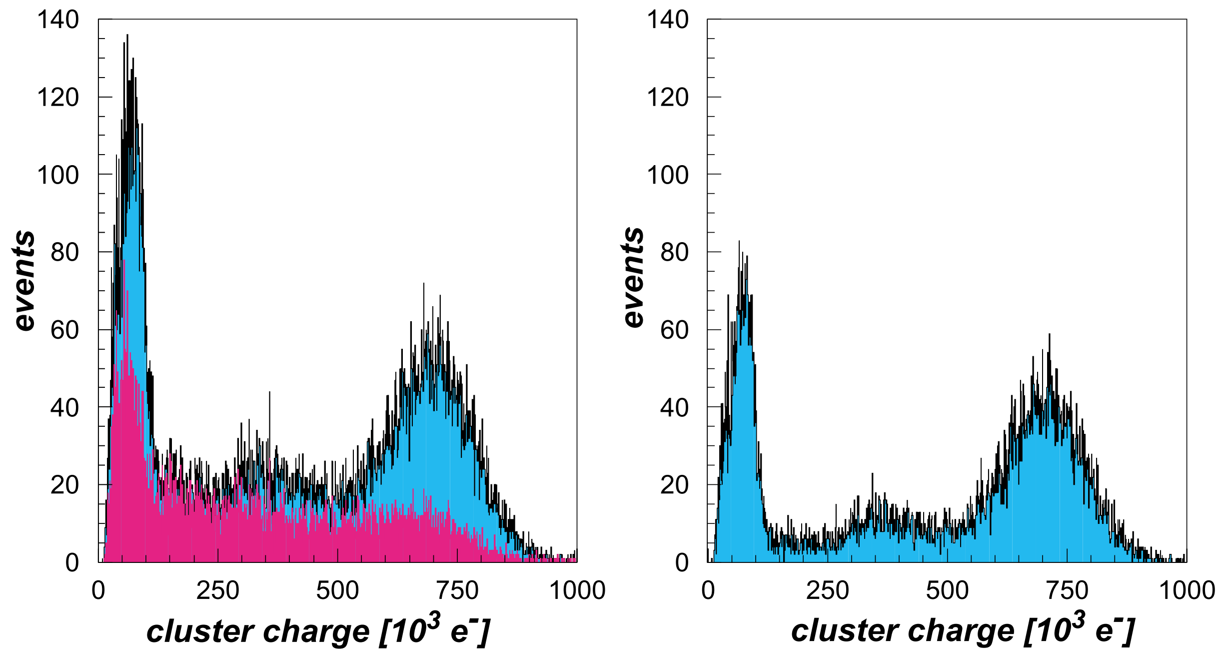

Figure 58 - ^{55}Fe spectra for GEM4 with Ar/C_3H_8. The plot on the left contains both the charge resulting from clusters without selection and the charge which could not be fully reconstructed (dark grey). On the right hand side, the spectrum of fully reconstructed clusters only is shown.

The rightmost peak is the ^{55}Fe line and called the *GEM peak*, because these signals have been amplified by the GEM. The same pulses for the events amplified by the MSGC part of the detector only are called *MSGC peak*. The small peak in the middle is the Argon escape peak for the charge amplified by the GEM. The escape peak for the interactions in the transfer region can not be seen due to poor energy resolution. It is possible to compare the gain from the MSGC and GEM part of the detector module by selecting only events from one of the peaks. A measurement has been carried out with the GEM at a potential of ΔU_{GEM} = 0V. The GEM acts as a drift cathode for the substrate in this configuration. An energy distribution like figure 13 is obtained in this configuration. The peak of the ^{55}Fe signal is then at the same position as the MSGC peak in figure 58. This proves that the association of the left peak with the MSGC signal from interactions in the transfer space is valid. The test for the validity of the assumption that the rightmost peak has its origin in drift region interactions is easy, too: While keeping the voltage U_{cath} on the MSGC substrate constant, the GEM potential difference ΔU_{GEM} is increased. The right peak moves towards higher energies, while the MSGC peak remains unchanged as a result. The Argon-escape peak lastly can be identified by its well-known energetic relation to the ^{55}Fe peak.
All important parameters for the desired gain measurements can be obtained from spectra like figure 58. From the COG of the GEM peak the total gain of the GEM+MSGC detector module can be calculated. The same is possible for the MSGC part of the module from the MSGC peak. The ratio of these two values yields the amplification of the GEM. The results will be presented in section 5.1. For a discussion of the errors, see section 4.2.3.

4.1.4 Experimental setup

The description of the laboratory experiments is not complete without the gas and HV systems used to provide a stable environment for the detector modules.

The gas system, whose circuit is shown in appendix I, provides a computer-controlled pressure regulation with a precision of 1±0.1mbar **[55][56]**. The system contains several filters to clean the counting gas from pollutants, like microscopic dust, steam or oxygen.
The HV power supply is a computer controlled stabilised 40-channel system **[57]**. While the power system is equipped with a current measuring system, its poor resolution of only 100nA was not sufficient for the demands of the experiments carried out. All HV lines were consequently monitored by CUMOs whenever possible **[53]**. These devices provide a current resolution of up to 100pA.

4.2 Multi-channel measurements

To overcome the limited detector area in the PreShape32 readout, its successor has been equipped with a multiplexing unit to allow the digitalisation of multiple strips of the substrate with a single FADC. The chip, called *PreMux128*, was additionally equipped with a double correlated sampling (DCS) circuit **[50]**. The frontend chip is based on the PreShape32's amplifier and shaper with the addition of the DCS and multiplexing unit. Each PreMux128 has 128 channels; the chips can be daisy chained. This results in the possibility to read out a whole substrate of 512 strips with only four PreMux128 and a single FADC.

4.2.1 Double correlated sampling and multiplexing

Each PreMux128 chip consists of four PreShape32 units (on die), a DCS circuit for each channel and a multiplexing unit. The pre-amplifying and shaping part of the chip (figure 59 a) is identical to the PreShape32 – only the buffer now adapts the output signal to the DCS input on the chip (figure 59 b). The 'switches' S1 and S2 are closed during sampling. Since their time constant is small compared to those of the pre-amplifier and shaping stage, the voltage on C1 and C2 closely follows the buffer output (figure 59 c + d). When a particle traverses the detector module, S1 and S2 are opened and the stored voltages on C1 and C2 are read out by a differential amplifier. As can be seen from figure 59 e + f, S1 is the voltage corresponding to 'no signal' and S2 is the voltage belonging to the signal's amplitude. Two different sampling modes are foreseen: Figure 59 e) shows the so-called 'collider mode'. The signal's baseline is sampled just before the pulse generated by the incident particle in this scenario. This has the advantage, that the position of the amplitude in time is well known – it is determined by the time constant of the shaper. Additional advantages are the small delay between the two samples and the automatic correction for event-to-event fluctuations of the baseline.
Since the collider-mode requires a trigger signal before the particle even reaches the detector module, this operation is extremely difficult to establish in a test beam experiment **[15]**. Throughout the measurements carried out for this thesis, the so-called 'dummy mode', which is depicted in figure 59 f), has been used. C1 is fixed at ground potential for this type of operation.

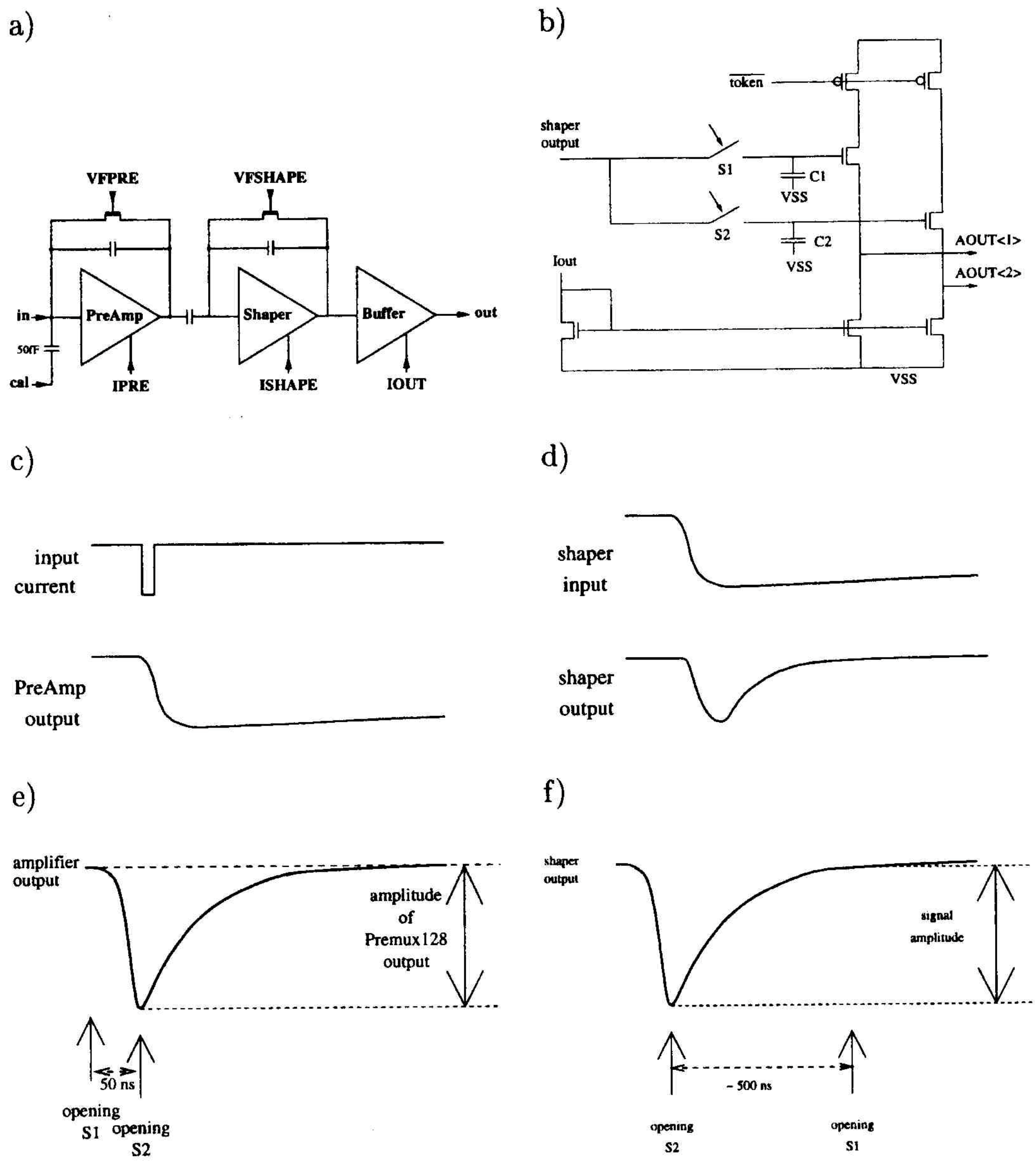

Figure 59 - Working principle of the PreMux128 chip: The amplification and shaping part is the same as for the PreShape32 (a). After the buffer section, double correlated sampling takes place (b). Amplifier response and shaping is sketched in (c) and (d). The DCS modes are shown in (e) and (f).

This has the advantage, that the baseline is sampled after the signal. The position of the signal's amplitude in time is not known for this mode of operation. It has to be found by varying the delay between S1 and S2, until the difference between the two voltages (and therefore the output signal after the DCS' differential amplifier) becomes maximal. This is done by varying the delay between the trigger signal and the sampling of S2. This mode of operation requires a trigger independent from the detector module and is usually provided by scintillators. The transition time of the photomultipliers used with the scintillators is small compared to the delay caused by a GEM+MSGC. The moment when S2 has to be opened is dependent on the detector module only. The exact timing is dependent on the field configuration of the GEM+MSGC, and has to be measured individually for all settings. These measurements are called *delay curves*. Figure 60 shows measurements of GEM6 for different field configurations.

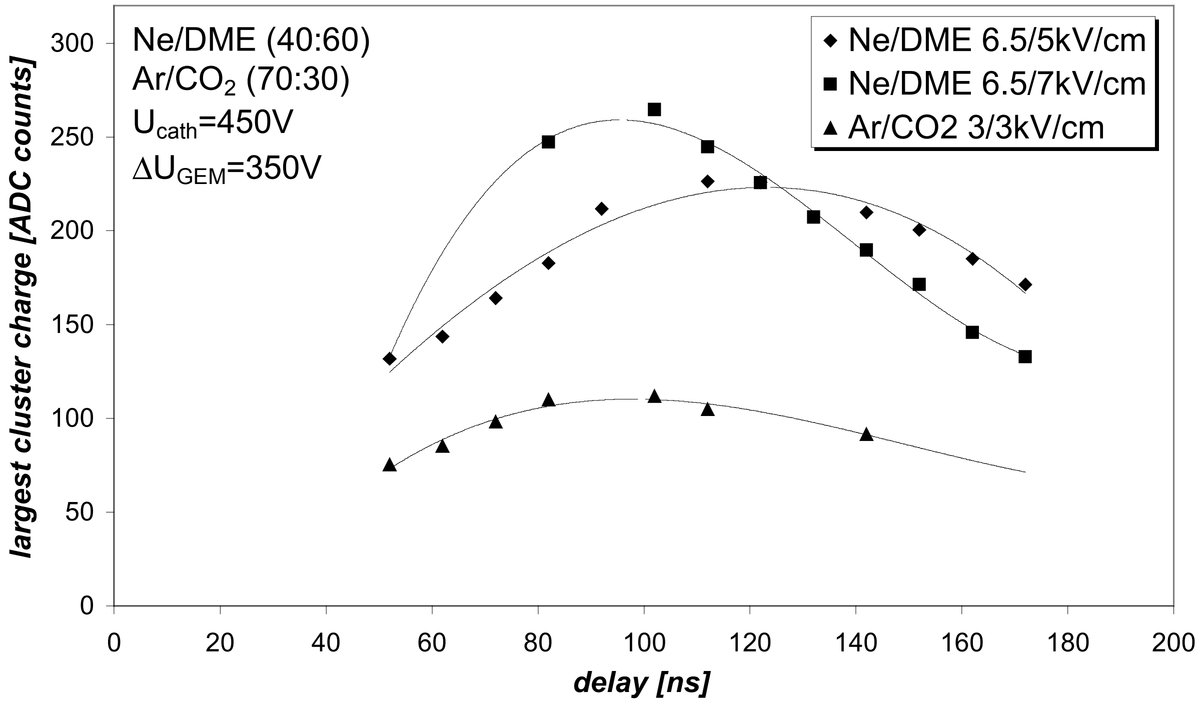

Figure 60 - Delay curves for different field configurations with GEM6. The measurements have been taken in the X5 test beam (see section 4.3 for details). The time scale is relative to the trigger.

The maxima for the Ne/DME measurements can be seen. The shape of the curves is similar to the PreShape32 signal shown in figure 54 – by varying the delay between trigger and the moment of digitalisation, one effectively digitises the shaper output of the PreMux128 and can make the analogue part of the signal visible. The rising edge of the curve has a time constant of $\approx$ 50ns which matches the PreShape32's. The effect of different field configurations can also be seen: The curve for the smaller drift field (5kV/cm) reaches its maximum later. This is caused by the reduced drift velocity. It can be noticed, that the width of the curve remains largely the same. This is different for a reduced transfer field: The delay curve for Ar/CO_2 shows a significantly broader curve due to the small transfer field of only 3kV/cm. This is caused by the increased diffusion in the transfer region. The reason for the 'early' maximum, even when operated at a drift field of only 3kV/cm, is the increased drift velocity of this gas mixture.

The signals of all 128 channels are multiplexed to a single line. This results in a single voltage value for each strip connected to the PreMux128. It is possible to read out a whole detector module with only one FADC channel when daisy chaining the chips. The information about the channel's signal development in time, as present in the PreShape32 readout, is lost for the benefit of multi-channel digitalisation. The FADC is synchronised to the PreMux128's multiplexer unit: Each memory position corresponds to the signal value of one strip that way.

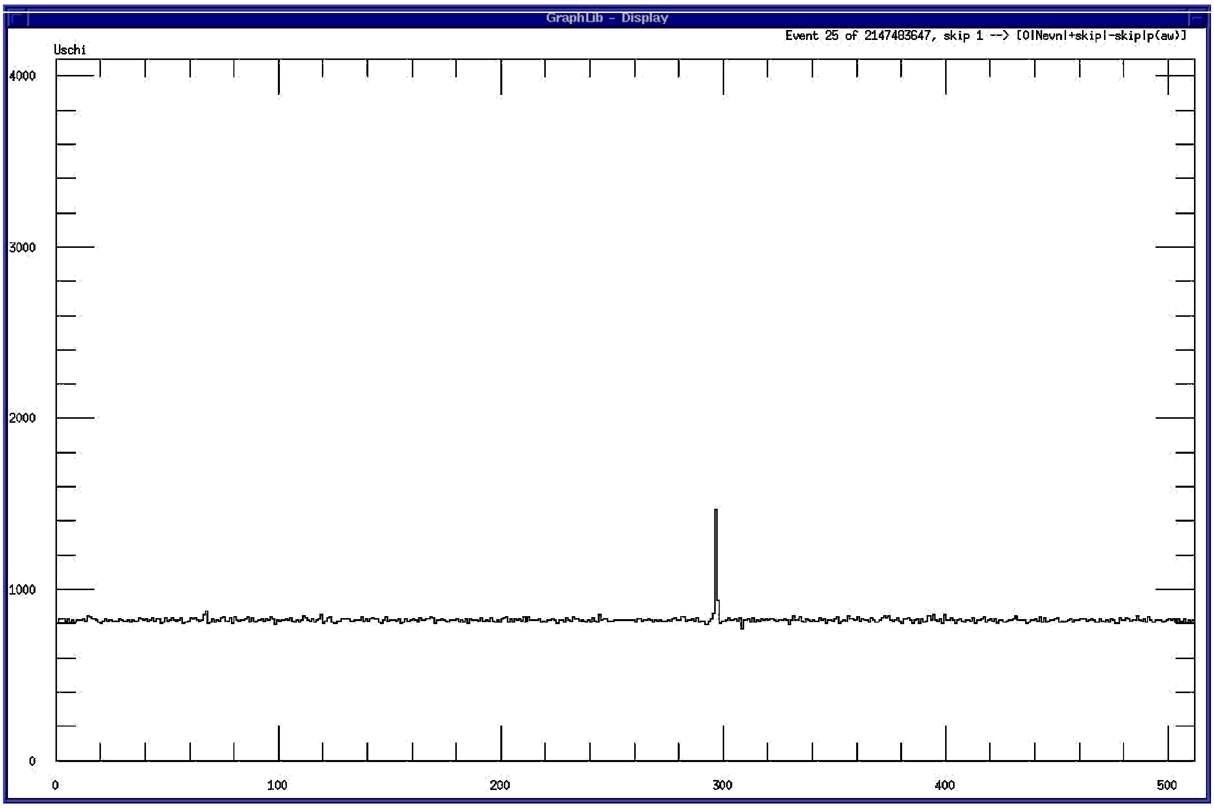

Figure 61 - The multiplexer output for a GEM+MSGC (four PreMux128 daisy-chained). The abscissa is in FADC counts and the ordinate is in strips/channels.

Figure 61 shows the resulting output of four daisy-chained PreMux128 chips: A signal on two consecutive strips can be seen while all other channels are on their baseline values.

4.2.2 Data acquisition

As mentioned in the section before, the PreMux128 readout has to be triggered externally. This requires a different logic than for the PreShape32 measurements. A coincidence of two scintillators is used as trigger. This signal is connected to the FADCs and sequencer module by a programmable delay, which allows to measure the delay curve and to set the optimal value for S2. The sequencer is a programmable pulse generator, which generates the rather complex timing information for driving the PreMux128 chips. Since detailed descriptions of the readout, along with a list of all modules used for the setup, are already available, only a short explanation of the data taking process will be given here **[15][35][47]**.

Figure 62 shows the setup for the PreMux128 DAQ. The two different GEM+MSGC modules, the CMS forward prototype module and an MS-9 type detector, can be seen at the bottom. The forward detector module is interfaced to the DAQ by a so-called ‘service board module’ (SBM) **[58]**. This contains all the line drivers to connect the PreMux128 chips to the DAQ modules, and some auxiliary components not used in this setup. The MS-9 type modules are connected to the readout via a motherboard. The central piece of hardware is the so-called ‘adapterboard’. This is a device specially developed for PreMux128 readout **[59]**. It contains the trigger logic, drivers for the calibration inputs of the PreMux128, a power supply for motherboards and SBMs (via an adapter, see figure 62), and a fan-out for the S1 signal.

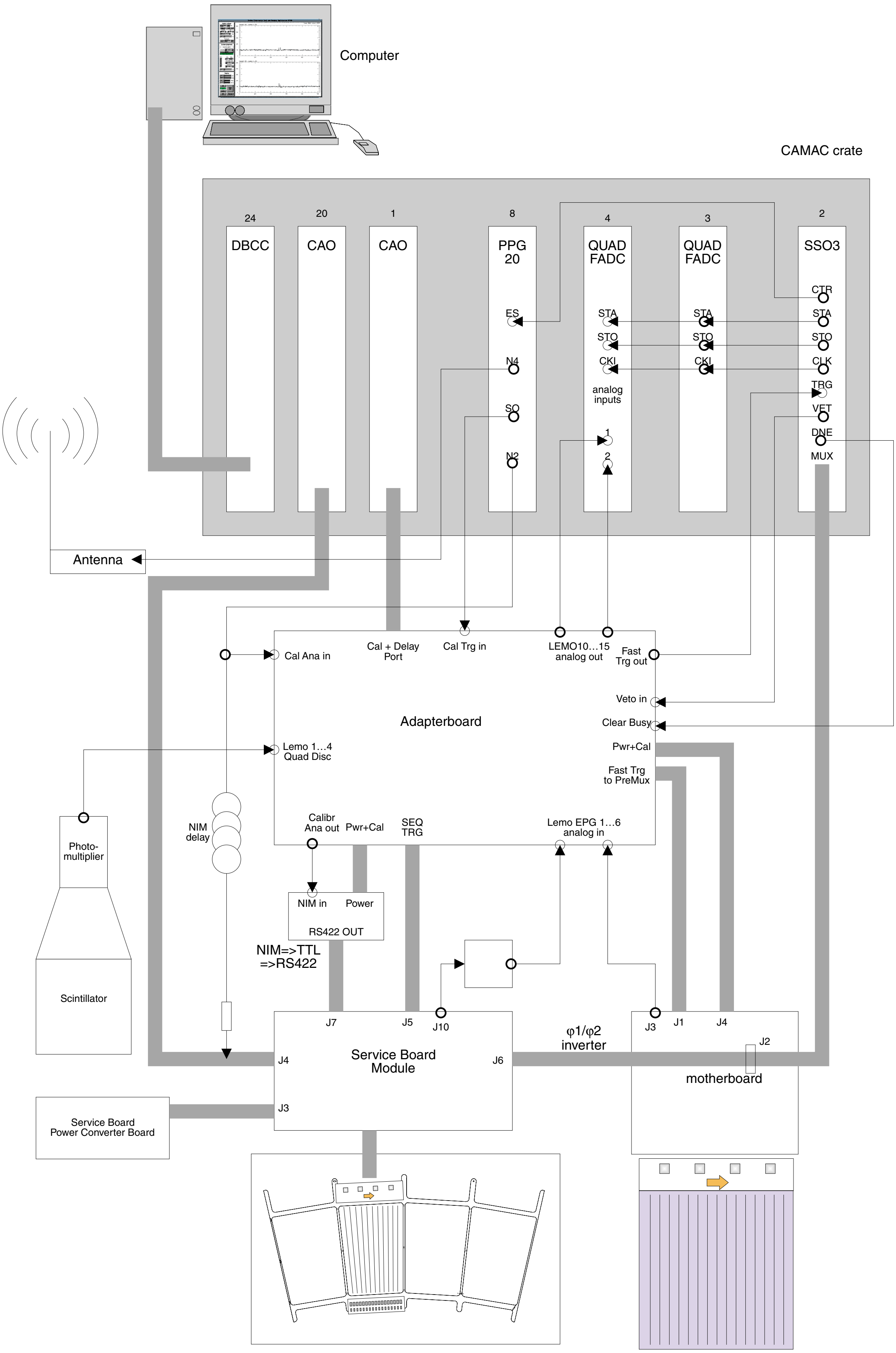

Figure 62 - Data acquisition system for PreMux128 readout.

The DAQ also includes a programmable pulse generator, which is used for generating random triggers (for testing purposes without source), calibration signals, and test pulses which are fed to the antenna. This tool is used to couple a signal inductively to the detector module for testing purposes or noise measurements.
A dedicated software package has been developed for the PreMux128 DAQ: *PreMux128 Electronic Test and Readout Application* (PETRA) **[47]**. This automates many of the tasks involved with PreMux128 detector operation, such as the measurement of delay curves via the programmable delay of the adapterboard, and tools for finding broken strips after assembly or irradiation tests.

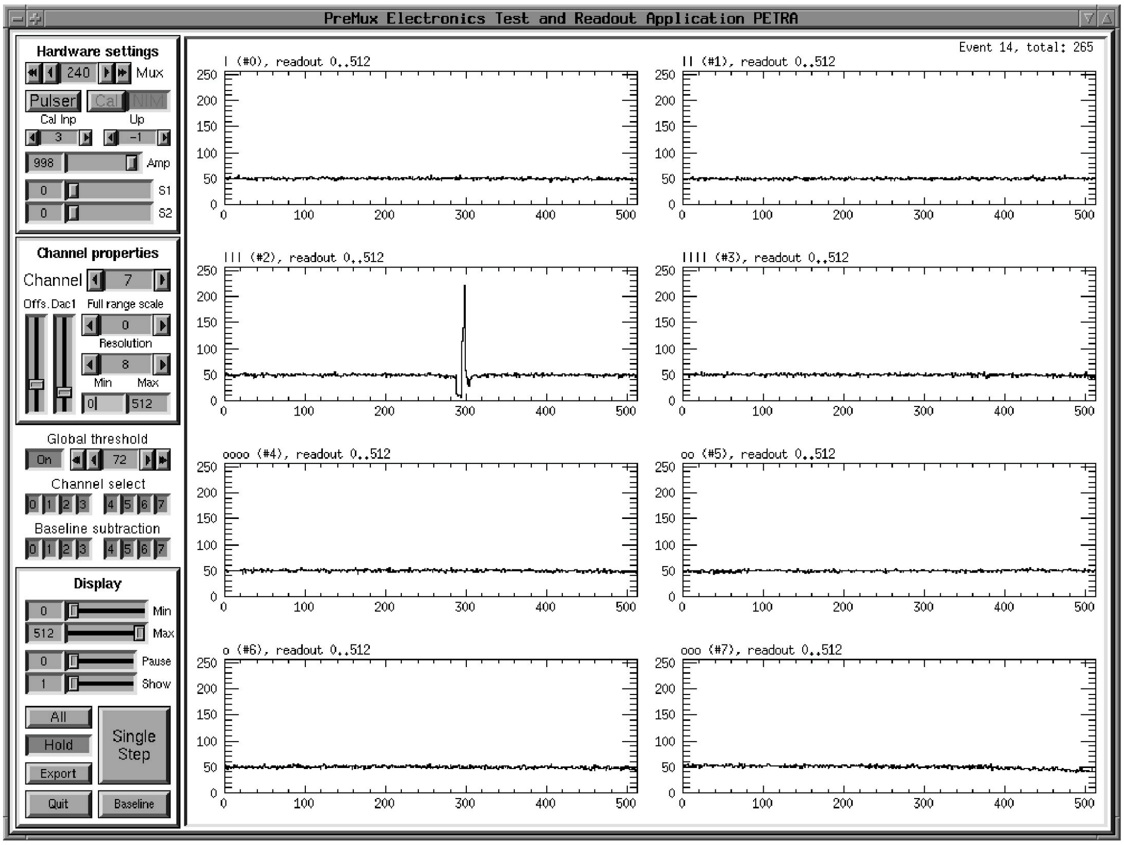

Figure 63 - Screenshot from PETRA. The data from eight substrates is shown. A large signal can be seen on module #2. The sidebar on the left shows several buttons and sliders to control the DAQ system and the displayed data.

The on-line display of PETRA can be seen in figure 63. The data of eight substrates is shown in this example. One detector module, number two, shows a large signal. Several buttons and sliders can be seen on the left hand side. These are used to control the behaviour of the DAQ system and the displayed data. The buttons on the lower left start and stop the data taking process. More complex operations, like the automatic measurements of delay curves, are controlled from a command line interface. The data is written in the same format as for the PreShape32.
PETRA does some of the analysis' steps described in the next section already on-line. These are mainly pedestal and common mode corrections, as well as simple noise measurements. Especially the noise analysis is mandatory for the broken strip detection mentioned before: The electronic noise of a channel is defined by the thermic noise of the PreMux128 chip and the external capacitance of the strip. The latter makes up for the largest part of the noise. A broken strip has a reduced length compared to the other strips. This results in a smaller external capacitance, and therefore a decreased noise in that channel. This can be seen more

clearly if two consecutive measurements are carried out: One with HV on, and one without powering the detector module. PETRA has the capability to calculate the difference of those two measurements' noise. The result of such a measurement can be seen in figure 64: The noise for all 512 channels of a substrate is shown. Five strips with a significantly reduced noise can be seen – those strips are broken. It is possible to find shorts between neighbouring anodes and cathodes, too: If a short circuit is occurring, the channel draws current because the HV supply is now grounded through the PreMux128 chip. This effect can be seen even better than a broken strip, since the baseline is drawn to zero in this case.

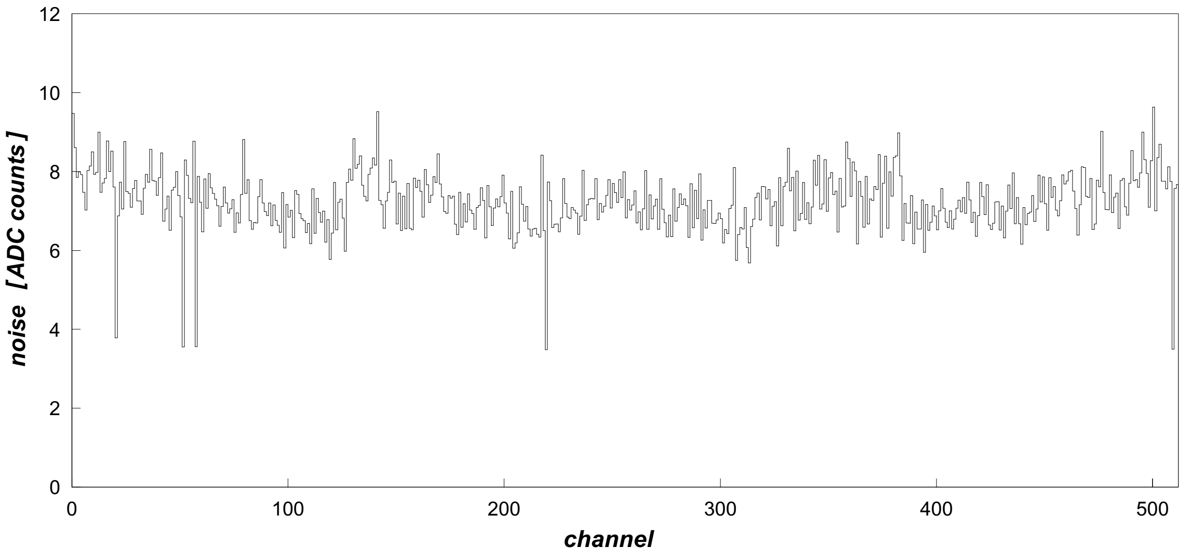

Figure 64 - The noise for every channel of a substrate. Five broken strips can be seen.

4.2.3 Analysis software

The analysis steps required for PreMux128 data are different from the PreShape32' signals. A peak finding is no longer necessary, since the output of the multiplexing amplifier directly yields the signals' amplitudes. The first task is the finding of a baseline and threshold to decide if a given signal height corresponds to a particle passing through the detector module or not. This is called *signal detection*. The next step is the cluster finding. Finally, the signal-to-noise ratio (SNR) for a given cluster is calculated.

The first 100 events of each measurement are taken and the average pulseheight s_i^{prel} for each of the i strips, together with the accompanying standard deviations σ_i^{prel} are calculated. This method yields a preliminary baseline and noise value for each channel. Possible signals on the strips are not detected by this method and increase the baseline value and the noise for that particular strip. The real baseline and noise values are calculated from the first 500 events of a measurement in a second step: All raw data values r_i are first reduced by the preliminary baseline:

$$d_i = | r_i - s_i^{prel} |$$

If in any event j this difference d_i is larger than $n_{cut} \cdot \sigma_i^{prel}$, this event is excluded from the common mode calculation for that i-th strip.

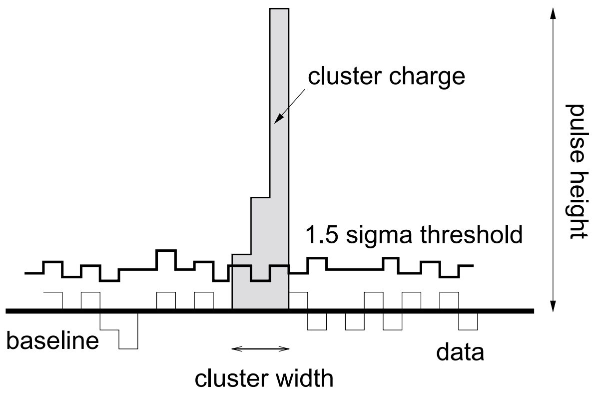

Figure 65 - Sketch showing the different parameters used in the cluster finder.

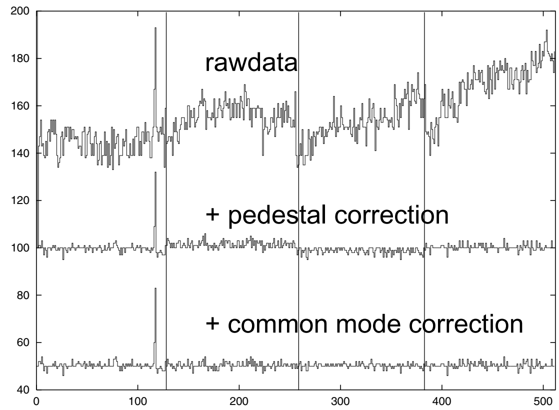

Figure 66 - The raw data (top) after correcting for pedestals (middle) and common mode (bottom).

n_{cut} is a threshold used to distinguish between signals and electronic noise fluctuations. Figure 65 shows its meaning. It was set to $n_{\text{cut}} = 1.5$ for all analyses described in this thesis. For all N events, the average pedestal value p_i is calculated for all i strips.

$$p_i = \frac{1}{N}\sum_{j=1}^{N} r_i$$

A signal s_i on the i-th strip could now be calculated by $s_i = | r_i - p_i |$. The effect on the raw data can be seen in figure 66. However, there are other effects which have to be taken care of: The baseline values for all 128 strips connected to a chip can change from event to event due to coupling of external noise to the PreMux128. This fluctuation is called *common mode* and can be corrected on a chip-by-chip basis. To accomplish this task, the raw data corrected by the pedestal values is averaged over the 128 channels of one chip. This yields the common mode correction c_k, which is unique for each of the k chips and every event:

$$c_k = \frac{1}{128}\sum_{i=1}^{128} s_i$$

The signal on the i-th strip now becomes $s_i = | r_i - p_i - c_k |$; the result can be seen in figure 66. The last correction to be applied takes care of the so-called *HV cross talk*. This effect describes a phenomenon generated by the HV supply. If a signal is measured on one or more strips, a current is drawn because the power supply must re-supply the charges to the cathodes. For large signals, the electrons are not delivered fast enough. This reduces the baseline for the affected HV group, since the potential is drawn to ground level. The calculation of the signal's amplitude gets wrong by this effect. A baseline restoration algorithm is therefore applied to the data: All G strips of the HV group g passing the $d_i > n_{\text{cut}} \cdot \sigma_i^{\text{prel}}$ condition are averaged. This value h_g is then added to the strips' signals s_i:[36]

$$h_g = \frac{1}{G}\sum_{i=1}^{G} s_i$$

In the last step, the final signal s_i for all i strips can be calculated for the N events:

$$s_i = r_i - p_i - c_k + h_g \tag{23}$$

[36] The two outermost strips are weighted by a factor of 0.5, because they contribute to two HV groups.

These values are stored in a histogram for each strip. The maximum of the histogram is determined after all N events have been processed. Starting from the maximum, the number of entries in each interval of the distribution is summed up consecutively to the left and right until 68.27% of the histogram's area are covered. Assuming a standard distribution, the summed up interval corresponds to 2σ. The difference between the left and right border found that way yields the noise σ_i for each channel when divided by two.
Now all events are processed. Each strip i showing a signal S_i, which passes the condition $S_i > n_{cut} \cdot \sigma_i$, is flagged as a candidate for a possible cluster. The cluster algorithm first selects the strip with the highest signal S_i. Starting from this position i, it is searched for the first position $i \pm n$ when S_i drops below $n_{cut} \cdot \sigma_i$. Since it is possible that the cluster's border found that way is a broken strip (see section 4.2.2), the algorithm always investigates the $(n+1)$-th strip. If this strip fulfils the $s_i > n_{cut} \cdot \sigma_i$ condition, it is added to the cluster. The total charge and cluster width are calculated that way. The parameters of the one with the highest cluster charge are stored.
It is now possible to calculate the SNR of the cluster: The total charge of the cluster of width w is divided by the quadratic mean of the strips' noise:

$$SNR = \frac{\sum_w s_i}{\sqrt{\frac{\sum_w \sigma_i^2}{w}}} = \frac{\sum_w s_i}{\sqrt{\sum_w \sigma_i^2}} \sqrt{w} \tag{24}$$

In case of MIPs, the total charge of the clusters follows the Landau distribution as discussed in section 2.1.1.1. Figure 67 shows such a spectrum.

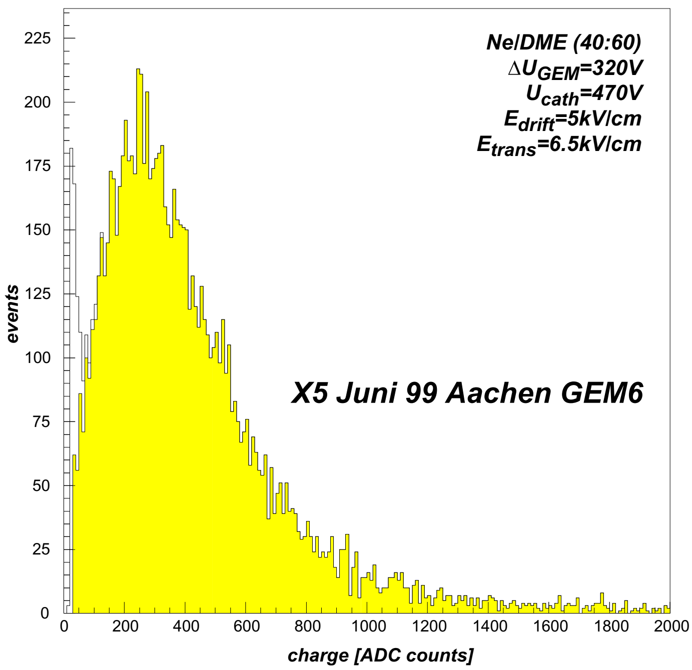

Figure 67 - Landau distribution for MIPs. The spectrum has been taken with GEM6 in the June 1999 test beam experiment at the X5B facility. The energy loss distribution is marked in grey; on the left, some 'accidental' signals not rejected by the cluster finder can be seen.

Since the parameter n_{cut} is kept as low as possible to reject only the noise, the algorithm always detects some 'signals' which later turn out to be only statistical fluctuations. This can be seen in figure 67, where a second peak on the left can be seen besides the Landau spectrum. An additional cut on the clusters' charge c_{cut} is introduced to exclude these signals from further analysis. It has been set to $c_{cut} = 4 \cdot \sigma_i$ for all analyses carried out in this thesis. This cut is applied after a possible candidate for a signal has been detected and on the highest strip of the cluster only[37]. It effectively rejects the accidental signals as can be seen in figure 67. A Landau function is fitted to the distribution acquired that way. The most probable value of the function – its maximum – is then taken as the input cluster charge for the SNR calculation. The error of this measurement is difficult to define: There are contributions from systematic errors of the cluster finder, the noise measurement and from the fitting of the Landau distribution to the data. The error of the noise measurement is of statistical nature and given by the number of events used for its determination. For the 500 events used for the calculation of the noise, it is 4,5%. The systematic error of the cluster algorithm is given by the amount of falsely identified signals. Assuming a Gaussian distribution for the possibility for a strip to exceed the n_{cut} threshold, one can compute this error:

$$\int_{n_{cut}}^{\infty} \frac{1}{\sqrt{2\pi}} \frac{1}{\sigma} \, e^{\left(-\frac{x^2}{2\sigma^2}\right)} \, dx \cong 0.01 \tag{25}$$

This error of 1% is negligible compared to the statistical error. In reality, this error is even smaller, since it has to be convoluted with the systematic error for the finding of the seed strip. This is dominated by the cut c_{cut}, and its computation by equation (25) yields an error of only 0.3%. The error on the Landau fit is small, mostly well below 2%, so it can be neglected, too. The overall error on the SNR measurements is therefore of the order of 5%. The diagrams shown in chapter 5 are given without error bars, because they are too small to be distinguishable from the symbols of the data points.

4.2.4 Experiments in the laboratory

The main aim of the PreMux128 based detector modules is their use in test beam experiments. However, there are several reasons to do lab measurements: The function of the detector modules has to be tested. All sorts of relative gain measurements can be carried out by using a ^{90}Sr source. Absolute measurements, like those done with ^{55}Fe for the PreShape32 based detector modules, are not possible. Those would require a well-known ionisation energy. This can not be achieved by using a β-source like ^{90}Sr due to the continuos energy spectrum. The use of a γ-source like ^{55}Fe is not possible, since an external trigger is required by the PreMux128. The addition of scintillators, read out by photomultipliers, is therefore necessary. A single scintillator of 10x10cm^2 size was used. This allowed to trigger the whole area of the MS-9 type detector modules, or one substrate of the forward module. The thickness was 1cm. The use of a coincidence with a second thin scintillator would have been desirable, but the construction of a thin plate of that size was not possible in due time. Efficiency measurements carried out with that setup are therefore only valid for the position of the efficiency plateau, but not for its absolute value.
The remaining part of the laboratory setup, e.g. gas and HV system, is identical to the one already described in section 4.1.4.

[37] By applying c_{cut} on the highest strip only, one rejects small signals. If the cluster is generated by statistically increased noise, there is a high probability that it consists of one strip only. By applying the cut, this cluster is rejected. On the other hand, if there is a small cluster just exceeding the threshold of c_{cut}, only the highest strip has to pass the condition of $4 \cdot \sigma_i$ – all the other strips have to fulfil the n_{cut} criterion only. This takes care of not throwing away too many strips of the cluster, and generating an error on the cluster charge that way.

4.3 Experiments with low intensity test beams

Test beam experiments provide an excellent opportunity to measure the efficiency and spatial resolution of detector modules. All measurements described in this section were carried out in the CMS tracker test facility at CERN's SPS X5B area **[60][61]**. Two experiments were carried out in September 1998 and June 1999. Besides a small difference in the beam composition, the experimental setups were identical. No difference between the two test beams will therefore be made.

4.3.1 Experimental setup

The X5B area at CERN is equipped with an optical bench. This allows aligned mounting of detector modules with respect to the beam axis. A beam telescope made up of four double planes[38] of silicon strip detectors with a spatial resolution of 5-10µm is provided **[62]**. The SPS provides a pion beam. However, all measurements were carried out using only the muons from the pion decay. The beam was operated in the 'tertiary mode' in September 1998, and in the 'secondary mode' in June 1999. The latter one uses only one target of the test facility, while two are used for the other operation mode. With the exception of an increased particle rate for the secondary mode, a muon energy of 70-120GeV/c^2 is achieved in both cases. The particle rate can be as high as 10^6Hz/cm^2, but only fluxes up to some 10^2Hz/cm^2 have been used. The reason is the tremendous amount of data which has to be stored due to the very high number of channels present in a test beam experiment.
A scintillator coincidence is mounted in front of the bench and the telescope. Trigger areas of 2x2cm^2 and 6x6cm^2 are available. The small trigger is adjusted to the active area of the silicon detectors; it was therefore used for all efficiency and spatial resolution measurements, which involve the telescope's signals. For other measurements, like the transparency scans presented in section 5.3, mostly the larger trigger was used.
The HV supply is the same as in the lab setup. The gas system is a simple open circuit: The bottles containing the different gases are connected to flowmeters, whose settings control the mixture. After flushing the detectors, the gas is driven through an exhaust line and dumped. Measurements both with Ne/DME (40:60) and Ar/CO_2 (70:30) have been carried out.

4.3.2 Data acquisition

The DAQ for the X5B test area works the same as the one described in section 4.2.2 **[64]**. However, due to the enormous amount of channels[39] the realisation is a more complex one. Different computers are used for running the sequencer and FADCs, and for pre-processing

[38] A 'double plane' describes two silicon strip modules which are mounted in a way that each module's strips are perpendicular to the other. Every double plane therefore yields a two-dimensional point in space.
[39] A typical detector module makes up for 512 channels; forward prototypes usually need at least 1024 channels. The beam telescope alone makes up for 3072 channels. With an average number of 10 modules per test beam experiment, roughly 10.000 channels have to be read out by the DAQ in the mean. This computes to 10kB of data per event (not taking into account the overhead generated by the storage system), which is stored with 100Hz. This enormous amount of 1MB/s has to be taken care of.

and storage of the data. Figure 68 shows the different functional blocks. The 'hold unit' is the part of the DAQ which corresponds to the programmable delay on the adapterboard in the lab setups. Since both silicon and gaseous detector modules are operated together in the test beam experiments, a more sophisticated trigger setup is required. This is caused by the very different delays those detectors need for S2. Silicon detectors are much faster and therefore need shorter total delays. What can be seen from figure 68, too, is the fact that data is no longer stored locally, but transferred by the local area network to CERN's central data recording facility (CDR). There the storage is done on tape in a database system.

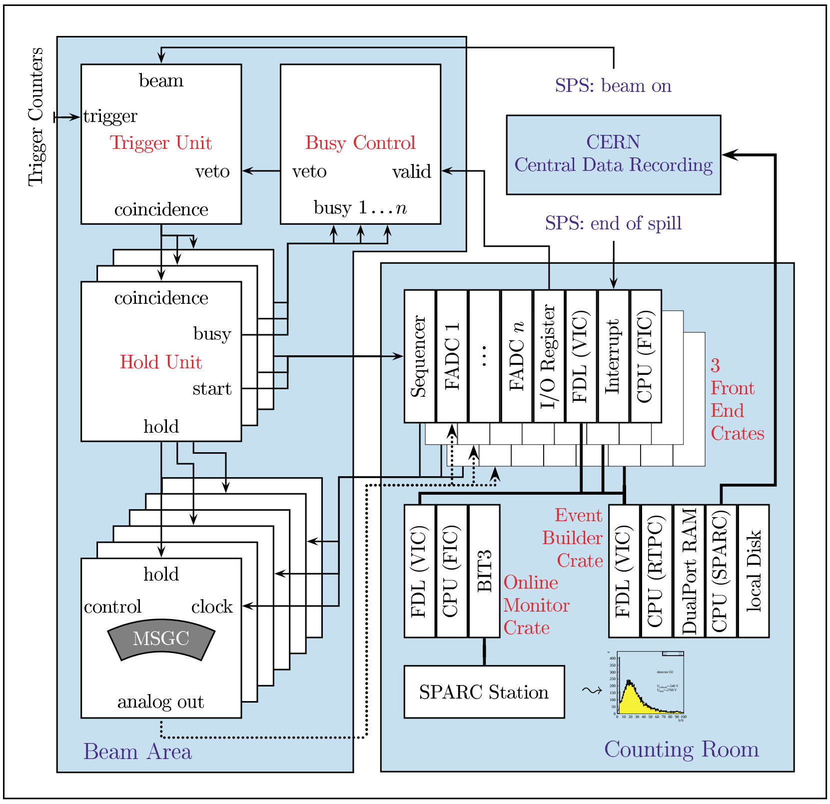

Figure 68 - The PreMux128 data acquisition system at the X5B test facility **[63]**.

4.3.3 Analysis software

The software is the same as discussed in section 4.2.3. This is simply due to the fact that the same data is analysed. The only modification to IRIS made for test beam experiments is an interface to the CDR database system[40].

Additional software is necessary to accomplish the task of measuring spatial resolution and efficiency. The analysis starts with a selection of events which are useful for the intended measurements: The creation of a so-called *reduced runfile* (RRF), which is a subsample of the complete measurement, meeting the conditions of the event selection. The geometrical alignment of the setup, and finally the spatial resolution and efficiency analysis, is done on the RRFs only.

The telescope provided by the X5B setup is used to calculate a particle's trajectory through all the other detectors. Since its spatial resolution is five times higher than that of the

[40] Other modifications include options for batch processing and using the CMS database management system, but these are purely of technical nature.

GEM+MSGC detector modules, a good prediction of the interaction point of the particle with the detector can be made. The silicon strip detectors of the telescope have to be analysed, too, to accomplish this task. This is done with the same algorithms and methods discussed in section 4.2.3.
It is mandatory to know that a particle has passed through the GEM+MSGC for the efficiency measurements. Since the silicon detectors are affected by inefficiencies, too, the event selection condition is to have exactly one hit in each of the telescope's planes. IRIS then generates a RRF including SNR, cluster width and position of the particle interaction for each of the silicon sensors and the GEM+MSGC detector module. This reduced sample of events is processed by another piece of software, called HODO **[65]**.
The analysis of spatial resolution and efficiency can be broken up into four steps: The alignment of the telescope and GEM+MSGC, the so-called 'tracking', which is the calculation of a particle's trajectory through the optical bench by using the information from the silicon sensors, and the calculation of the spatial resolution and efficiency of the gaseous detector module. The so-called 'residuum', which is the difference between the predicted impact point on the GEM+MSGC's plane and the measured one, is calculated and the width of the distribution acquired that way yields the spatial resolution of the detector.

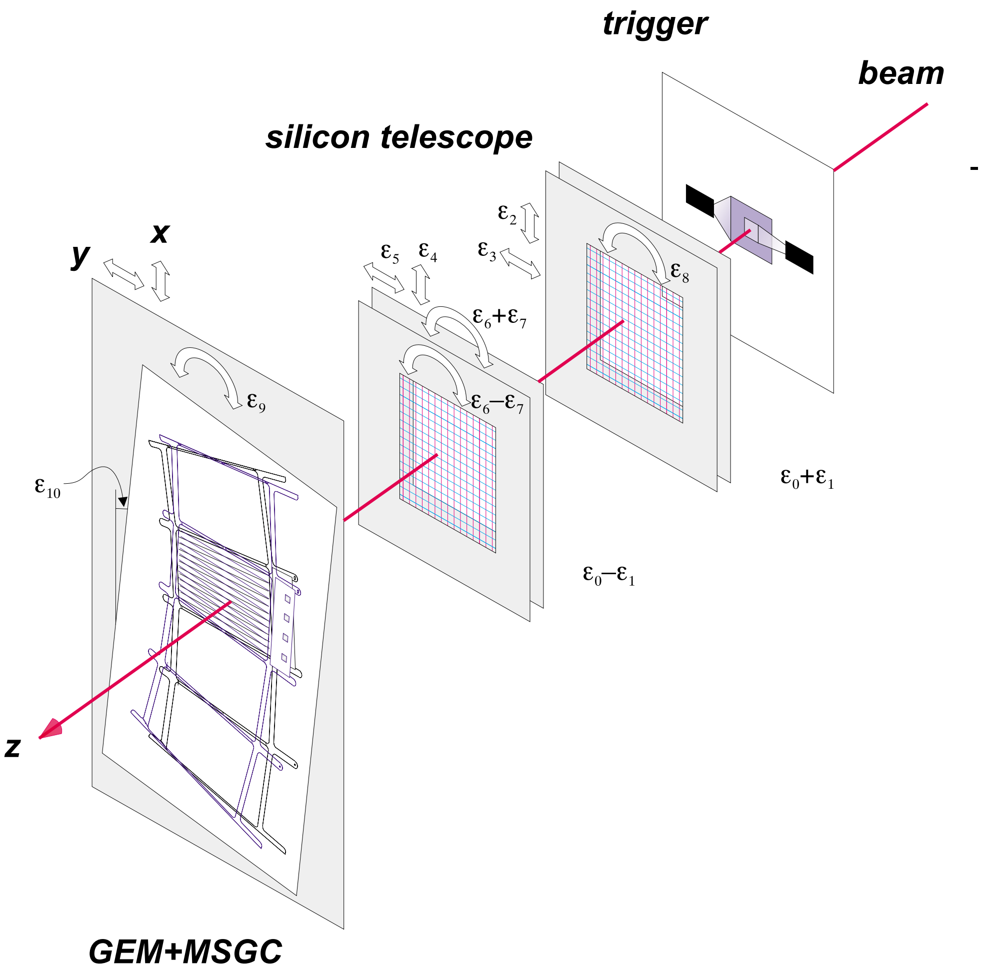

Figure 69 - A schematic of the X5B setup. The definition of the coordinate system can be seen: *z* is along the beam axis, *x* is perpendicular to the strips and *y* is along the anodes.

The first step is the alignment of the detectors: Figure 69 gives an impression of the multitude of free parameters ε_i which have to be taken into account. Each detector module has three degrees of freedom along the axes of the coordinate system as defined in the figure, plus an additional rotational parameter, which describes the angular position of a sensor with respect to the others. The latter one is called the 'tilt' of a detector. The alignment is done by the method of least root mean squares, or '$\chi^2 -$ fit'. An additional complication arises from the vast number of parameters and their dependence on each other. This multi-dimensional optimisation is done by an iterative lattice search algorithm: Since all the parameters have a common optimisation target, they can be varied individually to find local minima for each value. The common value is the spatial resolution of the whole setup. In a first iteration step, one of the parameters ε_i is varied until the spatial resolution is minimised. This is repeated for all ε_i. In a further iteration, the process is repeated until no more variation for the parameters is found. These values are then fixed for the telescope, and are calculated for the GEM+MSGC module in a new iteration. This process has to be performed only once per test beam experiment, if the detectors are not moved. The error on this measurement is given by the covariance matrix of the $\chi^2 -$ fit. Figure 70 shows two examples of the optimisation results on the variation of the *z*-position and tilt angle.

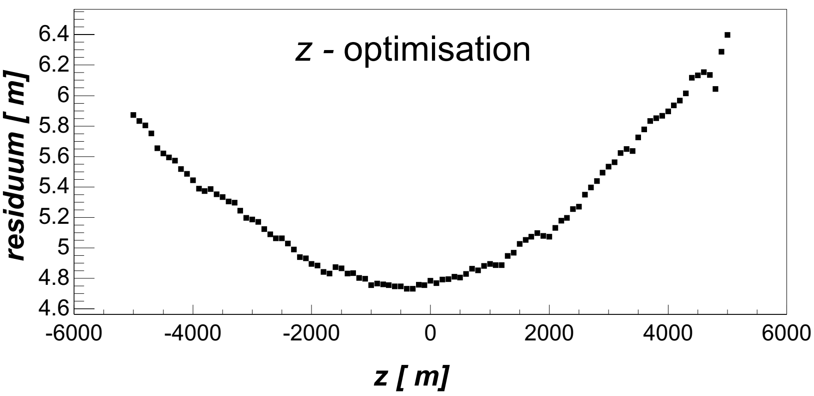

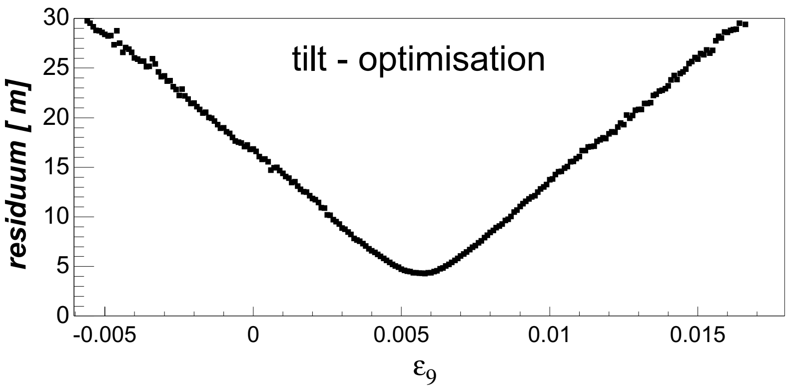

Figure 70 - Results for the variation of the *z*-position and tilt angle ε_9 are given.

After the alignment for all detectors has been done, the spatial resolution for the GEM+MSGC can be measured. A linear regression is carried out in both dimensions of the telescope's double planes for the impact position of the trespassing particle. Assuming that the tilt alignment has been done properly, the two coordinates acquired that way are independent from each other. They yield the impact coordinates at the plane of the GEM+MSGC detector module. The distance from the actual signal's position to the predicted one is measured. Since the MS-9 type GEMs are only sensitive on the particle's position in the *x*-direction, the *y*-position is discarded (it is only needed for the tilt correction).

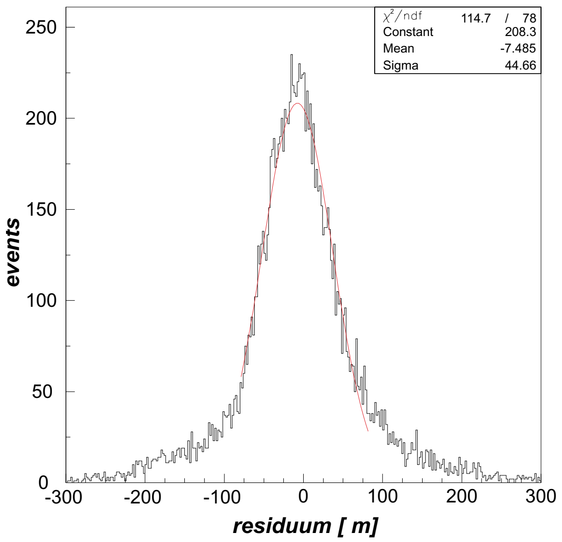

Figure 71 The residual distribution for GEM6, measured in the June1999 test beam experiment. Note the non-Gaussian extensions.

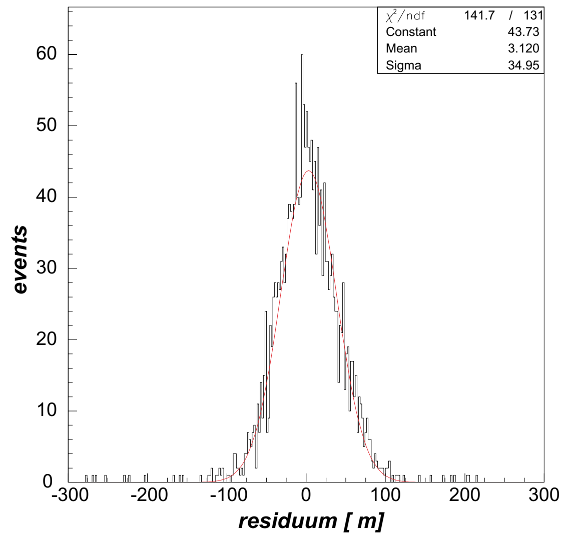

Figure 72 - The distribution assumes a Gaussian shape after selecting only regions without broken strips.

Figure 71 shows the residual distribution for GEM6. The spatial resolution is given by its r.m.s. The measurement has been taken in the June 1999 test beam experiment with Ne/DME (40:60). The applied voltages were $\Delta U_{\mathrm{GEM}} = 350\mathrm{V}$, $U_{\mathrm{cath}} = 450\mathrm{V}$ and the field configuration was $E_{\mathrm{drift}} = 5\mathrm{kV/cm}$, $E_{\mathrm{trans}} = 6.5\mathrm{kV/cm}$. While a reasonable spatial resolution of $< 45\mu\mathrm{m}$ is achieved, there are non-Gaussian extensions to the distribution which degrade this value. These extensions are caused by regions with broken strips. If the charge arriving at the substrate's surface is deposited in a region with one or more broken strips, the cluster charge is not lost, but collected on the strips neighbouring the dead space. This moves the COG off-centre and degrades the spatial resolution. If an additional event selection is performed inside of HODO, which selects only trajectories pointing towards a region of GEM6 without broken strips, a Gaussian distribution with an improved spatial resolution of $\approx 35\mu\mathrm{m}$ is achieved. This is shown in figure 72. Technically this is realised by selecting only tracks which point to a region on the GEM+MSGC module with at least two working anodes to the left and right of the predicted COG.

The selection criterion for working strips is applied for the efficiency measurement, too: From all events selected for the spatial resolution determination, the fraction with a signal in the GEM+MSGC module is divided by the total number of chosen events. This yields the efficiency. The error of this measurement is given by the variance of the inefficiency distribution. The probability p that the detector recorded r signals out of n, and therefore the probability for its inefficiency $q = 1 - p$, is given by the *Bernoulli distribution* **[66]**:

$$f(n,r,p) = \binom{n}{r} p^r q^{n-r} = \frac{n!}{r!\,(n-r)!} p^r q^{n-r} \qquad (26)$$

The distribution given by equation (26) has the expectation value $<r> = n \cdot p$ and the variance $\sigma^2 = n \cdot p \cdot q$. For an efficiency of 98%, which is typically reached with the detectors discussed in this thesis, the error on the measurement can be calculated:

$$\sigma = \sqrt{n \cdot p \cdot q} = \sqrt{100 \cdot 0.98 \cdot 0.02} = 1.4$$

The efficiency within its error can never exceed 100%, as it should be. The error on the efficiency measurement is in the order of magnitude of 1-2%, and has been omitted in the diagrams in section 5.3, because the error bars are smaller than the symbols for the data points.
With the information on the efficiency and the corresponding SNR, the so-called *working point* can be determined. It is defined as the voltage setting where the detector module reaches the efficiency plateau. Simulations show that an efficiency of 98% is needed to ensure proper operation of the CMS detector **[6]**.

4.4 High intensity test beam measurements

To study the effects of high intensity hadronic interactions on the detector modules, and to see if the limitations discussed in section 2.2.3 could be overcome, an experiment at the Paul-Scherrer Institut (PSI) in Villigen (CH) has been carried out in April 1999.
Pions of 350MeV/c momentum are passing through the detectors with a rate up to 10^4Hz/mm^2 in the test facility 'πM1'. The true rate for a given position along the beam axis is lower due to dispersion of the beam. An average rate of $3 \cdot 10^3$Hz/mm^2 can be assumed for the position of the detectors discussed in this section.
The goal of the measurements was to study the stability of the GEM+MSGC modules at voltages corresponding to the working point as defined by the measurements discussed in the previous section.

4.4.1 Experimental setup

The setup in the πM1 area is very similar to the one in X5B: The detectors are mounted on an optical bench with a pair of scintillators in front. The difference is the missing of a telescope. Measurements of spatial resolution and efficiency are therefore more difficult to acquire than in the X5B area. The PSI setup makes use of an additional scintillator couple at the downstream end of the bench. It is used to measure the difference in rate with respect to the upstream scintillators. A linear extrapolation to the expected particle rate at the location of the individual detectors on the bench can be done from this measurement.
The same open circuit gas system as in the CERN test beam experiments is used. Only measurements with Ne/DME (40:60) were carried out this time.

4.4.2 Data acquisition

Since PreMux128 frontend chips were used in this test beam, too, the DAQ system does not significantly differ from the ones already discussed.

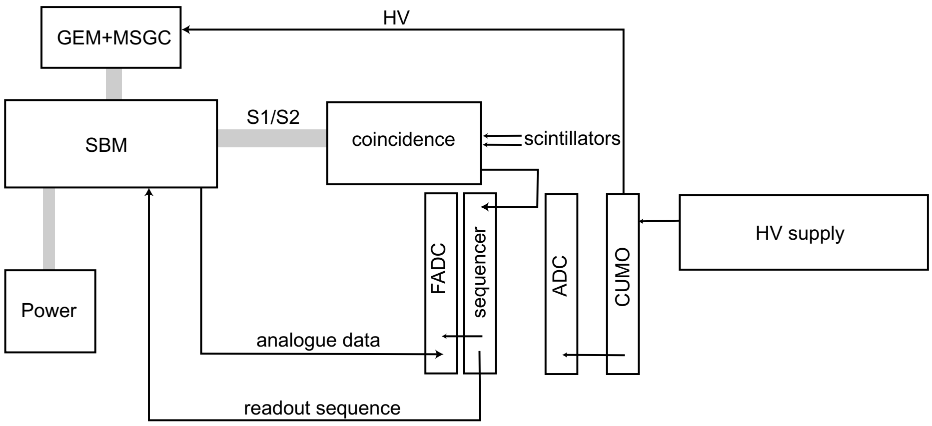

Figure 73 - The PreMux128 data acquisition system at the πM1 test facility.

If figure 73 is compared to figure 68, the same functional blocks can be identified. Something new in the DAQ is the readout of the current monitors connected to the different HV supply lines of the detector modules. The signals of the CUMOs are sampled every 2ms. To reduce the amount of data written to disk, only very few data from the GEM+MSGCs' strips is stored, because the paramount interest in this test beam was the analysis of the sparking behaviour.

4.4.3 Analysis Software

The same algorithms as discussed in section 4.2.3 have been used for the analysis of the GEM+MSGC detector data. The IRIS software was modified to be capable of handling the data from the current monitors **[67]**.
The monitoring of the currents on the HV lines of a GEM+MSGC has the goal of identifying discharges, and if possible, their origin and effect on strip damage. Even when in stable operational conditions, a detector module draws a current. This is caused by the simple necessity of replacing charge to the cathodes. The result is a rate- and gain-dependent current. It can have a very small value, e.g. for the lab experiments with ^{90}Sr and ^{55}Fe sources, where some nA were never exceeded[41], or rather high values, if it comes to high intensity experiments as discussed in this section. When operating at rates of some 10^3Hz/mm^2 and a gain of 2000-3000, typical values of 100-150nA are drawn by the substrate.

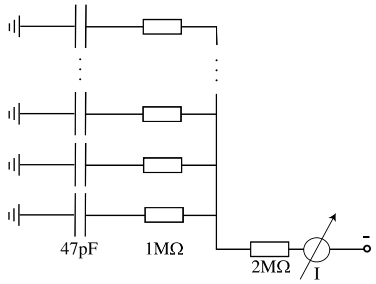

Figure 74 - A schematic representation of an MSGC substrate. The HV groups can be considered as coupled capacitances.

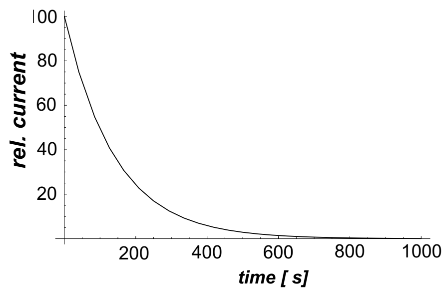

Figure 75 - Simulated charging behaviour of a RC-circuit as sketched in figure 74.

[41] If the detector module is operated at very high gains, e.g. 10.000, even in the lab considerable currents can be drawn. But these are no conditions one would refer to as 'stable'...

One can think of an MSGC substrate as a system of coupled capacitances. Its value is defined by the number of strips grouped within a HV group, and their pitch, width and length. A simulation carried out for the MS-9 type substrate with MAXWELL yields 47pF per HV group **[68]**. The charge stored in this group can be calculated for any given voltage U_{cath}. For U_{cath} = 450V one computes 21nC per group, to give an example. Since the smallest element in a GEM+MSGC detector module which can discharge is a HV group, one expects a charge distribution around that value. Results will be shown in section 5.6. Additional sources of discharges are obviously the GEM foil itself, which can be thought of a parallel plate capacitor, and the drift and transfer regions.
To get the charge deposited in the detector by a discharge, one has to analyse the signals from the current monitors. Figure 76 shows such an event:

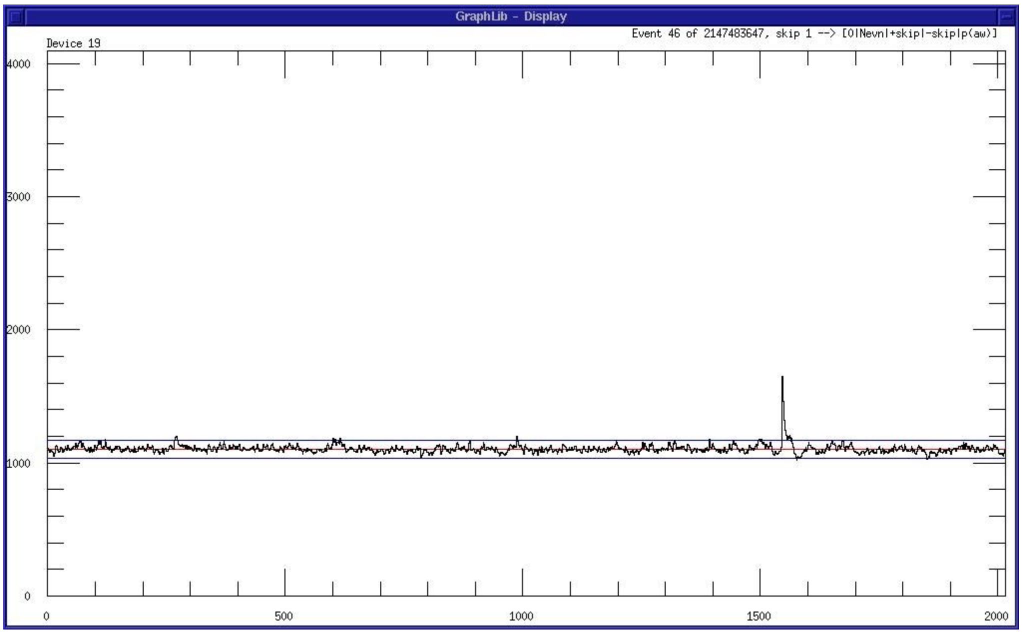

Figure 76 - A current signal as recorded by the ADCs. The abscissa is a time scale in units of 2ms, while the ordinate is in ADC counts. The current has a negative sign, but it is inverted by the ADCs' inputs. Current signals therefore appear in positive direction.

While the signal looks similar to a PreShape32 signal, some significant differences can be seen: The most important characteristic is the nearly zero rise time of the signal. A discharge happens almost instantly (within several nanoseconds, see section 2.1.2). This can not be resolved by the much slower regulation circuit of the HV supply and ADC time slice. No information about the real length of the signal can therefore be gained from the data. Even more important for the operation of such detectors is the time it takes the combined system of detector module and power supply to restore the former baseline. This is dominated by the time constant of the substrate (see figure 75), convoluted by those of the HV supply.
The interesting numbers for the current monitor analysis are: How many discharges were recorded in what time frame, where did they emerge from and what charge was deposited within a single event. The first value is called 'spark rate' and gives the number of discharges per unit time. The classification of the discharges will be discussed in section 5.6. The charge deposited in an event is given by the integration over the signal's area.
A peak finding algorithm like the one discussed in section 4.1.3 has to be implemented. However, there is significant difficulty involved: The peak finding starts by calculating the ADC's baseline. This has to be done for the current signals, too, but this time the baseline is not fixed. The difficulty with the current measurements is, that the baseline is now dependent from the particle rate and gain of the detector. There is no way of knowing the real particle

rate from anything else but the current monitor data. If there is an increase in the beam intensity during data taking, a simple peak finding algorithm would interpret that as a huge discharge, because the current drawn increases over many consecutive samples. The baseline would be adjusted to the new baseline position only in the next event. On the other hand, a beam loss, which frequently happens, results in a ‘dramatic’ reduction of the current, and the algorithm would conclude a breakdown of the detector’s gain.

For that reason, the baseline is calculated for every HV line and event individually, with additional crosschecks to the other HV lines connected to the detector module to avoid misinterpretations. In a first step, variations between consecutive samples of an ADC channel are calculated and filled into a histogram. The mean of this distribution will reflect the actual current drawn on this line. Possible current signals will be outside the distribution due to their steep rising edge (see figure 76), resulting in a bigger variation between two samples than the average. The mean of the distribution is taken as preliminary baseline, and all samples not within three times the variance of this distribution are excluded from the further baseline calculation. Additional crosschecks done at this level are a search for ‘baseline steps’ and ‘ADC crosstalk’. The latter phenomenon arises from an electrical fault of the ADCs used in the April 1999 test beam: The input connectors of the multi channel ADCs were not properly decoupled. A large signal on one of the inputs caused all other channels to record this signal, too. The baseline algorithm therefore checks that not all channels of a given ADC do record a baseline variation in the same event at identical positions in time. If that is the case, the event is excluded from further analysis, because there is no way to select the HV line which originally recorded the discharge. The other crosscheck is made for baseline steps: This describes an effect, which is represented by a sudden drop or rise of the whole baseline to a new average value, which is then sustained. Three possible sources for this effect could be identified: A beam loss, a change in intensity, or a GEM discharge. If the latter happens, the ADC is driven to the margin of its dynamic range. No further structure of the signal shape can be seen. Due to the huge charge stored in a GEM, it has a large time constant and it takes several seconds before the baseline is restored. Depending on when this discharge happens with respect of the ADC’s readout cycle, the effect can even spread over two events. The software recognises when the baseline assumes a new value after a large variation between two consecutive samples. The baseline’s value from the event before is then taken to analyse the actual signal. Now the baseline can be calculated by simply averaging over the remaining samples.

After the baseline is known by the software, a peak finding identical to the one discussed in section 4.1.3 is performed. As can be seen in figure 76, the baseline is not flat. A threshold is introduced to ensure that the peak finder does not accidentally analyse statistical fluctuations. A value of three times the r.m.s. of the baseline’s mean has been found to be sufficient.

The charge is calculated from the integral of the signal’s area. A calibration of the current monitors used is necessary. It is performed by connecting a well-defined resistor to the individual HV lines and then setting different voltages while measuring the current. Assuming a linear behaviour, the slope of this measurements yields the calibration constants. The results are given in appendix J.

5 RESULTS

The final chapter of this thesis presents the results acquired by the different experiments. The discussion begins with the gain behaviour of GEM+MSGC modules. Closely related to that topic are the cluster size of the detector signals and the transparency. Results for the efficiency of GEM+MSGCs and their spatial resolution will be given. The chapter closes with a study of the behaviour of the detectors in an LHC-like environment.

5.1 Amplification

Measurements of the gain with photons

The gain measurements were carried out with GEM4 and a ^{55}Fe γ-source in Ar/C_3H_8. The results are shown in figure 77.

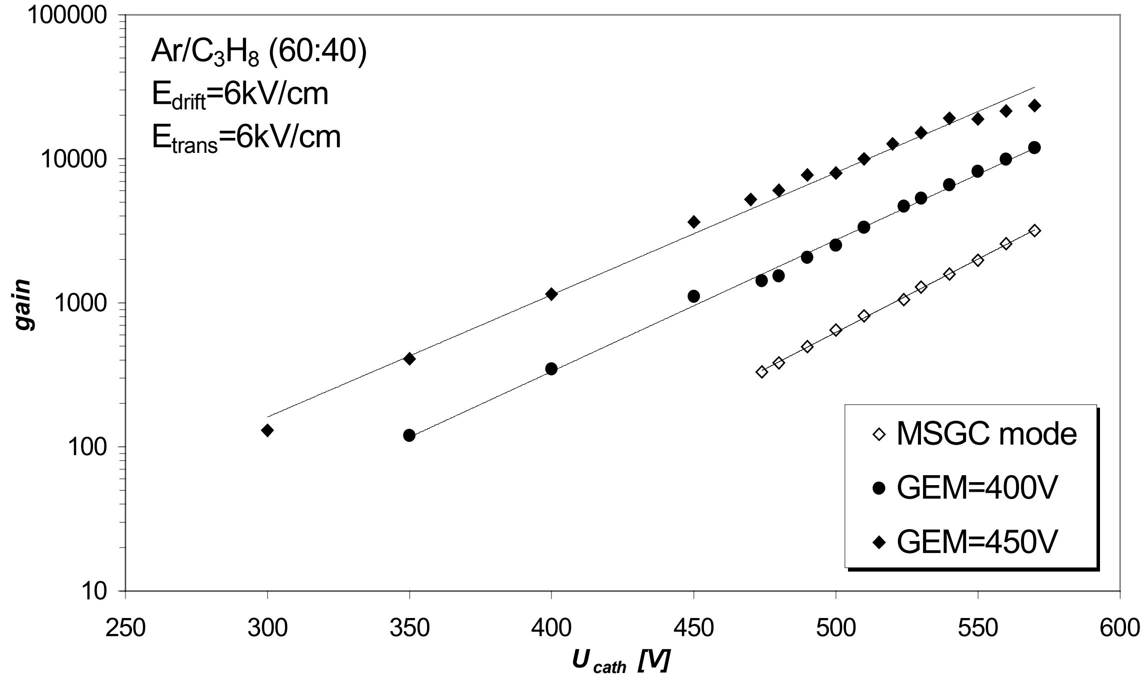

Figure 77 - Gain measurements with GEM4 and a ^{55}Fe γ-source in Ar/C_3H_8 (60:40).

All settings, except the cathode voltage U_{cath}, have been kept fixed for these measurements. The hollow symbols represent the so-called 'MSGC mode' as discussed in section 2.2.2. They are used as a reference for comparing the results of the GEM+MSGC gain to those of an MSGC. A different potential difference ΔU_{GEM} has been used for each curve. The total amplification of the detector module increases with the GEM voltage. Gains up to 23.000 have been achieved. The small deviation for the highest values of the $\Delta U_{GEM} = 450V$ curve are caused by saturation effects of the PreShape32 preamplifiers. An exponential dependence of the gain on the cathode voltage, as expected from equation (14), can be seen.

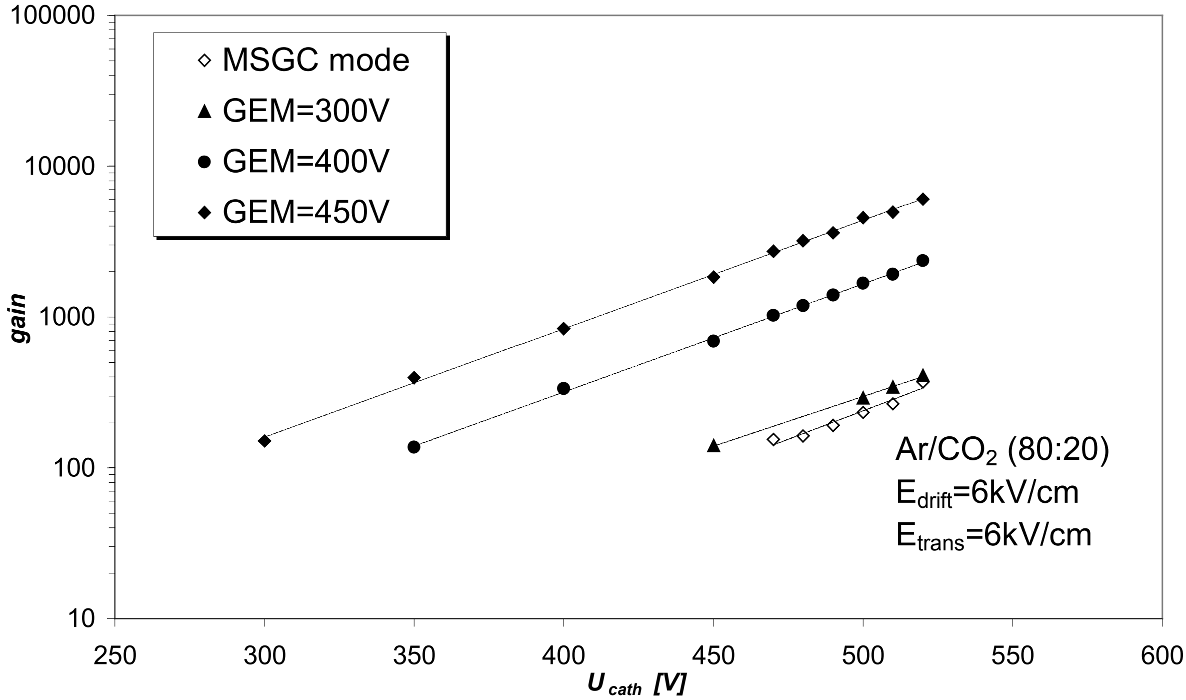

Figure 78 - Gain measurements with GEM4 and a ^{55}Fe γ-source in Ar/CO_2 (80:20).

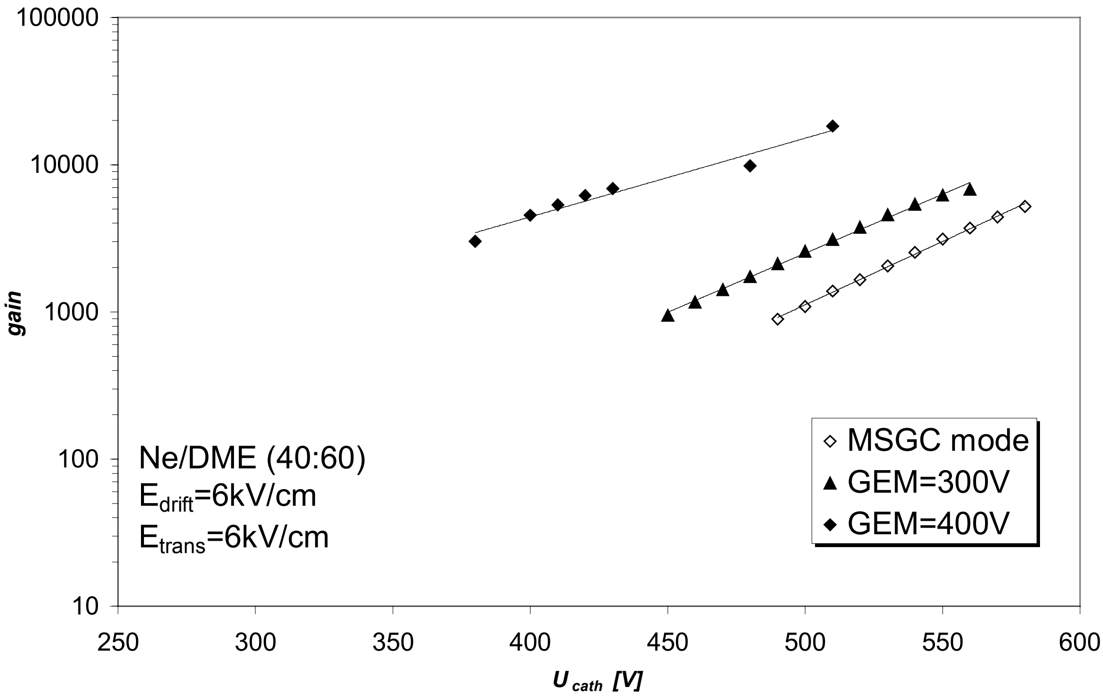

Figure 79 - Gain measurements with GEM4 and a ^{55}Fe γ-source in Ne/DME (40:60).

Additional measurements were carried out using Ar/CO_2 (80:20). Since it is cheap and not flammable, it combines two features the Ne/DME mixtures used in MSGCs can not provide.

Ar/CO_2 is not used in MSGCs because only small gains are reached, as can be seen in figure 78. A cathode voltage of $U_{cath} = 520V$ results in a gain of only 370. Much higher cathode voltages would be needed to reach full detection efficiency, making the operation of the detector unstable. With the addition of a GEM, gains up to 6000 can be reached with convenient cathode voltages.

Finally measurements using the standard CMS mixture of Ne/DME (40:60) have been carried out. The very good amplification can be seen in figure 79.

The amplification of the GEM can be obtained by fixing the cathode voltage to e.g. $U_{cath} = 510V$, and calculating the ratio between the gain of the MSGC mode measurement and the different ΔU_{GEM} settings from figures 77 - 79. The results for the different gas mixtures are shown in figure 80.[42] The superior performance of Ne/DME when compared to the other gas mixtures can be clearly seen. The dependence of the GEM gain on the voltage ΔU_{GEM} is exponential, as expected from equation (14).

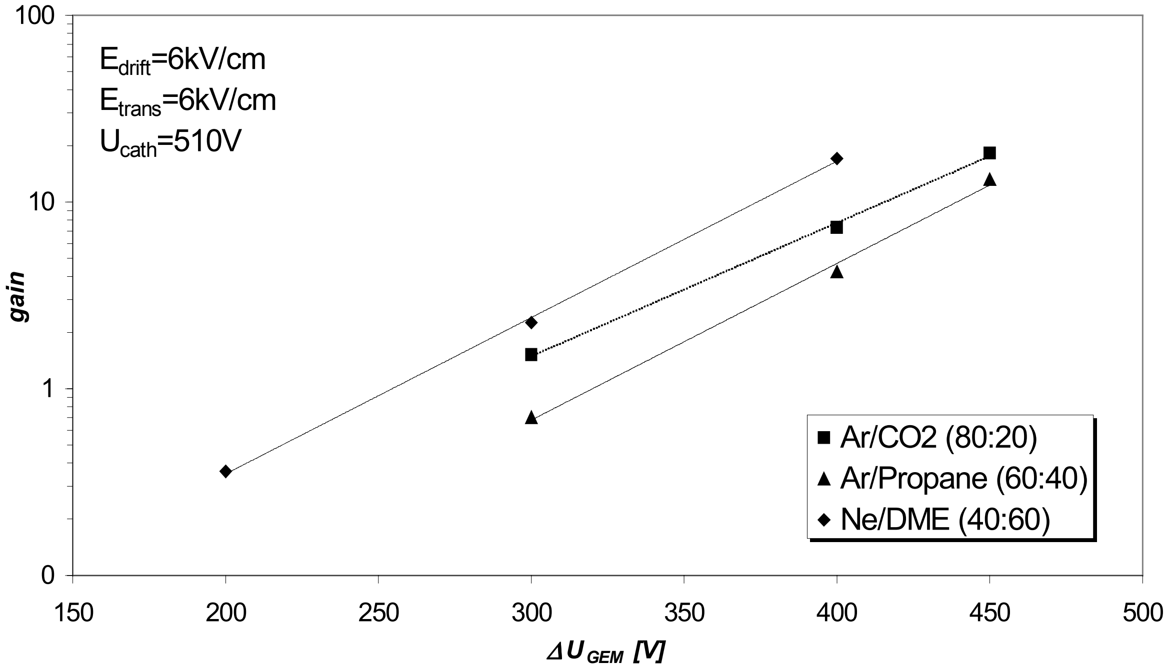

Figure 80 - Gain of the GEM for the different gas mixtures.

A compilation of the amplification behaviour of GEM+MSGC modules with different gas mixtures can be found in figure 81.

Measurements of the gain with MIPs

A direct measurement of the gain with MIPs or ^{90}Sr is not so simple, because these particles ionise the counting gas along their tracks through the detector module. A distinction between the charge produced in the drift region, and the charge generated within the transfer region is not possible. The share of the total amplification generated by the GEM is therefore unknown. However, the total amount of charge can be measured. Such measurements have been carried out in the June 1999 X5 test beam experiment, which has been introduced in section 4.3. The total charge is expressed in units of SNR, as defined in section 4.2.3. The results of these measurements are shown in figure 82 for Ne/DME (40:60), and figure 83 for Ar/CO_2 (70:30).

[42] For a discussion of GEM gains < 1 see section 5.5.

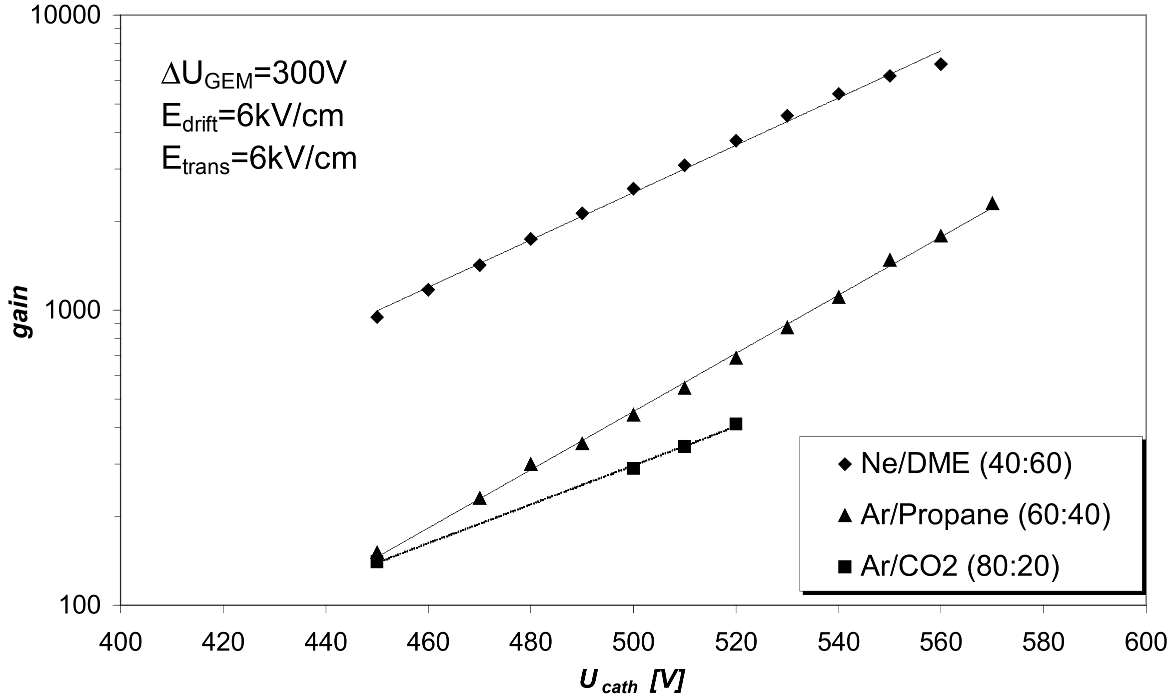

Figure 81 - Compilation of GEM4's amplification behaviour with different gas mixtures.

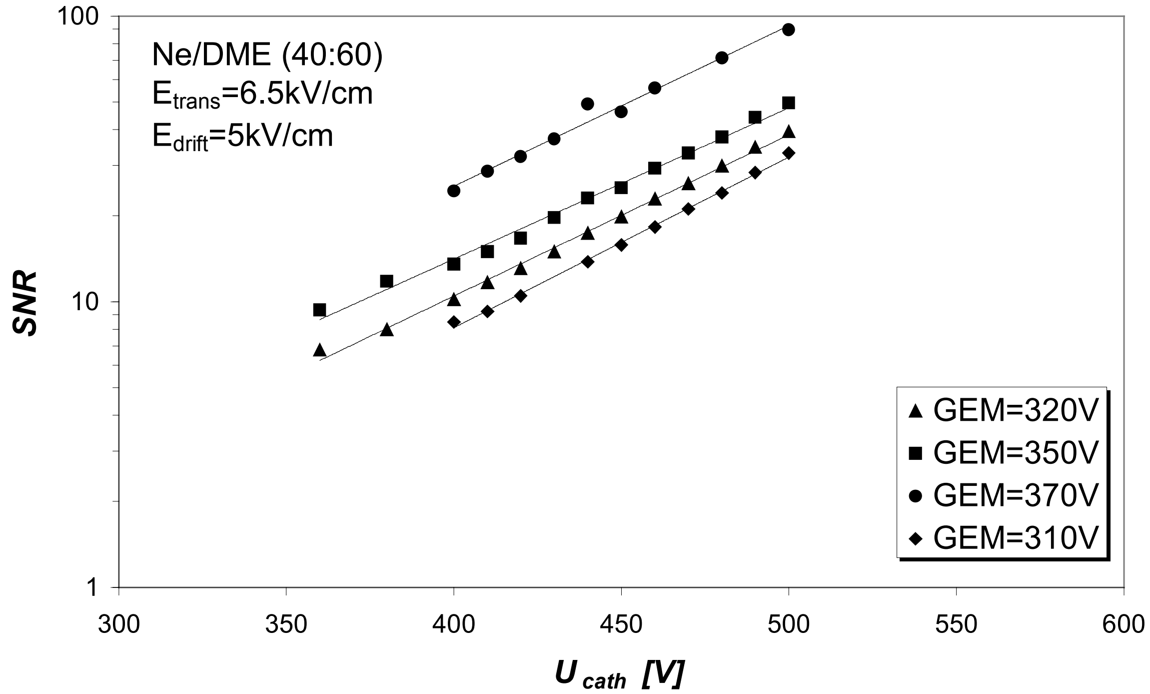

Figure 82 - Gain measurement for GEM6 in the June 1999 test beam with Ne/DME (40:60).

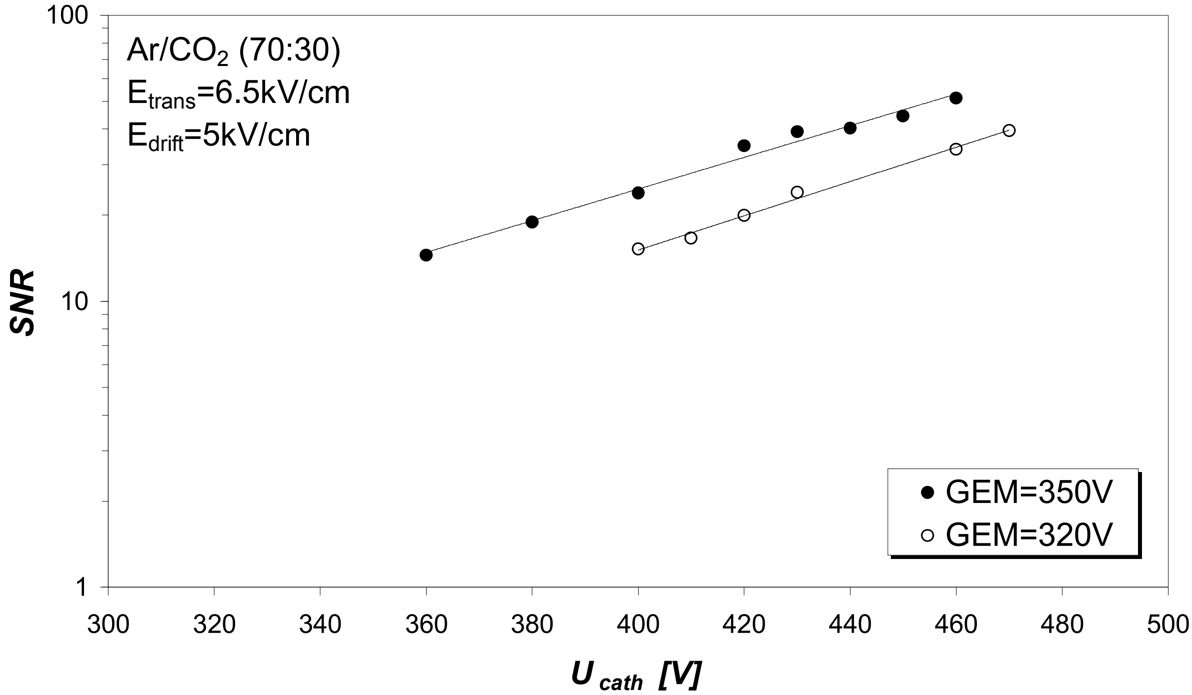

Figure 83 - Gain measurement for GEM6 in the June 1999 test beam with Ar/CO_2 (70:30).

Comparison of two generations of plasma etched GEM foils

As discussed in section 2.3.2, an improved foil processing was expected to result in better GEM amplification. This can be seen in figure 84.

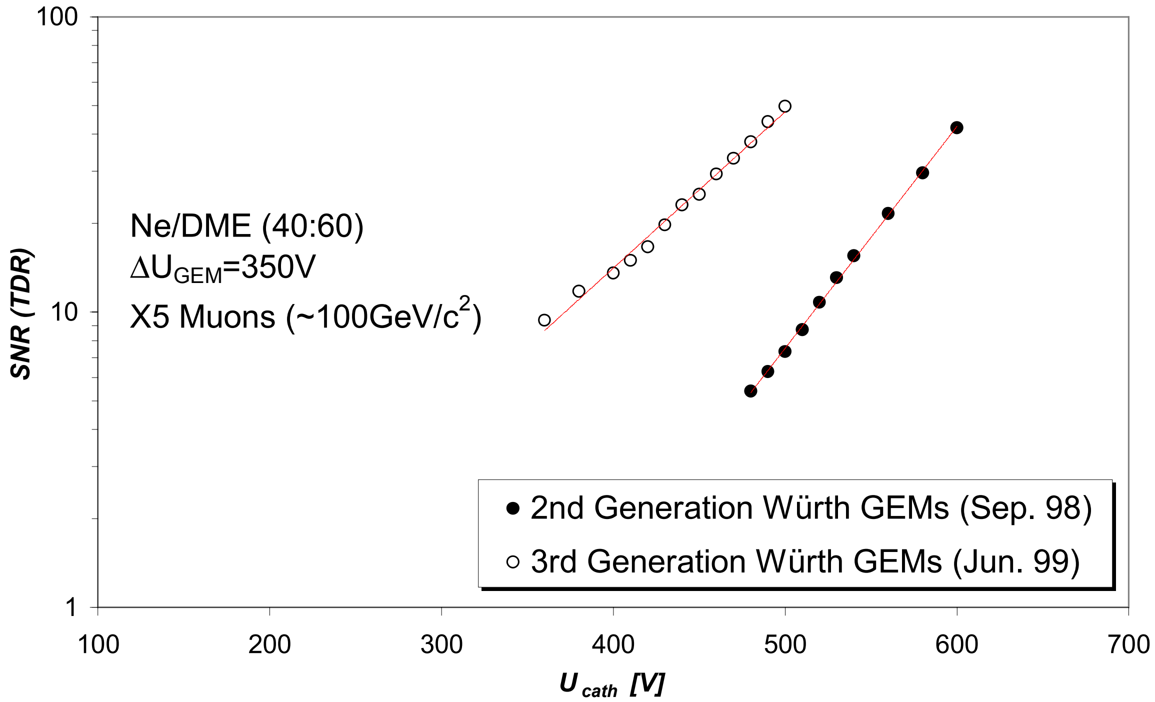

Figure 84 - Comparison of two generations of plasma etched GEMs.

It shows a comparison of two gain measurements taken in the X5 test beam experiments in September 1998 and June 1999. The 1998 measurement was done using GEM5, which was equipped with a GEM of the second generation. In the 1999 test beam experiment, GEM6 with a third generation foil has been used. All voltages were the same for the two detectors in figure 84. The increased amplification of the third generation GEM foil can easily be seen: The cathode voltage could be reduced by 130V, while still achieving the same total amplification as with the first generation GEM foil.

Gain measurements for the forward prototype module

Figure 85 shows a gain measurement for the CMS forward prototype module with a ^{90}Sr β-source.

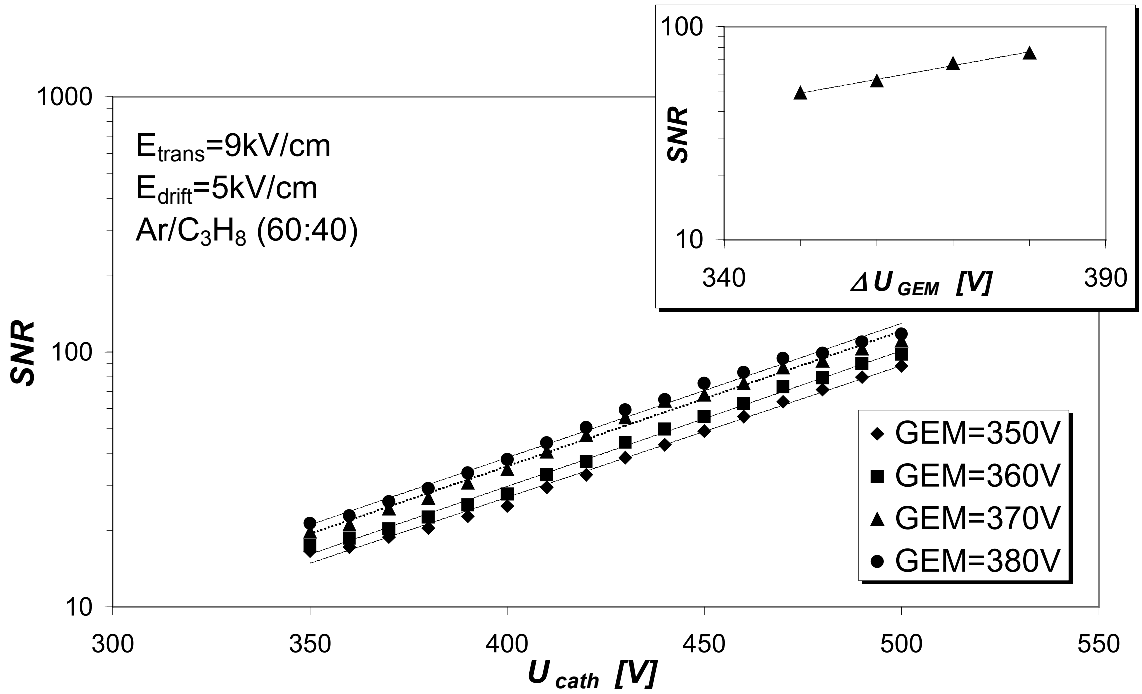

Figure 85 - Gain measurements with the forward prototype module. A ^{90}Sr β-source was used for this measurement. The dependence of the gain on ΔU_{GEM} is shown for U_{cath} = 450V in the small plot.

The exponential dependence of the amplification both on U_{cath} and ΔU_{GEM} can be seen. Gains up to SNR=100 have been achieved.
Figure 86 shows a direct comparison of the Landau-shaped energy loss distributions for the MS-9 type GEM6 and the CMS forward prototype module at identical voltages. The measurement was carried out at the PSI test beam experiment in April 1999. The same cluster charge is generated for identical voltage settings in the two detector modules, although the GEM foils are of different shape and were produced in different production runs. Both detector modules therefore operate at the same gain for a given set of voltages. This is a proof of the very good reproducibility of the foils produced in the plasma etching process. The SNR spectrum for the same measurement is shown in figure 87. A difference of ≈ 60% can be seen. This can be explained by the longer strips on the forward prototype substrates (15cm instead of 10cm). The longer strips result in higher external capacitances coupled to the PreMux128 inputs. This results in an increase of ≈ 50% in noise and explains the effect on the SNR.

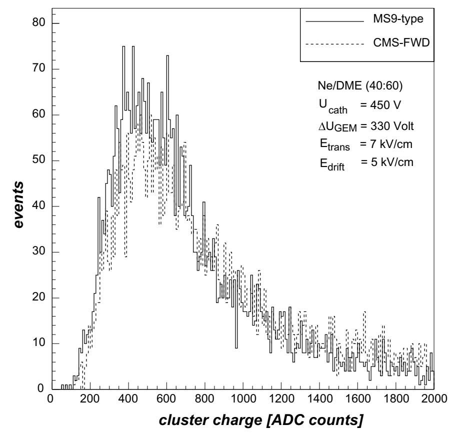

Figure 86 - Comparison of the charge for the MS-9 type module and the forward prototype (abbreviated as 'CMS-FWD') at identical voltages.

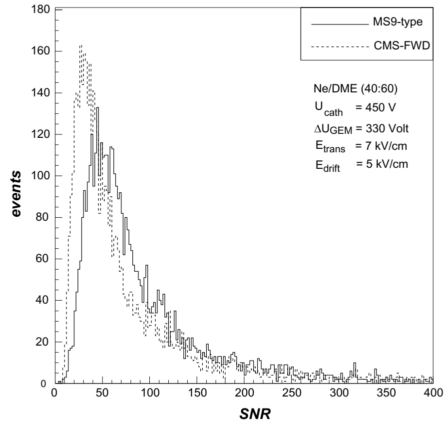

Figure 87 - Comparison of the SNR for the MS-9 type module and the forward prototype (abbreviated as 'CMS-FWD') at identical voltages.

5.2 Cluster size

The cluster size is closely related to the gain of the detector. The amount of charge generated in the amplification process affects the spread of the charge cloud when traversing the detector. It is expressed in the number of strips to which the charge is distributed. The mean cluster width is calculated by fitting a Gaussian distribution to the data; average cluster sizes with fractional numbers of strips are the result.

The minimum cluster width possible in any gas mixture is given by the diffusion in that medium, and the spread of the charge cloud due to δ- *electrons*. These are electrons liberated in the ionisation process, which are ejected with a high probability perpendicular to the direction of the incident particle. Their energy can be as high as the maximum possible energy transfer E_{max} given by equation (2). The range R in the gas can be calculated by integrating the Bethe-Bloch formula (1) over R, and requiring the integral to equal the energy of the δ-electron. Practically, this yields a bad representation of the total range, because multiple collisions are not covered by this approach. For energies up to several hundred keV, the approximation $R = 0.71 \cdot E^{1.72}$ [g cm^2] has been found to be valid **[13]**. E has to be given in MeV. As an example, the expected width of the charge cloud will now be calculated for Ar/CO_2: The range of a 3keV δ-electron in Argon is 100µm **[13]**. This number has to be convoluted by the spread due to diffusion, given by equation (11). A simulation with MAGBOLTZ for a 5kV/cm electric field yields a linear diffusion of 160µm/cm **[17]**. A diffusion of 88µm is therefore expected for the 3mm thick drift region. These numbers have to be added quadratically when assuming a Gaussian distribution for the spread. The result is a charge cloud of 133µm width at the top side of the GEM. This number is larger than the diameter of the holes. The charge is therefore spread over two holes at least: The resulting cloud has a width of 210µm at the lower side of the GEM. This number is simply the pitch of the foil plus two times the radius of the holes. Now the diffusion in the 2mm transfer region has to be taken into account. A spread of 72µm can be calculated. Convoluted with the extension of the charge cloud just below the GEM, a width of 222µm can be derived. A minimum cluster size of 1.1 strips can be expected by this approximation. This is in good agreement with the experimental results, as can be seen in figure 88:

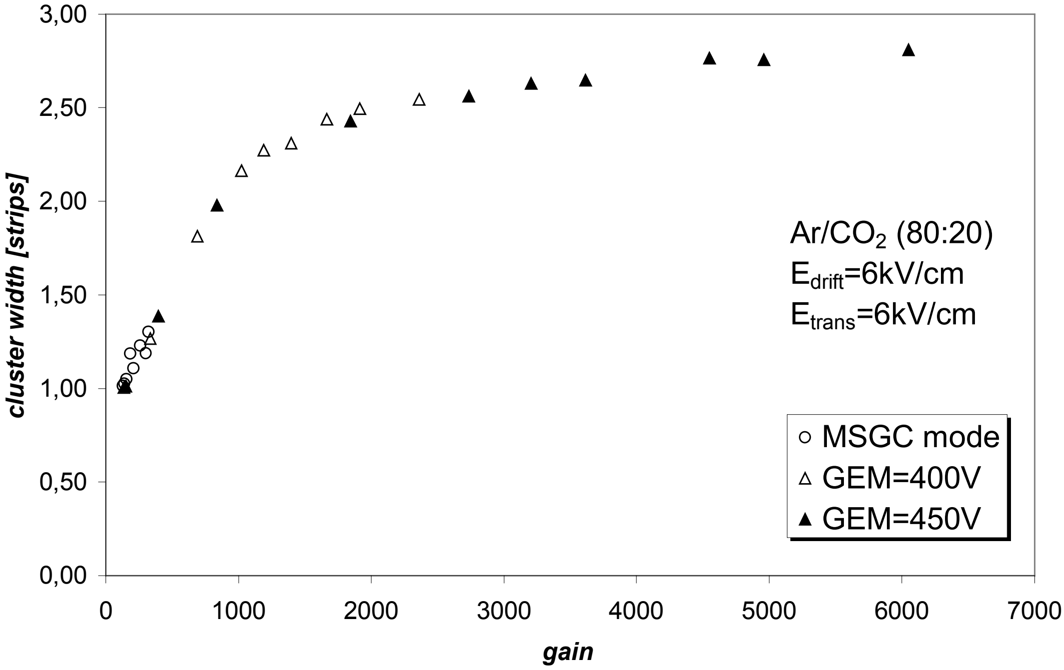

Figure 88 - Measurement of the cluster size with GEM4 in Ar/CO_2 and an ^{55}Fe source.

The cluster width only depends on the total gain of the detector. The points in figure 88 correspond to the measurements shown in figure 78. The width reaches a value of ≈ 2.75 strips. Then it grows only slowly for higher gains. The precise value depends on the gas mixture. The higher the gain, the more free charges are generated. These do not only add to the size of the charge cloud, but also smear the width of the distribution due to multiple scattering, or production of additional δ-electrons.

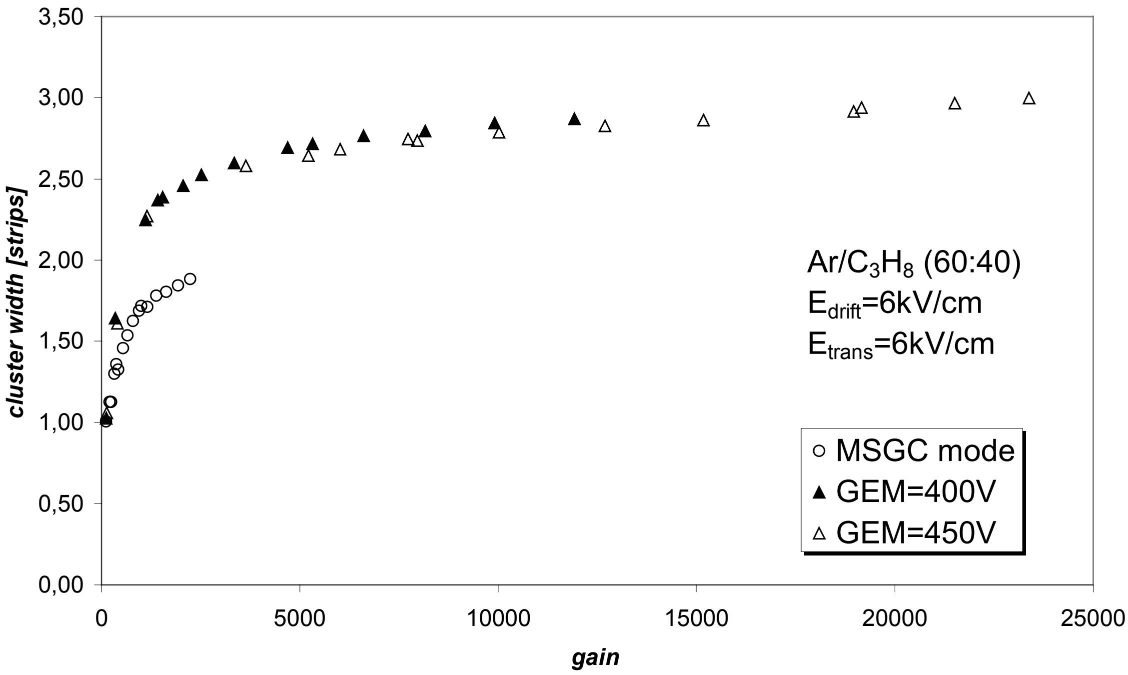

Figure 89 - Measurement of the cluster size with GEM4 in Ar/C_3H_8 and an ^{55}Fe source.

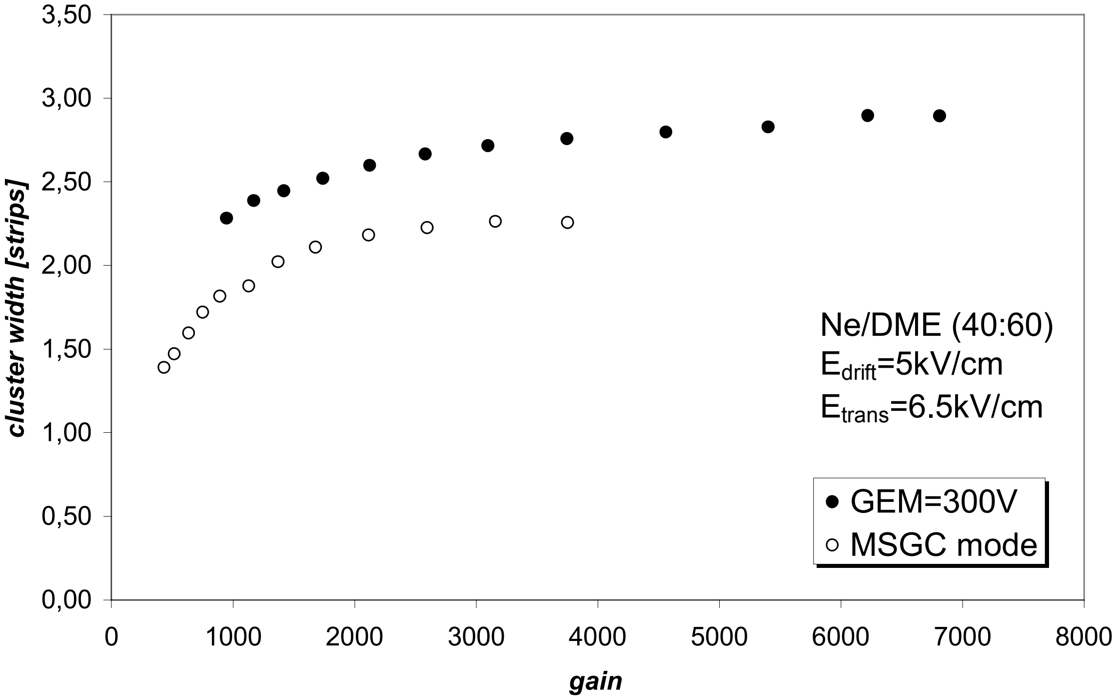

Figure 90 - Measurement of the cluster size with GEM4 in Ne/DME and an ^{55}Fe source.

Figures 89 and 90 show measurements for Ar/C_3H_8 (60:40) and Ne/DME (40:60). The corresponding gains have been presented in figures 77 and 79 respectively. A separation between the curves for the MSGC mode signals and those amplified by the GEM can be seen. This is caused by the fact that the spread due to the charge distribution over two GEM holes is absent for the MSGC-only signals. The range for diffusion is smaller, too. The only reason why this effect cannot be seen in figure 88 is the limited gain of the MSGC substrate in Ar/CO_2 – it is too small to reach the region where the two curves separate.

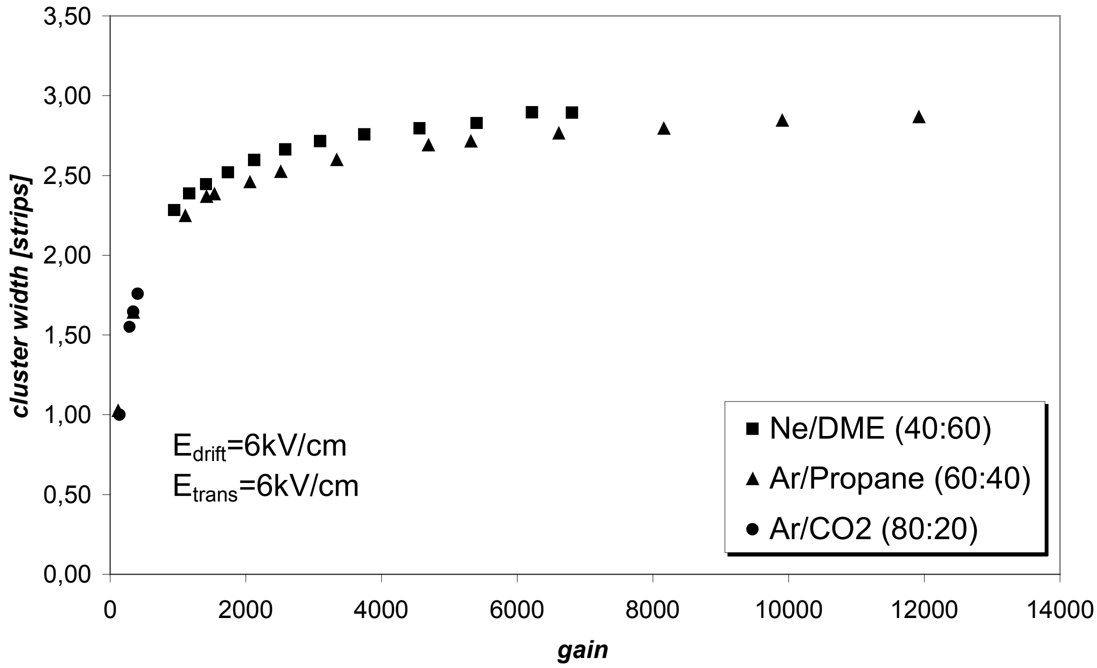

Figure 91 - Comparison between the cluster sizes for the different gases.

A comparison of the results for the different gas mixtures is shown in figure 91. Only measurements signals amplified by the GEM are shown. A small increase in cluster size in the order of 5% can be seen for Ne/DME when compared to Ar/C_3H_8. A larger effect would be expected from the different diffusion constants: The cluster width for Ne/DME should be ≈ 20% larger compared to Ar/C_3H_8 **[17]**. The absence of this effect is understood, because the difference is in the order of 20-30µm over a drift space of 5mm. This is smaller than the spatial resolution of the GEM+MSGC detector module, as will be shown in section 5.4.

5.3 Efficiency

Efficiency measurements have been carried out with a ^{90}Sr source in the lab, and 90-120GeV muons in test beam experiments at CERN's X5B area. Ar/C_3H_8 (60:40), Ne/DME (40:60) and Ar/CO_2 (80:20) mixtures have been used. The data acquisition systems are described in sections 4.2.2 and 4.3.2. The SNR values have been calculated using the algorithms and cuts introduced in section 4.2.3; a tracking analysis as described in section 4.3.3 has been carried out for the efficiency measurements, except for the lab results: These have been achieved using the simple setup described in section 4.2.4. Efficiency for these measurements is defined by the ratio

$$\varepsilon = \frac{n_{hits}}{n_{tot}}$$

n_{hits} denotes the number of events with a signal over the threshold, and n_{tot} the total number of events triggered by the scintillators.

Efficiency measurements for the forward prototype module

Figure 92 shows efficiency measurements for different GEM voltages ΔU_{GEM} for the CMS forward prototype module.

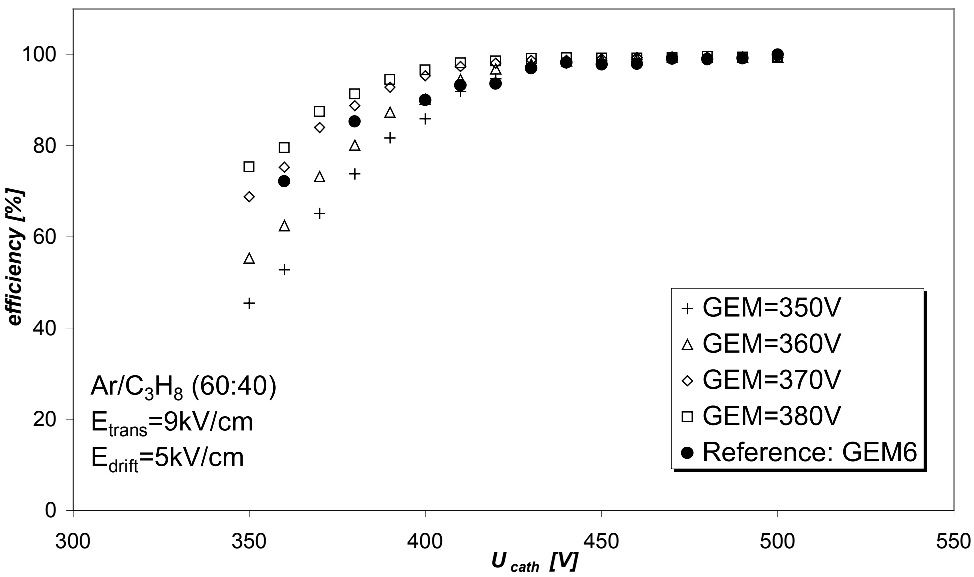

Figure 92 – Efficiency vs. cathode voltage U_{cath} for the forward detector module. A measurement of GEM6 with ΔU = 350V has been added as a reference.

A ^{90}Sr source and Ar/C_3H_8 (60:40) as gas mixture were used. The curves for the reference measurement with GEM6, and for the forward detector module at $\Delta U = 350$V, reach the plateau at the same cathode voltage of $U_{cath} = 430$V. The number of 99% at the plateau level should not be taken too seriously, since this sort of measurement is known to be inexact. To determine the absolute efficiency of a detector module, a full tracking analysis has to be carried out, as done for the test beams.
SNR has been chosen as parameter to determine the 'working point' at which a detector operates at maximal achievable ('full') efficiency. This allows the comparison of different detector modules by eliminating effects arising from different read out electronics or detector modules. The working point is an important parameter for experiments where the direct measurement of the efficiency is not possible. The high rate studies at PSI, which have been described in section 4.4, are examples.

Efficiency measurements at the X5 test beam experiment

Figure 93 shows an efficiency measurement from the June 1999 test beam at X5. The voltage on the GEM has been kept at $\Delta U = 320$V, and the cathode voltage was varied from $U_{cath} = 400$-500V. The fields were set to $E_{trans} = 6.5$kV/cm and $E_{drift} = 5$kV/cm. Figure 82 shows the correlation of cathode voltage U_{cath} to SNR. It can be seen from figure 93 that a particle detection efficiency of 99% is reached for SNR > 20, and an efficiency of 98% is reached for SNR > 17. SNR = 13 and SNR = 18 at the 98% efficiency level have been reported for the CMS barrel **[6]** and forward modules **[45]** respectively. No increased SNR is therefore necessary for a GEM+MSGC. This result is expected, since the GEM shares the amplification of the primary ionisation with the substrate. The absolute charge needed to reach full detection efficiency is independent of the detector construction, or the origin of the amplification.

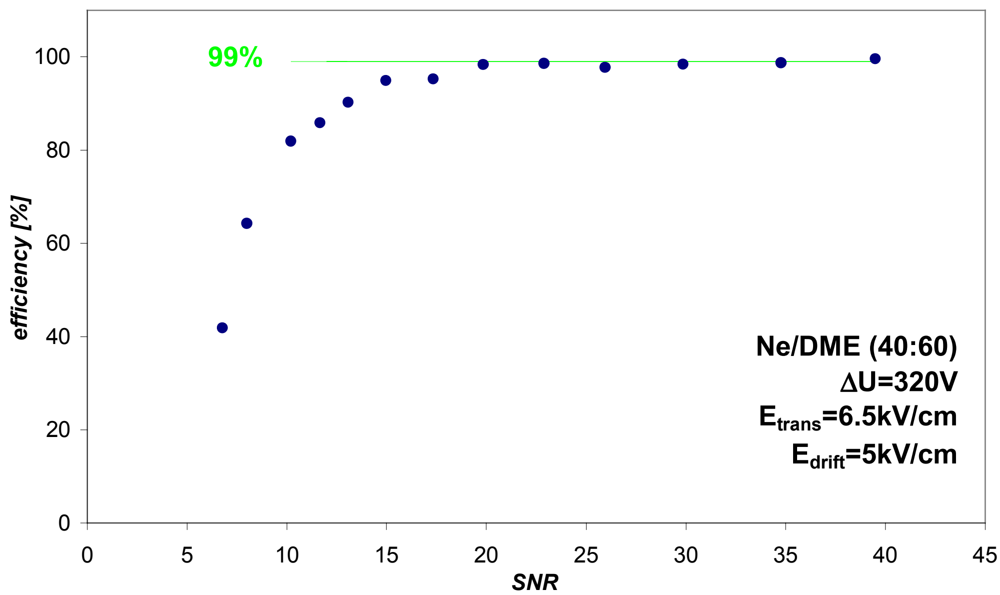

Figure 93 – Efficiency vs. SNR in Ne/DME for GEM6; the measurement has been carried out with 100-120 GeV muons in the June 1999 X5 test beam. The plateau at 99% is reached for SNR ≈ 20.

Impact of the GEM gain on the efficiency

The working point is independent of the sharing of the amplification between the GEM and MSGC. This can be seen in figures 94 and 95. The GEM voltage ΔU_{GEM} has been varied from

300V to 400V in figure 95, and the cathode voltage has been fixed to $U_{cath} = 440V$. The plateau is reached at SNR = 20 for a wide range of voltages, regardless of modifying ΔU_{GEM} or U_{cath}. It can be concluded, that the gain needed to reach full detection efficiency depends only on the total amplification of the detector module.

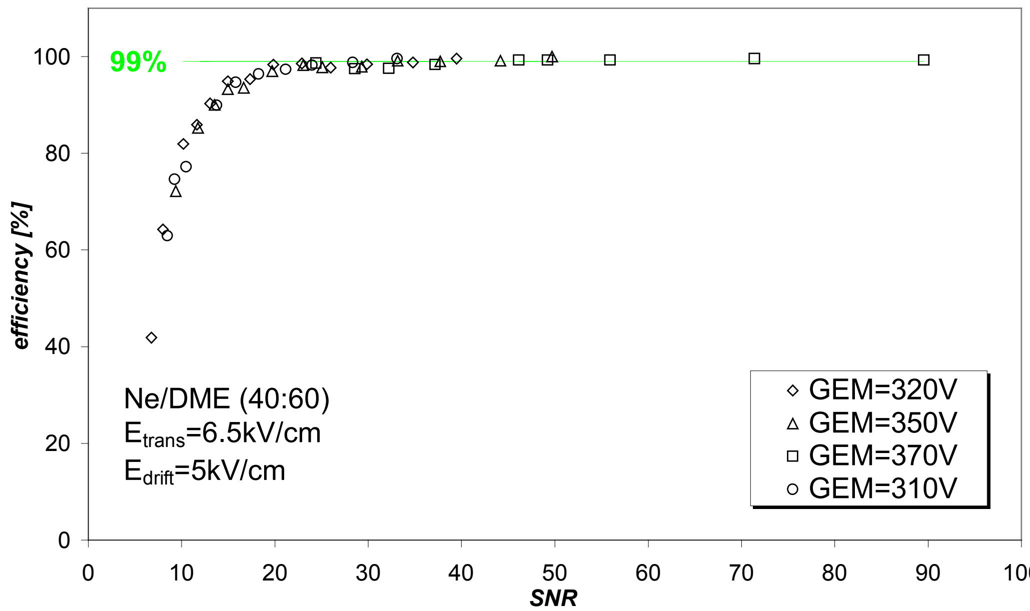

Figure 94 – Efficiency measurements for different GEM voltages. The plateau at 99% is always reached at the same value of SNR ≈ 20, independent of the sharing of the gain between GEM and MSGC. The cathode voltages were varied from 360-500V.

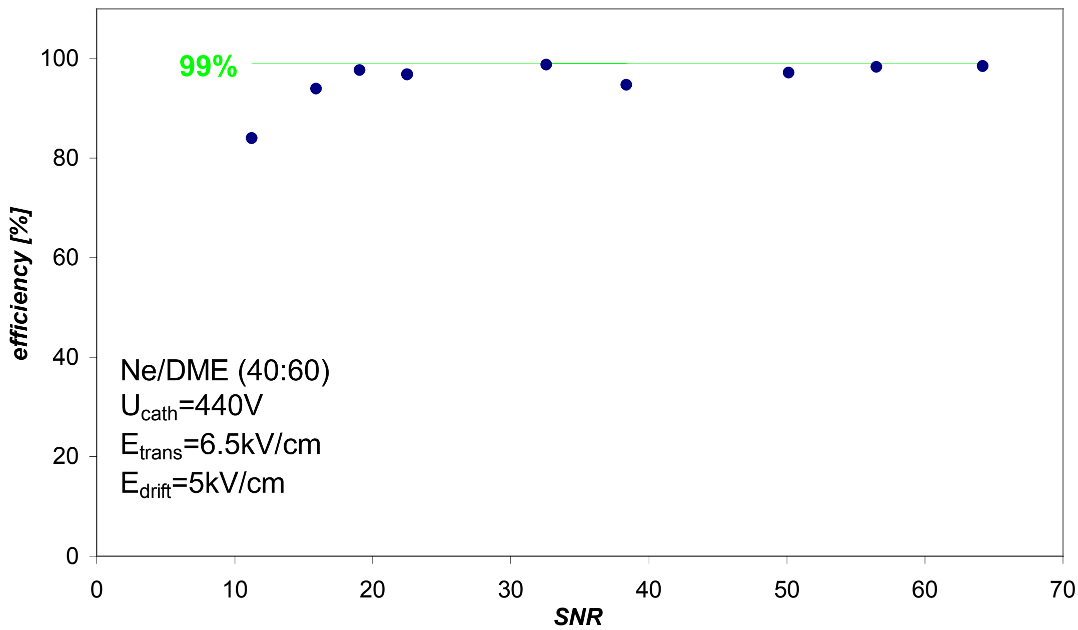

Figure 95 – Efficiency vs. SNR in Ne/DME for GEM6; the measurement has been carried out with 100-120 GeV muons in the June 1999 X5 test beam. The cathode voltage has been kept at 440V, and the GEM voltage has been varied. The plateau at 99% is reached for SNR ≈ 20.

Efficiency measurements with Ar/CO_2

Since the introduction of the GEM, Ar/CO_2 has been looked at carefully. Because it is a cheap and non-flammable mixture, it was an attractive alternative to the expensive, flammable, and reactive Ne/DME mixtures.

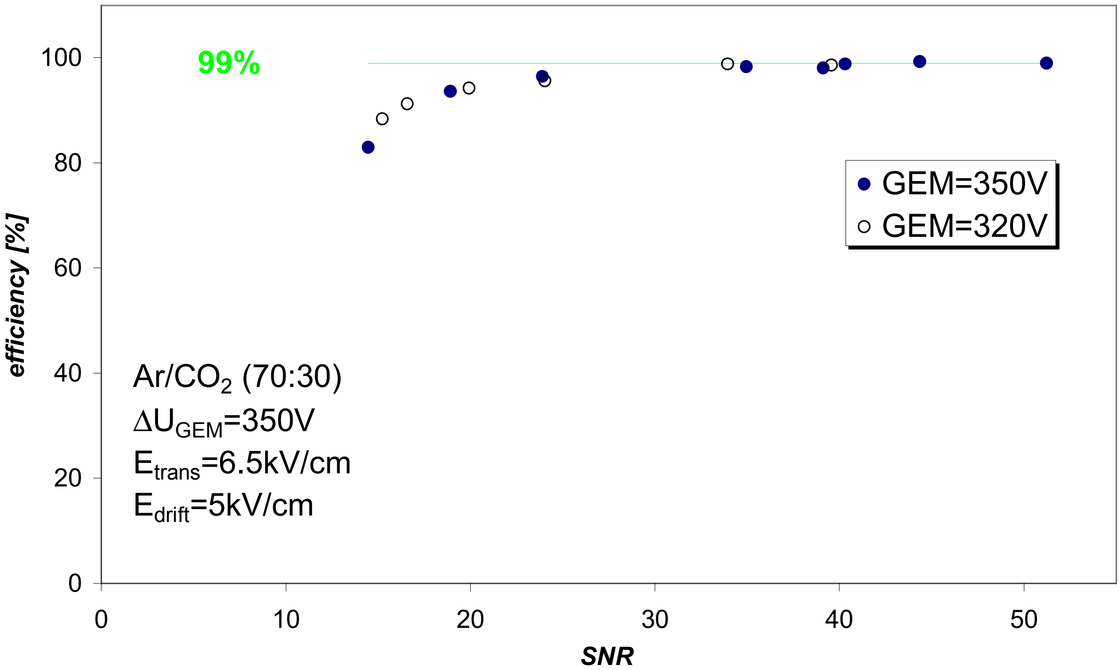

Figure 96 – Efficiency vs. SNR in Ar/CO_2 for GEM6; the measurements have been carried out with 100-120 GeV muons in the June 1999 X5 test beam. The plateau at 99% is reached for SNR ≈ 27.

Operation of an MSGC without a GEM in Ar/CO_2 is difficult, since stable operation is hard to achieve as has been shown in section 5.1. With the addition of a GEM, stable operation is possible. Figure 96 shows efficiency measurements with Ar/CO_2 (70:30). The GEM voltage has been kept at $\Delta U_{GEM} = 320V$ and $\Delta U_{GEM} = 350V$ respectively, while the cathode voltage was varied from $U_{cath} = 360\text{-}460V$. Figure 83 shows the correlation from voltage to SNR. The plateau at 99% efficiency is reached for SNR ≈ 27. It can be seen again that the working point is independent of the sharing of amplification between the GEM and MSGC.

5.4 Spatial Resolution

Measurements of the spatial resolution have been carried out in the June 1999 X5 test beam with Ne/DME (40:60) and Ar/CO_2. The setup with the beam telescope is described in section 4.3. Because the spatial resolution of the telescope is nearly a full order of magnitude more precise than the GEM+MSGC's, an absolute measurement is possible.
Figure 97 shows the spatial resolution for various amplifications in Ne/DME. The error of the variance, calculated from the Gaussian fit to the data as shown in figure 72, is given as error bars in the plot. The spatial resolution converges to a value around 39µm. This is in good agreement with previous measurements **[69]**, and as good as the spatial resolution reported for MSGCs **[45]**.

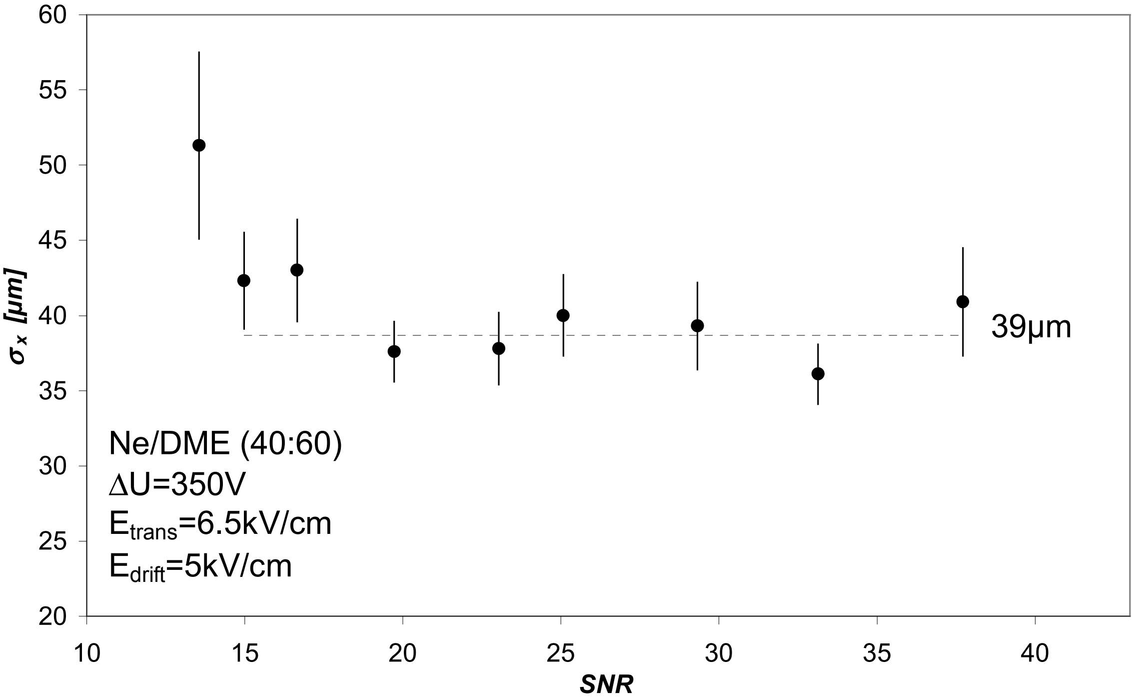

Figure 97 - Spatial resolution of GEM6 with Ne/DME (40:60)

It can therefore be concluded, that no degradation in performance for the GEM+MSGC with respect to an MSGC exists. The spatial resolution achieved is better than the CMS tracker's requirements of 43µm **[6]**.
The initial reduction of the spatial resolution can be explained from the cluster size as shown in figure 90: A reduced spatial resolution is measured for the smaller clusters. This result is expected from equation (20) and the discussion in section 2.2.2.

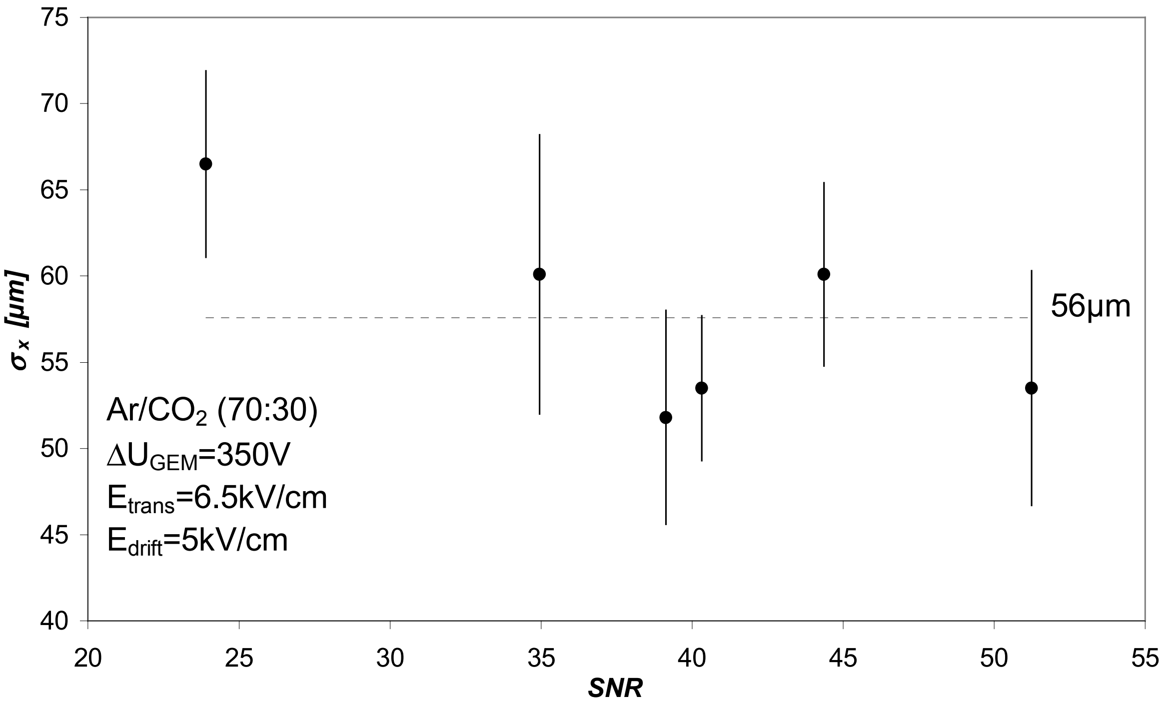

Figure 98 - Spatial resolution of GEM6 with Ar/CO_2 (70:30)

The spatial resolution in Ar/CO_2 (70:30) is worse than in Ne/DME. Figure 98 shows the results of the measurements. A spatial resolution of ≈ 56μm has been achieved. The increase in resolution for small gains can still be seen, but is much less apparent than for Ne/DME.
Since all the measurements rely on the spatial resolution of the beam telescope, it was closely monitored throughout the measurements, which took two weeks. Figure 99 shows the measurements of the absolute position with respect to the beam axis for all silicon detectors. Their movement in time during the two weeks can be clearly seen. Reasons for the shifts are vibrations in the experimental area, or simply shakes and pushes to the optical bench when installing or removing detectors. When looking at detectors mounted together to form one of the double planes of the telescope, e.g. '1X' and '2X' or '3Y' and '4Y', it can be seen that these modules always perform the same movements, but in opposite directions. This is due to the fact that a displacement in one module causes the track to be tilted in that direction. The other plane then shows a virtual displacement in the opposite direction when reconstructing the track. For the calculation of the spatial resolution for the GEM+MSGC, these effects have been corrected.
Figure 100 shows the spatial resolution of all silicon detectors over time: Nearly no variation can be seen. The errors on the variance calculation are ≈ 2% and therefore too small to be printed as error bars. The two 'ribbons' around 5μm and 10μm respectively are caused by the different spatial resolution for the x- and y-planes of the telescope.

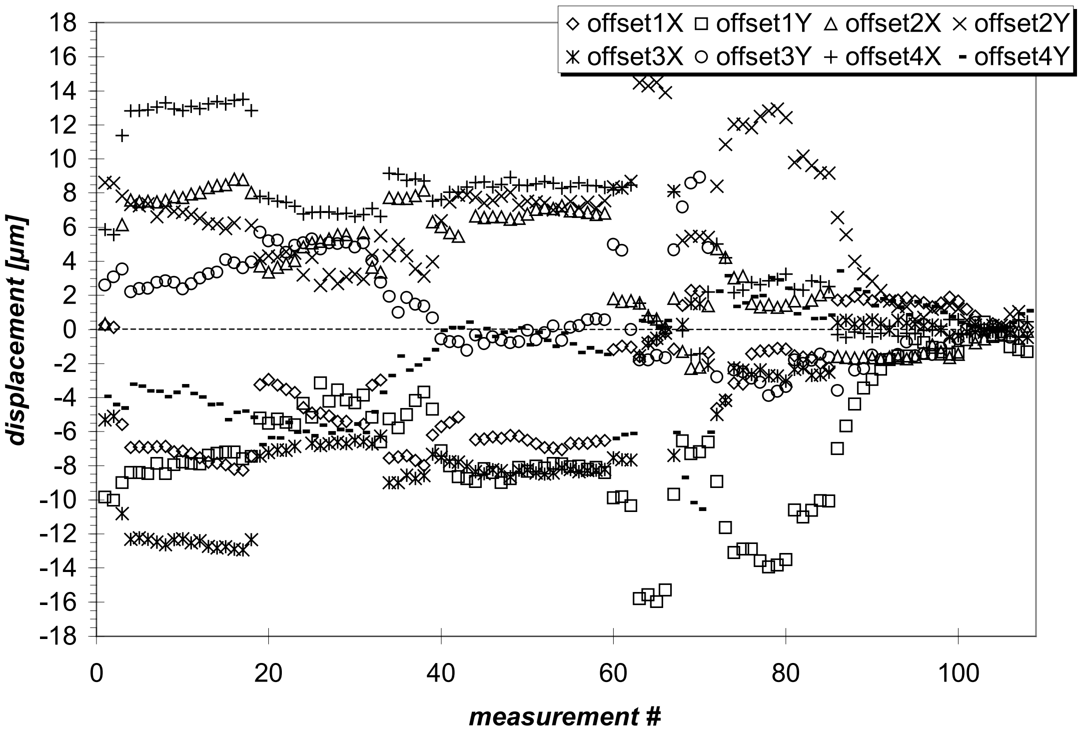

Figure 99 - Measurements of the absolute positions of the four double planes of the silicon detectors making up the beam telescope. The measurements cover a time of approximately two weeks.

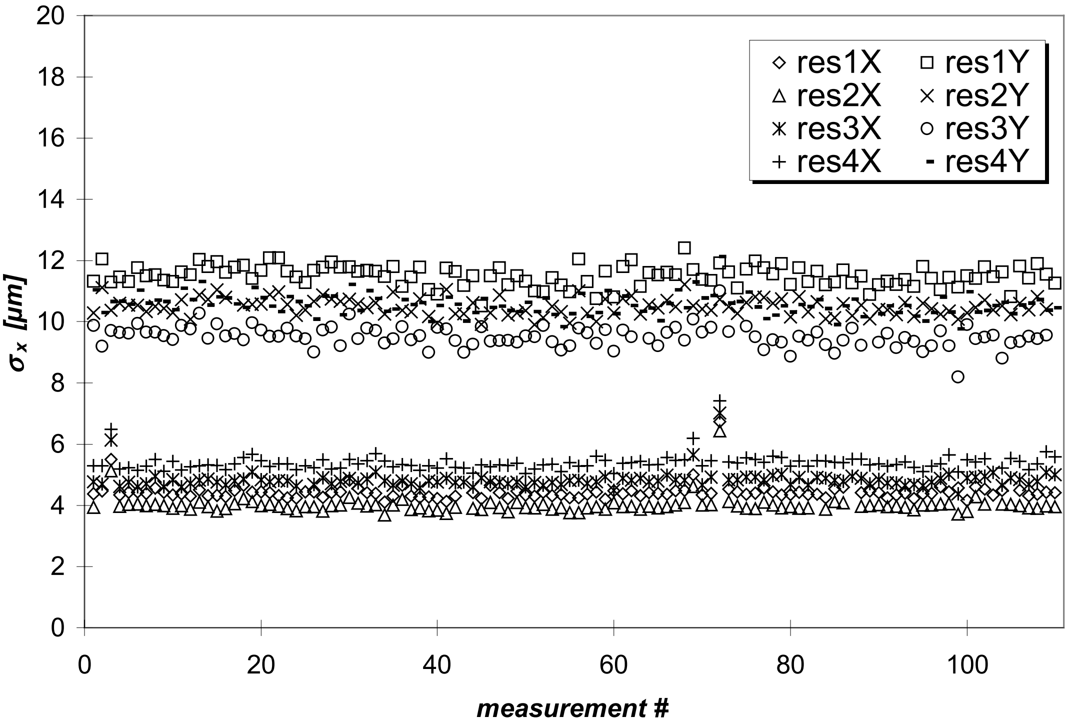

Figure 100 - Measurements of the spatial resolution for the silicon detectors making up the beam telescope. The two different resolutions of 5µm and 10µm respectively belong to the x- and y-planes of the telescope.

5.5 Transparency

There are two types of transparency which should not be mixed: The optical and electrical transparency. The first one is defined as the ratio between the 'open' (the holes) and copper-clad area on a GEM, and the latter one refers to the fraction of charge produced on one side of the GEM able to traverse the foil. The transparency is one (or 100%) if every field line in the drift region reaches the transfer space. Numbers for the optical transparency have already been given in section 2.3.1. Both optical and electrical transparency have to be looked at together. The latter depends on the fields applied both to the drift and transfer spaces, and to the GEM. The order of magnitude in which effects show up depends on the optical transparency, too **[41]**.
There are three sources which affect the electrical transparency: The two fields on each side of the GEM, and the field of the foil itself. Since the field inside the GEM is an order of magnitude larger than the drift and transfer fields (60-80kV/cm compared to 5-10kV/cm), the fields outside the GEM are decoupled. There are interactions of the drift and transfer fields with the GEM field, however.

Transparency effects on the gain

Figure 101 shows the effect of the GEM field on the transparency: The plot shows the same information as figure 77 from section 5.1. A measurement with a small GEM voltage of ΔU_{GEM} = 200V has been added this time.

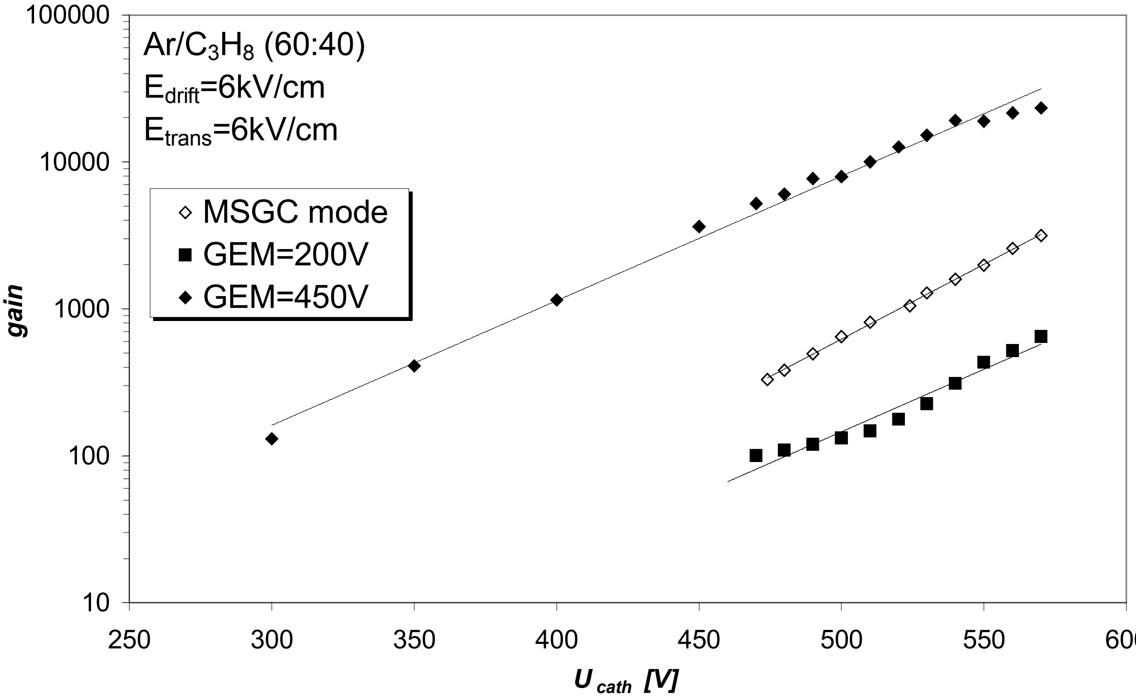

Figure 101 - The gain measurement from figure 77 – this time with an additional measurement for a GEM voltage ΔU_{GEM} = 200V where the transparency is reduced.

The behaviour of the GEM amplification is reversed for small voltages of ΔU_{GEM}. The foil no longer acts as an amplification stage, but as an attenuator. Particles which have passed through the GEM show a reduced total amplification when compared to the MSGC signal. This effect is not caused by the gas: Figures 102 and 103 show the same effect for two different gas mixtures.

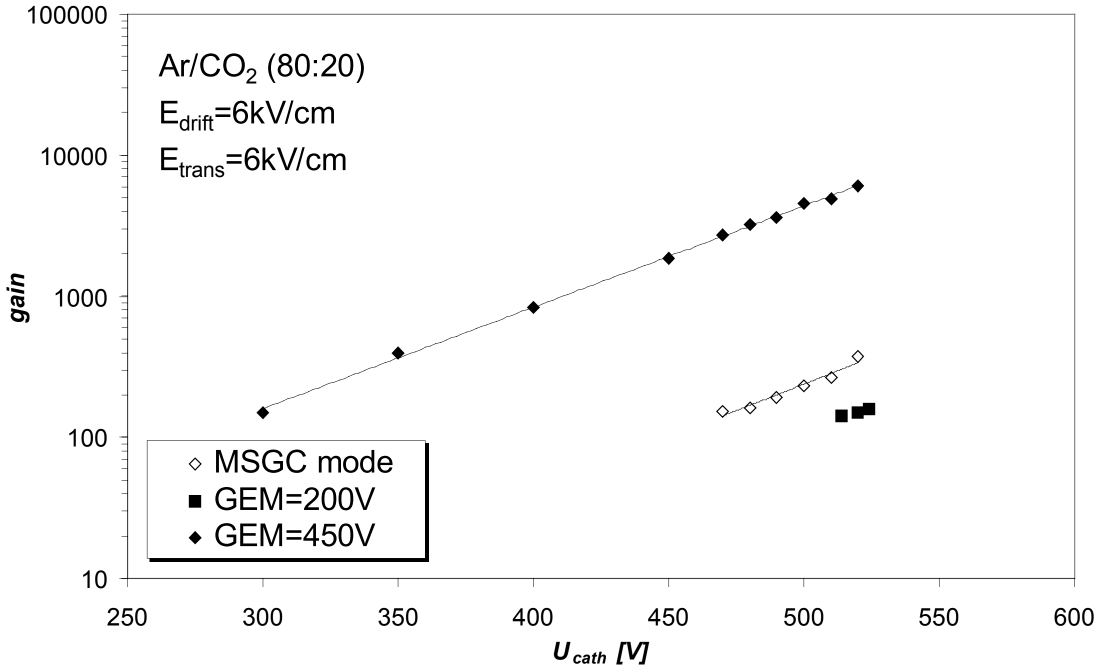

Figure 102 - Transparency effects in Ar/CO_2 for GEM4

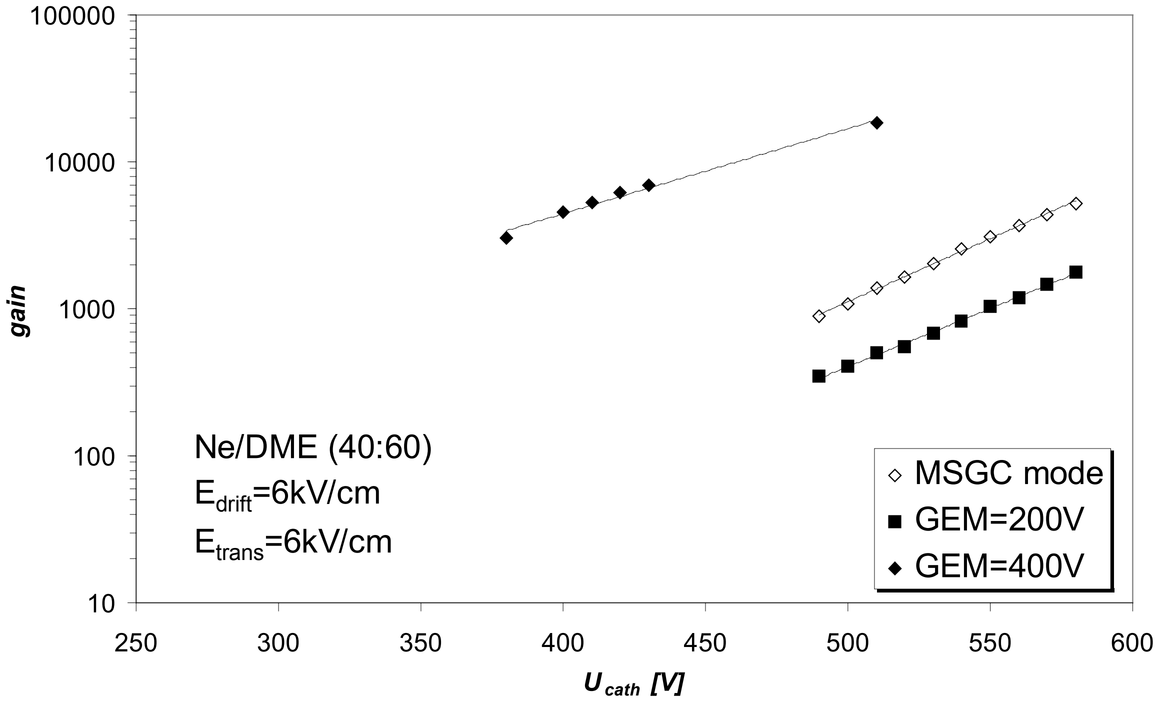

Figure 103 - Transparency effects in Ne/DME for GEM4

The reason for that effect is a too low GEM field. Figure 104 shows a schematic representation of the field lines as given in figure 38. All particles from the drift region are able to traverse the foil. When ΔU_{GEM} is reduced, the number of drift lines going from the top side of the GEM to the transfer region is decreased. This situation is depicted in figure 105. Due to the reduced field inside the GEM, the shielding of the bottom GEM side to the drift field is weakened. Some of the field lines from the drift region now reach the lower side of the foil and deposit the charge there. The field lines reaching from the top side of the GEM to the transfer region disappear as a consequence
.

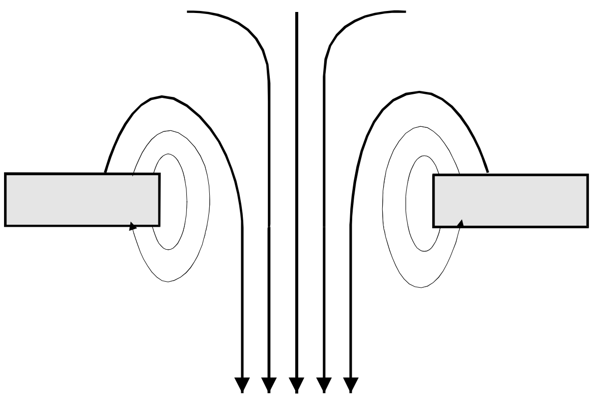

Figure 104 - Schematic sketch of figure 38

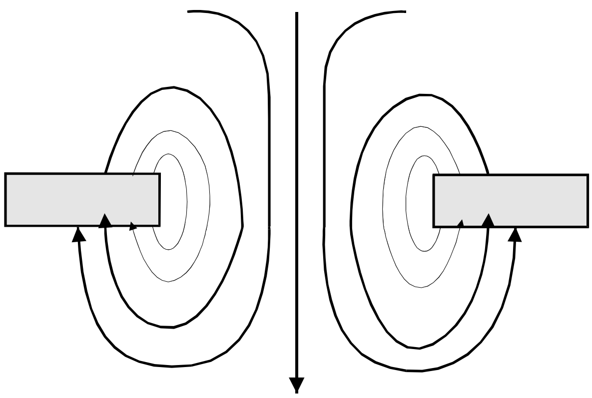

Figure 105 - Effect of a small field in the GEM

Transparency effects on the cluster size

This theory is supported when looking at the cluster sizes which belong to the gain measurements shown in figures 101 - 103:

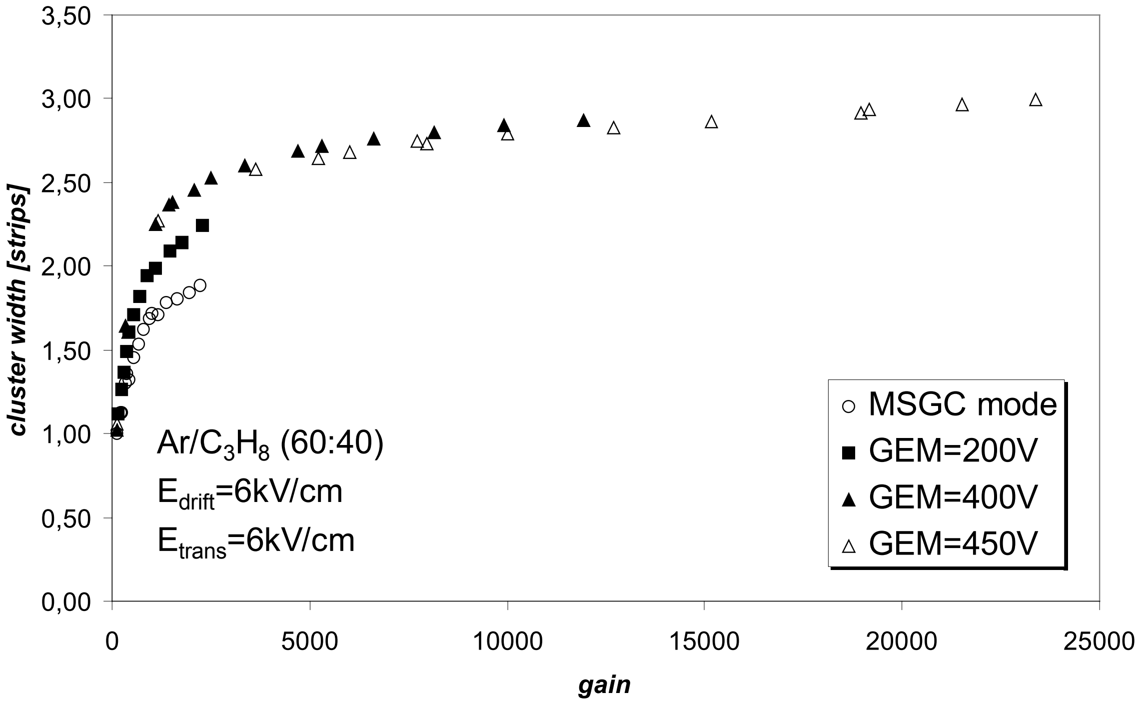

Figure 106 - Transparency effects on the cluster size in Ar/C_3H_8 for GEM4

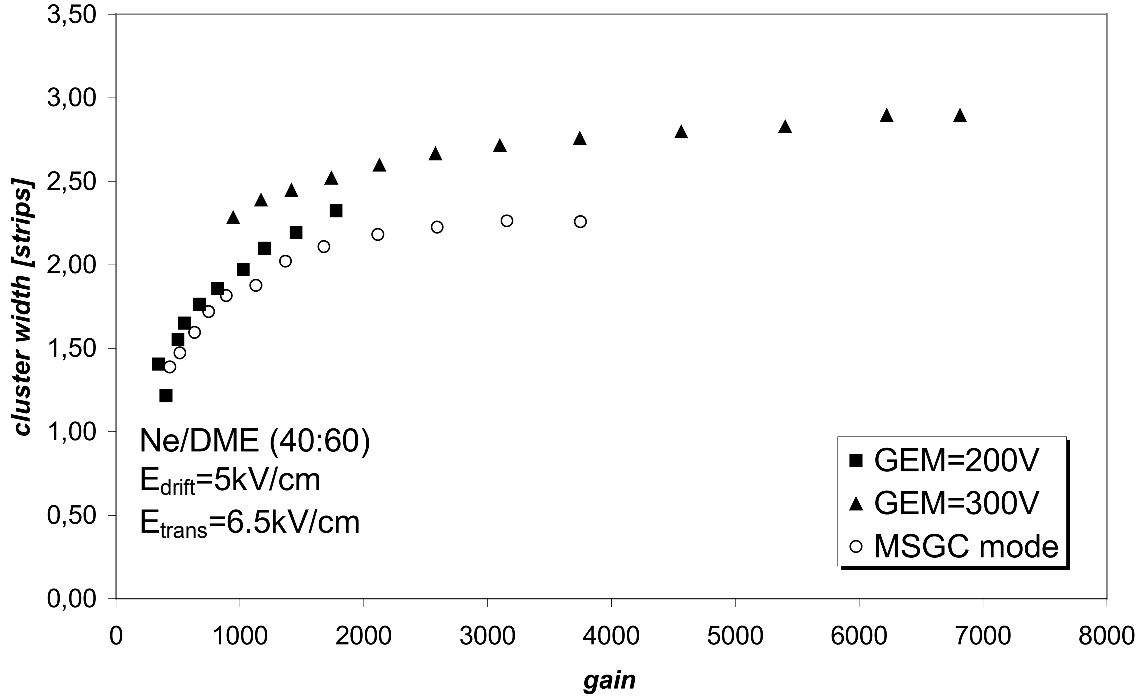

Figure 107 - Transparency effects on the cluster size in Ne/DME for GEM4

A third curve is visible when compared to figures 89 and 90. It has a cluster size between that of the MSGC mode and the GEM amplified measurements when operated at full transparency. As discussed in section 5.2, travelling through the GEM causes the charge cloud to spread over two GEM holes at least. The total width of the cluster is increased by this effect. As shown in figure 105, some drift lines now go to the bottom side of the GEM. These are the outermost field lines. The result is a cropping of the charge cloud on its outer perimeter. The cluster size is reduced with respect to the width measured with a GEM operating at full transparency. Due to the longer way this charge has to travel before reaching the substrate, it still has a larger spread than the MSGC mode signals.

Transparency measurements with photons

Giving an absolute number for the transparency is difficult. This would involve a dedicated experimental setup able to inject a known amount of charge in the drift region, and to measure the charge in the transfer region. This would allow the calculation of the transparency from the ratio of the charge on both sides of the foil if the amplification of the GEM is known.
A localised ionisation takes place either in the transfer or drift region of the detector when using a ^{55}Fe γ-source. Due to the small thickness of the gas volume inside the foil the possibility of an ionisation inside the GEM can be neglected. Since it is possible to distinguish between an ionisation in the drift and transfer spaces from the ^{55}Fe spectrum as shown in section 4.1.3, a measurement of the relative transparency is possible.

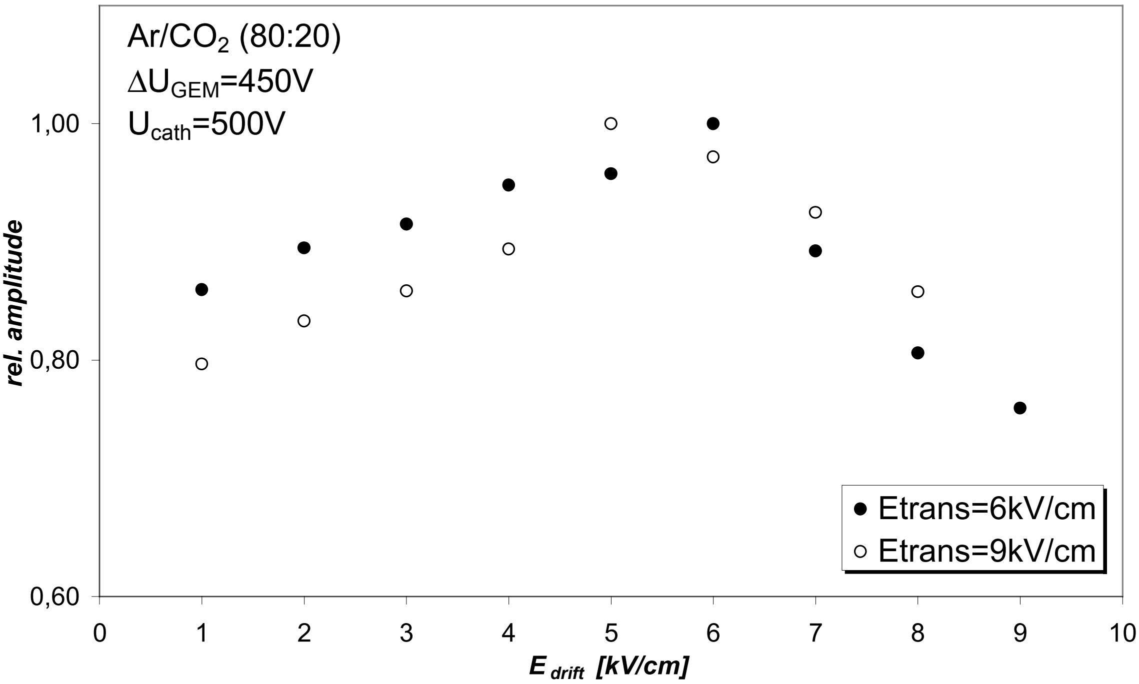

Figure 108 - Measurement of the relative pulse height as a function of the drift field for two different transfer fields with GEM4. The gas mixture is Ar/CO_2 (80:20), and a ^{55}Fe γ-source has been used.

Figure 108 shows the results of such a measurement. Only the signals from photons ionising the gas in the drift region of the detector have been taken. For both transfer fields used, the curves have been normalised to the maximum signal amplitude. The cathode voltage U_{cath} = 500V and GEM voltage ΔU = 450V have been kept fixed for all measurements. A 20% effect on the signal amplitude can be seen. The maximum signal height, and therefore the maximum transparency, is reached for a drift field of E_{drift} = 5-6kV/cm. The situation for small drift fields is sketched in figure 109. Fewer field lines are able to pass through the GEM channels, because the transfer region is shielded from the drift field by the field inside the foil. They are bent outwards and reach the upper side of the GEM instead. Only a fraction of the secondary charges produced in the ionisation in the drift region reach the amplification field inside the GEM. A reduced signal height is the result. This can be seen in the rising edge of the curve in figure 108.

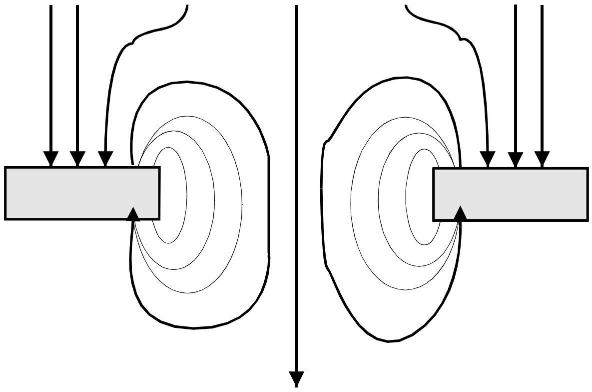

Figure 109 - Effect of a small drift field

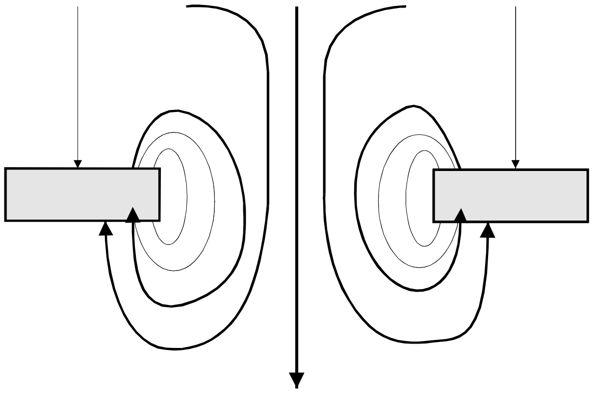

Figure 110 - Effect of a high drift field

This effect disappears with increasing field strength. After the optimal field strength has been reached, a further increase of E_{trans} reduces the signal amplitude again. This situation is depicted in figure 110. The drift field now reaches the top side of the GEM by itself, depositing the charge there. This effect can be reduced by optimising the optical transparency. As an additional effect, the drift field is again strong enough to reach the bottom side of the GEM.

Transparency measurements with MIPs

Figure 111 shows a similar measurement with GEM5 in Ne/DME (40:60) from the September 1998 beam test. The measurements have been carried out with minimum ionising muons. These particles ionise the gas along their track through the detector both in the drift and transfer regions.

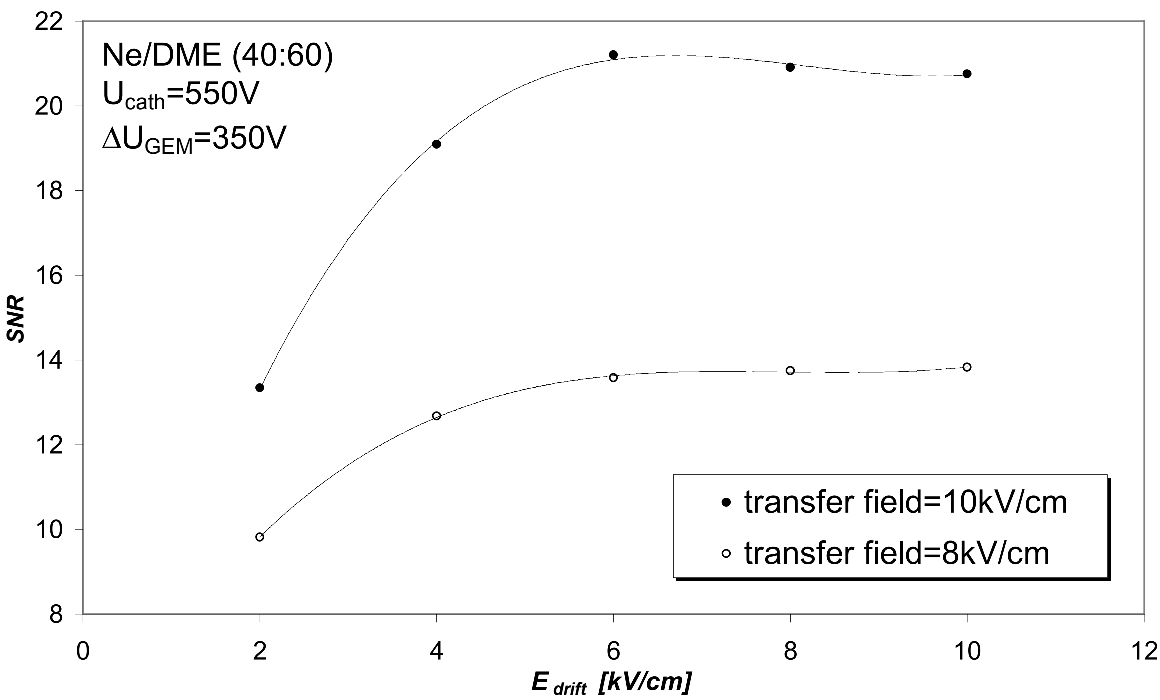

Figure 111 – Dependence of SNR on the drift field. The measurement has been carried out with 90-120GeV muons in the September 1998 X5 test beam. Results for two different settings of the transfer field are shown. The cathode and GEM voltages have been kept fixed.

Since the generation of primary ionisation is a statistical process, it is not known which amount of the charge has been amplified by the GEM. For that reason, absolute values for the SNR are given. It should be noticed, that the overall smaller SNR of the measurement with a 8kV/cm transfer field in figure 111 is not related to a transparency effect, but to the lower amplification in the transfer region. The two curves are nearly identical in their shape. This proves that there is no coupling between the drift and transfer fields. If the effects depicted in figures 105 and 109-110 would be dependent on the fields' ratio, the shape of the curves should vary when changing E_{trans}. The decrease for low drift fields can be found again, and is in the same order of magnitude as for the ^{55}Fe measurements (30%). The decrease for high fields is nearly absent. This is due to the improved optical transparency of the GEM used in GEM5 (see section 2.3.1).

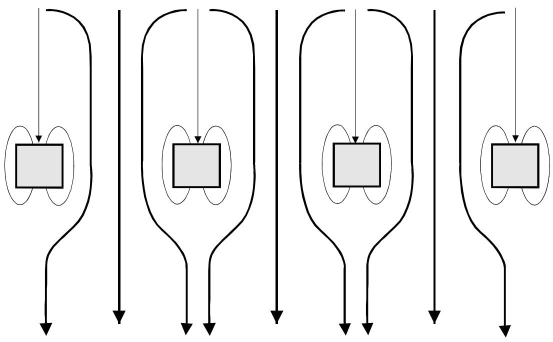

Figure 112 - The effect of an increased optical transparency

Field lines from the drift region are still bent by the GEM field, but this time they reach another hole due to the reduced copper on the top side of the GEM. The probability of a charge to disappear at the upper GEM side is simply smaller. The decreased opacity of the foil allows operation in a bigger range of field strengths. This is an encouraging result for the operation of such devices in strong magnetic fields, like the 4T field foreseen in CMS. High fields are required in those environments to cope with the Lorentz angle.

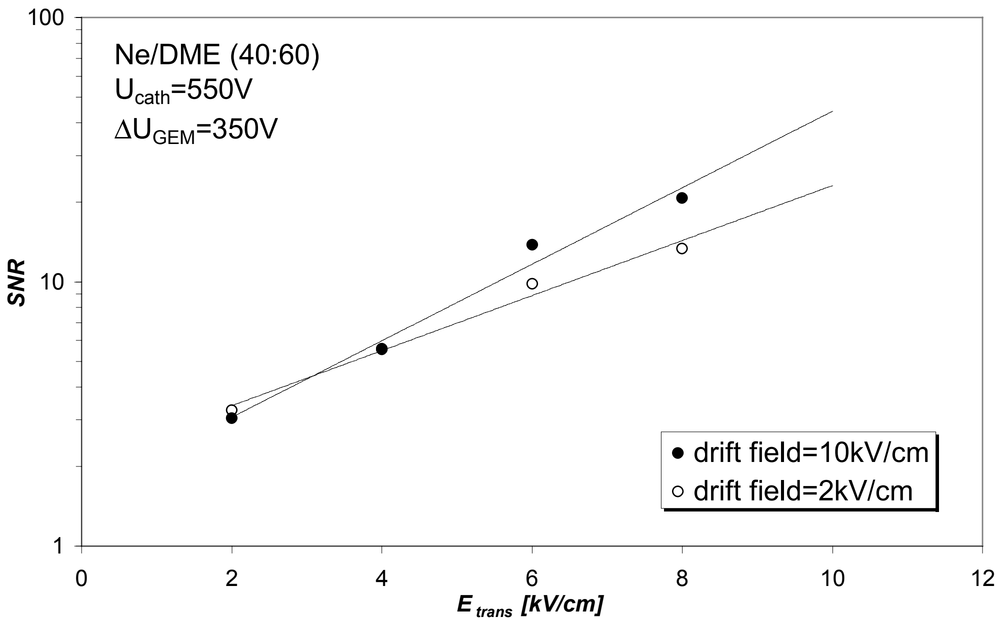

Figure 113 - Dependence of SNR on the transfer field. The measurement has been carried out with 90-120 GeV muons in the September 1998 X5 test beam. Results for two different settings of the drift field are shown. The cathode and GEM voltages have been kept fixed.

A nearly exponential dependence of the total amplification of the GEM+MSGC on the transfer field can be seen in figure 113. This effect is well known from MSGCs and expected from equation (14) **[45].**
The effects on the signal amplitude directly translate to the efficiency measurements. This is shown for the drift field variation in figure 114. Note the range of the ordinate: There is nearly no variation of the efficiency with the strength of the drift field. The smaller total efficiency for the measurement with $E_{trans} = 8$kV/cm is only caused by the reduced SNR at that field strength, as has been shown in the previous section.

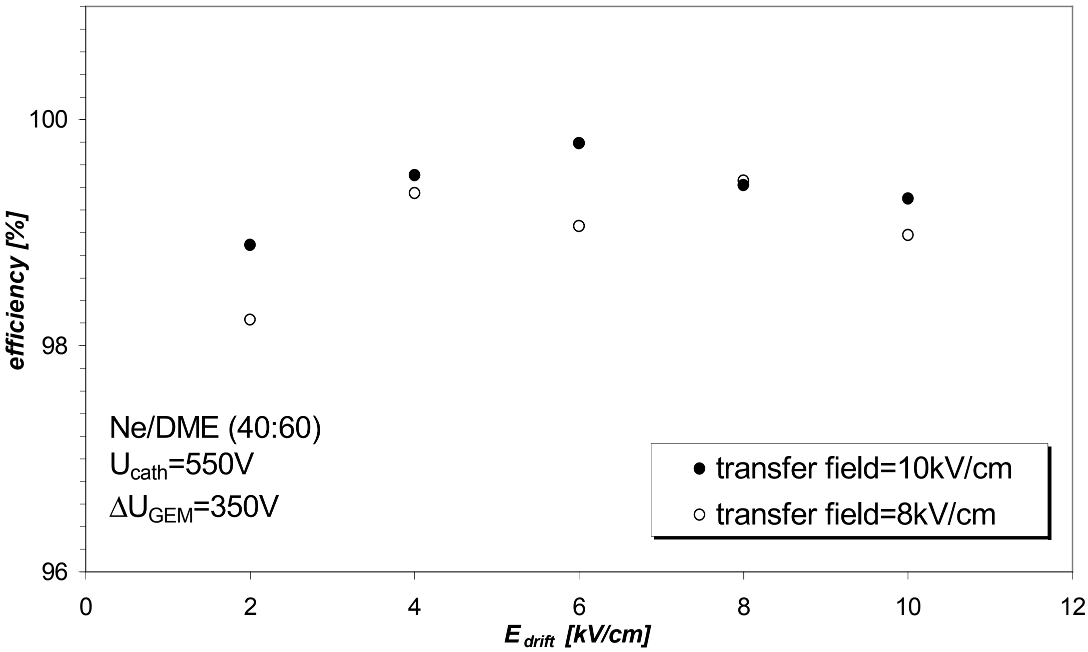

Figure 114 - Efficiency measurements for the amplification studies shown in figure 111. The variation of the efficiency with the drift field is < 1%.

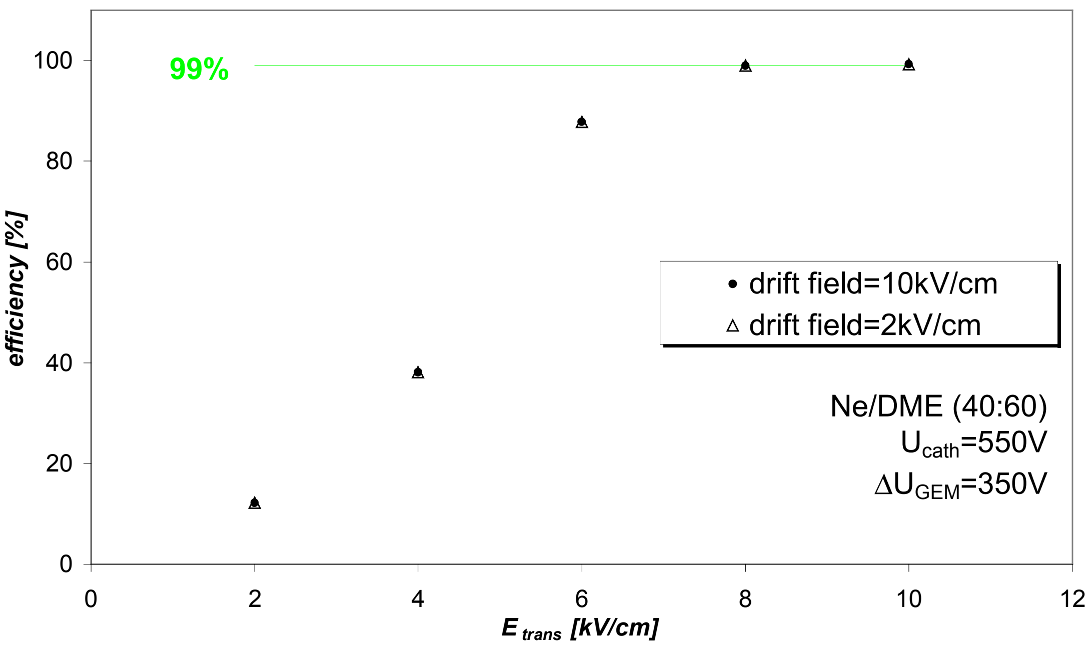

Figure 115 - Efficiency measurements for the amplification studies shown in figure 113.

Obviously, this is different for the dependence on the transfer field: Since the efficiency is directly correlated to the SNR, this effect is seen for a variation of E_{trans} as well. Figure 115 shows the result of the gain variations caused by the different transfer field settings shown in figure 113. Even when choosing two completely different values for the drift field, the measurement of the dependence of the efficiency on the transfer field yields the same result. This shows that the two fields are truly decoupled.

5.6 High intensity behaviour

The measurements in the high intensity environment of the PSI πM1 facility had only one goal: To find out, if stable operation of GEM+MSGC modules at the CMS working point of 98% detection efficiency is possible. Finding the origin of discharges in the detector module, and possible correlations between their frequency and the loss of strips, was of additional interest.

Identification of discharges

The methods of finding discharges in the detector modules have been described in section 4.4. Since the GEM+MSGC had been developed to provide stable operation in high intensity environments, such activities are rare during the measurements. For the discussion of the different types of discharges in this section, the data from almost 48h of measurements had to be compiled. A variation of the cathode voltage, whose results will be shown later, has been carried out during this period. Since this included operation at very high gain to find out when the detector module becomes unstable, all types of discharges were generated.

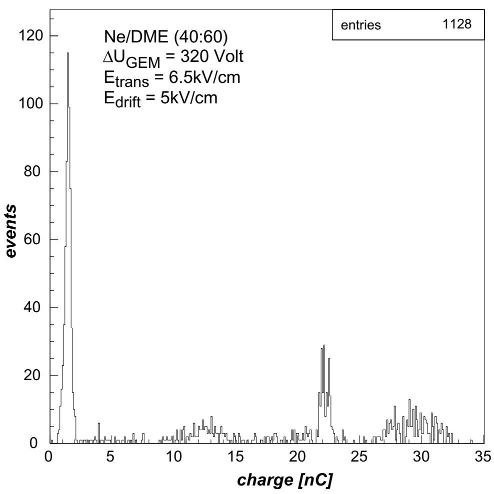

Figure 116 - Charge distribution for all measured discharges in GEM6.

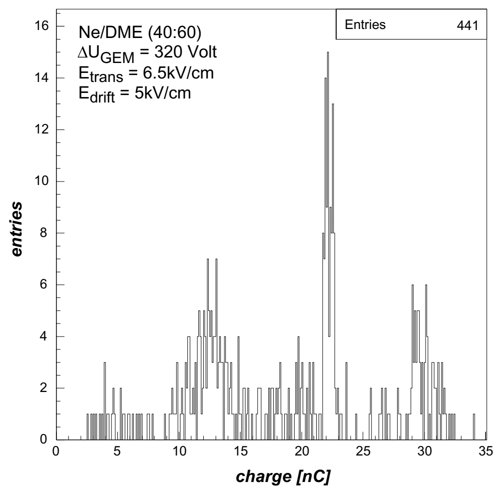

Figure 117 - The same plot as to the left – streamers have been removed here.

Figure 116 shows the distribution if the charges of all signals in the cathode current monitor are put into one histogram. Four separate peaks can be seen. The first task is now to distinguish discharges, which may be harmful to the detector module, from so-called *streamers*, which generally do not damage the GEM+MSGCs. Possible sources for streamers are HIPs, e.g. α-particles, or so-called *micro-discharges*, which may originate from microscopic imperfections on the strips' edges. Both cause an increase in current temporarily. Since the smallest active unit on an MSGC substrate is one HV group, all discharges

depositing a charge smaller than the one stored in such a group are considered to be streamers. Using the considerations from section 4.4.3, discharges are expected to have a charge of 23nC at a potential of U_{cath} = 450V. A distribution centred around that value can be clearly seen in figure 116. The leftmost peak can be identified as originating from streamers. Figure 117 shows the charge distribution without them. Comparing the number of entries from figures 116 and 117, it can be seen that the majority of activities (about two thirds) in the detector module is originating from streamers.
The detection of a discharge on the substrate is fairly easy: The charge of the signal has to be larger than that of a streamer, and no activity in any other of the current monitors of the detector module (GEM and drift cathode) is allowed. Figure 118 is the result if these events are selected. The peak matches the one in figure 117, and the measured charge is in agreement with the calculation. The corresponding signal to such an event, as recorded by the current monitor, is shown in figure 119. The steep rising edge of the signal can be seen. The expected exponential decay on the falling edge is absent, however. An oscillation can be seen instead. This is caused by the current regulation circuitry of the HV power supply. Due to the comparatively small input protection resistors on the HV connection board (see figures 74 and 138), the regulation of the supply when restoring the current to the HV group can be seen. The oscillation has been excluded from the charge measurement.

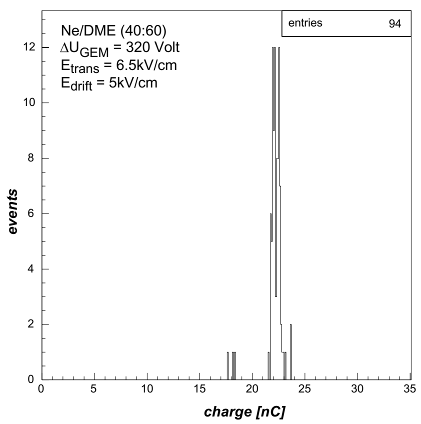

Figure 118 - Charge distribution of substrate discharges

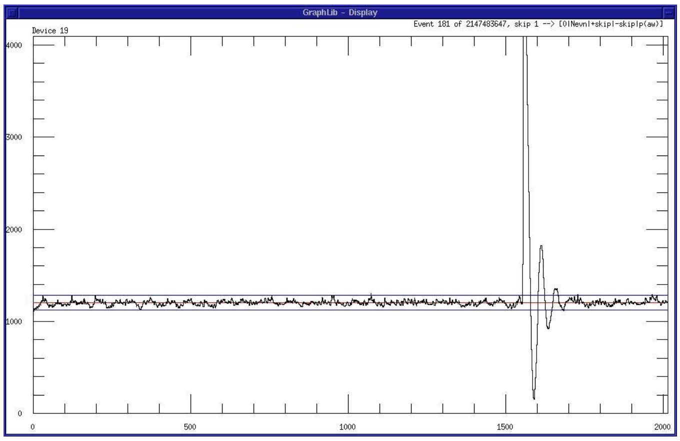

Figure 119 - A discharge on the substrate as recorded by the current monitor. The ordinate is in units of two milliseconds and the abscissa in arbitrary units

The remaining two distributions in figure 117 are more difficult to explain. Figure 121 shows a discharge in the GEM. The top diagram shows the current on the top side of the GEM. After a steep rising edge, the current drawn by this HV line exceeds the dynamic range of the ADC. This is due to the enormous capacity a GEM foil represents.
It takes several hundred milliseconds before the current decreases back to its previous value. Here the exponential decay can be seen, because the time constant for the coupled system of HV line and GEM foil is larger than the HV supply's. The current for the MSGC substrate is shown on the bottom diagram in figure 121. At exactly the same time when the discharge in the GEM appears, an increase in the current of the substrate can be seen. This is caused by the large charge cloud created by the discharge in the GEM channel which is ejected to the transfer region, eventually causing a discharge on the substrate itself. Judging by the shape of the signal, it could be misinterpreted as a HV group discharge. But the smaller charge and correlation to the GEM activity allows to distinguish between these two types of discharges.

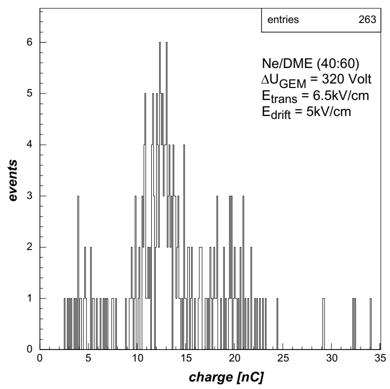

Figure 120 - Charge distribution of activities generated by GEM discharges.

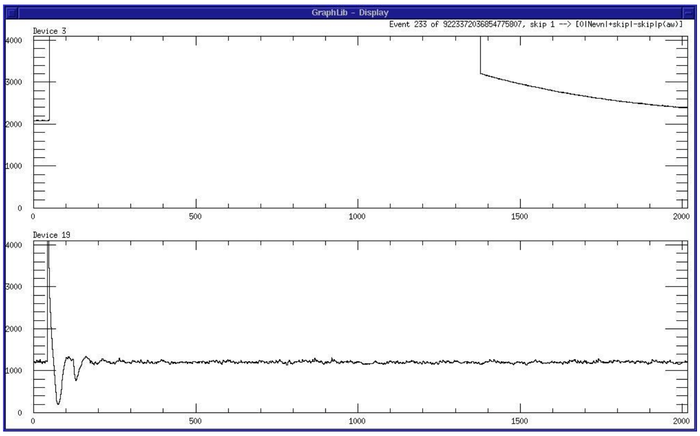

Figure 121 - A GEM discharge as recorded by the current monitors on the foil (top) and substrate (bottom).

The resulting charge distribution is shown in figure 120, if these events are selected. The third distribution in the spectrum can be identified when comparing with figure 117. It is interesting to notice that the current on the cathode remains stable after the spike caused by the GEM discharge. Even if the GEM draws current for several hundred milliseconds, the gain as measured on the substrate remains constant. The detector module therefore does not become 'blind' during a GEM discharge.

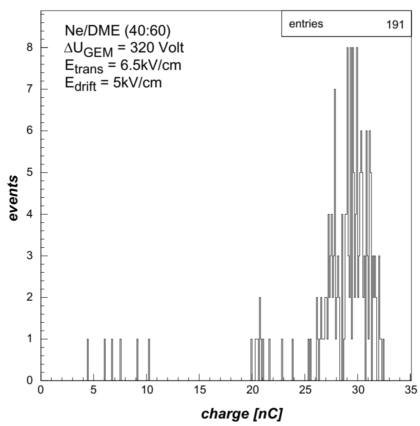

Figure 122 - Charge distribution of the substrate's reaction to a severe GEM discharge

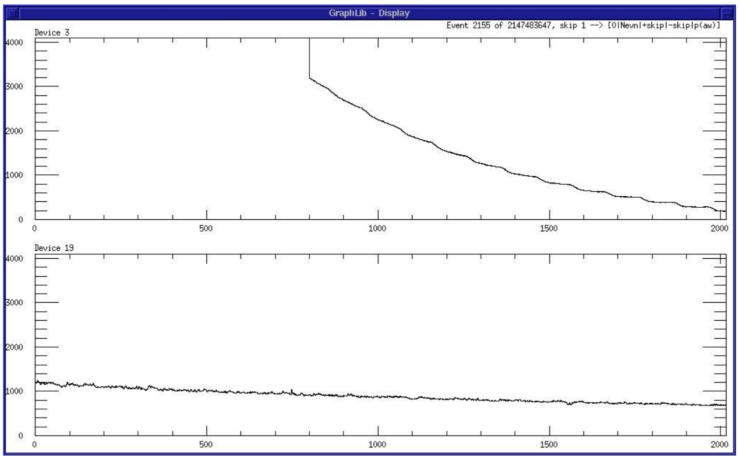

Figure 123 - A severe GEM discharge (top), which caused the power supply to shut down. The breakdown in amplification can be seen at the substrate's current (bottom).

The rightmost distribution cannot be explained by the discharge of more than one HV group: This would require a multiple of 23nC. It is caused by the most severe events encountered during high intensity test beam experiments: Discharges in the GEM, which cause the HV supply of the detector to perform an emergency shutdown. The power supply has selectable current limits, which avoid short circuits. If a discharge in the GEM or on the substrate deposits a charge cloud which is large enough, a short circuit between anodes and cathodes, or between the top and bottom sides of the GEM can happen.

The power supply switches the HV lines off in this case. Figure 123 shows such an event. The discharge in the GEM, which looks like figure 121 in the beginning, can not be seen. The deposited charge in that event is so huge, that it takes more than 4s for the current to reach the dynamic range of the ADC again. Only the last part of the discharge can be seen in figure 123. The shutdown of the HV power supply can be seen on the current of the GEM (top diagram), which is reduced to zero. The current on the MSGC substrate (bottom diagram in figure 123) decreases, too. This is caused by the loss of the GEM amplification. The rightmost distribution in charge spectrum of figure 116 is revealed (figure 122) when selecting these events. A discharge emerging from the drift cathode could also happen, but not a single event was found during two weeks of high intensity measurements.

Correlation of discharge rate to strip mortality

The most important information one wants to gain from measurements in high intensity beams is the stability of the detector modules. An indicator is the number of anodes lost due to discharges. It is therefore interesting to know the correlation between the number of discharges per unit time, and the amplification of the detector module. The latter is given in SNR, as discussed in sections 4.2.3 and 5.1. The discharge rate is given in ‘sparks/h’ – this is short for ‘activities which are not streamers’ per hour. The SNR measurement at the PSI test beam facility has one complication, however: The value becomes rate dependent.

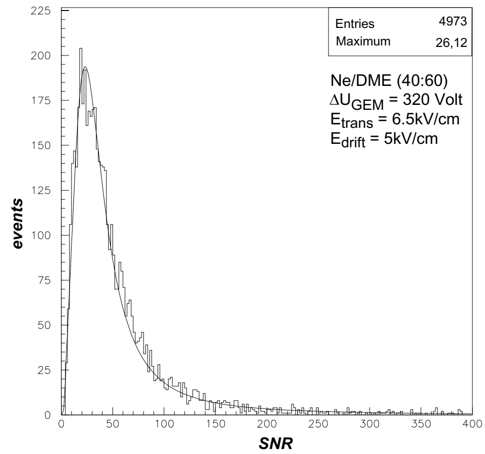

Figure 124 - Landau distribution for GEM6 when operated at PSI with a flux of ≈ 10^2Hz/mm^2

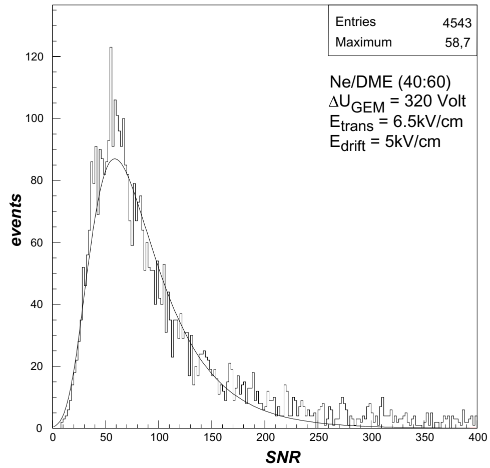

Figure 125 - Landau distribution for GEM6 when operated at PSI with a flux of ≈ 10^3Hz/mm^2

Figures 124 and 125 show that effect. Both SNR distributions have been measured with the same voltage settings, but show a difference of nearly a factor two in the position of the maximum.

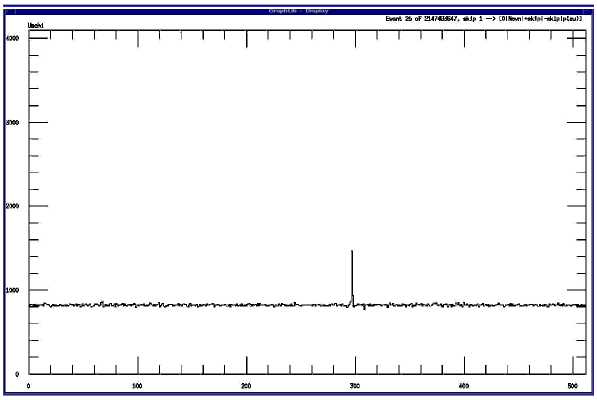

Figure 126 - A low intensity event. The ordinate is the strip number and the abscissa in ADC counts.

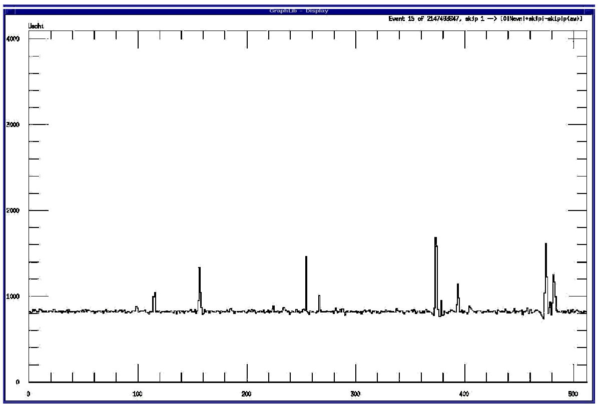

Figure 127 - A typical event at high intensity

The effect can be explained when looking at the particle signals for a typical event measured at low and high intensity: While usually one particle traverses the detector module per event in low intensity, an average of eight particle signals is recorded at high intensity. Since the analysis software always takes the signal with the largest charge, the Landau distribution is systematically shifted to higher values. This effect can only be coped with by using a fast beam hodoscope, which was not available.[43] Measurements with low intensity beam conditions therefore had to be carried out for every set of voltages applied to the GEM+MSGC as a reference. This was necessary to compare the results with the efficiency measurements from the X5 test beam experiment.

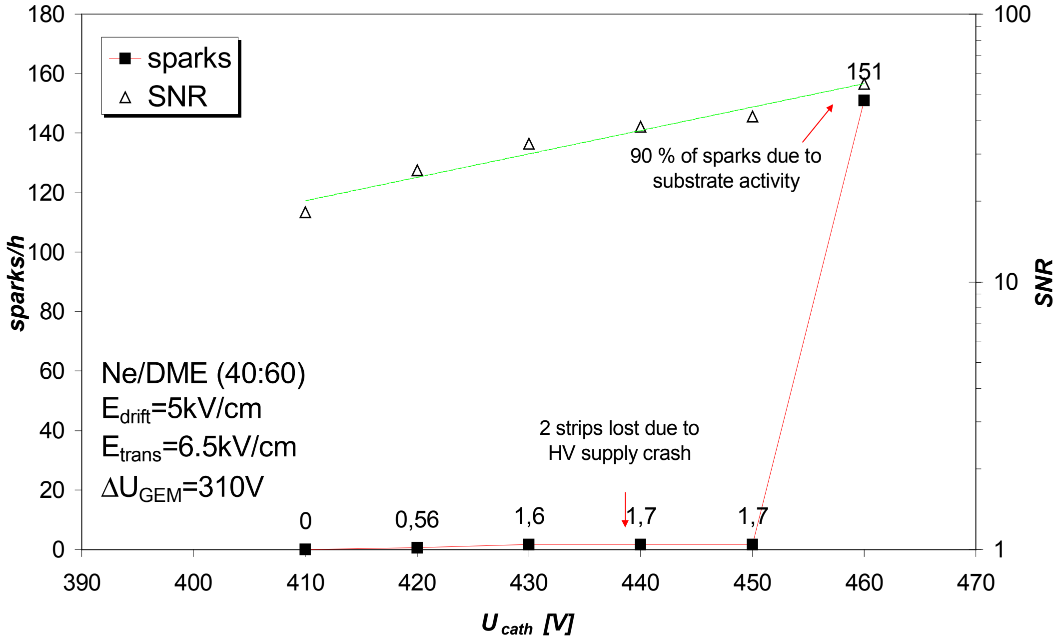

Figure 128 - Measurement of the spark rate of GEM6 for ΔU_{GEM} = 310V. The spark rate is given on the left axis, and the SNR measured at low intensity is denoted on the right axis.

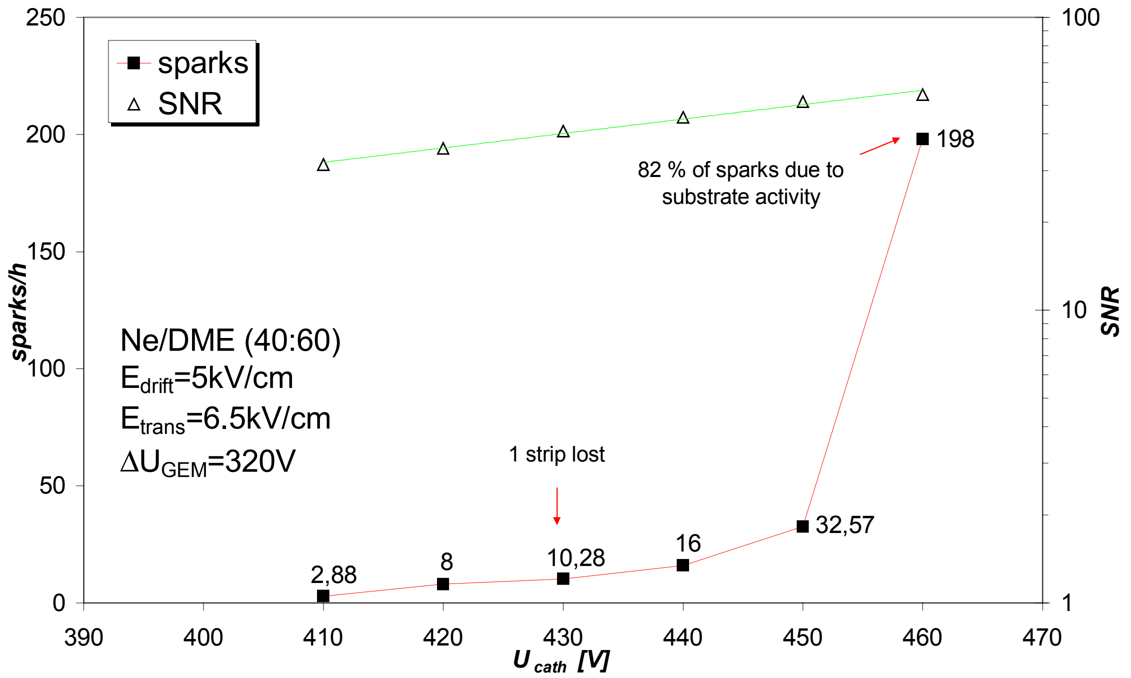

Figure 129 - Measurement of the spark rate for ΔU_{GEM} = 320V.

[43] No hodoscope is available at the PSI πM1 facility.

Figures 128 and 129 show the spark rate measurements for two different GEM potential differences ΔU_{GEM}. A 'spark-free' region ranging from SNR ≈ 20-45 can be seen. A sudden rise in the spark rate is visible in both figures. Two strips were lost in the spark free region in figure 128; this was caused by a system crash of the HV power supply, which caused a shutdown of all HV lines. There is no explanation for the strip lost in figure 129, because even at higher spark rates no broken strip was recorded. In this region, where up to several hundred sparks/h were recorded, stable operation is no longer possible.
The advantage of a GEM-equipped detector module can be clearly seen in figures 128 and 129: When the detector module reaches the edge of the plateau where safe operation is possible, it can be extended by shifting the amplification between the MSGC substrate and the GEM. This leads to an extended plateau.

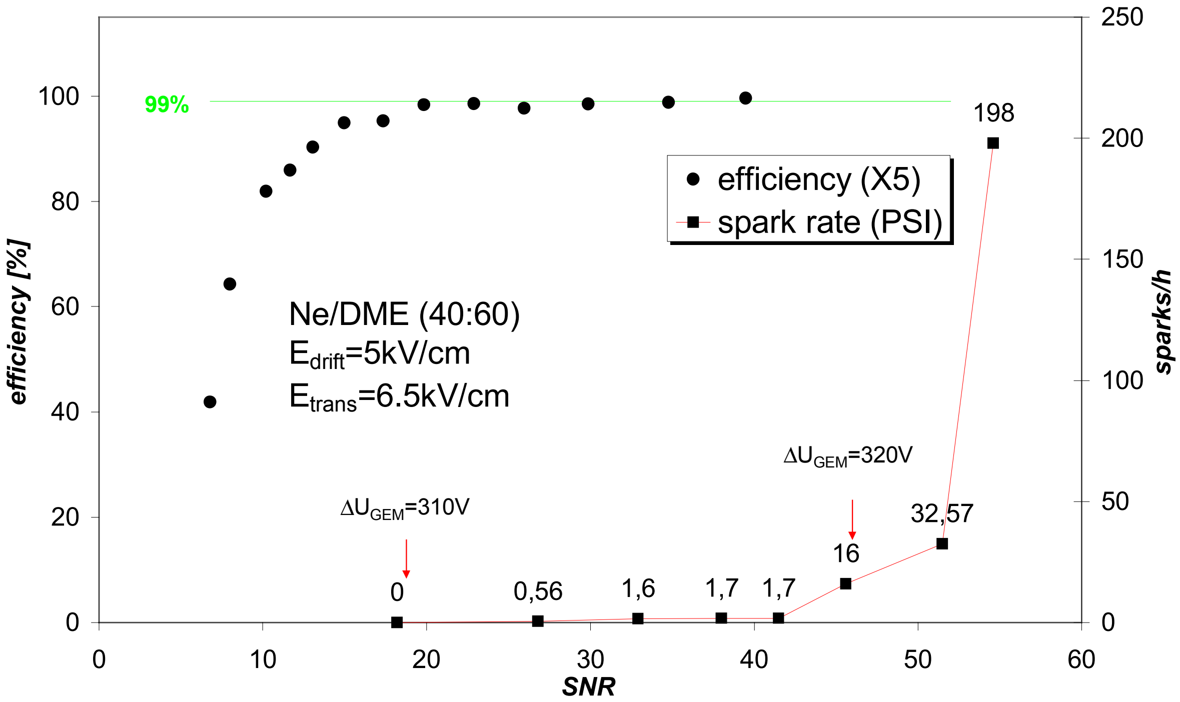

Figure 130 - A compilation of the efficiency and spark rate measurements for GEM6.

All data available for GEM6 from the efficiency measurements at the X5B test facility in June 1999 and the PSI test beam in April 1999 have been compiled in figure 130. The plateaux for efficiency and spark rate can be seen. It can be concluded, that safe operation at full detection efficiency is possible in a range up to SNR = 52. Since full efficiency is already reached for SNR ≈ 20, this provides a large safety margin. It is therefore possible to increase the gain if required for some reason, e.g. ageing, during the running period of LHC. This margin of a factor two is degraded by the next generation of frontend electronics. Due to the mode of operation of these chips, a SNR increased by a factor of 2.2 compared to the PreMux128 chip will be required to reach the working point **[70]**. A SNR of 37 is therefore needed to reach the CMS requirement of 98% detection efficiency, which is reached for SNR = 17 with the present amplifiers. This reduces the safety margin to 30%, but stable operation even at this considerably high gain could be proven.

Stability of the detector module and strip losses

Figure 131 shows the noise of the 512 strips of GEM6 right after commissioning of the detector module. Six strips are broken in total, recognisable by the reduced noise on these anodes. Two strips were short circuited to the neighbouring cathodes due to production

failures, and the other four strips were lost in the process of building the detector module. Figure 132 shows the situation after > 140h in the high intensity PSI test beam: A total number of 44 strips were lost.
The GEM+MSGC was operated at very high SNR (up to SNR = 100) in low intensity beam conditions in the beginning of the test beam. The detector was operated with a transfer field of E_{trans} = 9kV/cm for high SNR during that period of nearly six days. The analysis of broken strips showed that 27 strips were lost during that time. Only 14 strips were lost in an identical time interval after a decrease to E_{trans} = 7kV/cm.

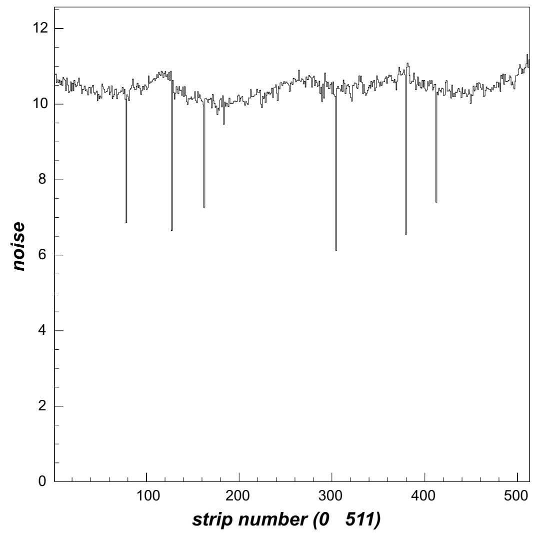

Figure 131 - Dead strips before the high intensity beam test

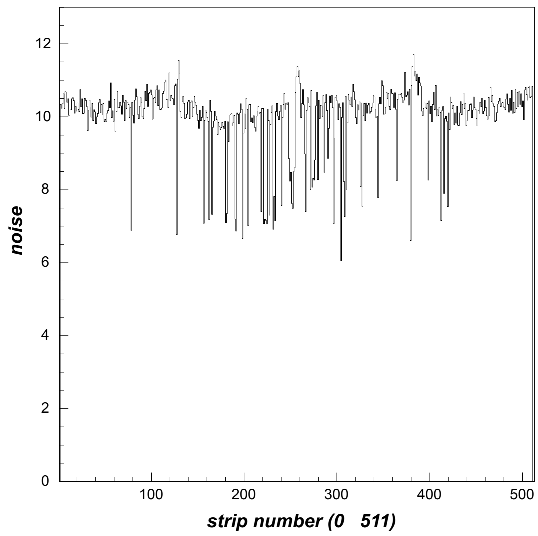

Figure 132 - Dead strips after the high intensity beam test.

A further decrease to the final value of E_{trans} = 6.5kV/cm allowed to carry out all the experiments discussed in this section, while only losing two strips in the HV supply crash. Only one strip was lost due to a discharge. A strong correlation between the probability to break a strip and the transfer field can therefore be concluded. The majority of the strips (27 + 14 = 41) were lost in the first 40h of the test beam with a 9kV/cm transfer field, while operating mostly at low intensity with a negligible spark rate. Only one more strip has been lost due to a discharge in the remaining 100h of the test beam!

5.7 Charging effects

The high rate available in the high intensity test beam experiment at the PSI in April 1999 provided the opportunity to look at effects of charging on the GEM foil. As can be seen in figure 38, there are always some drift lines ending on the bare polyimide inside a GEM channel. The material is charged up locally by this effect, just like discussed in section 2.2.2 for the MSGC substrate. Contrary to the effect on an MSGC, a charging up on the GEM increases the gain. This is caused by the cylindrical geometry of the GEM channels: A charge deposition on the wall of a channel causes a confinement of the drift lines to the centre of the hole. The effective diameter is reduced that way. As a result, the amplification is increased as shown in figure 41.

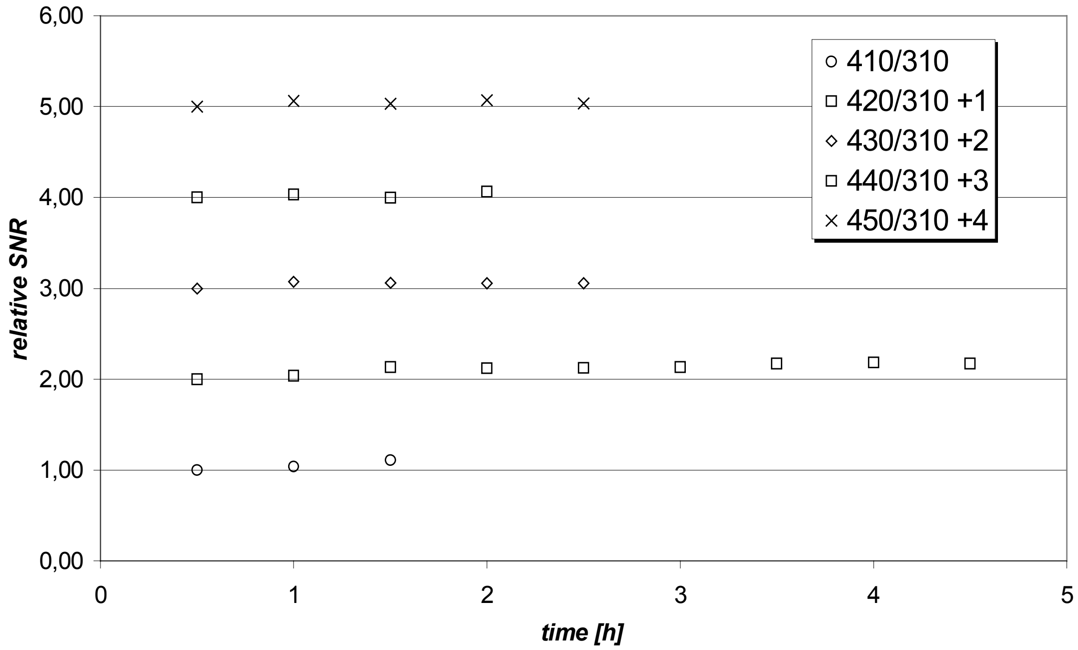

Figure 133 - Measurements of charging effects with GEM6 in the April 1999 PSI test beam. A mixture of Ne/DME (40:60) was used. The field configuration was E_{drift} = 5kV/cm and E_{trans} = 6.5kV/cm. The GEM voltage was set to ΔU_{GEM} = 310V. The first number in the legend denotes the cathode voltage U_{cath}. The development over time of the relative SNR, normalised to the first measurement with that particular voltage, is shown. For a better readability, the measurements for separate cathode voltages are shifted by a constant factor, as indicated in the legend.

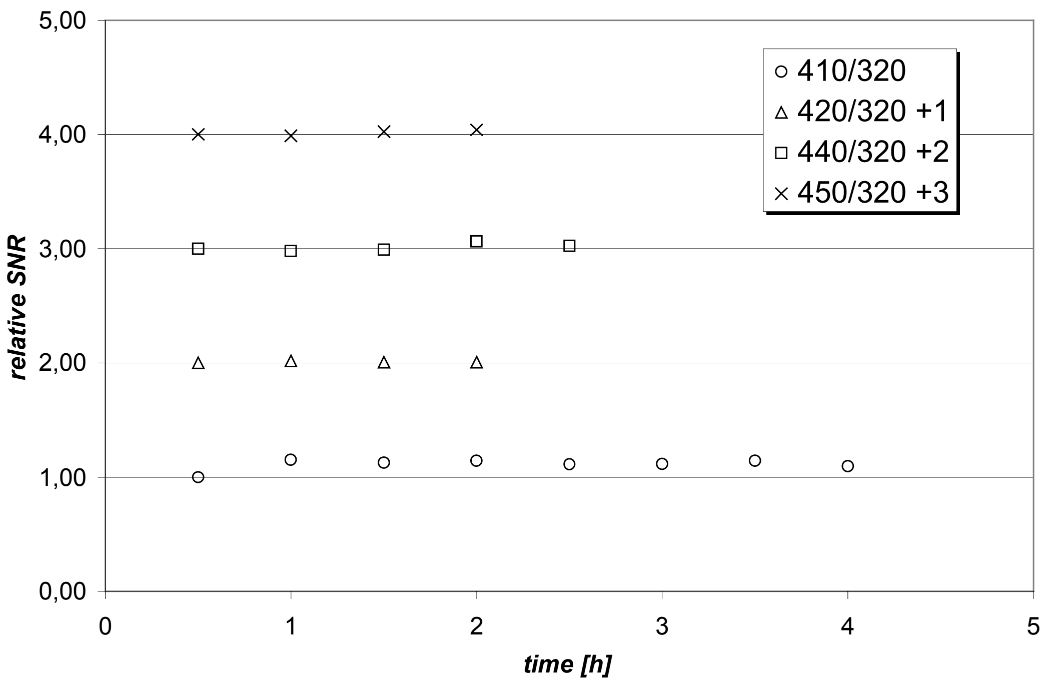

Figure 134 - The same measurements as in figure 133, but for a higher ΔU_{GEM}

Figure 133 shows the stability of GEM6 over time for different voltage settings. All parameters were kept constant for the curves in the diagram, and successive measurements were carried out over time. The SNR values are normalised to the first one for each curve. No increase[44] of the amplification with time is visible for all voltage settings. This is independent of the GEM potential difference ΔU_{GEM} as can be seen in figure 134.

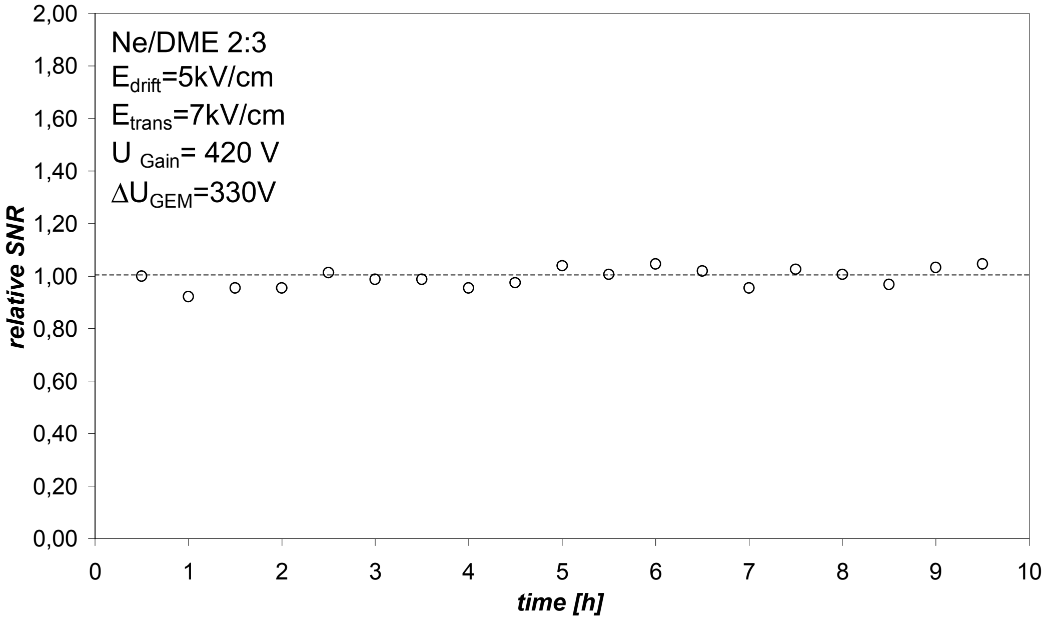

Figure 135 - Stability of the gain in the CMS forward prototype module as measured in the April 1999 PSI test beam experiment. No charging up in the high intensity beam is visible.

No charging up effects were present for the CMS forward tracker prototype, as can be seen in figure 135. Figure 136 shows the stability of the absolute SNR over time: The beam conditions were changed to low intensity for one measurement every eight hours. It was carried out immediately at reference voltages corresponding to a SNR of 15. No variation with time is visible as can be seen in the figure. The parabolic shape for the middle two measurements is probably due to temperature changes.

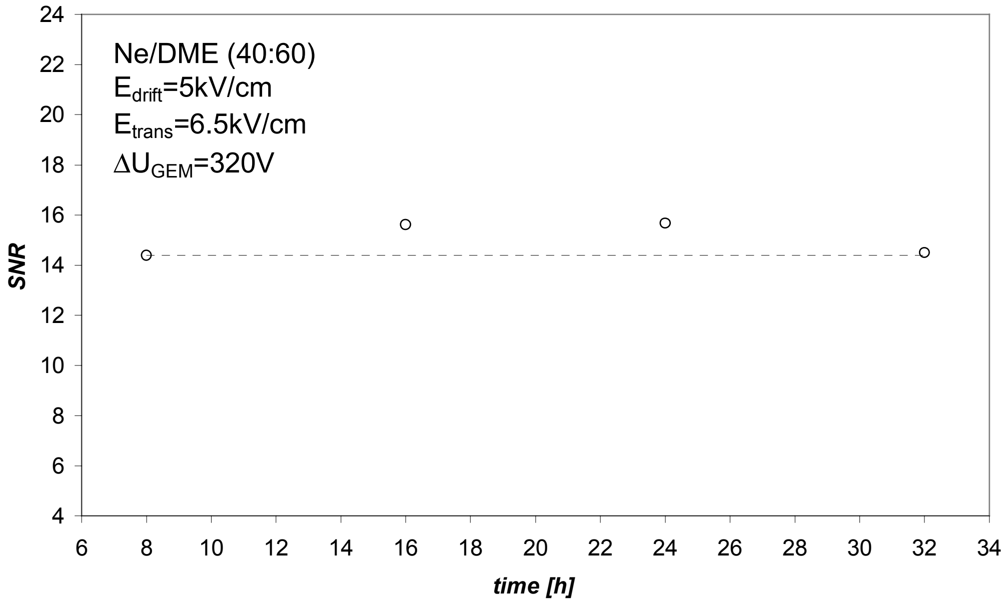

Figure 136 - Stability of the absolute SNR for GEM6 over time.

[44] A possible charging effect on the substrate would cause the SNR to drop with time as discussed in section 2.2.2. No evidence for charging up of the substrate was found.

6 CONCLUSIONS

Triggered by limitations discovered in the operation of Micro Strip Gas Chambers in LHC-like environments, this thesis introduces MSGCs with an additional GEM as second amplification stage as a possible solution for the CMS experiment. A forward prototype module, based on the first MSGC tracker milestone has been built. Adjustments to the original design have been made, and tools for the construction of GEM-based detector modules have been developed.
The GEM foils have been successfully developed and produced together with an industrial partner, and their reproducibility and reliability could be proven.
Several smaller GEM+MSGCs have been built to study the performance and their capability to operate in LHC-like conditions. The amplification behaviour was studied in the standard CMS gas mixture of Ne/DME (40:60), as well as in Ar/CO_2 (80:20) and Ar/C_3H_8. Gains up to 20000 in Ne/DME were reached, exceeding the performance of an MSGC at similar voltages by a factor of ten at least. The spatial resolution and efficiency in Ne/DME and Ar/CO_2 were measured in two test beam experiments. A detection efficiency of 99% for MIPs at a SNR > 15 for Ne/DME, and SNR > 27 for Ar/CO_2 was measured. It could be shown for the first time that the detection efficiency is independent of the origin of the charge amplification. The spatial resolution was found to be < 40µm in Ne/DME.
Extensive measurements of the choice of fields' impact on the detector performance have been carried out. It could be shown that the two drift fields are decoupled. Evidence for the correctness of the theory on transparency effects in GEM+MSGCs was found in a measurement of the cluster size of the particle signals, shown for the first time in this thesis.
A high intensity beam test with LHC-like conditions was carried out to study the robustness of GEM+MSGCs. A correlation of the probability to lose a strip in a discharge with the strength of the transfer field was found. No evidence for a correlation between the spark rate and the number of lost strips was found.
No evidence of charging up of the detector modules has been found. It therefore seems to be feasible to operate GEM+MSGC modules without coating, significantly reducing the costs of the substrates.
A plateau of nearly spark-free operation, while maintaining a detection efficiency of 99%, has been identified. Stable operation up to a SNR of 55 has been shown.

The results are comparable to those achieved with the MSGC-only technology. GEM+MSGC modules have the additional benefit of the possibility of sharing the gain between the two amplifying stages. This gives one a greater flexibility in adopting the detector module to the environment. Even poor MSGC substrates can be recuperated by shifting a larger amount of the gain necessary for operation to the GEM or vice versa. This is extremely valuable when thinking of a large scale mass production, and the possibility to optimise the yield of the detector modules' production by this feature unique to the GEM+MSGCs. Another high rate beam test has been carried out in November 1999 with 18 CMS forward prototype modules, consisting of a total number of 72 MSGC substrates and large area GEMs, covering the whole detection surface. The detectors' stability excelled the results given in this thesis and showed the mass production readiness of this technology.

7 BIBLIOGRAPHY

[1] P. Higgs, **Broken symmetries, massless particles and gauge fields**, Phys. Rev. Lett. 12 (1964), 132
[2] P. Higgs, **Broken symmetries and the mass of gauge bosons**, Phys. Rev. Lett. 13 (1964), 508
[3] P. Higgs, **Spontaneous symmetry breakdown without massless bosons**, Phys. Rev. Lett. 145 (1966), 1156
[4] E. Ferrer, **Standard Model Higgs Search at LEP200**, 35th Rencontres de Moriond, Les Arcs, March 2000, to be published in the proceedings
[5] The LHC study group, **The Large Hadron Collider – Conceptual Design**, CERN/AC/95-05 (LHC), 1995
[6] The CMS Collaboration, **Tracker Technical Design Report**, CERN/LHCC 98/6, April 1998
[7] The CMS Collaboration, **Electromagnetic Calorimeter Technical Design Report**, CERN/LHCC 97/33, 1997
[8] The CMS Collaboration, **Hadron Calorimeter Technical Design Report**, CERN/LHCC 97/31, 1997
[9] The CMS Collaboration, **Muon Project Technical Design Report**, CERN/LHCC 97/32, 1997
[10] A. Oed, **Position-sensitive detector with microstrip anode for electron multiplication with gases**, NIM (263A) 351-359, 1988
[11] O. Pooth, **Untersuchung eines Mikrostreifengasdetektors**, PITHA 95/32, RWTH Aachen, November 1995
[12] F. Sauli, **The Gas Electron Multiplier**, NIM (386A) 531ff, 1997
[13] F. Sauli, **Principles of Operation of Multi Wire Proportional and Drift Chambers**, CERN 77-09, May 1977
[14] W. Blum, L. Rolandi, **Particle Detection with Drift Chambers**, ISBN 3-540-56425-X, Springer Verlag, 1994
[15] S. Bachmann, **Investigation of Microstrip Gas Chambers and their application in the CMS experiment**, PITHA 98/25, RWTH Aachen, August 1998
[16] O. Pooth, **Micro Strip Gas Detector Modules: Development and Integration in the Forward Tracking System of the CMS Experiment**, PITHA 99/29, RWTH Aachen, September 1999
[17] http://consult.cern.ch/writeup/garfield/gas/welcome.html
[18] http://www.photcoef.com
[19] M.J. Berger, J.H. Hubbell, **XCOM: Photon Cross Sections on a Personal Computer**, NBSIR 87-3597, National Bureau of Standards, 1987
[20] E. Storm, H.I. Israel, **Photon Cross Sections from 0.001 to 100MeV**, LA-3753, UC-34-Physics TID-4500, Los Alamos Scientific Laboratory, 1967
[21] D.E. Cullen et al., **Tables and Graphs of Photon-Interaction Cross Section from 10eV to 100GeV**, UCRL-50400 Vol.6 Rev.4, Lawrence Livermore National Laboratory Evaluated Photon Library (EPDL), October 1989

[22] A. Peisert, F. Sauli, **Drift and Diffusion of Electrons in Gases: A Compilation**, CERN 84-08, July 1984

[23] S. Ramo, **Currents induced in electron motion**, Proceedings IRE 27 (584), 1939

[24] V. Radeka, **Low-noise techniques in detectors**, Nuclear Particle Science 217-77, 1988

[25] R. Bellazzini et. al., **Electric field, avalanche growth and signal development in micro strip gas chambers and micro gap chambers**, INFN Pisa 94/02, February 1994

[26] MAGBOLTZ 2 by S. Biagi, plots done by R. Veenhof, personal communications, January 2000

[27] G. Charpak et al., **The use of multiwire proportional counters to select and localise charged particles**, NIM (62A) 262, 1968

[28] J. Florent et al., **The electrostatic field in microstrip chambers and its influence on detector performance**, CERN-PPE/92-78, CERN, 1992

[29] J. Bohm et al., **High rate operation and lifetime studies with micro-strip gas chambers**, NIM (360A) 34-41, 1995

[30] F. Sauli, **Development of high rate MSGCs: Overview of results from RD-28**, Proceedings of the 5th International Conference on Advanced Technology and Particle Physics, Como, October 1996

[31] F. Angelini et al., **Operation of MSGCs with gold strips built on surface treated thin glasses**, NIM (382A) 461-469, 1996

[32] B. Bláha et al., **Electrical properties of semiconducting glass**, Preprint submitted to NIM, November 1997

[33] R. Bouclier et. al, **High rate operation of micro-strip gas chambers on diamond coated glass**, NIM (369A) 328-331, 1996

[34] O. Pooth, **Report on the CMS forward-backward milestone**, NIM (419A) 375-380, Proceedings of the Vienna Wire Chamber Conference, 1998

[35] D. Macke, **Bau und Test eines Hodoskops zur Untersuchung von Mikrostreifen-Gasdetektoren**, PITHA 97/9, RWTH Aachen, Januar 1997

[36] S. Visbeck, **Untersuchungen von Prototypen der Mikrostreifen-Gaskammern (MSGC) des inneren Spurkammersystems des HERA-B Experiments**, diploma thesis, Physikalisches Institut der Universität Heidelberg, September 1996

[37] R. Bellazzini et al., publication in preparation

[38] M. Hoch, **Development of Fast Tracking Detectors: Micro Strip Gas Chamber and Gas Electron Multiplier**, Thesis, Institut für Angewandte und Technische Physik, Technische Universität Wien, April 1998

[39] J. Kostelnik, personal communication, Würth Elektronik, Rot am See, Germany

[40] H. Park, personal communication, Würth Elektronik, Rot am See, Germany

[41] S. Bachmann et al., **Charge Amplification and Transfer Processes in the Gas Electron Multiplier**, CERN-EP/99-48, April 1999

[42] V. Zhukov, personal communication

[43] J. Benlloch et. al, **Further Developments of the Gas Electron Multiplier (GEM)**, CERN-EP/98-50, March 1998

[44] R. Bouclier, **Study of materials outgassing and their effect on gaseous detector lifetime**, CMS TN96/38, March 1996

[45] M. Ackermann et al., **Large scale test of wedge shaped Micro Strip Gas counters**, NIM (436A) 313-325, 1999

[46] T. Barvich et al., **Investigation of a two-stage amplifying detector module with a fourfold sensor plane**, CMS Note 1999/036, CERN, June 1999

[47] J. Kremp, **Entwicklung eines Mikrostreifengasdetektormoduls für den inneren Spurdetektor bei CMS**, PITHA 97/47, RWTH Aachen, December 1997

[48] J. Benlloch et al., **Further developments of the Gas Electron Multiplier**, Proceedings of the Wire Chamber Conference 1998, NIM (419A), 1998

[49] L. Jones et al., **PreShape32 User Manual 1.0**, Rutherford Appleton Laboratory, 1993

[50] L. Jones et al., **PreMux128 Specification 2.3**, Rutherford Appleton Laboratory, 1995

[51] A. Nowack, **Steigert eine Gas-Elektronen-Vervielfachungsfolie die Betriebssicherheit eines Mikrostreifengasdetektors?**, PITHA 98/30, RWTH Aachen, August 1998

[52] D. Macke, A. Nowack, **Datenerfassung für die Detektorentwicklung in der Hochenergiephysik,** Proceedings Virtuelle Instrumente in der Praxis, Hüthig-Verlag Heidelberg, ISBN 3-7785-2729-0, 1998

[53] F. Beißel, **CUMO – HV Current monitor**, instruction manual, III. Physikalisches Institut B, RWTH Aachen, September 1997

[54] http://www.physik.rwth-aachen.de/group/IIIphys/CMS/tracker/software/software.html

[55] S. Masson, **Entwicklung, Bau und Betrieb universeller Anlagen zur Gasversorgung für das innere Spurkammersystem des H1-Detektors,** PITHA 94/50, RWTH Aachen, 1994

[56] K. Hangarter, F. Beißel, **Low Cost Gas System**, instruction manual, III. Physikalisches Institut B, RWTH Aachen, 1994

[57] CAEN, **High Voltage System Model SY127**, instruction manual, April 1991

[58] B. Baiboussinov et al., Readout and slow control system for the forward MSGC prototype, CERN documentation, May 1997

[59] V. Commichau, **PREMUXADO00**, instruction manual, III. Physikalisches Institut B, RWTH Aachen, 1996

[60] http://cern.web.cern.ch/CERN/Divisions/SL/spspage.html

[61] L. Gatignon, **The West Experimental Area at the CERN SPS,** CERN SL-99-013 EA

[62] L. Celano et al., **A high resolution beam telescope built with double sided silicon strip detectors**, NIM (381A) 49-56, 1996

[63] O. Bouhali et al., **CMS Forward-Backward MSGC milestone,** CMS NOTE 1998/095, CERN, 1998

[64] F. Drouhin et al., **MF1 Data Acquisition,** presentation given at the forward tracker meeting, Bruxelles, March 1997

[65] C. Knöß, **Erweiterung eines Hodoskops mit dem Ziel der Vermessung von Stereo-Mikrostreifengasdetektoren**, PITHA 99/26, RWTH Aachen, Juni 1999

[66] C. Grupen, **Teilchendetektoren**, ISBN 3-411-16571-5, BI Wissenschaftsverlag

[67] M. Gottschalk, **Bau und Test eines GEM-verstärkten MSGC-Moduls für den CMS Vorwärtsbereich**, PITHA 03/00, RWTH Aachen, Januar 2000

[68] A. Papanestis, personal communication, INFN Pisa

[69] W. Beaumont et al., **Studies of an MSGC equipped with a GEM grid as a tracking device**, Proceedings of the Wire Chamber Conference 1998, NIM (419A) 394-399, 1998

[70] G. Hall, **What is the possible time precision of MSGCs in CMS?**, CMS IN 1998/015, CERN, May 1998

A GAS PROPERTIES

Gas	*Z*	*A*	*ρ* [g/cm^{-3}]	*I_0* [eV]	*W* [eV]	*dE/dx* [kV/cm]	*n_p* [cm^{-1}]	*n_t* [cm^{-1}]
He	2	4	$1.66 \cdot 10^{-4}$	24.6	41	0.32	5.9	7.8
Ne	10	20.2	$8.39 \cdot 10^{-4}$	21.6	36	1.56	12	39
Ar	18	39.9	$1.66 \cdot 10^{-3}$	15.8	26	2.44	29.4	94
C_3H_8 (Propane)	26	44.1	$2.4 \cdot 10^{-3}$	10.8	23	4.27	67.6	176.5
C_2H_6O (DME)	26	46	$2.2 \cdot 10^{-3}$	10	23.9	3.9	55	160

Table 2 - Properties for common counting gases. *Z*: atomic number; *A*: atomic mass; *ρ*: density; I_0: average ionisation energy; *W*: average energy for ion pair production; *dE/dx*: energy loss; n_p: number of primary ion pairs; n_T: total number of ion pairs. Source: **[13]**, **[15]** - **[17]**.

Gas	*Ion*	*μ* [cm^2 V^{-1} s^{-1}]
He	He^+	10
Ar	Ar^+	1
C_3H_8 (propane)	$C_3H_8^+$	0.793
C_2H_6O (DME)	DME^+	0.56

Table 3 - Mobility *μ* of ions in different gases at atmospheric pressure **[17]**.

B DRIFT VELOCITIES

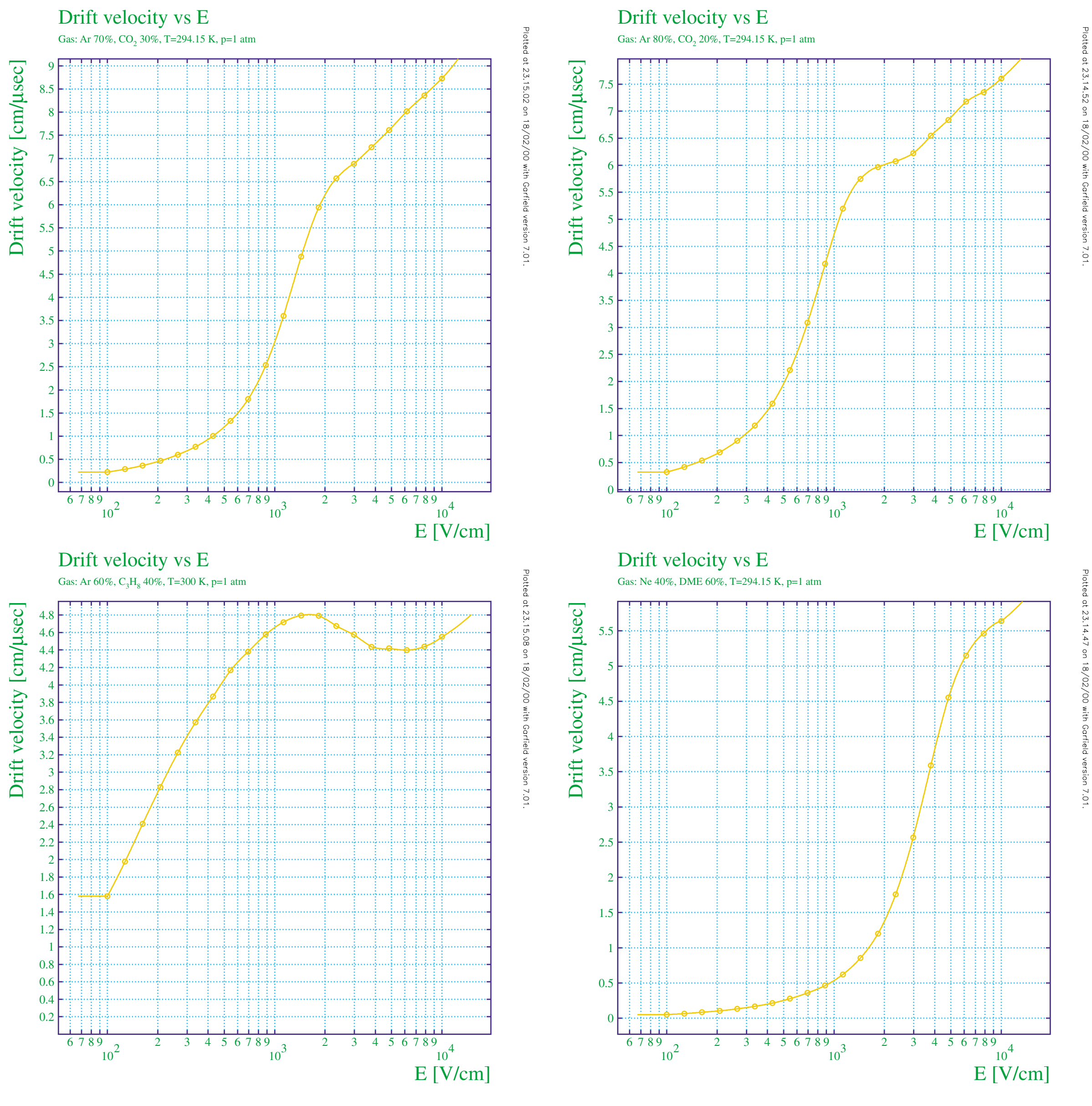

Table 4 - Drift velocities for the gas mixtures used in this work. The plots have been calculated using *MAGBOLTZ 2* **[26]**.

C SUBSTRATE ETCHING PROCESS

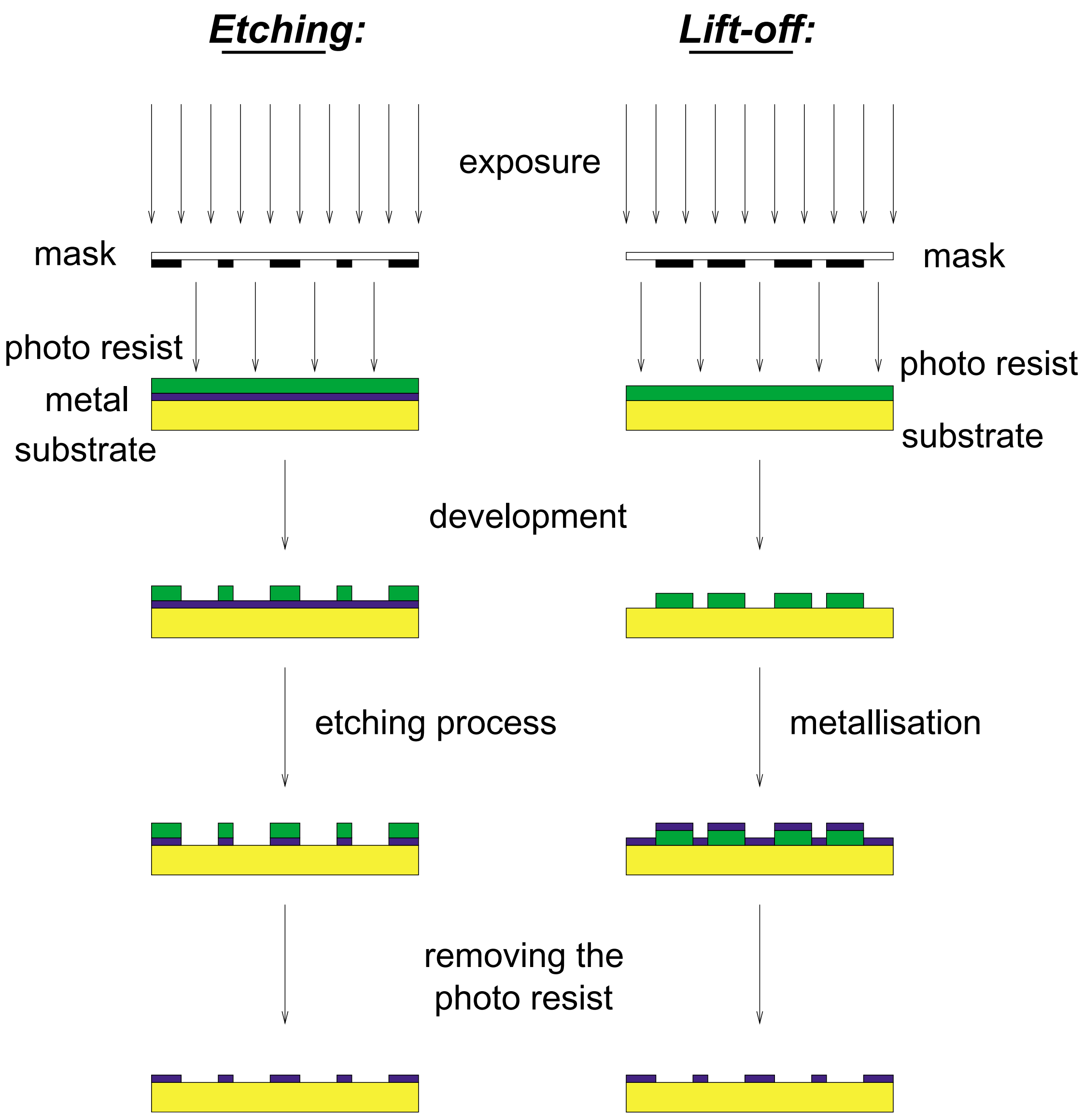

Figure 137 - Substrate etching process for positive ("etching") and negative ("lift-off") processes. The lift-off process is usually used for metals requiring an adhesive layer, e.g. titan or chromium, to stick to the glass, because no additional alignment process is required.

D HIGH VOLTAG E CONNECTION CIRCUIT

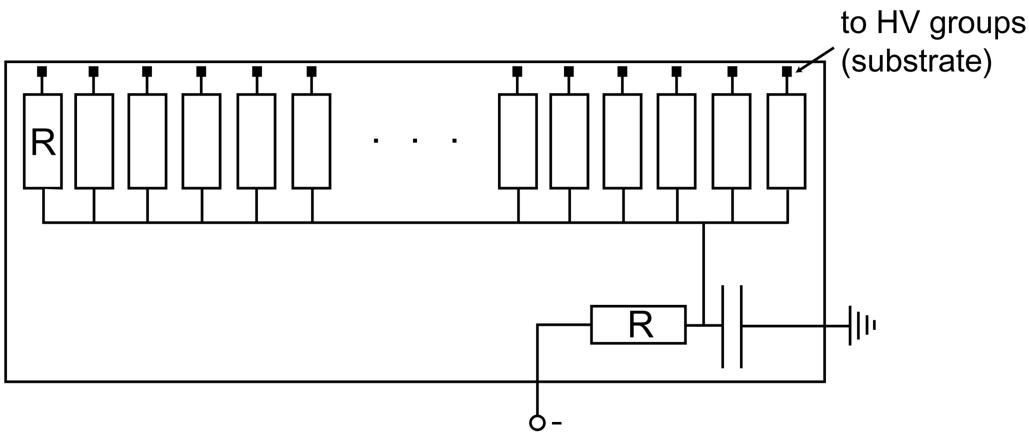

Figure 138 - HV connection circuit for the MS-9 type detector modules. R = 1MΩ.

E CLEANING PROCEDURES

Substrates and drift cathodes

The part requiring the most careful cleaning is the substrate. Even microscopic spoils or dust particles can modify the detector module's electric field, and decrease the performance. The first step after the cutting of the substrate is therefore the optical inspection with a microscope. All faults in the artwork and broken strips due to the production process and cutting are recorded.
The next step is cleaning with deionised water in an ultrasonic bath. This is done for 15min with a temperature of 50°C. The side of the glass plate carrying the artwork is on the bottom. This assures that dust particles or glass splinters from the cutting fall off the substrate. After the cleaning, the MSGC is dried with nitrogen.
The glass drift cathodes used for GEM4, GEM5 and the forward prototype module were cleaned in the ultrasonic bath, too. This was done to remove glass chips created in the cutting process. The foil drift cathode used for GEM6 was only dusted off by flushing with dry nitrogen.

GEM

Just like the substrates, the GEM foils are first inspected visually. For the very first detector modules, namely GEM4 and GEM5, the cleaning procedure with deionised water in the ultrasonic bath was performed, too. Since HV tests with both cleaned and 'fresh-from-the packet' GEMs showed no difference in performance, this cleaning step was abandoned. Only thorough flushing with dry nitrogen was used for the latest detector modules.

Frames

All frames are first cleaned with isopropyl alcohol. This removes not only small fragments and dust from the milling process, but fat and grease from the handling of the parts, too. This is extremely important, since a clean surface is necessary for proper gluing. Then the parts are cleaned with deionised water in the ultrasonic bath.

F SUBSTRATE AND GEM LAYOUTS

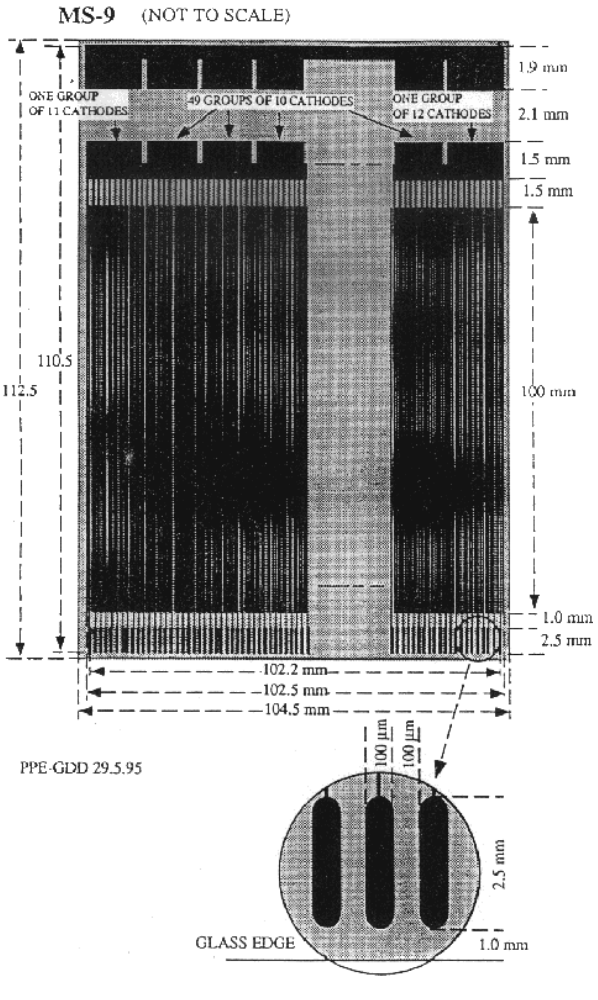

Figure 139 - Layout of the MS-9 MSGC substrate.

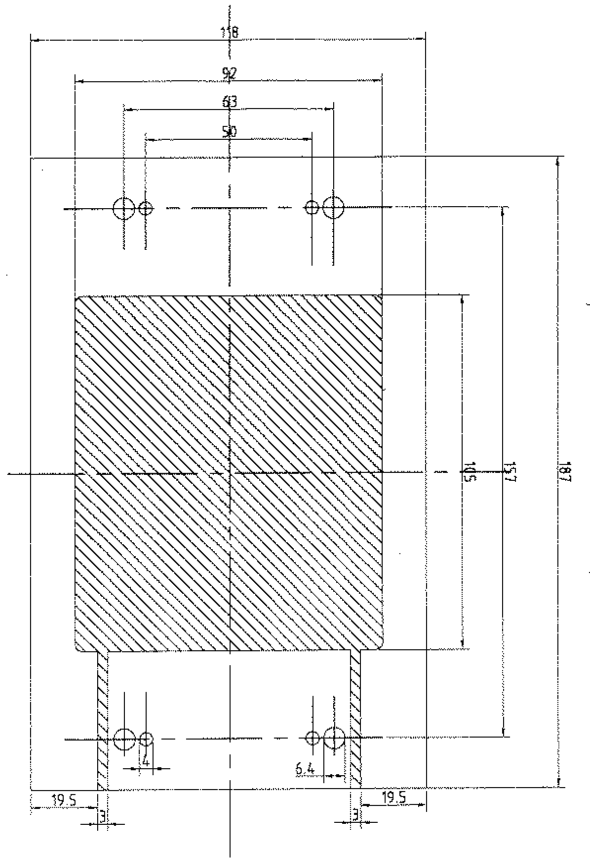

Figure 140 - The GEM Layout used for all MS-9 type detectors (GEM4-GEM6).

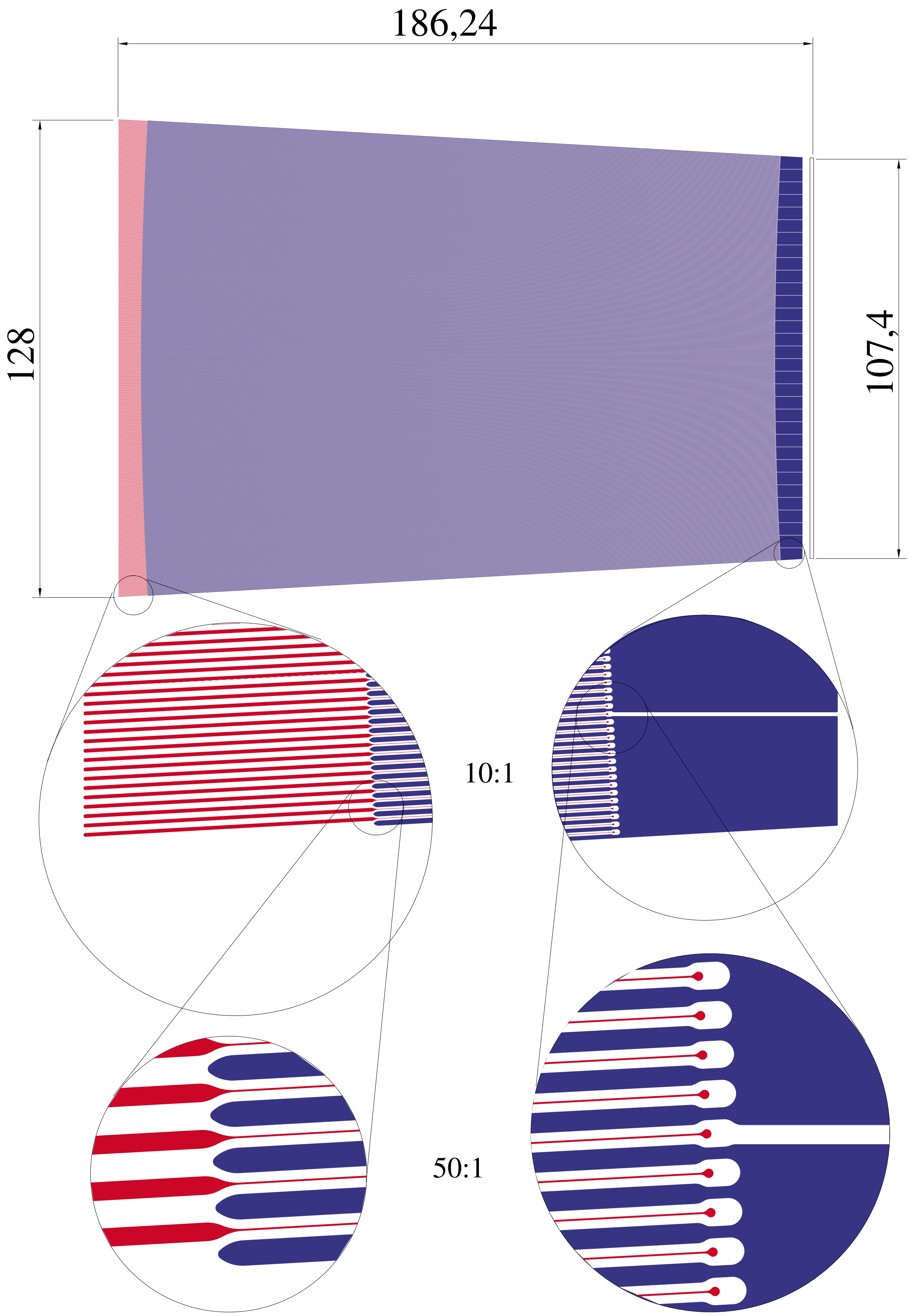

Figure 141 - Layout of the substrate for the CMS forward prototype module.

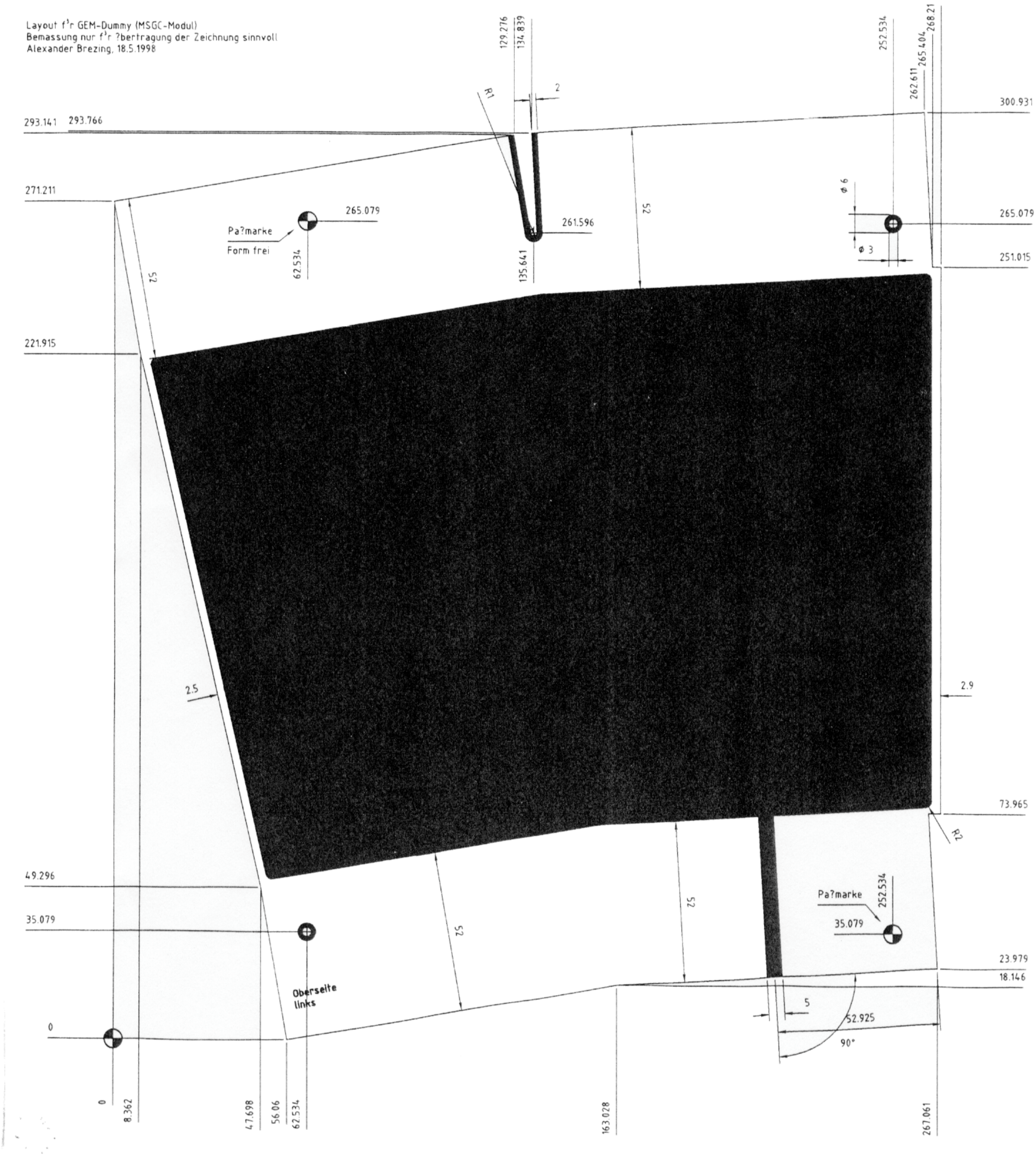

Figure 142 - The layout of the GEM foil used for the CMS forward prototype module.

G MECHANICAL PARTS

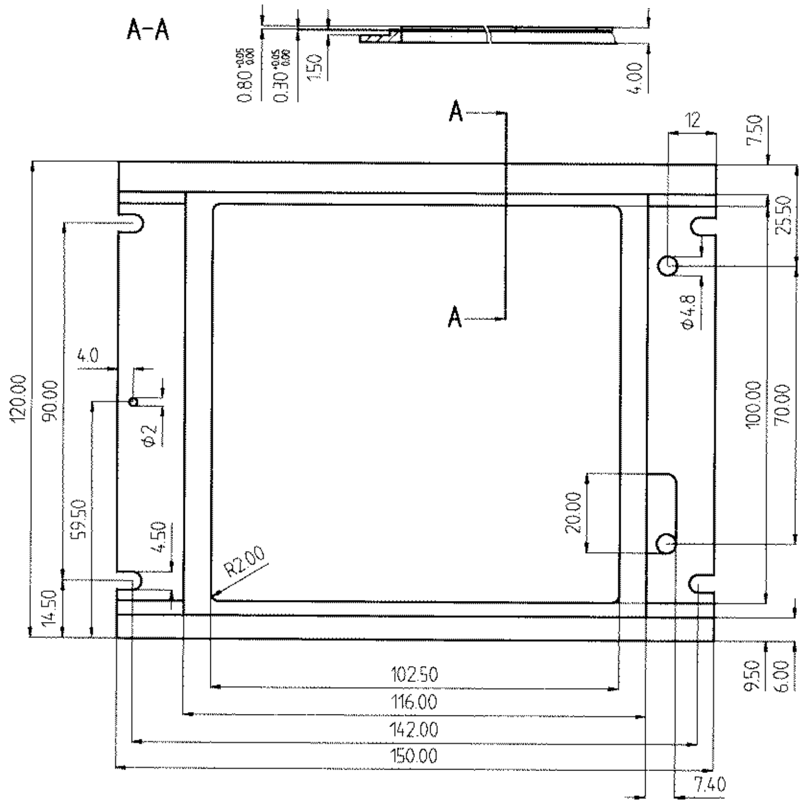

Figure 143 - Base plate of the MS-9 type modules.

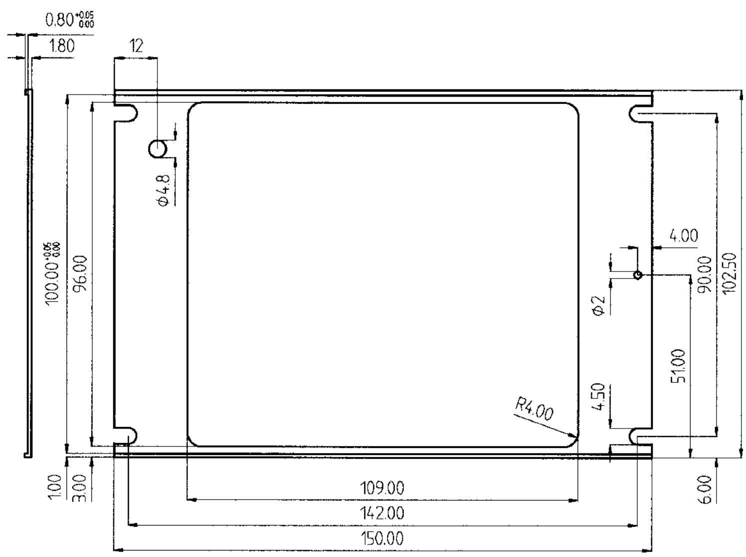

Figure 144 - Lower spacer frame defining the transfer region.

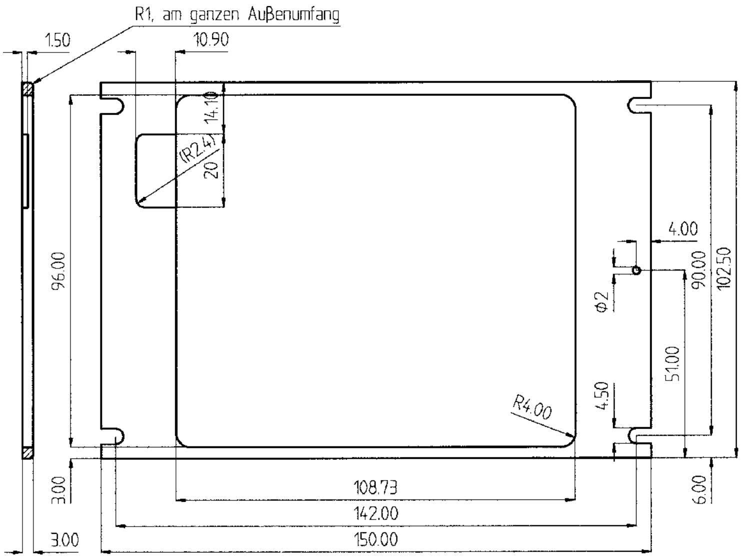

Figure 145 - Top frame of the MS-9 type modules. This part defines the drift space.

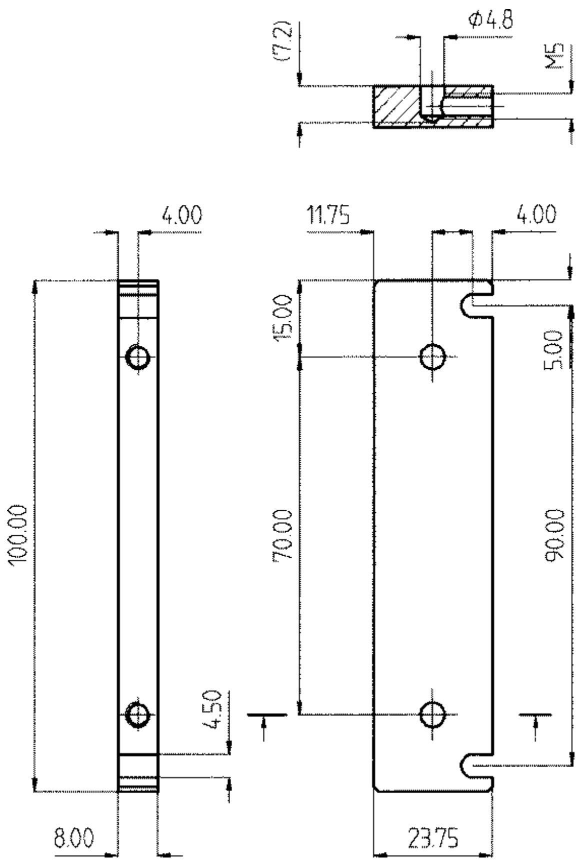

Figure 146 - This part is glued under the base plate (figure 143) and hold the gas fittings.

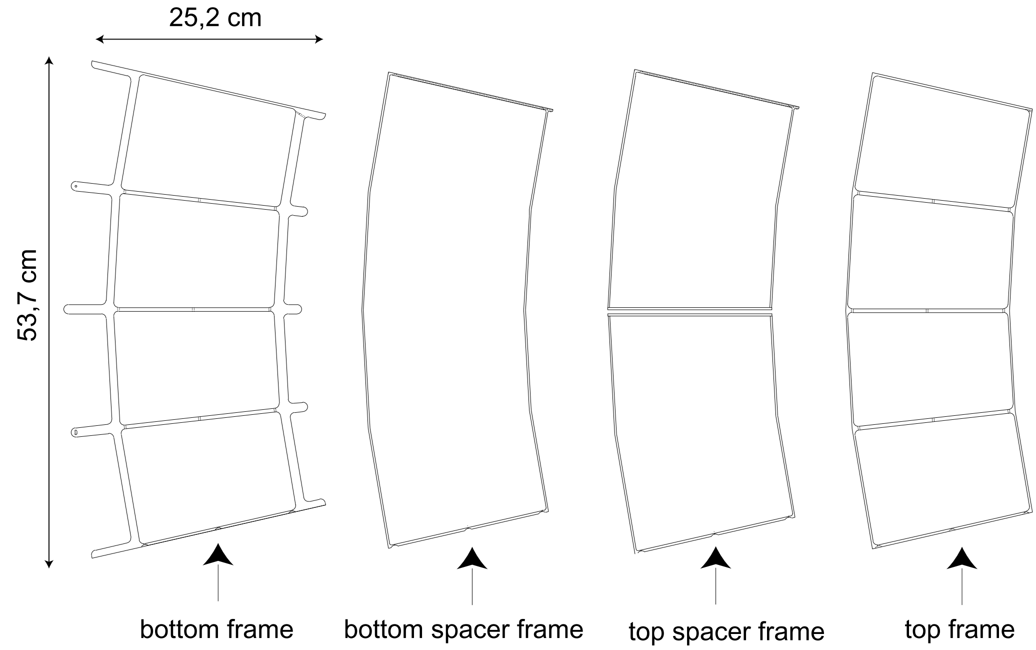

Figure 147 - The parts for the CMS forward prototype. All frames except the top spacer frame are identical to the modules used for the CMS milestone experiment **[45]**. A more detailed description, including finite element simulations for mechanical stresses, can be found in **[16]**.

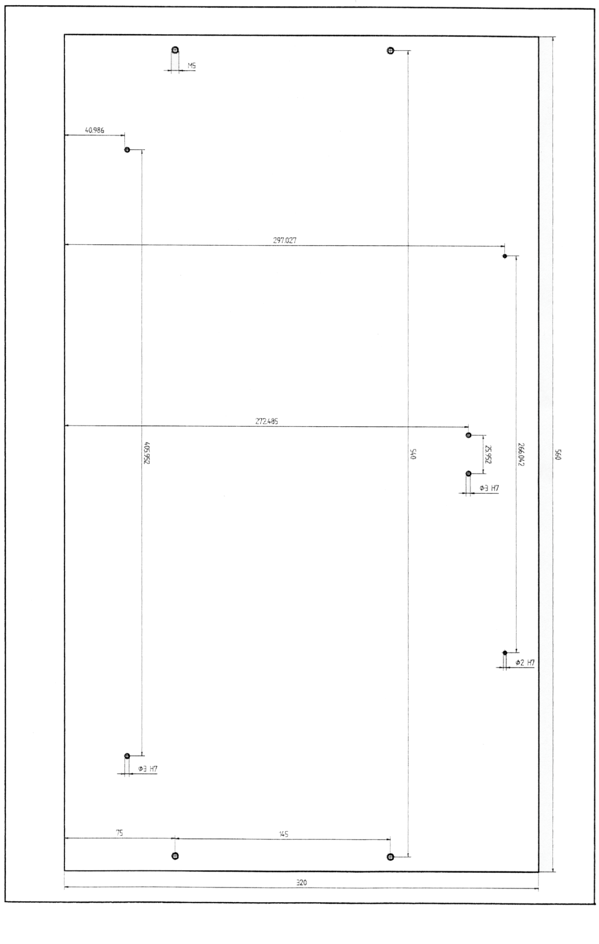

Figure 148 - Gluing jig for the CMS forward module. Precision pins are inserted into the holes. The GEM (appendix F, figure 142) has precision holes which fit to the pins. The foil is aligned to the top spacer frame that way.

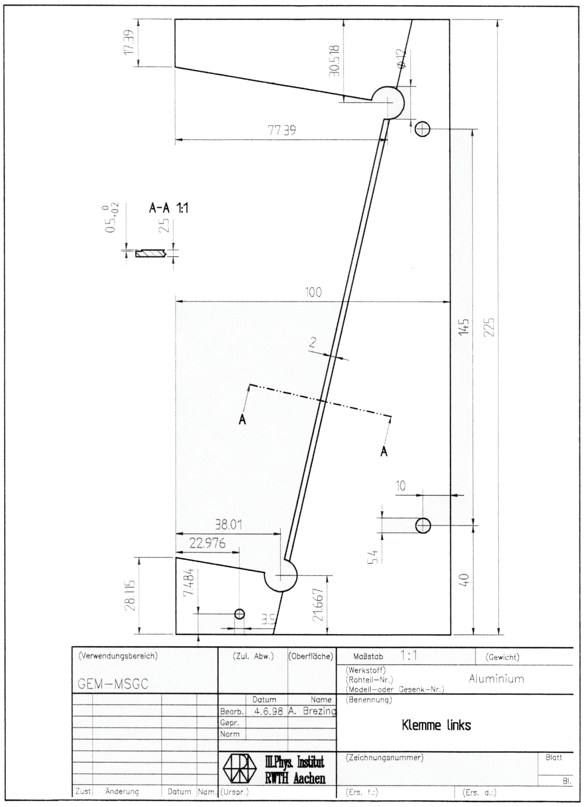

Figure 149 - Clamp to position the top spacer frames on the gluing jig (figure 148). This is the left side version. A corresponding item for the right hand side exists, too.

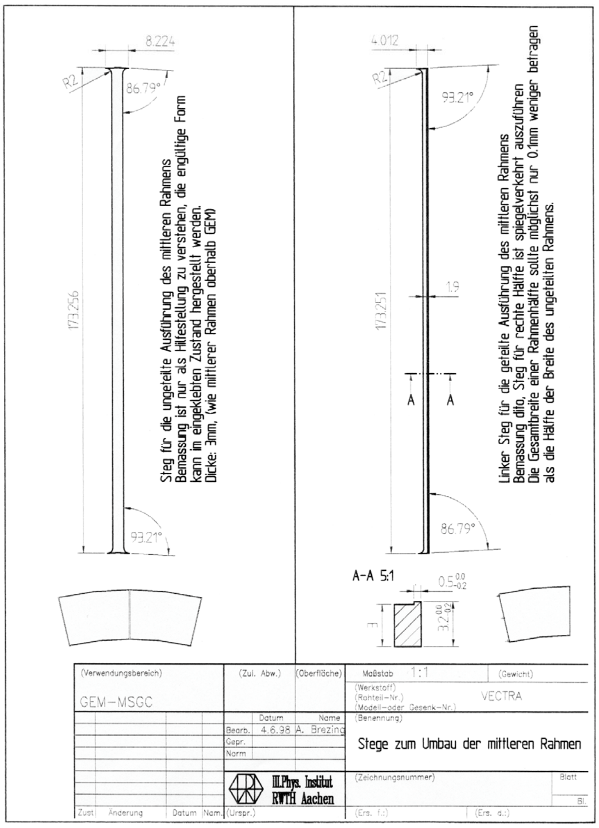

Figure 150 - The middle bars of the top spacer frame. They are used to jam the flaps of the GEMs foils.

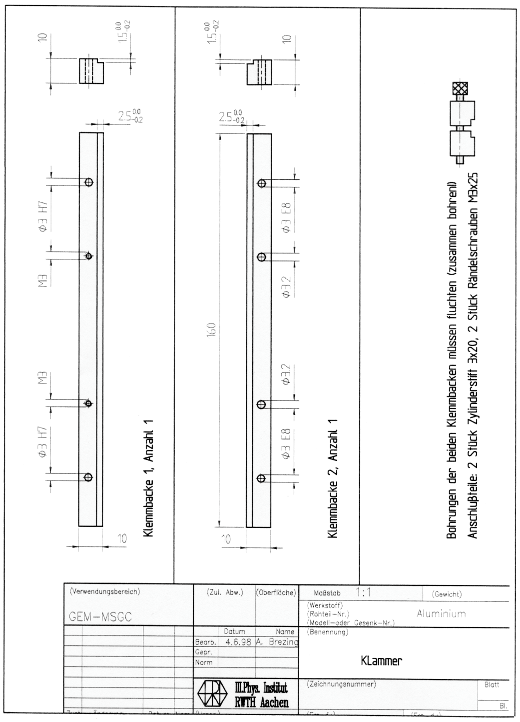

Figure 151 - Clamp to hold the two parts of the top space frame together while gluing.

H FORWARD PR O TOTYPE MODULE ASSEMBLY

All parts are cleaned according to the procedures described in appendix E. At first, the substrates are cut. This is a delicate process, since the cut has to be done with a position accuracy of 5µm. The reason for this requirement is the layout of the detector module: Since four substrates are placed side by side in a forward module, the cuts on the substrates have to be done in a way not modifying the pitch between consecutive MSGC plates. Since this is not possible due to the roughness of the glass plates' edges, the space of one anode is left out between the substrates. For each 513th anode the pitch is doubled that way. After cutting, the substrates have to be aligned on the bottom frame. Special care has to be taken to ensure that the outermost strips on neighbouring substrates are parallel. This is done by a fibre optic alignment system, developed for this purpose **[47]**. Since only a region of ≈ 10cm diameter can be irradiated in the test beam facilities, only half of the module is equipped with substrates – the other half is made of glass plates.

After the substrates are glued to the bottom frame, they are sealed gas tight from the back with EPO93L. The bottom spacer frame is then glued on top of the substrates. Since this large and thin PEEK piece is very flexible, a mounting tool is necessary. This consists of an aluminium plate, which has a negative of the bottom spacer frame engraved on it. The engraving has a depth of only 1mm. The PEEK frame is put into the aluminium plate, and kept in shape that way. The bottom frame with the glued substrates is then fixed on another aluminium plate with two precision pins, which keep the frame in place. The plate with the spacer frame is then lowered on top of the substrates. The alignment with respect to the bottom frame is done by the precision pins. The spacer frame is glued in the exact position and shape to the bottom frame by that procedure. The aluminium plates are removed after curing of the glue. Figure 152 shows the pre-assembled 'lower' part of the module.

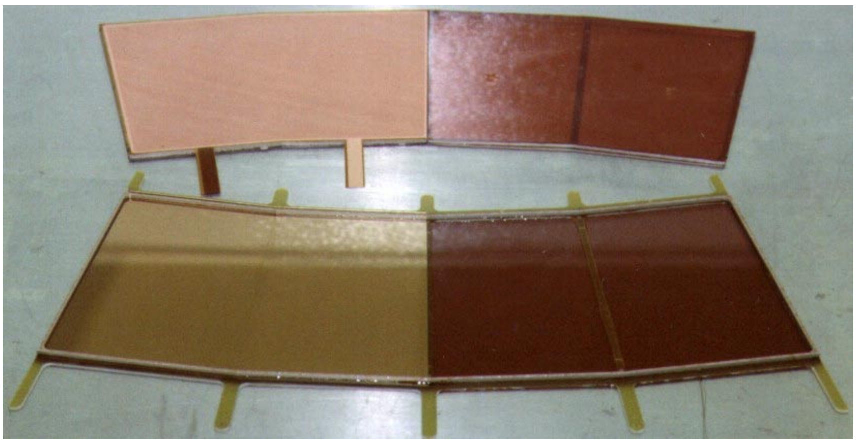

Figure 152 - The pre-assembled module halves. The upper part of the module consisting of the drift cathodes, drift region, top frame and GEM can be seen on top of the picture. The lower half of the module, made of the substrates, bottom spacer frame and bottom frame, can be seen on the bottom.

The next step is the assembly of the so-called ‘upper’ part of the detector module. First of all, the GEM foil has to be mounted. Due to limits imposed on the geometry by the production centre, the GEM had to be split in two parts. The layout of the GEM foil, which is depicted in appendix F, figure 142, was chosen in a way that only one type of foil had to be produced. Thus two of the foils could be laid side by side to form the complete foil. To safely connect the two parts at the intersection, a flap has been foreseen. It can be seen in figure 142 on the left. This flap is folded upwards and jammed between the middle bars of the two-part top spacer frame (appendix G, figure 147).

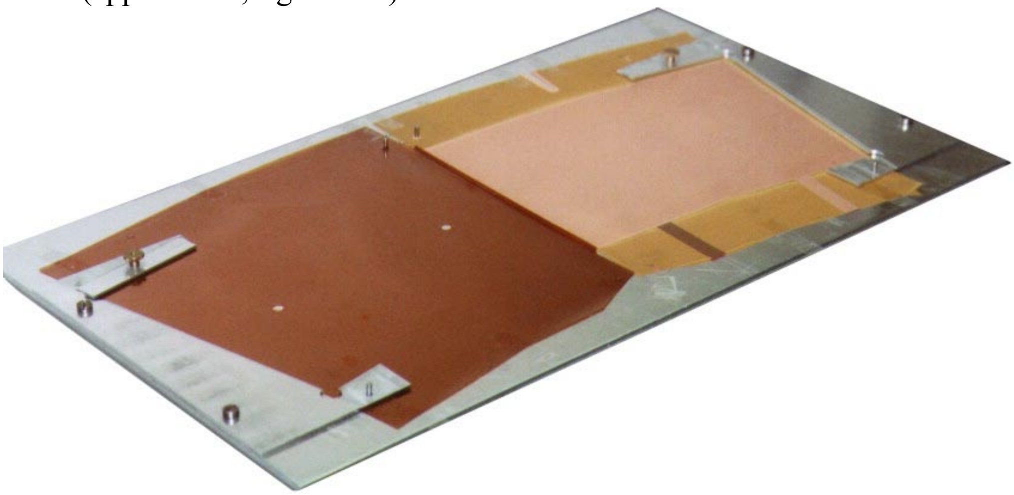

Figure 153 - The two-part GEM foil mounted ready for assembly. Like for the substrates, only half of the detector module is equipped with a GEM. A mock-up foil, made of uncoated Kapton, is used for the other half.

The two parts of the GEM are then mounted on a gluing jig. A drawing of this aluminium plate can be found in appendix G, figure 148. Since only half of the detector module is equipped with substrates, only one half of the GEM+MSGC is equipped with a real GEM foil, too. A mock-up, made of bare Kapton, has been used for the other half. The foils are positioned on the jig by means of two precision pins for each half. The pins fit into precision holes produced with the same accuracy as the GEM channels. The holes in the foils are copper-enforced to avoid ripping of the material when stretching the GEMs. The two parts are then flatly stretched and fixed by adhesive tape. Figure 153 gives an impression of the jig with the GEM. The two upward bent flaps can be seen in the middle. Now two aluminium brackets are mounted on top of the foils. These are used to keep the top spacer frame’s two PEEK parts in shape. The shape of the brackets exactly fits the small sides of the spacer frame. Drawings for the brackets and frames can be found in appendix G, figures 147 + 149. The frames are now glued on top of the foils. The flaps are jammed in between the two middle bars (appendix G, figure 150) of the top spacer frames.

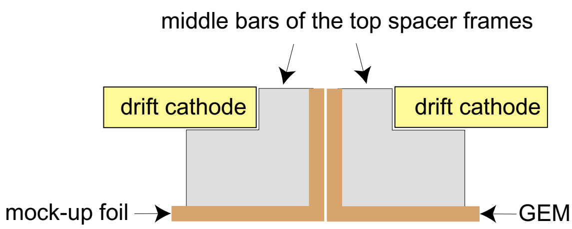

Figure 154 - Schematic cross section of the intersection of the GEM foils. The mock-up foil, coming from the left, and the GEM, coming from the right, have upward-bent flaps. The middle bars of the top spacer frames jam those flaps between them.

Figure 154 shows a schematic cross section of the intersection of the two foils. The two upward-bent flaps of the mock-up foil (left) and GEM (right) are in the middle of the figure. After putting the two parts of the top spacer frame into the brackets and jamming the foils, the two middle bars are pressed together by a clamp, depicted in appendix G, figure 151. This tool is removed after curing of the glue. Figure 155 shows the assembled foils and parts of the top spacer frame. The clamp to hold the spacer frame together while curing of the glue is still in place.

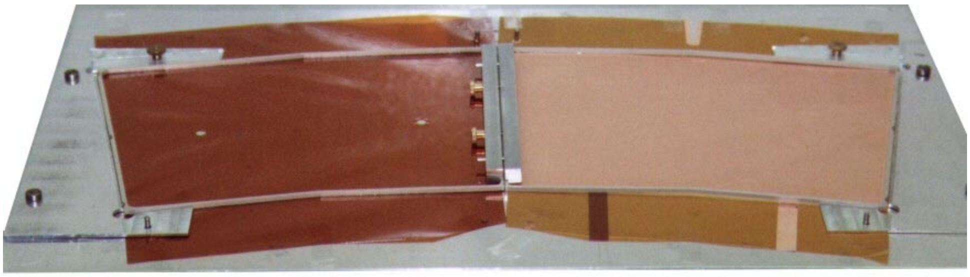

Figure 155 - The assembled GEM and top spacer frame.

Now the drift cathodes are glued on top of the structure. They are enforced by the top frame, which is glued onto them.

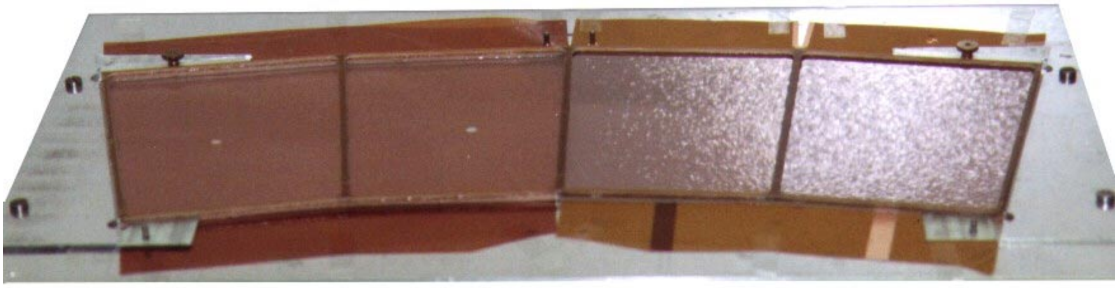

Figure 156 - The upper half of the forward module with the drift cathodes and the top frame.

Like the GEM and the substrates, only half of the detector module is equipped with ‘real’ drift cathodes. Bare D263 glass plates are used for the other half. This structure is now rigid enough to keep the top spacer frames’ PEEK parts in shape. All parts can be removed from the gluing jig and the GEM is cut to size.

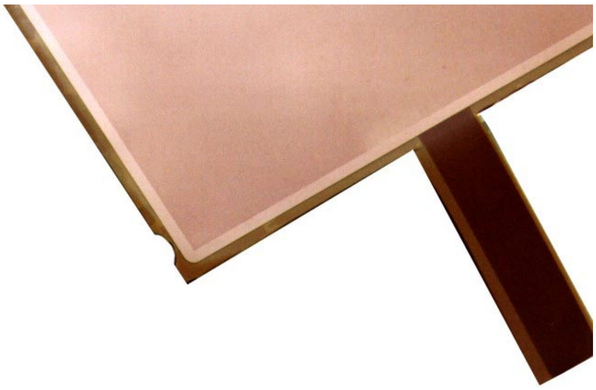

Figure 157 - Photograph of one corner of the GEM. It is already glued to the top spacer frame. The small border around the area with the holes can be noted. It can be seen, that the frame is not glued to the copper surface of the GEM.

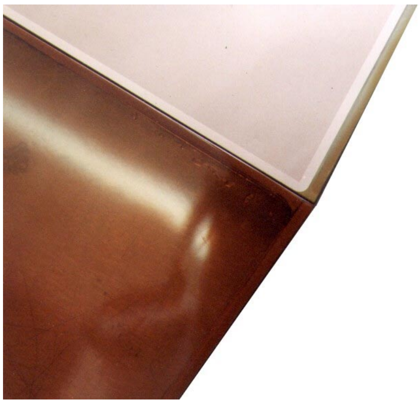

Figure 158 - The middle region of the upper module part. The interconnection between the two halves of the GEM foil can be seen. On the lower side, only bare polyimide is present, since a mock-up foil was used there.

Figures 157 and 158 show details of the cut-out GEM: in the first photograph a corner of the upper module half can be seen. The good quality of the alignment of the frames with respect to the artwork on the GEM foil is apparent: The frame is glued on the polyimide-only part of the foil. The glue does not stick well on metal and the durability of the structure is increased that way. Figure 158 shows the intersection of two parts of the GEM. If two 'real' foils would have been used, only the bottom metallisations of the two parts would be in contact. The upper sides would be isolated from each other by the polyimide flaps. Electrical problems and short circuits at the intersection are avoided that way.
The upper and lower module halves are glued together finally. The last assembly step is the application of the Kapton foil on the top and bottom frames.

Figure 159 - The completed CMS forward GEM+MSGC module.

The upper Kapton foil is cut in a way that two flaps remain on each of the small sides of the module. They are folded around the frames and are glued onto the lower foil. This provides the gas flow as depicted in figure 50. All grooves between the frames are sealed with glue from the outside. Figure 159 shows the complete forward GEM+MSGC module. The readout electronics and HV connection boards are already mounted. Two copper HV connection pads for the GEM can be seen on top of the photograph. The only parts still missing are the gas connection lines, which are glued into appropriate holes in the frames.

I GAS SYSTEM

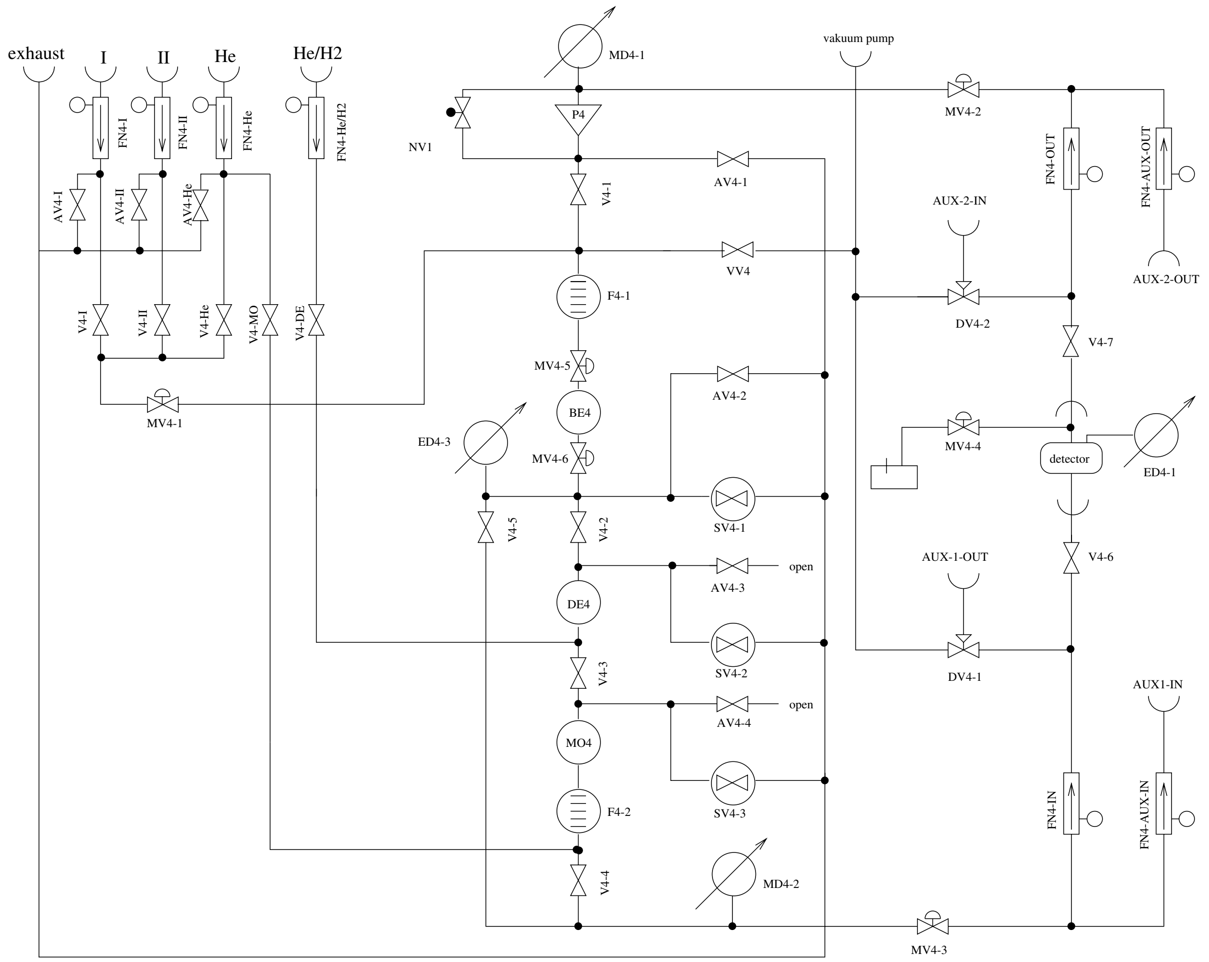

Figure 160 - Diagram of the gas system.

J CALIBRATION OF THE CURRENT MONITORS

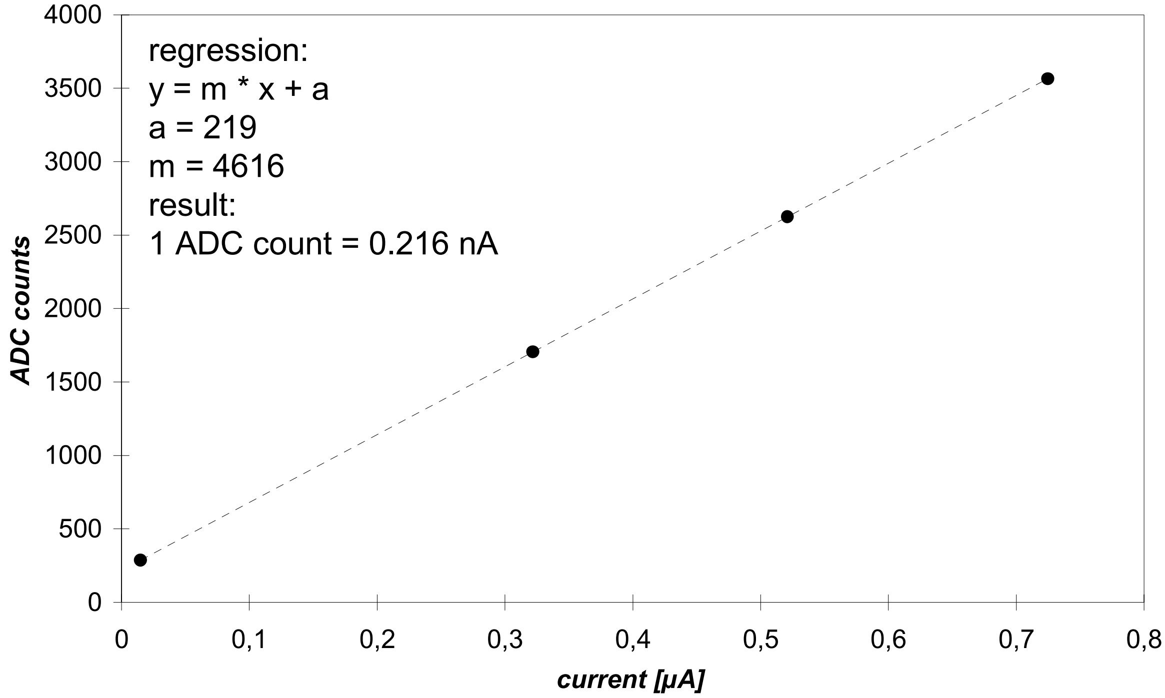

Figure 161 - Calibration of the substrate current monitor

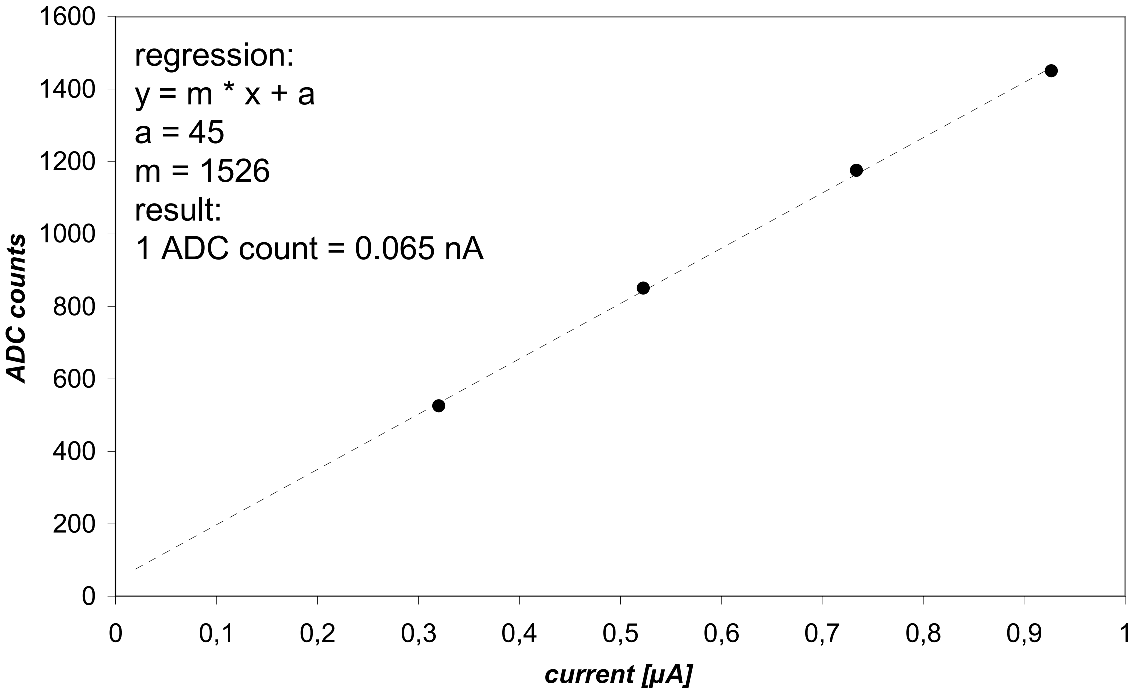

Figure 162 - Calibration of the GEM current monitor

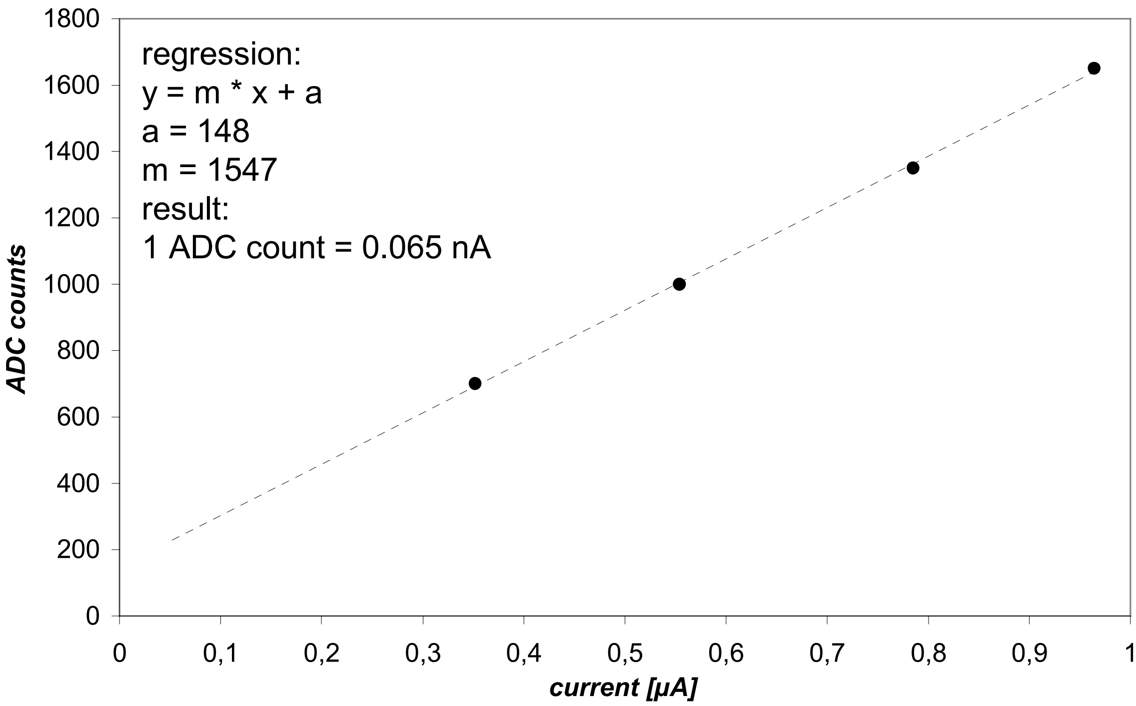

Figure 163 - Calibration of the drift cathode current monitor

Acknowledgements

In the first place, I wish to thank Prof. Flügge for the possibility to work on the exciting topic of GEM+MSGCs. I appreciated most your trust and encouragement during the first year of this work, when it was not apparent that these devices would ever reasonably work. I would like to thank Priv.Doz.Dr. Struczinski especially for the helpful discussions. You were always at hand to think even about the weirdest theories about transparency...

Dr. Reiner Schulte is the one who keeps everything together in the Aachen gas detector group. Thanks for your support in all parts of my work at the institute, and for taking the major load of all the organisational issues.

Nothing of the lab measurements would have been possible without the help and support of Dr.Commichau, Mr. Beißel, Dr. Hangarter and Mr. Camps. Thanks for building all the electronic devices and your help in understanding how the fronted electronics worked. Or at least, how they were supposed to work.
Of same importance was the help of the people in the mechanical workshop, namely Mr. Boffin, Mr. Bock and Mr. Jahn. Thanks for your patience with last-minute changes, 'I need this yesterday'-jobs and my unskilled drawings. All the tools built for the lab and beam tests were made possible by your good ideas and advice.

It was a great time to work with Sebastian and Oliver and see the group evolve. I will never forget all the weeks we spent at test beam experiments or our photo session at the lake Geneva during the April 1997 test beam. I wish to credit 'manic miner' Jürgen for PETRA, and Christof for the tracking software and his help at the September 1998 test beam.

The construction of the GEM+MSGCs would not have been possible without the help of Alex Brezing, who contributed to the MS-9 type detector design and helped with the realisation of the GEM foils' layouts.

It was always great to work with Andreas, first on detector modules, and later on the LabVIEW and IRIS programs. All the best for your thesis!
Matthias made the April 1999 test beam a lot of fun, and helped to make the timely analysis of the data possible. No Hurricane could ever stop us (and I hope to face some more!).
It was a pleasure to work with Anette, especially during the June 1999 test beam. All the best for the future.

It was a good time working together with the CMS MSGC forward collaboration (in no particular order): Demetrios, Catherine, Pascal, Christophe, Valery, Valerie, Francesca, Laurent, Michel, Didier, Gerard, Hans-Jürgen, Peter, Wolf-Hagen, Manuel, Dirk, Kurt, the Franks of Karlsruhe, Lev, Andrei, Alexei, Wim, Amina, Isabelle and Isabelle. It was also great to work together with the barrel group, namely Gloria, Luca, Nick, Sandro, Ronaldo and Ariella. I wish to say a particular heartily 'thank you' to Jean-Marie Brom, Walter van Doninck and Thomas Müller – you gave me a lot of support, far beyond the scope of the CMS experiment. Thanks to Peter Mättig, who always made participation on the test beam experiments possible. Piero Giorgio and Frederic were a great help for the DAQ at all the X5 test beams. In fact, the two are the DAQ. Sort of.

All the bonding jobs were done by Ogmundur Runolffsson. Thank you for finding always the time to help us.

Curriculum vitae

Name:	Dirk Macke
Date and place of birth:	19.5.1971 in Mönchengladbach – Neuwerk, Germany

Educational record:

1977-1981	Primary school “Hubertusschule” in 47877 Schiefbahn, Germany
1981-1990	St. Bernhard Gymnasium (High School) in 47877 Willich, Germany
1990	Abitur
1990-1996	Study of physics, University of Technology Aachen, Germany
1992	Vordiplom
1996	Diplom – “Bau eines Hodoskops zur Untersuchung von Mikrostreifengasdetektoren”
Since October 1996	Staff and PhD student at the III.Physikalisches Institut B, University of Technology Aachen, Germany